# THE CHARACTERISATION OF THE INTERACTION BETWEEN ATMOSPHERIC AEROSOL AND WATER VAPOUR

A thesis submitted to the University of Manchester
for the degree of Doctor of Philosophy
in the Faculty of Engineering and Physical Sciences

2010

Martin Irwin
School of Earth, Atmospheric and Environmental Sciences

# Contents

Word Count: 41,282

# Abstract

Understanding the interaction between atmospheric aerosol and water vapour is key in assessing the impacts of anthropogenic influences on the earth's radiative budget, both directly through scattering and absorbing incident solar radiation, and indirectly through changing cloud properties, with considerable uncertainty in the magnitude of the estimated forcings of the latter. Although aerosol particle water uptake is well defined for inorganic compounds, the effects of the aerosol organic fraction on cloud droplet formation and cloud condensation nuclei (CCN) properties are relatively poorly characterised, due to the large number of organic compounds present in atmosphere and their highly complex influences on properties such as water solubility and surface tension.

This thesis presents extensive field measurements of CCN/aerosol hygroscopicity from three different environments, together with a novel error model, which has been developed to propagate instrumental uncertainties from measurements in the sub- and supersaturated regimes through to commonly used data products used in large-scale models. This study illustrates that a single hygroscopicity framework is not able to reconcile the measurements within errors, for different measurement environments. The sensitivity of this type of reconciliation study was assessed using several different scenarios, making different assumptions in each case; sensitivity tests using a 'typical regional aerosol particle water uptake or number-size distribution, demonstrate that it is not possible to apply a constant correction to data to guarantee reconciliation, that the best reconciliation was achieved for size-resolved high-temporal water uptake and aerosol number-size distribution data, and that the application of single-parameter hygroscopicity models requires further examination. It is concluded that high-temporal size-resolved measurements of sub- and supersaturated particle water uptake are fundamental to providing a thorough characterisation of the interaction between atmospheric aerosol and water vapour, and are essential in order to achieve the best possible predictive capability from large-scale models.

# Declaration

No portion of the work referred to in this thesis has been submitted in support of an application for another degree or qualification of this or any other university or other institute of learning.

# Copyright

# Acknowledgements

I would like to thank my parents for their continual support, both emotionally and financially over the duration of my life to this point. I hope I have made you proud. I'd like to thank my brother for his support, mostly through the medium of computer games, over the last few years. You were the best flat mate I ever had. I would also like to thank Charlie for her help and support during the latter and more difficult part of my Ph.D. You give me the confidence to grab what I want in life with both hands.

Many thanks to my supervisor, now Professor, Gordon McFiggans for his support, 'tough love' and inspiration. Though the Ph.D has been a rollercoaster of such magnitude to put Alton Towers to shame, Gordon's passion for the subject matter never dwindles and he is constantly striving for answers, even at 2am - cheers for the emails! Many thanks to James Allan for his beard-twiddlingly-good© impromptu Igor Pro tutorials, assistance in numerous field campaigns, for always being at the end of an MSN conversation and for '*Mentos and Coke*'. Thanks to Dave, for putting up with my endless questioning, for helping me right down to the wire and for someone to talk to about Japanese cars. Thanks to everyone at the University of Manchester that I had the pleasure of getting to know over the course of my Ph.D. Special thanks to Jonny for some very memorable times during the COPS campaign, to Nick for your help fixing instruments at all hours, to Niall for your support in OP3 through some pretty dark times and to James Dorsey, Keith and Mike for effectively teaching me how to set up and install an entire aerosol characterisation study single handedly.

Special thanks to all of the people involved in all of the field projects I have taken part in, the memories will stay with me forever. Special thoughts go to Kate. The world is a different place without you, but you have provided me with daily motivation to finish this work.

Finally, '*arigatō gozaimasu*' to Keito and Tomohiro, for letting me stay with you between the OP3 campaigns. '*Ganbatte*' to both of you for your studies! Special thanks to Stefan for umpteen motivational emails and all the White Russians! I look forward to seeing you all next year in Japan!

I was supported by a National Environmental Research Council (NERC) Ph.D Studentship NER/S/A/2006/14036.

# 1 Introduction

The term aerosol is defined as solid and/or liquid particles suspended in a gaseous medium. The majority of atmospheric particulate matter is confined to the lowest region of the Earth's atmosphere; the troposphere (Seinfeld and Pandis, 1998), where around 80% by volume is confined to the planetary boundary layer (PBL, < circa 2km; Heintzenberg, 1989). Atmospheric aerosols, whilst ubiquitous in the Earth's atmosphere, are location dependent in terms of number, size and composition. The rich variety of particles seen throughout the atmosphere can be attributed to both natural and anthropogenic sources and sinks and governed by various transport regimes (Pandis et al., 1993; Raes et al., 2000; Rodriguez, 2004; Andreae and Rosenfeld, 2008). This variation in number, size and mass in addition to the wide range of physicochemical properties of atmospheric aerosol, results in significant impacts on air quality and risks to respiratory health through their inhalation (Dockery and Pope, 1994; Kittelson, 1998), and atmospheric chemistry and clouds, with wider implications on a climatic scale (Aalto, 2004; Forster et al., 2007).

The amount of carbon dioxide in the atmosphere has grown from 280 to over 379ppm (in 2005), since the beginning of the Industrial Revolution in the late 18th Century, mainly due to the burning of fossil fuels and changes in land-use (IPCC, 2007). Likewise, there has been substantial increase in the amount of other greenhouse gases such as methane and nitrous oxide. Though it is accepted that this increase in greenhouse gas levels is causing the Earth's average surface temperature to rise, other factors both contributing and counteracting this effect make it difficult to accurately estimate the rate of this rise. One of these factors, currently credited with the largest uncertainty, is the aerosol indirect effect on climate; the modification of cloud properties by anthropogenic particulate emissions

(Forster et al., 2007).

Clouds play an essential role in the Earth's hydrological cycle, scavenge both gaseous and particulate matter, affect the redistribution of trace compounds, provide a medium for aqueous-pahse chemical reactions and have significant impact on the Earth's radiation budget (Seinfeld and Pandis, 1998). Clouds comprise numerous super-micron sized droplets which govern their ability to reflect sunlight back into space and prevent the loss of longwave surface radiation. A cloud's reflectivity, or albedo, is dependent on its optical depth, which is a function of cloud droplet number concentration, liquid water content and thickness. For the same liquid water content (LWC), an increase in aerosol number may lead to an increase in cloud droplet number, which in turn could lead to an increase in cloud reflectivity resulting in a negative forcing (Twomey, 1974, 1977). Furthermore, an increase in aerosol number for the same LWC may result in smaller droplets which have a lower terminal velocity and are therefore less likely to coalesce and form raindrops, leading to a decrease in precipitation and thus longer lifetime (Albrecht, 1989). More recently however, it has been shown that the second indirect effect is less trivial and is dependent on variable parameters such as the magnitude of the updraft velocity and the shape of the cloud nucleus spectrum, which can change cloud droplet concentrations further complicating predictions of drizzle formation, evaporation, dynamical feedbacks and net forcing (Feingold et al., 1996, 1997; Feingold and Cotton, 1999; Feingold and Kreidenweis, 2000). Due to the diversity of the effects of anthropogenic emissions on cloud droplet formation, is essential to understand the interactions between atmospheric aerosol and water vapour in order to improve climate model predictions of global warming.

The subset of the atmospheric aerosol that activate into cloud droplets at atmospherically attainable supersaturations ($<$ ca 2%; Hudson, 1993) are commonly termed cloud condensation nuclei (CCN, Seinfeld and Pandis 1998). CCN populate air masses over both ocean and land, and are typically several tens of nanometre and upwards in diameter. Observations show continental air masses to be richer in CCN concentration than maritime air masses (Pruppacher and Klett, 1997), though the fraction of aerosol that has the propensity to act as CCN may be higher (Squires and Twomey, 1966; Roberts et al., 2001). An aerosol particle's ability to take up water and subsequently activate is determined by its size and composition. Cloud droplet formation is very well characterised for water soluble inorganic compounds such as sodium chloride (e.g. particles formed from

sea spray) and ammonium sulphate (e.g. particles formed from gaseous anthropogenic emissions), however the role of multicomponent aerosol particles in cloud droplet formation is less well understood, largely resulting from the presence of organic compounds. Such components are ubiquitous with large variability in physicochemical properties.

The rich variety of atmospheric particulate matter results from their numerous physical, chemical and biological sources both natural and anthropogenic. Atmospheric aerosol sources are commonly divided into two categories; primary and secondary. A primary source is one from which particulate matter is mechanically generated, i.e. directly emitted. Natural primary aerosols include soil dust, sea salt, volcanic dust and biological debris. Secondary aerosol typically refers to those produced via gas-to-particle conversion processes such as binary homogeneous nucleation, heterogeneous nucleation and condensation (Twomey, 1977). Examples of natural secondary aerosol include sulphates from biogenic and volcanic gases and organic matter from biogenic volatile organic compounds (VOC) (Fitzgerald, 1991; O'Dowd et al., 1997). Organic material can be directly emitted from sources or produced from atmospheric reactions involving gaseous precursors. Goldstein and Galbally (2007) estimate there to be 10,000 to 100,000 different organic compounds that have been measured in the atmosphere. The complexity of the organic fraction is compounded further by the fact that each VOC can undergo a number of atmospheric degradation processes to produce a range of oxidised products which may or may not contribute towards secondary organic aerosol (SOA) formation and growth (Hallquist et al., 2009).

As a result of the wide variety of sources and atmospheric lifetimes of atmospheric aerosol, their composition varies widely within each size distribution. The distribution of the constituent chemicals amongst the aerosol is defined as the mixing state. For example, a population of particles of an identical composition (identical mole fraction of components) would be described as being an internal mixture. If a population of particles comprised particles of two or more compositions, it would be an external mixture. The mixing state greatly affects the aerosol's physicochemical behaviour. Particles of different compositions will absorb gases such as water vapour differently, leading to some particles growing in size due to condensation. Typically the atmospheric aerosol is an external mixture of quasi-internally-mixed particles, with multiple compositions spanning the size distribution. This has been illustrated by measurements of the hygroscopicity

of the aerosol (its capacity to take on water), which have shown a wide variability in aerosol mixing states with respect to aerosol water uptake (Swietlicki et al., 2008). An aerosol which appears to be internally mixed (i.e. comprising one composition), is unlikely to be of homogeneous composition throughout. Some organic compounds are surface active i.e. tend to concentrate on the droplet surface and decrease surface tension (Li et al., 1998). However, it has been shown by theoretical, laboratory and field studies that the partitioning of the surfactant between the bulk and the surface not only has to be considered when evaluating the surface tension effects, but also the effects on droplet concentration (Sorjamaa et al., 2004; Prisle et al., 2008; Fors et al., 2010). Numerous other studies, both experimental and theoretical, confirm the diverse effects of atmospheric organic compounds on CCN activation (e.g. Hansson et al., 1998; Facchini et al., 2000; Cruz and Pandis, 2000; Hori et al., 2003; Lohmann and Feichter, 2005; Ervens et al., 2007; Rose et al., 2010).

The work presented in this thesis focusses on characterising the interactions between ambient atmospheric aerosol and water vapour. In particular, the objectives include conducting particle water uptake measurements from different environments in both the sub- and supersaturated regimes, attempting to reconcile these measurements to within instrumental uncertainty using a popular single parameter hygroscopicity model (**Paper I, II and III**) and the comparison of the results for these reconciliation studies (**Paper IV**).

## 1.1 Particle Water Uptake

Water vapour is abundant in the atmosphere and as such plays an important role in the processing of atmospheric aerosol. The relationship between water vapour and particulate matter can be modeled using well established theoretical constructs.

The equilibrium distribution of material between the gas and condensed phase can be described by Raoult's law (Eq. 1.1), which states that the vapour pressure of an ideal solution is dependent on the vapour pressure of each chemical component and the mole fraction of the component present in the solution:

$$p_X = p_X^* x_X \tag{1.1}$$

where $p_X$ is the partial pressure of the compound $X$, $p_X^*$ is the vapour pressure

of the pure component $X$ and $x_X$ is the mole fraction of compound $X$ in solution (Seinfeld and Pandis, 1998). In more simple terms; the greater the concentration (mole fraction) of $X$, the greater the equilibrium vapour pressures above the solution. Raoult's law only applies to ideal solutions (where the enthalpy of mixing is zero - i.e. no loss of energy during mixing).

In reality, it is possible to have hundreds or thousands of compounds in atmospheric aerosols and this complex mixture of a wide range of chemical components, with varying strengths of solution, meaning that most solutions are non-ideal and thus deviations from the idealised Raoult's Law are required. The multi-component aqueous solutions in the atmosphere will comprise water ($H_2O$) and one or more solute.

The equilibrium position is found when the Gibbs free energy of the system is minimised. The Gibbs free energy, $G$, can be represented by:

$$G = U + pV - TS \tag{1.2}$$

where $U$ is the internal energy of a system, $p$ is the pressure, $V$ is the volume, $T$ is the temperature and $S$ is the entropy.

Differentiating Equation 1.2:

$$dG = dU + pdV + Vdp - TdS - SdT \tag{1.3}$$

and substituting $U$ for the standard chemical potential, $\mu_x = \left(\frac{\partial U}{\partial n_X}\right)_{S,V,n_j}$ we obtain:

$$dG = -SdT + Vdp + \sum_{x=1}^{k} \mu_X dn_X \tag{1.4}$$

where $n_X$ is the number of moles of compound $X$. The chemical potential can also be represented in terms of the Gibbs free energy:

$$\mu_i = \left(\frac{\partial G}{\partial n_X}\right)_{T,p,n_j} \tag{1.5}$$

A solution is defined as ideal if the chemical potential of every component is a linear function of the logarithm of its aqueous mole fraction according to the relation:

$$\mu_X = \mu_X^*(T,p) + RT \ln x_X \tag{1.6}$$

where $\mu_X^*$ is the standard chemical potential of pure compound $X$ (i.e. $x_X = 1$) at temperature and pressure $(T, p)$ and $R$ is the universal gas constant.

The equilibrium between the gas and the condensed phase $H_2O(g) \rightleftharpoons H_2O(aq)$ can be energetically represented as:

$$\mu^\circ + RT \ln p_w = \mu^* + RT \ln a_w \tag{1.7}$$

where $p_w$ is the water vapour pressure and $a_w$ the water activity in solution. For ideal solutions, water activity is simply the mole fraction, but for non-ideal (i.e. real atmospheric) solutions an activity coefficient is required. As water vapour is so abundant in the atmosphere, at equilibrium the water activity in the condensed phase is the same as RH/100 for a flat surface, where RH is the relative humidity; the amount of water vapour in a gaseous mix of water vapour and air. RH is usually expressed as a percentage and water activity is usually expressed as a value between 0 and 1 (i.e. pure water has a water activity of exactly 1).

For simplicity, the previous discussions of equilibrium water content have assumed that the aqueous aerosol solution has a flat surface. In reality, aerosol particles cannot be treated as such; they are of small enough diameter that their shape plays an important factor. The surface available to the exchange process is determined by the aerosol's surface area. It can be assumed that a wet aerosol in solution will be spherical in shape, and as such the curvature in the surface changes the vapour pressure, increasing it to above the saturation value over a flat solution of condensates above the solution. This change in the vapour pressure is known as the Kelvin effect and will approach a value of 1 as the droplet diameter approaches infinity (but is often neglected above 100nm) and thus the curvature decreases. It can be expressed for the generalised Köhler equation (described in detail in 1.1.2) for component $X$:

$$p_X = p_X^\circ exp\left(\frac{4\sigma M}{RT\rho D}\right) \tag{1.8}$$

where $p_X$ is the vapour pressure of compound $X$, $p_X^\circ$ is the partial pressure of $X$ over a flat surface, $\sigma$ is the surface tension, $M$ is the molecular weight, $\rho$ is the density of the droplet and $D$ is the diameter of the droplet. The Kelvin

effect tells us that the vapour pressure over a curved surface always exceeds that of the same substance over a flat surface (Seinfeld and Pandis, 1998). In physical terms, there are fewer molecules in the gas phase adjacent to molecules in the aqueous droplet with increasing curvature.

### 1.1.1 Hygroscopic growth

Aerosol particle water uptake is dependent on the ambient relative humidity. The hygroscopicity of a particle describes its equilibrium water content at a known humidity (Hallquist et al., 2009). If we consider a dry ($< 20\%$RH) inorganic salt particle, as the ambient RH increases the particle will remain solid until a critical relative humidity is reached, at which the particle will spontaneously absorb water. This phase transition is referred to as the deliquescence relative humidity (DRH; Seinfeld and Pandis, 1998).

As a particle takes on water, it will grow to larger sizes. A particle's growth factor, GF, is defined as the wet particle diameter, $D_p$, divided by the dry particle diameter, $D_0$:

$$GF = \frac{D_p}{D_0} \tag{1.9}$$

The change in particle growth factor with increasing RH for three inorganic salts is shown in Fig. 1.1. The deliquescence point (DRH) of $(NH_4)_2SO_4$ at STP is $79.9 \pm 0.5\%$, before which the particle growth factor remains unchanged with increasing RH. Increasing the RH still further, the now wet particle diameter increases exponentially.

If the RH is then decreased, the wet particle solution does not crystallise at the DRH. Rather, if we follow the efflorescence (water loss) branch of the growth factor/humidity profile, we reach a point of crystallisation around 40% RH. This hysteresis phenomenon is not the same for all inorganic compounds; e.g. the very hygroscopic salt $H_2SO_4$ shares the same smooth deliquescence and efflorescence branches with both increasing and decreasing ambient RH (shown also in Fig. 1.1) as it is always a liquid and therefore cannot deliquesce or effloresce.

### 1.1.2 Köhler theory

Aerosol particle hygroscopic growth can be described by Köhler theory (Köhler, 1936), connecting the water vapour saturation above the surface of a droplet to

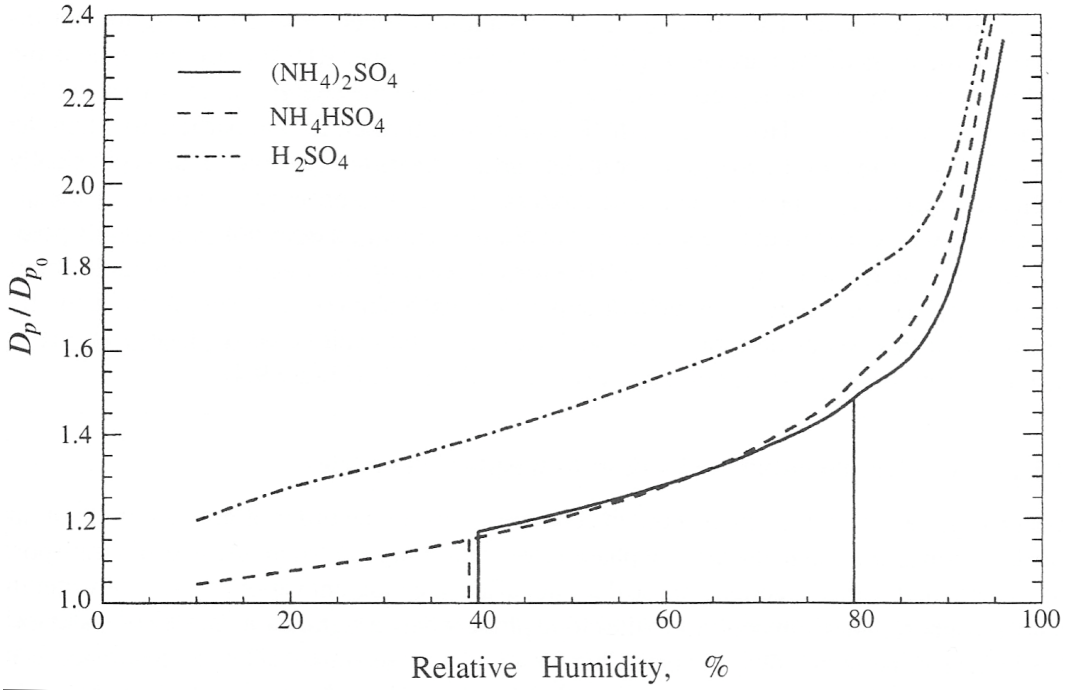


Figure 1.1: Particle growth factor changes as a function of ambient relative humidity. Taken from Seinfeld and Pandis (1998).

the droplet diameter. This can be regarded as the general equilibrium relation for two phases separated by a curved interface (Pruppacher and Klett, 1997). If we begin with Equation 1.7, for pure water $a_w = 1$ and $p_w = p_{w,sat}$ (the saturation vapour pressure of water), at temperature $T$:

$$\mu^{\circ}_{H_2O} - \mu^{*}_{H_2O} = RT \ln p_{w,sat} \tag{1.10}$$

Substituting Equation 1.10 into Equation 1.7 leads to:

$$a_w = \frac{p_w}{p_{w,sat}} \tag{1.11}$$

As previously discussed, the relationship between the partial pressure and saturation vapour pressure of water vapour is the relative humidity:

$$a_w = RH \tag{1.12}$$

However, over a curved surface, the Kelvin effect (Eq. 1.8) increases the equilibrium vapour pressure over a droplet of a given composition. Thus for a specific

saturation ratio of water vapour, the equilibrium water activity reduces:

$$a_w = \frac{RH}{K_e}, \text{where } K_e = \exp\left(\frac{4v_{aq}\sigma}{RTD}\right), \text{and } v_{aq} = \frac{M_w}{\rho_w} \tag{1.13}$$

where $v_{aq}$ is the partial molar volume of water in the solution and $\rho_w$ is the density of water and $M_w$ is the molecular weight of water.

In ideal solutions the partial molar volume is equal to the molar volume of pure water, also known as the volume additivity assumption (Seinfeld and Pandis, 1998). Whilst a more accurate expression accounts for the derivative of the density with respect to mole fraction of water (e.g. Kreidenweis et al., 2005), for organic solutions, in particular, the idealised assumption of volume additivity has to be employed as empirical data is lacking (Topping et al., 2005b).

Equation 1.13 can be rearranged to its more conventional format:

$$\frac{p_w}{p_s} = a_w \exp\left(\frac{4M_w\sigma}{RT\rho D}\right) = a_w \exp K_e \tag{1.14}$$

This is the general form of the Köhler equation, coupling the Raoult and Kelvin terms described previously.

If we picture an aerosol particle, as the RH is increased towards 100%, the droplet size increases accordingly. For a fixed dry diameter, the Raoult term approaches 1 with increasing wet droplet diameter as the concentration of the droplet solution decreases (pure water has a water activity of 1). If the RH is above 100%, the regime is said to be supersaturated with respect to water vapour. In this regime, the Köhler equation is dominated by the Kelvin term, though the relative importance of the Kelvin term and Raoult term switches as we approach droplet activation. The Kelvin term approaches unity with an increasing droplet size as the surface of the droplet becomes less curved, reducing the water vapour supersaturation above the droplet as more water vapour condenses onto the aqueous droplet.

The solid line in Figure 1.2 denotes the sum total of the Kelvin and Raoult terms and is commonly referred to as the Köhler curve. The maximum supersaturation shown on the curve is referred to as the critical supersaturation, $S_c$, which is associated with the droplets critical radius, $r_c$ (or critical diameter, $D_c$). Once a droplet grows beyond its critical diameter (i.e. as the ambient $S$ increases above $S_c$), the droplet will exhibit unimpeded runaway growth unless the ambient $S$ reduces below the equilibrium value of $S$ at the instantaneous value of $D$

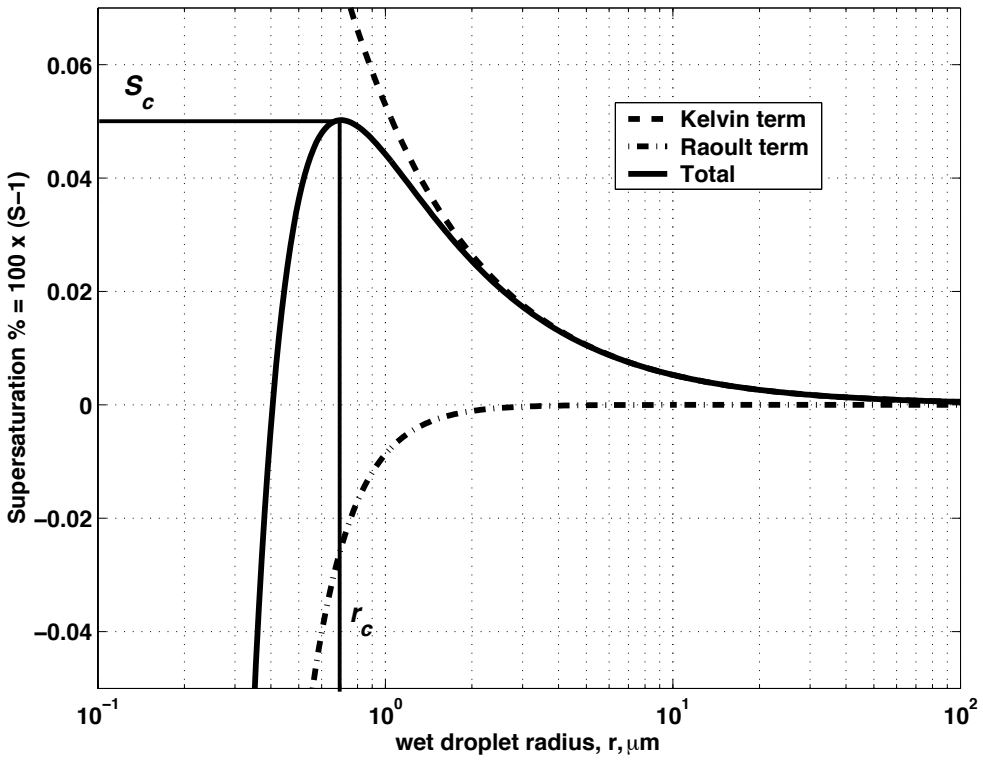


Figure 1.2: The Köhler equation can be envisaged as the competition between the curvature (Kelvin) term and the solute (Raoult) term (McFiggans et al., 2006).

(McFiggans et al., 2006).

## 1.2 Reconciliation

Aerosol particle hygroscopic growth and droplet activation may be probed in both laboratory and field measurements using the Hygroscopicity Tandem Differential Mobility Analyser (HTDMA) and CCN counter (CCNc) respectively, described in detail in Chapter 2. Deriving the critical supersaturation for ambient measurements from their hygroscopic growth using Köhler theory and comparing the measured and modeled critical supersaturations constitutes a CCN reconciliation study, often referred to as CCN closure. The level of agreement achieved determines the level of confidence in our understanding of the processes underpinning hygroscopic growth and activation.

As previously discussed, organic matter is ubiquitous in the atmosphere, comprising a significant fraction of the ambient aerosol. The hygroscopic growth of SOA has recently been investigated in chamber studies, with no observed efflorescence or deliquescence behaviour (Baltensperger et al., 2005; Varutbangkul et al., 2006; Duplissy et al., 2008b). The chamber studies of Baltensperger et al. (2005) and (Duplissy et al., 2008b) reported an increase in hygroscopic growth with aging time, consistent with the oxidation of the SOA particles during the aging process. Furthermore, an increased hygroscopic growth was found for a decreasing chamber VOC concentration (Duplissy et al., 2008b), which may be explained by partitioning of higher volatility compounds to the aerosol at high concentrations, decreasing the VOC precursor and hence molecular abundance of partitioning organics and aerosol loadings down to atmospherically relevant values, resulting in an increased hygroscopic growth factor (Hallquist et al., 2009). Humic-like substances are often used as model compounds for SOA, and have shown similar hygroscopic growth (Gysel et al., 2004; Baltensperger et al., 2005; Wex et al., 2007).

Calculating the water content for a droplet is possible provided the water associated with all components is accounted for. Data is readily available for inorganic systems of atmospheric importance but are seldom available for atmospherically representative organic compounds, and thus models have been used to predict the water activity in the aqueous organic solution (Hallquist et al., 2009). The Zdanovskii, Stokes and Robinson (ZSR; Stokes and Robinson, 1966) mixing rule is based on semi-ideality, which states that the total aerosol water content at a particular water activity (relative humidity) can be obtained by summing the contributions by the individual species. The use of ZSR allows the growth factor for a mixture to be estimated from the sum of the growth factors of the individual components of the aerosol and their respective volume fractions. Models invoking ZSR assume that the particles are spherical and there is no volume change upon mixing, and that there is independent water uptake by organic and inorganic components. Though some laboratory studies have shown the ZSR relationship to be valid within experimental uncertainty (Choi and Chan, 2002; Sjogren et al., 2008), there are studies which show deviation from ZSR (Cohen et al., 1987; Svenningsson et al., 2006). Furthermore, there are few studies where HTDMA measurements were performed in tandem with sufficiently detailed chemical measurements to allow for full hygroscopic reconciliation.

Organic molecules may influence both the Raoult and Kelvin terms of the Köhler equation through their effect on water activity and droplet surface tension. Similarly to the hygroscopic properties of SOA in chamber experiments, VanReken et al. (2005) observed an increasing critical supersaturation with aging time for SOA from several biogenic precursors, though the opposite was observed by Duplissy et al. (2008a) (though the HTDMA measurements for each case were in agreement with CCNc measurements).

For inorganic systems, where the required data is available, the Köhler equation can be solved by minimising the Gibbs free energy (e.g. Wexler and Clegg 2002; Topping et al. 2005a). Topping et al. (2005a) introduced the Aerosol Diameter Dependent Equilibrium Model (ADDEM), providing a thermodynamic modeling framework to predict the equilibrium behaviour of mixed inorganic salt aerosols, coupled with a technique for finding a solution to the Köhler equation. ADDEM can be used to model organic-aqueous aerosol using a well established mole fraction based activity model UNIFAC (Topping et al., 2005a). This model is proven to work well for the inorganic fraction, but the inclusion of organic material and its interaction with other material (in particular, other solutes) is hindered by a lack of experimental data (Topping et al., 2005b). Single-component and some multi-component particles have been successfully modeled with simplifications of Köhler theory (Raymond and Pandis, 2002, 2003; Svenningsson et al., 2006), but the applications of these theories require all properties of all the compounds to be known (Shulman et al., 1996; Kulmala et al., 1997)

Calculations of water activity have generally been based on Raoult's law, which states that water activity equals the mole fraction of water in solution. Approximations of water activity are required due to the wide variety of atmospheric aerosol constituents. Rissler et al. (2004) achieved good agreement between predicted and measured CCN concentrations by using an approximation of the Köhler equation focussing on the number of soluble molecules/ions available for condensation of water vapour, applied to HTDMA growth factor measurements at 90% RH. For each dry size measured, the number of soluble molecules or ions, in the individual particles was calculated in an approach similar to Brechtel and Kreidenweis (2000), Covert et al. (1998) and Zhou et al. (2001). The mixing state was accounted for by performing the calculation for each hygroscopic group. The soluble volume fraction was estimated from the HTDMA data, assuming a particle density of a known inorganic salt and the

surface tension of water (therefore also negating possible influences of surface active compounds). Only the Raoult term (water activity) is dealt with using this approach, though the importance and influences of the Kelvin term in predicting CCN concentrations are a topic of much debate (e.g. Sorjamaa et al., 2004; Cubison et al., 2008; Wex et al., 2008; Wang et al., 2010).

Robinson and Stokes (1959) describe the water activity of a substance in an aqueous solution to be:

$$a_w = \exp\left((\phi v n_s)/n_w\right) \tag{1.15}$$

where $\phi$ is the osmotic coefficient (accounting for the non ideality of the solution), $v$ is the number of ions per solute molecule, and the number of solute and water molecules $n_s$ and $n_w$ respectively. Wex et al. (2007) take this approach to define an ion density parameter $\rho_{ion}$, which represents the number of ions (or moles is not dissociated) that can go into solution per volume of the dry substance:

$$\rho_{ion} = (\phi v \rho_s / M_s) \tag{1.16}$$

$\rho_{ion}$ can be calculated for measured equilibrium diameters (i.e. HTDMA growth factor data). The full Köhler equation (Eq: 1.14) is used to calculate the equilibrium diameters and growth factors of a particular compound (e.g. HULIS; Wex et al., 2007) above 80% RH, and $\rho_{ion}$ is varied until the calculated hygroscopic growth factors were equal to the measured values. To probe the effects of possible reductions in the surface tension of the droplets (as this approximation is Raoult-term based), upper and lower boundaries of surface tension were used ($\sigma_{H20} = 72.5\text{mNm}^{-1}$ and $\sigma_{HULIS} = 50\text{mNm}^{-1}$). A dependence of $\rho_{ion}$ on RH was found, implying a dependence of $\rho_{ion}$ on the concentration of HULIS in the droplets. $\rho_{ion}$ increases with increasingly dilute solutions (Wex et al., 2007), indicating a change in the osmotic coefficient, $\phi v$. The calculation of the osmotic coefficient from organic functionality requires precise information of the organic species within the aerosol, which is difficult as there many thousands of organic species present in the ambient atmosphere (Goldstein and Galbally, 2007), and size-resolved Aerosol Mass Spectrometer data are determined in terms of mass and not number (Canagaratna et al., 2007). Furthermore, the AMS doesn't measure molecular components, rather reports summed organic mass or, at best, specific organic factors.

Petters and Kreidenweis (2007) also developed a single parameter hygroscopicity model based on Köhler theory, called the $\kappa$-Köhler model. The hygroscopicity parameter $\kappa$ represents a quantitative measure of aerosol water uptake characteristics and CCN activity. Similar to $\rho_{ion}$, $\kappa$ is defined through its effect on the water activity of the solution:

$$\frac{1}{a_w} = 1 + \kappa \frac{V_s}{V_w} \tag{1.17}$$

where $a_w$ is the water activity, $V_s$ is the volume of the solute and $V_w$ is the volume of water. Part of the versatility of this model is its applicability to both sub- and supersaturated regimes, i.e. data on hygroscopic growth factor and CCN activity may be used to derive $\kappa$. The derivation of $\kappa$ is different from that of $\rho_{ion}$ as the latter is tied to the choice of an assumed model salt with which to base the prediction, whereas $\kappa$ is tied to an assumed surface tension, typically that of water and temperature, often 298.15K. $\kappa$ values usually fall between 0 and 1 with higher values representing more hygroscopic particles and $\kappa = 0$ representing wetting by pure water, shown in Figure 1.3. As with $\rho_{ion}$, it is possible to derive critical supersaturation from hygroscopic growth factor using a constant $\kappa$ and is therefore suitable for reconciliation studies.

The current detection limit for diameter growth factor measurements of 1.02 translates to a minimum in $\kappa \leq 0.006$ (Petters and Kreidenweis, 2007). For compounds such as adipic or succinic acid, no water uptake is observed in the sub-saturated domain, though their CCN activity derived $\kappa$ is large ($\kappa \geq 0.1$). The solubility of these compounds is small and thus the water activity of the saturated solution is large, thereby raising the deliquescence relative humidity. Therefore, the CCN activation is controlled by the solubility limit instead of its intrinsic hygroscopicity and will not observe the $-3/2$ rule shown in Figure 1.3 (Petters and Kreidenweis, 2007). However, as the majority of the ambient aerosol is internally mixed to some degree (Murphy et al., 1998), it has been postulated to be unlikely that compounds such as these should influence the reconciliation abilities of the $\kappa$-Köhler model (Petters and Kreidenweis, 2007), though it is possible that there are slightly soluble compounds that will only be soluble at water content above that at the RH of the HTDMA but below that in the CCNc.

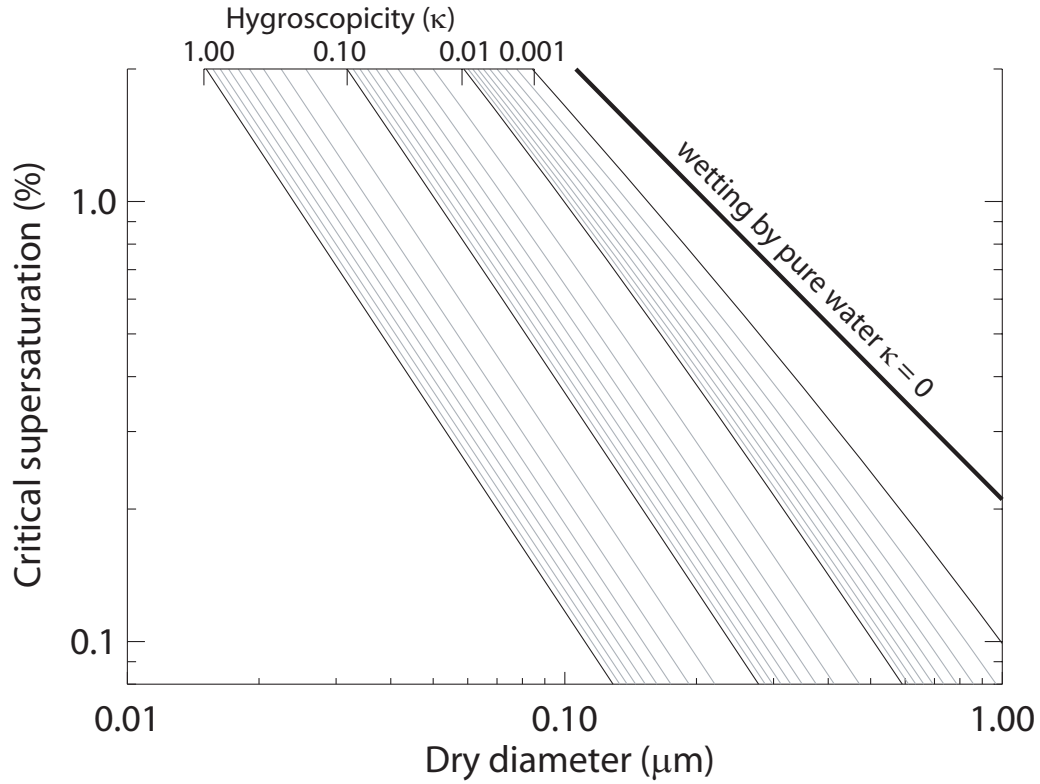


Figure 1.3: The $\kappa$-Köhler model calculated critical supersaturations for $0 < \kappa < 1$ computed for $\sigma = 0.072\text{Jm}^{-2}$ and T= 298.15K. The grey lines are linearly spaced intermediates. Taken from Petters and Kreidenweis (2007).

The assumption of the surface tension of water ($\sigma = 0.072\text{Jm}^{-2}$) in the $\kappa$-model was based on the successful reconciliation (within instrumental uncertainties) of fulvic acid (Petters and Kreidenweis, 2007), even though it is known that this surface active compound reduces surface tension in bulk samples (Svenningsson et al., 2006). The inclusion of surfactants will lower droplet surface tension as they reduce the efficiency of hydrogen bonds in water, therefore reducing the critical supersaturation and increasing the number of activated droplets thus increasing cloud albedo (Facchini et al., 1999). However, if partial or complete partitioning of these compounds between the bulk and the surface phase within the droplet occurs in the ambient atmosphere, the Raoult term will be reduced due to the reduction of the number of molecules in solution (Sorjamaa et al., 2004; McFiggans et al., 2006), possibly offsetting the effects in the Kelvin term or even resulting in an increased critical supersaturation when considering these

effects (Sorjamaa et al., 2004).

As $\kappa$ attributes a single value to the aerosol, its dependence on composition cannot be ignored. Typical values for $\kappa$ are an upper limit of 1.4 for most hygroscopic species found in the atmosphere (e.g. sodium chloride), and $\kappa \leq 0.2$ for organic species (Petters and Kreidenweis, 2007). Where the aerosol is dominated by organics (up to 90% of the total aerosol concentration), reconciliation ability has been shown to be highly sensitive to $\kappa$ (Wang et al., 2008), and therefore accurately representing $\kappa$ in a larger model is key to their success. Furthermore, the ability to reconcile HTDMA and CCNc measurements is highly dependent on the RH of the growth factor measurement, as Kreidenweis et al. (2008) show that for RH $< 90\%$ there are significant ($> 20\%$) deviations between measurement and prediction using the $\kappa$-model even for highly soluble marine aerosol. The relative simplicity of these hygroscopicity models is required for their inclusion in large scale models to assess anthropogenic impacts on climate for regional and global scales. Thus, it is important that the simplifications include an accurate description of the complex processes involved.

# 2

# Measurements of Aerosol Properties

## 2.1 Particle Number, Size and Composition

### 2.1.1 Particle Number

The ability to count aerosol particulate matter in realtime has been commercially available for some time. The condensation particle counter (CPC; e.g. TSI 3776) can count particles with dry diameters as low as 2.5nm, by growing sampled particles before counting them optically. Butanol is the most common chemical used within CPCs as it will grow particles of both polar and non-polar chemicals. However, more recent technical advances have allowed continuous-flow CPCs (e.g. TSI 3786) to use water as a condensing fluid to enlarge submicrometer particles to sizes typically greater than 1$\mu$m, which are then large enough to be counted optically.

### 2.1.2 Particle Number and Size

As CPCs grow the aerosol particles in order to count them, they are not an appropriate instrument to measure the aerosol particle size. In order to provide information on the number-size distribution of the aerosol population, a common technique is to couple a differential mobility analyser (DMA) to a CPC (Knutson and Whitby, 1975). The DMAs used in **Papers I and II** are of the Vienna design, introduced by (Winklmayr et al., 1991). The device consists of a hollow, earthed cylinder with a concentric rod in the centre, to which a positive voltage is applied. Before entering the DMA, the polydisperse aerosol distribution is passed through a charge neutraliser (typically $^{85}$Kr or $^{210}$Po), which ensures a

well-defined Fuchs charge distribution amongst the particles. The number of multiply charged particles can be predicted base on the measured number of singly charged particles of the same electromobility (Fuchs, 1963; Wiedensohler, 1987). A particle free airstream known as the 'sheath' air passes up the space between the central rod and the outer cylinder. The charge-equilibrated sample aerosol flow is introduced to the DMA with zero radial velocity at a knife edge on the outer cylinder and the particles are carried along the DMA by the moving sheath air, whilst being attracted to the central rod due to the potential difference. A narrow slit at the end of the central rod provides an exit for particles within the aerosol sample flow on specific trajectories, allowing for the aerosol to be sized by a finite diameter range. A TSI 3081 DMA is used for the work presented in **Paper III**, and operates in a similar fashion to the Vienna design. A charge-neutralised polydisperse aerosol distribution is supplied close to the inner walls of the column and a negative central rod attracts positively charged particles towards it, repelling negatively charged particles. Uncharged particles exit with the sheath flow down the DMA and positively charged particles within a narrow mobility range exit as psuedo-monodisperse aerosol.

The size, shape and charge of a particle will determine it's motion through the DMA, described by its electrical mobility, $Z_p$,

$$Z_p = \frac{neC}{3\pi\mu D_p} \tag{2.1}$$

where $n$ is the number of charges, $e$ is the elementary charge ($1.6\text{x}10^{-19}$ Coulomb), $C$ is the Cunningham slip correction factor, $\mu$ is the gas viscosity and $D_p$ is the particle mobility diameter. The Cunningham slip correction factor is used when the size of the particles is similar in magnitude to the distance between gas molecules, causing the relative velocity between the particles and the gas in which they are suspended to be non-zero, causing the particles to settle more quickly.

Knutson and Whitby (1975) determined the relationship between the particle electrical mobility and the parameters of the DMA to be:

$$Z_p = \frac{Q_{sh}}{2\pi V L} \ln\left(\frac{r_2}{r_1}\right) \tag{2.2}$$

where $Q_{sh}$ is the sheath air flow, $V$ is the applied voltage, $L$ is the length of the central rod and $r_1$ and $r_2$ are the inner and outer radii of the DMA respectively.

For a given voltage, a range of particle mobility diameters close to that of the selected mobility diameter by the DMA may pass through the slit. This defines the DMA transfer function, which for an ideal DMA (ignoring particle diffusion and broadening of trajectories) is taken to be triangular and described by:

$$\Delta Z_p = Z_p \frac{Q_a}{Q_{sh}} \tag{2.3}$$

where $\Delta Z_p$ is the half width of the transfer function and $Q_a$ is the sample aerosol flow. As a result, the DMA selects a quasi-monodisperse aerosol sample, due to the finite width of the transfer function. Though Birmili et al. (1997) determined the empirical correction factors for a variety of DMAs to account for the effects of the transfer function, the Vienna style DMAs used in this work, and the TSI DMA used in **Paper III**, have all been calibrated on a case by case basis before the processing of data.

The Differential Mobility Particle Sizer (DMPS; Williams, 1999) used in this work makes use of two DMAs in parallel to measure the size distribution of the aerosol from 3nm - 1$\mu$m. As equation 2.2 has shown, the selected diameter is dependent on column length, and so this large measurement range is achieved through the use of both short and long column DMAs. Each DMA is set to a specific voltage, long enough for equilibrium to be achieved and the particle concentration counted with a CPC. The particle concentration for a given voltage is then recalculated using Equation 2.1, solved for $D_p$. This procedure is repeated over a variety of voltage steps, producing a particle number-size distribution.

An alternative method for obtaining a number-size distribution using DMAs is the Scanning Mobility Particle Sizer (SMPS; Wang and Flagan, 1990). Here, only a single DMA is used and the voltage is ramped down continuously, and particle concentration counted. The particle number-size distribution is then processed using an inversion which takes into account the known residence time of the instrument (i.e. DMA to CPC).

The analysis of both the DMPS and SMPS data can be corrected for multiple charged particle events at the analysis stage, as the positive and negative charges are distributed amongst the particles in a predictable manner.

An advantage of the SMPS is its temporal resolution; one scan can be completed every 2 minutes, compared with the 10 minutes required by the DMPS, though these are user-definable settings. However, the DMPS has improved counting statistics and a less complex inversion technique (Collins and Flagan, 2002).

The DMPS system has been used to supply number-size distributions for the majority of the work presented in this thesis.

As previously described, CPCs count particles optically once they have grown to a sufficiently larger diameter. Optical Particle Counters (OPCs; e.g. GRIMM) illuminate the particles with a light source and measure the light scattered at a particular angle. The optical diameter, $D_{opt}$ is dependent on a particle's refractive index, geometry, internal structure and physical size. OPCs are calibrated by measuring spherical particles of a known diameter, whereby the diameter of a particle is inferred from the amount of scatter as described by Mie theory (Mie, 1908). OPCs are best used when sampling particles of spherical shape to avoid unpredictable results. Many commercial instruments make use of OPCs are the final detection stage in their measurement, such as the Droplet Measurement Technologies CCN counter (to be described in Section 2.3.2).

### 2.1.3 Particle Composition

Particle composition can be measured offline by the analysis of a variety of techniques involving drawing an air sample onto a filter. Size resolved composition measurements can be achieved with cascade impactors, which work on the principle that the smaller particles follow the flow streamline better than large ones, so moving them round bends is easier. If you move the airstream round tighter and tighter bends, then you sequentially impact out the particles with decreasing size. Temporal resolution is low (hours, days or weeks) and size resolution is poor.

Online measurements of particle composition can be measured using instruments such as the Particle-into-Liquid Sampler (PiLS; Sorooshian et al., 2006). The initial designs of Khlystov et al. (1995) and Simon and Dasgupta (1995) pioneered this measurement, whereby ambient particles were mixed with steam, the subsequent droplets grown were impacted onto a plate and collected for ion chromatography or flow injection analysis. The detection limits of these instruments was between $0.6 - 5\mu\text{gm}^{-3}$ for an 8 minute sample. Weber et al. (2001) designed a Particle-into-Liquid Collector (PiLC) with a rapid automated online technique, providing continuous bulk composition measurements with a detection limit below $0.1\mu\text{gm}^{-3}$ for each 7 minute sample. The aforementioned PiLS (Sorooshian et al., 2006) builds further on the technique of Weber et al. (2001), by collecting the samples in vials on a rotating carousel rather than using an online analytical detector. Aerosol mass and concentrations can be accurately

predicted through the use of a model. The instrument has a collection efficiency of 96%, though the relatively high volatility of $NH_4^+$ reduces this to 88%, but this was improved by ensuring a temperature stability of 100°C at the point where the ambient air mixes with the steam. Though the temporal resolution is high, there are no size-resolved data from PiLS.

Realtime submicron aerosol size, mass and composition is often measured with the use of an Aerosol Mass Spectrometer (AMS, Aerodyne Inc., Jayne et al., 2000). A High-Resolution Time-of-Flight Aerosol Mass Spectrometer (HR-AMS, Aerodyne Research Inc., DeCarlo et al., 2006; Canagaratna et al., 2007) was used for the majority of the work presented in this thesis to probe non-refractory aerosol particle composition. The instrument is capable of measuring particles from 40nm to 700nm vacuum aerodynamic diameter (DeCarlo et al., 2004). Briefly, an aerodynamic lens focusses an aerosol particle sample into a beam, then subsequently vapourised. The evolved gas is then ionized by electron impact whilst in a vacuum and a mass spectrometer analyses the mass ($m$) and charge ($z$) of the particles, reported as the ratio $m/z$ for a given species. Species measured by the AMS are $SO_4$, $NH_4$, $NH_3$, $NO_3$ and organic compounds.

## 2.2 Sub-saturated aerosol water uptake

*In situ* measurements of the water activity of individual aerosol particles can be made with the use of the electrodynamic balance (EDB; Liang and Chan, 1997), whereby an aerosol particle is levitated through a combination of AC and DC fields. A charged particle will experience an electrostatic force due to the DC field, a time-varying force due to the AC field, gravitational force and air resistance due to any relative movement in the ambient air (drag). A variable RH feed is introduced to the EDB, changing the ambient RH near the particle or droplet, resulting in either the evaporation of water molecules from the droplet or condensation to the droplet in order to maintain equilibrium. Water activity is derived by measuring the mass fraction of solute and the weight of the droplet, therefore knowing the concentration of water in the droplet, giving the water activity for a given RH. Particles measured by EDBs are typically 1$\mu$m in diameter or larger, meaning that the Kelvin (surface tension) effect cannot be investigated. Furthermore, as the measurement is performed on one particle at a time, the EDB is not a suitable tool for probing the hygroscopicity of atmospheric aerosol

particles during field studies.

### 2.2.1 HTDMA

Nanometre-sized particle hygroscopicity at relative humidities below 100% can be investigated using a Hygroscopic Tandem Differential Mobility Analyser (HTDMA, Rader and McMurray, 1986; Cubison et al., 2005; Swietlicki et al., 2008). A polydisperse aerosol sample is passed through a charge neutraliser and subsequently a drier before being supplied to a DMA. This DMA is operated with a dry sheath air flow (typically below 10% RH), and quasi-monodisperse size selects the aerosol sample. The airstream is then passed through a humidifier and into a second DMA with sheath air RH equal to that of the now humidified sample flow (typically 90% RH), where the voltage is stepped to measure the diameters of all particles after being subjected to the humid environment, which are finally counted by a CPC (simple schematic shown in Fig. 2.1). Depending on the number of measured dry sizes, DMA2 growth factor scan ranges and CPC counting statistics, the time resolution for most HTDMA field measurements is between 0.5 and 1h.

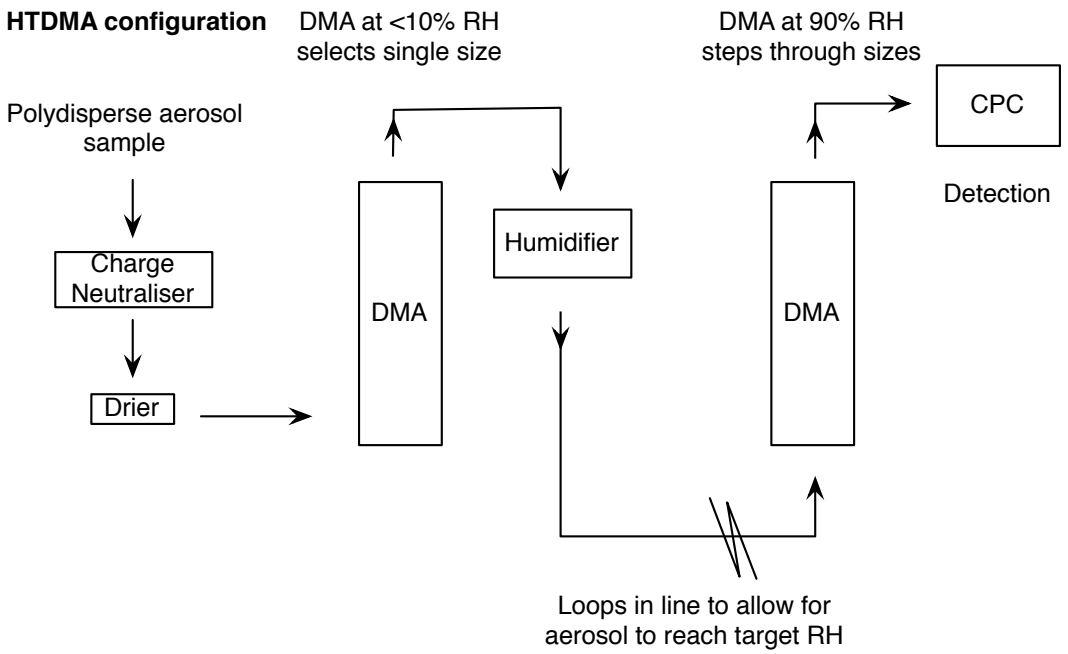


Figure 2.1: A simple schematic showing the HTDMA configuration used at The University of Manchester.

The ratio of wet particle diameter to the initial dry diameter defines the hygroscopic growth factor for that particle, as previously described in Section 1.1.1. The stepping of the second DMA through a range of voltages, and thus diameters, allows HTDMA measurements to obtain the distribution of growth factors exhibited by the particles; the growth factor probability density function, $p(GF)$. The increase of particle diameter (and thus also particle volume) is postulated to be caused by the condensation of water vapour to the particle under the elevated RH due to the thermodynamic equilibrium between the condensed water and the surrounding water vapour (Swietlicki et al., 2008), though there is the possibility that attaining the equilibrium is kinetically limited because there is insufficient time in the instrument with an elevated RH.

The instrument allows the RH of the second DMA to be set anywhere between the RH of DMA1 and effectively 99%RH, though ∼90%RH is more common due to the high risk of condensation in the instrument at high RH, difficulties in controlling temperatures, the high sensitivity of water content to slight RH variations in this range and the increasing importance of surface tension effects. This great flexibility in measurement allows the HTDMA to probe the aerosol RH hysteresis behaviour, previously discussed in Section 1.1.1. Aerosol humiograms are performed through the careful control of the relative humidity the aerosol particles are exposed to between DMAs, building up a profile of the growth factor as a function of relative humidity for a given monodisperse dry diameter.

At present, there are no commercially available HTDMA instruments, and all existing instruments are constructed and operated by various research groups. The University of Manchester have two such instruments, though the HTDMA used for this work is a modified version of that previously used by Cubison et al. (2005, 2006), Gysel et al. (2007) and references therein.

There are three inversion routines commonly used on HTDMA data, summarised in the review of Swietlicki et al. (2008). TDMAFit, developed by Stolzenburg and McMurray (1988), allows for the existence of multiple groups of particles with distinctly different hygroscopic behaviour (Swietlicki et al., 2008). Groups in the $p(GF)$ are assumed to have a Gaussian type normal distribution with variable standard deviation, allowing for different, distinct growth factor 'modes' of different hygroscopicity. A benefit of this technique is the inclusion of the transfer function of both DMAs (typically termed broadening of the transfer function). A particular disadvantage of the TDMAFit approach is that the sensitivity to

modes in close proximity in growth factor space is low, and so small differences in water uptake and thus composition may be lost. Cubison et al. (2005) made use of the optimal estimation method (OEM), using a quasi-inverse matrix of the TDMA kernel function in order to retrieve the $p(GF)$ at discrete bin positions, objectively determines the minimum group separation that can be resolved and furthermore provides estimates of the retrieval error. Gysel et al. (2007) developed an inversion algorithm, which represents the $p(GF)$ as a piecewise linear function, with the added benefit of an inversion independent to the initial guess. Additionally, the inversion can also be tested for sensitivity to changes in the number of measurement events, outputting error parameters which can be propagated through to further data products, described further in **Paper 1**.

## 2.3 Supersaturated aerosol water uptake

An aerosol particles critical supersaturation defines its propensity to act as as a cloud condensation nuclei (CCN). CCN are typically defined as particles which activate into cloud droplets in the presence of a water vapour supersaturation below 2% (Seinfeld and Pandis, 1998). Supersaturations of 2% or lower are atmospherically realistic, as water vapour is lost to the aqueous phase due to the high number of aerosol particles throughout the atmosphere and as such ambient supersaturations are rarely higher than a couple of percent.

The homogeneous nucleation of gaseous water vapour into an aqueous water droplet is extremely unlikely due to the energy required to initiate the phase change. In fact, in particle free air it would take an ambient supersaturation of several hundred percent before water droplets nucleated homogeneously (Seinfeld and Pandis, 1998). However, such supersaturations are not atmospherically realistic, as the atmosphere is densely packed with a rich variety of particulate matter, which can act as possible sites for nucleation.

As a reference point, the term *condensation nuclei* (CN) refers to particles of diameters above the lower limits of Condensation Particle Counters (e.g. $\sim$10nm; TSI 3010). For the purposes of this thesis and for a given size range, the number of CN is taken to be equal to the total aerosol number concentration at that size.

The number of cloud condensation nuclei, $N_{CCN}$, is a function of supersaturation, particle dry diameter and composition. For an aerosol population of uniform size-independent composition,

$$N_{CCN(S)} = \int_{D_{thres}}^{\infty} N(D_p) dD_p \tag{2.4}$$

where $N(D_p)$ is the number distribution of the aerosol population and $D_{thres}$ is the threshold dry diameter for activation at a supersaturation of $S$ (Seinfeld and Pandis, 1998). If all particles are of identical composition, only the threshold diameter for activation and the number-size distribution of the aerosol population is required in order to calculate $N_{CCN}$.

Due to the competition for the available water vapour, the number of CCN does not equal the cloud droplet number concentration (CDNC). Assuming a constant updraught velocity in a cloud, for a given size, composition and supersaturation, particle activation is dependent on its dry diameter. As more and more particles grow and begin to activate, the supersaturation within the cloud will start to decrease. Should the cloud supersaturation decrease below the critical supersaturation required to activate a particle, it will stop growing and start to evaporate at the expense of the already activated droplet's uninhibited growth. However, if a particle has already activated into a cloud droplet, it will continue to grow provided the supersaturation remains above the equilibrium supersaturation for a doplet of that size. Twomey (1959) provided an analytical solution to this problem, though it does not account for the multi-component size and composition of the CCN population. Ghan et al. (1998) and O'Dowd et al. (1999) illustrated how, for typical maritime cloud conditions, an increase in $N_{CCN}$ does not necessarily result in an increased CDNC; the composition and size distribution of the CCN was found to impact heavily on the resultant CDNC, with strong dependences on updraught velocity and condensation rates (O'Dowd et al., 1999; Ervens et al., 2005; McFiggans et al., 2006).

CCN populate air masses over both ocean and land, and observations show continental air masses to be richer in CCN concentration than maritime air masses (Pruppacher and Klett, 1997). It should be noted however, that continental air masses typically have an overall higher number of CN. To account for the relative total particle number, the fraction of aerosol activated at a given supersaturation and dry diameter, $F_A(S, D_0)$ is often reported as a primary-level data product,

$$F_A(S, D_0) = \frac{N(S, D_0)}{N(D_0)} \tag{2.5}$$

where $N(D_0)$ is the total number of condensation nuclei (equivalent to the

the total aerosol number) for a given dry diameter, $D_0$.

The CCN activity of an atmospheric particle can be described precisely using the Köhler equation, which can be applied to atmospheric systems where all variables are parameterised (i.e. composition, activity coefficients, surface tension, molecular weights, densities). However, it is rare for all of these components to be measured satisfactorily, if at all, and so the development of model simplifications of the Köhler equation are required.

Measurements of aerosol hygroscopicity in environments of water supersaturation provide a direct estimation of the propensity aerosol to form cloud droplets, i.e. to behave as cloud condensation nuclei (CCN). As previously discussed, the number of CCN ($N_{CCN}$) is reported as a function of supersaturation. Cloud condensation nuclei counters (CCNc) have become the *de facto* standard for this measurement, with commercial instruments suitable for field deployment in production.

### 2.3.1 CCN counters

CCN concentration measurements are reported as an aerosol particle number concentration as a function of supersaturation. One of the first instruments to perform this measurement reliably was the static thermal diffusion chamber, consisting of two parallel horizontal metal plates, with opposing wetted surfaces (Twomey, 1963). A near-parabolic supersaturation profile is achieved through holding the two plates at different, constant temperatures. Should particles between the two plates have a critical supersaturation below that of the peak supersaturation generated, they will activate into cloud droplets. Those with critical supersaturations higher than the peak achieved by the instrument will merely absorb water until they reach an equilibrium diameter (i.e. not experience runaway growth into droplets). The supersaturation between the plates was typically inferred through the measurement of the temperatures of the wetted surfaces of the plates. A significant amount of time (several minutes) is required to achieve a new supersaturation profile in the instrument, in order to build up a CCN spectrum. Lala and Jiusto (1977) developed an automated thermal gradient diffusion chamber using light scattering to determine $N_{CCN}$. The achieved supersaturation range was between 0.2% - 2% $S$, which is not low enough to match supersaturations found in some marine stratus clouds (Seinfeld and Pandis, 1998). The

CCN concentration is linearly related to the scattered light signal at a fixed supersaturation, but a $S^{0.55}$ dependence was found over a range of supersaturations. The low temporal resolution and large uncertainties in measurement, especially at the lowest supersaturation settings, assisted the development of alternative CCN measurement techniques.

Continuous flow parallel-plate diffusion chambers such as that developed by Sinnarwalla and Alofs (1973), have a much higher time resolution than the static thermal diffusion chambers due to the continuous sample flow. The precision of measurement is increased through the use of a sheath flow, confining this sample flow such that all particles experience the same supersaturation in the instrument. Fukuta and Saxena (1979) extended this design through the utilisation of a temperature gradient transverse to the flow direction, giving a supersaturation profile through the instrument. The lower limit of these instruments is typically to the order of 0.1% supersaturation.

Isothermal Haze Chambers (IHC; Laktionov, 1972) do not activate droplets (hence the name *Haze*), but rather measure the equilibrium diameter of particles in a saturated atmosphere (RH = 100%). Köhler theory (Section 1.1.2) is then used to derive the critical supersaturation of the particle from this equilibrium diameter. The instrument is highly sensitive to the precision of the RH, as even deviations of 0.5% RH can significantly systematically over or under predict the critical supersaturation (Chuang et al., 2000). IHCs do not directly measure CCN activity, and thus the effects of surface active compounds on droplet activation cannot be easily probed.

More recently, CCN activation spectra are obtained from step-wise scans of supersaturation and are presented as cumulative distributions (McFiggans et al., 2006). The streamwise thermal gradient CCN spectrometer developed by Hudson (1989), inferred the spectrum of critical supersaturations, $S_c$, of dry particles from the output of a droplet spectrum from a diffusion cloud chamber. The instrument supersaturation is sensitive to flow rate and the temperatures and wetness of the two parallel plates straddling the aerosol sample flow. Each droplet passes individually through a white light beam that intersects the sample flow from the cloud chamber. A photomultiplier tube detects the near-forward scattered light and produces a pulse proportional to the size of the particle, measured by a Royco optical counter (Hudson, 1989). The reported supersaturation range of the instrument was much broader, at around 0.01% to 1%, covering most of the range

of interest for warm cloud activation study. Chuang et al. (2000) combined the concepts of Hudson (1989) with those of Hoppel (1979), to produce a cylindrical CCN spectrometer with an alternating gradient technique with supersaturation the range 0.1% to 2%. The instrument is capable of making accurate, high frequency (>0.1Hz) measurements of CCN at a fixed supersaturation and is suitable for aircraft use.

### 2.3.2 DMT-CCNc

Over the past few years, CCN activity has been measured at the University of Manchester using the Droplet Measurement Technologies Cloud Condensation Nuclei counter (DMT-CCNc), developed by Roberts and Nenes (2005). The continuous flow CCN spectrometer allows high time resolution measurements and combines the important features of continuous flow parallel plate diffusion chambers and cylindrical diffusion chambers (Roberts and Nenes, 2005). It was designed to operate on a ground-based or airborne measurement platform, with the supersaturation range 0.06% to 3%. An ambient sample is introduced into the instrument, whereby it is split into a particle free, heated and humidified sheath flow and the aerosol sample flow. The aerosol sample is introduced at the top of a 50cm long cylindrical column of inner radius 11.5mm with wetted inner ceramic surface. A temperature gradient down the column ($\Delta T$), generates the supersaturation in the column as heat and water vapour are transported towards the centre of the column by diffusion. Water vapour that is saturated with respect to the wall temperature will diffuse faster than heat, generating a supersaturation down the centreline of the column (Roberts and Nenes, 2005; Lance et al., 2006). The pressure, flow and temperature gradient all dictate the centreline supersaturation. Finally, the particles are detected and counted by and OPC at the bottom of the column. Lance et al. (2006) map the operation of the DMT-CCNc in detail, providing a fully coupled numerical flow model simulating the supersaturation, temperature, velocity profiles and CCN growth for its entire range of operation.

The ability of a particle to act as a CCN at a given $S$ depends on the number of potential solute molecules it contains, which is a function of its size and composition (Dusek et al., 2006). Linkage of size-resolved CCN measurements to other size-resolved measurements such as composition or sub-saturated water uptake could provide valuable information on particle water uptake behaviour

in the ambient atmosphere. Size-resolved CCN measurements can be obtained

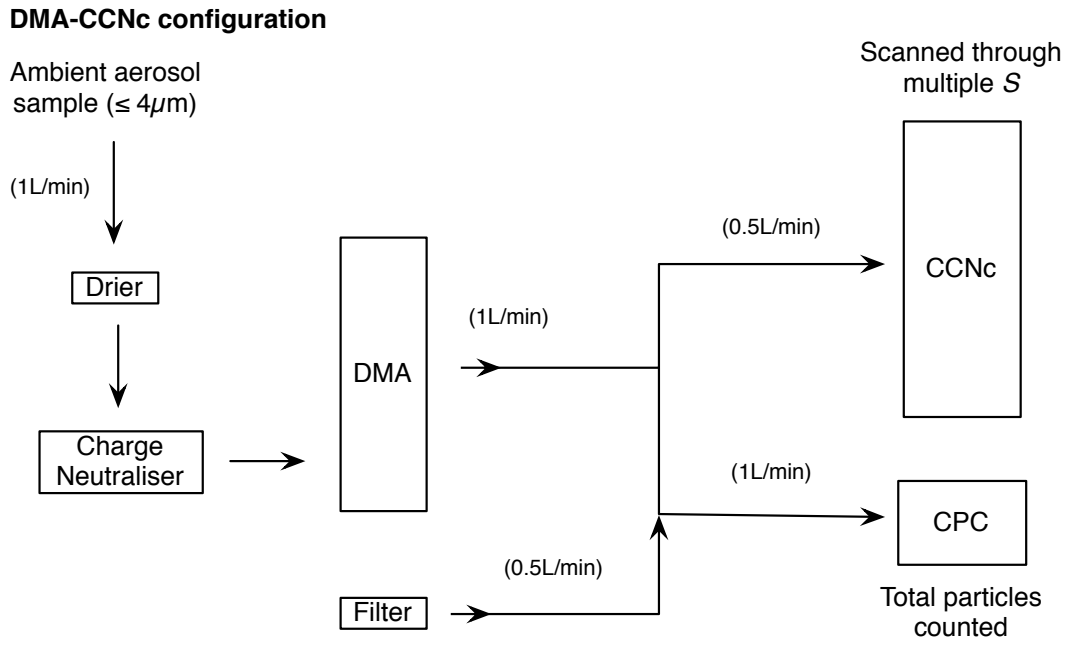


Figure 2.2: A simple schematic showing an example of the CCNc configuration used at The University of Manchester.

by coupling a CCN counter to a DMA. The DMA can provide a specific target dry diameter for prolonged sampling of a size of interest (useful for instrument calibrations Good et al. (2010a) and this work). Alternatively, the DMA can operate in either a DMPS or SMPS 'mode' of operation upstream of the CCNc. We have used the DMA in a stepping function similar to that of the DMPS, as the scanning procedure of SMPS measurements requires a more complex inversion (though both techniques will require the treatment of multiply charged particles). Figure 2.2 shows a simple schematic of such a possible CCNc configuration.

Secondary data products such as critical supersaturation and the diameter at which 50% of the particles have 'activated', $D_{50}$, are typically derived by fitting the CCN fraction activated curve as a function of supersaturation or dry diameter respectively. Rose et al. (2008) fit CCN data with cumulative Gaussian distribution function using a non-linear least squares fitting routine (Gauss-Newton method, Matlab, MathWorks, Inc.). This work presents CCN data fitted with a sigmoidal curve, using orthogonal distance regression (ODR), weighted according to the associated measurement errors, using the Igor Pro software package and associated libraries (ODRPACK95, Boggs et al., 1989). The data analysis and

propagation of measurement errors are described in detail in Section 3, Paper 1.

# 3

# Summary of the papers

This thesis consists of four research articles assessing the reliability of using a single parameter hygroscopicity model to compare the reconciliation ability of two state-of-the-science aerosol instruments. **Paper I** describes a methodology for the propagation of instrumental uncertainty through to final data products. The subsequent papers each take this methodology and apply it to measurements from different environments around the world. **Paper II** evaluates the reconciliation ability for aerosol measured during the Convective and Orographically-induced Precipitation Study in 2007 at a site in Southwest Germany. **Paper III** applies the methodology to results from the Oxidant and Particle Photochemical Processes (OP3) campaign in Borneo, Malaysia between March and July 2008. **Paper IV** considers the effects of assuming a temporally-homogeneous composition and/or size distribution on the reconciliation ability of the predicted number of CCN for different measurement environments, with implications on the scaling-up of a single parameter to global models.

**Paper I** describes a methodology for the propagation of instrumental uncertainty from the HTDMA and CCNc through to commonly used data products, such as $\kappa$ and subsequently the number of CCN. The elegance of single hygroscopicity parameterisations, such as $\kappa$, lies in its simplicity. This simplicity however, does not negate the requirement that uncertainty in such a model is adequately represented. Instrumental uncertainties were arithmetically propagated through analysis procedures such that the uncertainty in $\kappa$ was assessed for real-world measurements. These uncertainties were further propagated through to other common data products including estimates of the number of CCN. The evaluation of these errors is an important step in assessing the reconciliation ability of such a model.

**Papers II** and **III** explore the hygroscopicity of the atmospheric aerosol as measured in Continental Europe and the in the tropical rainforest of Borneo respectively. In addition to the propagation of errors, the papers explore the effects of the aerosol mixing state on the reconciliation ability through deviations between the measured mean growth factor and the peak of the growth factor probability distribution. The results show that the mixing state alone cannot account for discrepancies in the reconciliation, where differences between prediction and measurement were observed in both regions.

**Paper IV** takes the measurements from COPS, OP3 and the Reactive Halogens in the Marine Boundary Layer (RHaMBLe, 2007) experiments and explores the sensitivity of the predicted number of CCN to averaging with respect to aerosol compositional information (i.e. $\kappa$) and the number-size distribution. Though it was found that the reconciliation ability was greater influenced when assuming a constant number-size distribution for a particular environment, assuming a constant $\kappa$ for regions reduced the confidence of the predictions. Furthermore, the a priori application of a correction factor to HTDMA data varied between regions and so size-resolved hygroscopicity and CCN activity measurements are essential in achieving the best reconciliation between the two saturation regimes.

# 4

# Conclusions

Understanding aerosol particle water uptake is crucial when estimating the indirect effects on climate. It has long been known that an aerosol particle's water uptake ability is dependent on its size and composition, with the relative importance of each parameter under continued discussion. Anthropogenic sources and sinks of aerosol impact on the number-size distribution both regionally and globally, perturbing the number of cloud condensation nuclei and thus cloud droplet number. These perturbations result in changes in cloud albedo, longevity and precipitation patterns, impacting on the earth's radiative budget and hydrological cycle.

The study of aerosol particle water uptake is not new, though recently the importance of organic compounds on the ability of particles to nucleate cloud droplets has been recognised and studied from both experimental and theoretical angles. The sheer variety of organic species within the atmosphere further complicate our ability to fully understand interactions between water vapour and the ambient aerosol, as the exact physicochemical implications of the inclusion of such compounds is not fully understood. As our knowledge of the composition of the atmospheric aerosol increases through improvements in measurement ability, the complete solution to the Köhler equation remains elusive as there are still many parameters left unaccounted. Furthermore, the inclusion of the full Köhler equation in global models is not currently possible due to its inherent complexity.

In efforts to simplify the Köhler equation such that the number of CCN can be accurately estimated for different environments, and even be predicted from measurements of particle growth factor, a number of single hygroscopicity parameter models have been developed. Such models are attractive due to their relative

simplicity and their ability to offer reconciliation pathways for sub- and supersaturated measurements. However, as these models make assumptions regarding composition and surface tension, which are fundamental to particle water uptake, their use must be treated with caution. The reason for this caution is further highlighted by a lack of real-time measurements of size-resolved composition and surface tension measurements, which are still in their relative infancy.

The thesis presents an error model, whereby measurement uncertainty from sub- and supersaturated size-resolved water uptake measurements and CCN activity is propagated through to the single hygroscopocity parameter $\kappa$ and final derived data products such as $N_{CCN}$. The full inclusion of measurement uncertainty allows for a more informed interpretation of the reconciliation ability of such models as $\kappa$-Köhler. It was found that the instrument uncertainty alone could not account for the discrepancy observed between the two instruments, for the different environments. Furthermore, the effects of aerosol mixing state on reconciliation ability were found to have little influence for the different measurement environments. Though it was possible to reconcile some of the measurements by applying much lower values of surface tension to that of water, there is no evidence to support that there were surfactants present in the aerosol capable of performing this task, and this 'correction' is also mathematically possible through changing other parameters in the $\kappa$-model, such as temperature.

The reconciliation discrepancies were not consistent for all environments, illustrating that the application of a constant 'correction' factor to reconcile these measurements is not possible. The disagreement was also dependent on size and supersaturation, indicating that perhaps such models cannot capture all of the necessary information from which to achieve complete agreement between predicted and measured $N_{CCN}$. Finally, the discussion of the relative importance of size and composition was approached through the application of different averaging methods to the final size-resolved data products. It was found that the influence of assuming a constant size distribution for a region resulted in weaker correlation to fully size-resolved data that when assuming a constant composition (or $\kappa$). The best reconciliation in terms of overall agreement and strong correlation was found when comparing results from fully size-resolved data, which are important for improving understanding at the process level and for use in regional scale-up.

A discussion on the impacts of different values of $\kappa$ and $N_{CCN}$ on the uncertainty of the first aerosol indirect effect was presented by Wang et al. (2008). They derive an uncertainty in the first indirect effect, denoted $\Delta F_c$, which can be predicted from $\kappa$ and the aerosol size distribution and $N_{CCN}$:

$$\Delta F_c = -0.7 \frac{n(\ln D_{50})}{N_{CCN}} \ln \left( \frac{0.70(1 - x_{org}) + 0.12 x_{org}}{0.70(1 - x_{org}) + \kappa_{org} x_{org}} \right) \quad (4.1)$$

where $n(\ln D_{50})$ is the number-size distribution $x_{org}$ is the volume fraction of organic compounds and $\kappa_{org}$ is the derived hygroscopicity parameter for organic compounds.

For assumed organic fractions of 60% or lower, $\Delta F_c$ was found to be less than $0.2\mathrm{W/m^2}$ for a typical $\kappa_{org}$ between $0 - 0.25$. Conversely, when the organic fraction is as high as 90%, $\Delta F_c$ can vary from a negative forcing of $-1.0\mathrm{W/m^2}$ to as high as $0.6\mathrm{W/m^2}$, for the same $\kappa_{org}$ range. However, it was noted that $\Delta F_c$ may be substantially less for concentrations of aerosol comprising a wide mixing state range and thus wide ranges of $\kappa_{org}$. It was therefore postulated that, over time, $\Delta F_c$ could be substantially less than $0.2\mathrm{W/m^2}$.

Wang et al. (2008) predicted $N_{CCN}$ from measurements of the aerosol number-size distribution and composition, and compared these values directly to simultaneously measured values of $N_{CCN}$. For free tropospheric and boundary layer aerosols, the predicted $N_{CCN}$ was shown to be insensitive to the properties of organics (Wang et al., 2008). The predicted $N_{CCN}$ showed little variation and agreed with the measured $N_{CCN}$ to within 15% when $\kappa_{org}$ is assumed to be in the range $0 - 0.25$. The range of $\kappa$ values presented in this thesis are between $0.15 - 0.2$ and $0.1 - 0.5$ for HTDMA and CCNc derived hygroscopicity during COPS, and between $0.17 - 0.37$ and $0.05 - 0.37$ for HTDMA and CCNc derived hygroscopicity during OP3. In agreement with the results from **Paper IV**, changes in the hygroscopicity parameter (which can be viewed as a proxy for composition), influence $N_{CCN}$ reconciliation less than changes to the number-size distribution. It was postulated that a reason for this insensitivity of $N_{CCN}$ to $\kappa$ was due to the inorganic fraction dominating the aerosol volume and thus number of soluble ions, which dictate particle CCN activity. Conversely, for regions above cloud, there was a high dependence of $N_{CCN}$ reconciliation ability on $\kappa$, where organic compounds contributed to up to 90% of the total aerosol volume at $D_{50}$ (Wang et al., 2008). The results of Wang et al. (2008) and those shown in this thesis further stress the requirement for high-resolution data both spatially and

temporally of aerosol number, size, composition and hygroscopicity. Though it is possible to achieve accurate predictions with sufficient accuracy in many cases, the reasons behind successes is still a topic of debate.

The results presented in this thesis show that there are currently issues in using a single parameter hygroscopicity model to predict CCN concentrations for multiple environments outside of instrumental uncertainty, and therefore recommend that more work is still required in probing such simplifications which tend to work well for inorganic laboratory experiments. Various studies from around the world have reconciled similar measurements with varying degrees of success, but a lack of knowledge of high temporal resolution size-resolved compositional information of the aerosol and the influences of the rich variety of atmospheric compounds on droplet surface tension leave much to be discovered.

### Future Work

Though instrumental uncertainty has been propagated, this thesis shows that HTDMA and CCNc measurements do not consistently reconcile within these instrumental errors. An initial assumption might be to therefore postulate that the instruments are not measuring the same particle. An assessment of the differences between the measured aerosol from both instruments is recommended for future work.

The impacts of kinetic limitations to aerosol growth and the consequences of not reaching equilibrium in both the drying and humidification sections of both instruments is discussed in detail in **Papers II** and **III**. It is postulated from the results of Good et al. (2010b) that if non-equilibrium behaviour is responsible for any variability, it would most likely be in the drying section for these particular aerosol systems. Laboratory tests and measurements relating to the drying efficiencies of counterflow nafion driers (or similar), for the flow rate and line length used in HTDMA and CCNc systems is recommended. Ensuring that the aerosol is dried equally in both instruments prior to measurement is a challenge yet to be tackled. Furthermore, the influence of scrubbers in the humidification systems of the instruments should also be quantified, as the influences of the different amounts of condensible material are not yet quantified in these systems and exploration into kinetic limitations to growth and particle morphology are becoming increasingly popular.

Improvements such as these, in both understanding the particle-level processes and their resultant influences on global climate forcing, will improve our understanding of the interactions between atmospheric aerosol and water vapour and its role in the radiative budget.

# Bibliography

Aalto, P.: Atmospheric ultrafine particle measurements, Report Series in Aerosol Science, 64, 2004.

Albrecht, B.: Aerosols, cloud microphysics, and fractional cloudiness, Science, 245, 1227–1230, 1989.

Andreae, M. and Rosenfeld, D.: Aerosol–cloud–precipitation interactions. Part 1. The nature and sources of cloud-active aerosols, Earth Science Reviews, 89, 13–41, 2008.

Baltensperger, U., Kalberer, M., Dommen, J., Paulsen, D., Alfarra, M. R., Coe, H., Fisseha, R., Gascho, A., Gysel, M., Nyeki, S., Sax, M., Steinbacher, M., Prevot, A. S. H., Sjoren, S., Weingartner, E., and Zenobi, R.: Secondary organic aerosols from anthropogenic and biogenic precursors, Faraday Discussions, 130, 265–278, 2005.

Birmili, W., Stratmann, F., and Wiedensohler, A.: Determination of differential mobility analyzer transfer functions using identical instruments in series, Aerosol Science and Technology, 27, 215–223, 1997.

Boggs, P., Donaldson, J., Byrd, R., and Schnabel, R.: Algorithm 676: ODRPACK: software for weighted orthogonal distance regression, ACM Transactions on Mathematical Software (TOMS), 15, 364, 1989.

Brechtel, F. J. and Kreidenweis, S. M.: Predicting Particle Critical Supersaturation from Hygroscopic Growth Measurements in the Humidified TDMA. Part II: Laboratory and Ambient Studies, Journal of the Atmospheric Sciences, 57, 1872–1887, 2000.

Canagaratna, M. R., Jayne, J. T., Jimenez, J. L., Allan, J. D., Alfarra, M. R., Zhang, Q., Onasch, T. B., Drewnick, F., Coe, H., Middlebrook, A., Delia, A., Williams, L. R., Trimborn, A. M., Northway, M. J., Decarlo, P. F., Kolb, C. E., Davidovits, P., and Worsnop, D. R.: Chemical and microphysical characterization of ambient aerosols with the aerodyne aerosol mass spectrometer, doi:10.1002/mas.20115, 2007.

Choi, M. Y. and Chan, C. K.: The effects of organic species on the hygroscopic behaviors of inorganic aerosols, Environmental Science & Technology, 36, 2422–2428, 2002.

Chuang, P., Nenes, A., and Smith, J.: Design of a CCN instrument for airborne measurement, American Meteorological Society, 17, 1005–1019, 2000.

Cohen, M., Flagan, R., and Seinfeld, J.: Studies of Concentrated Electrolyte Solutions Using the Electrodynamic Balance. 2. Water Activities for Mixed-Electrolyte Solutions, Journal of Physical Chemistry, 91, 4575–4582, 1987.

Collins, D. and Flagan, R.: Improved inversion of scanning DMA data, Aerosol Science and Technology, 36, 1–9, 2002.

Covert, D., Gras, J., and Wiedensohler, A.: Comparison of directly measured CCN with CCN modeled from the number-size distribution in the marine boundary layer during ACE I at Cape Grim, Tasmania, Journal of Geophysical Research, 103, 16,597–16,608, 1998.

Cruz, C. N. and Pandis, S. N.: Deliquescence and hygroscopic growth of mixed inorganic-organic atmospheric aerosol, Environmental Science & Technology, 34, 4313–4319, 2000.

Cubison, M., Alfarra, M., Allan, J., Bower, K., and Coe, H.: The characterisation of pollution aerosol in a changing photochemical environment, Atmospheric Chemistry and Physics, 2006.

Cubison, M. J., Coe, H., and Gysel, M.: A modified hygroscopic tandem DMA and a data retrieval method based on optimal estimation, Journal of Aerosol Science, 36, 846–865, 2005.

Cubison, M. J., Ervens, B., Feingold, G., Docherty, K. S., Ulbrich, I. M., Shields, L., Prather, K., Hering, S., and Jimenez, J. L.: The influence of chemical composition and mixing state of Los Angeles urban aerosol on CCN number and cloud properties, Atmospheric Chemistry and Physics Discussions, 8, 5629–5681, doi:10.5194/acpd-8-5629-2008, 2008.

DeCarlo, P., Slowik, J., Worsnop, D., Davidovits, P., and Jimenez, J.: Particle

Morphology and Density Characterization by Combined Mobility and Aerodynamic Diameter Measurements. Part 1: Theory, Aerosol Science & Technology, 38, 1185–1205, doi:10.1080/027868290903907, 2004.

DeCarlo, P., Kimmel, J., Trimborn, A., Northway, M., Jayne, J., Aiken, A., Gonin, M., Fuhrer, K., Horvath, T., Docherty, K., Worsnop, D., and Jimenez, J. L.: Field-Deployable, High-Resolution, Time-of-Flight Aerosol Mass Spectrometer, Analytical Chemistry, 78, 8281–8289, 2006.

Dockery, D. and Pope, C.: Acute respiratory effects of particulate air pollution, Annual review of public health, 1994.

Duplissy, J., Gysel, M., Alfarra, M., Dommen, J., Metzger, A., Prevot, A., Weingartner, E., Laaksonen, A., Raatikainen, T., and Good, N.: Cloud forming potential of secondary organic aerosol under near atmospheric conditions, Geophys. Res. Lett, 35, 2008a.

Duplissy, J., Gysel, M., Sjogren, S., Meyer, N., Good, N., Kammermann, L., Michaud, V., Weigel, R., dos Santos, S. M., Gruening, C., Villani, P., Laj, P., Sellegri, K., Metzger, A., Mcfiggans, G. B., Wehrle, G., Richter, R., Dommen, J., Ristovski, Z., Baltensperger, U., and Weingartner, E.: Intercomparison study of six HTDMAs: results and general recommendations for HTDMA operation, Atmospheric Measurement Techniques, 2, 363–378, doi: 10.5194/amtd-1-127-2008, 2008b.

Dusek, U., Frank, G., Hildebrandt, L., Curtius, J., Schneider, J., Walter, S., Chand, D., Drewnick, F., Jung, D., Borrmann, S., and Andreae, M. O.: Size Matters More Than Chemistry for Cloud-Nucleating Ability of Aerosol Particles, Science, 312, 1375–1378, 2006.

Ervens, B., Feingold, G., and Kreidenweis, S.: Influence of water-soluble organic carbon on cloud drop number concentration, Journal of Geophysical Research, 110, D18 211, 2005.

Ervens, B., Cubison, M., Andrews, E., and Feingold, G.: Prediction of cloud condensation nucleus number concentration using measurements of aerosol size distributions and composition and light scattering enhancement due to humidity, J. Geophys. Res., 112, D10S32, doi:10.1029/2006JD007426, 2007.

Facchini, M., Mircea, M., Fuzzi, S., and Charlson, R.: Cloud albedo enhancement by surface-active organic solutes in growing droplets, Nature, 40, 257–259, 1999.

Facchini, M. C., Decesari, S., Mircea, M., Fuzzi, S., and Loglio, G.: Surface tension of atmospheric wet aerosol and cloud/fog droplets in relation to their organic carbon econtent and chemical composition, Atmospheric Environment, 33, 4853–4857, 2000.

Feingold, G. and Cotton, W.: The impact of giant cloud condensation nuclei on drizzle formation in stratocumulus: Implications for cloud radiative properties, Journal of the Atmospheric Sciences, 56, 4100–4117, 1999.

Feingold, G. and Kreidenweis, S.: Does cloud processing of aerosol enhance droplet concentrations?, Journal of Geophysical Research, 2000.

Feingold, G., Stevens, B., and Cotton, W.: The relationship between drop in-cloud residence time and drizzle production in numerically simulated stratocumulus clouds, Journal of the Atmospheric Sciences, 53, 1108–1122, 1996.

Feingold, G., Boers, R., and Stevens, B.: A modeling study of the effect of drizzle on cloud optical depth and susceptibility, J. Geophys. Res., 102, 13 527–13 534, 1997.

Fitzgerald, J.: Marine aerosols: A review, Atmospheric environment. Part A, General topics, 25, 533–545, 1991.

Fors, E. O., Rissler, J., Massling, A., Svenningsson, B., Andreae, M. O., Dusek, U., Frank, G. P., Hoffer, A., Bilde, M., Kiss, G., Janitsek, S., Henning, S., Facchini, M. C., Decesari, S., and Swietlicki, E.: Hygroscopic properties of Amazonian biomass burning and European background HULIS and investigation of their effects on surface tension with two models linking H-TDMA to CCNC data, Atmospheric Chemistry and Physics, 10, 5625–5639, doi: 10.5194/acp-10-5625-2010, 2010.

Forster, P., Ramaswamy, V., Artaxo, P., Berntsen, T., Betts, R., Fahey, D., Haywood, J., Lean, J., Lowe, D., Myhre, G., Nganga, J., Prinn, R., Raga, G., Schulz, M., and Dorland, R. V.: Changes in Atmospheric Constituents and in Radiative Forcing. In: Climate Change 2007: The Physical Science Basis. Contribution of Working Group I to the Fourth Assessment Report of the Intergovernmental Panel on Climate Change, 2007.

Fuchs, N.: On the stationary charge distribution on aerosol particles in a bipolar ionic atmosphere, Pure and Applied Geophysics, 56, 1420–9136, 1963.

Fukuta, N. and Saxena, V.: A horizontal thermal gradient cloud condensation nucleus spectrometer, Journal of Applied Meteorology, 18, 1352–1362, 1979.

Ghan, S., Guzman, G., and Abudul-Razzak, H.: Competition between sea salt and sulfate particles as cloud condensation nuclei, Journal of the Atmospheric Sciences, 55, 3340–3347, 1998.

Goldstein, A. and Galbally, I.: Known and unexplored organic constituents in the earth's atmosphere, Environmental Science & Technology, 2007.

Good, N., Coe, H., and McFiggans, G.: Instrumentational operation and analytical methodology for the reconciliation of aerosol water uptake under sub-and supersaturated conditions, Atmospheric Measurement Techniques Discussions, 3, 359–403, 2010a.

Good, N., Topping, D. O., Duplissy, J., Gysel, M., Meyer, N. K., Metzger, A., Turner, S. F., Baltensperger, U., Ristovski, Z., Weingartner, E., Coe, H., and McFiggans, G.: Widening the gap between measurement and modelling of secondary organic aerosol properties?, Atmospheric Chemistry and Physics, 10, 2577–2593, 2010b.

Gysel, M., Weingartner, E., Nyeki, S., Paulsen, D., Baltensberger, U., Galambos, I., and Kiss, G.: Hygroscopic properties of water-soluble matter and humic-like organics in atmospheric fine aerosol, Atmospheric Chemistry and Physics, 4, 35–50, 2004.

Gysel, M., Crosier, J., Topping, D. O., Whitehead, J., Bower, K. N., Cubison, M. J., Williams, P. I., Flynn, M. J., McFiggans, G. B., and Coe, H.: Closure study between chemical composition and hygroscopic growth of aerosol particles during TORCH2, Atmospheric Chemistry and Physics, 7, 6131–6144, 2007.

Hallquist, M., Wenger, J. C., Baltensperger, U., Rudich, Y., Simpson, D., Claeys, M., Dommen, J., Donahue, N. M., George, C., Goldstein, A. H., Hamilton, J. F., Herrmann, H., Hoffmann, T., Iinuma, Y., Jang, M., Jenkin, M., Jimenez, J. L., Kiendler-Scharr, A., Maenhaut, W., McFiggans, G., Mentel,

T. F., Monod, A., Prévôt, A. S. H., Seinfeld, J. H., Surratt, J. D., Szmigielski, R., and Wildt, J.: The formation, properties and impact of secondary organic aerosol: current and emerging issues, Atmospheric Chemistry and Physics, 9, 5155–5236, doi:10.5194/acpd-9-3555-2009, 2009.

Hansson, H., Rood, M., and Koloutsou-Vakakis, S.: NaCl aerosol particle hygroscopicity dependence on mixing with organic compounds, Journal of Atmospheric Chemistry, 1998.

Heintzenberg, J.: Fine particles in the global troposphere. A review, Tellus. Series B, Chemical and physical meteorology, 41, 149, 0280-6509, 1989.

Hoppel, W.: Measurement of the size distribution and CCN supersaturation spectrum of submicron aerosols over the ocean, J. atmos. Sci, 36, 2006–2015, 1979.

Hori, M., Ohta, S., Murao, N., and Yamagata, S.: Activation capability of water soluble organic substances as CCN, Journal of aerosol science, 2003.

Hudson, J.: An instantaneous CCN spectrometer, Journal of Atmospheric and Oceanic Technology, 6, 1055–1065, 1989.

Hudson, J.: Cloud condensation nuclei, Journal of Applied Meteorology, 32, 596–607, 1993.

Jayne, J., Leard, D., and Zhang, X.: Development of an aerosol mass spectrometer for size and composition analysis of submicron particles, Aerosol Science and Technology, 33, 49–70, 2000.

Khlystov, A., Wyers, G., and Slanina, J.: The Steam-Jet Aerosol Collector, Atmospheric Environment, 29, 2229–2234, 1995.

Kittelson, D.: Engines and nanoparticles: a review, Journal of Aerosol Science, 29, 575–588, 1998.

Knutson, E. and Whitby, K.: Aerosol classification by electric mobility: apparatus, theory, and applications, Journal of Aerosol Science, 6, 443–451, 1975.

Köhler, H.: The nucleus in and the growth of hygroscopic droplets, Transactions of the Faraday Society, 32, 1152–1161, doi:DOI:10.1039/TF9363201152, 1936.

Kreidenweis, S., Petters, M., and DeMott, P.: Single-parameter estimates of aerosol water content, Environmental Research Letters, 3, 035 002, 2008.

Kreidenweis, S. M. S., Koehler, K., DeMott, P. J., Prenni, A. J., Carrico, C. M., and Ervens, B.: Water activity and activation diameters from hygroscopicity data - Part I: Theory and application to inorganic salts, Atmospheric Chemistry and Physics, 5, 1357–1370, 2005.

Kulmala, M., Laaksonen, A., Charlson, R., and Korhonen, P.: Clouds without supersaturation, Nature, 388, 336–337, 1997.

Laktionov, A.: A constant-temperature method of determining the concentrations of cloud condensation nuclei, Atmos. Oceanic Phys., 8, 672–677, 1972.

Lala, G. and Jiusto, J.: An automatic light scattering CCN counter, Journal of Applied Meteorology, 16, 413–418, 1977.

Lance, S., Medina, J., Smith, J., and Nenes, A.: Mapping the operation of the DMT continuous flow CCN counter, Aerosol Science and Technology, 40, 242–254, 2006.

Li, Z., Williams, A., and Rood, M.: Influence of soluble surfactant properties on the activation of aerosol particles containing inorganic solute, Journal of the Atmospheric Sciences, 55, 1859–1866, 1998.

Liang, Z. and Chan, C.: A fast technique for measuring water activity of atmospheric aerosols, Aerosol Science and Technology, 26, 255–268, 1997.

Lohmann, U. and Feichter, J.: Global indirect aerosol effects: a review, Atmos. Chem. Phys, 5, 715–737, 2005.

McFiggans, G., Artaxo, P., Baltensperger, U., Coe, H., Facchini, M. C., Feingold, G., Fuzzi, S., Gysel, M., Laaksonen, A., Lohmann, U., Mentel, T. F., Murphy, D. M., O'Dowd, C. D., Snider, J. R., and Weingartner, E.: The effect of physical and chemical aerosol properties on warm cloud droplet activation, Atmospheric Chemistry and Physics, 6, 2593–2649, 2006.

Mie, G.: Beiträge zur Optik trüber Medien, speziell kolloidaler Metallösungen, Annalen der Physik, 30, 377–445, 1908.

Murphy, D., Thomson, D., and Mahoney, M.: In situ measurements of organics, meteoritic material, mercury, and other elements in aerosols at 5 to 19 kilometers, Science, 27, 1664–1669, 1998.

O'Dowd, C., Smith, M., Consterdine, I., and Lowe, J.: Marine aerosol, sea-salt, and the marine sulphur cycle: A short review, Atmospheric Environment, 31, 73–80, 1997.

O'Dowd, C., Lowe, J., Smith, M., and Kaye, A.: The relative importance of non-sea-salt sulphate and sea-salt aerosol to the marine cloud condensation nuclei population: An improved multi-component aerosol-cloud droplet parametrization, Quarterly Journal of the Royal Meteorological Society, 125, 1295–1313, 1999.

Pandis, S. N., Wexler, A. S., and Seinfeld, J. H.: Secondary Organic Aerosol Formation and Transport .2. Predicting the Ambient Secondary Organic Aerosol-Size Distribution, Atmospheric Environment Part a-General Topics, 27, 2403–2416, 1993.

Petters, M. and Kreidenweis, S.: A single parameter representation of hygroscopic growth and cloud condensation nucleus activity, Atmospheric Chemistry and Physics, 7, 1961–1971, 2007.

Prisle, N., Raatikainen, T., and Sorjamaa, R.: Surfactant partitioning in cloud droplet activation: a study of C8, C10, C12 and C14 normal fatty acid sodium salts, Tellus B, 60B, 416–431, 2008.

Pruppacher, H. and Klett, J.: Microphysics of Clouds and Precipitation, vol. 18, Kluwer Acad., Norwell, Mass., 1997.

Rader, D. and McMurray, P.: Application of the Tandem Differential Mobility Analyser to Sudies of Droplet Growth or Evaporation, Journal of Aerosol Science, 17, 771–787, 1986.

Raes, F., Dingenen, R. V., Vignati, E., Wilson, J., Putaud, J. P., Seinfeld, J. H., and Adams, P.: Formation and cycling of aerosols in the global troposphere, Atmospheric Environment, 34, 4215–4240, 2000.

Raymond, T. and Pandis, S.: Cloud activation of single-component organic aerosol particles, Journal of Geophysical Research-Atmospheres, 2002.

Raymond, T. and Pandis, S.: Formation of cloud droplets by multicomponent organic particles, Journal of Geophysical Research-Atmospheres, 2003.

Rissler, J., Swietlicki, E., Zhou, J., Roberts, G., Andreae, M. O., Gatti, L. V., and Artaxo, P.: Physical properties of the sub-micrometer aerosol over the Amazon rain forest during the wet-to-dry season transition - comparison of modeled and measured CCN concentrations, Atmospheric Chemistry and Physics, 4, 2119–2143, doi:10.5194/acp-4-2119-2004, 2004.

Roberts, G., Andreae, M., Zhou, J., and Artaxo, P.: Cloud condensation nuclei in the Amazon Basin:"Marine" conditions over a continent, Geophys. Res. Lett, 28, 2807–2810, 2001.

Roberts, G. C. and Nenes, A.: A continuous-flow streamwise thermal-gradient CCN chamber for atmospheric measurements, Aerosol Science and Technology, 39, 206–221, 2005.

Robinson, R. and Stokes, R.: Electrolyte Solutions, (revised), London: Butterworth, 1959.

Rodriguez, M. A.: IMAGES-SCAPE2: A modeling study of size- and chemically resolved aerosol thermodynamics in a global chemical transport model, Journal of Geophysical Research, 109, 1–18, doi:10.1029/2003JD003639, 2004.

Rose, D., Gunthe, S., Mikhailov, E., Frank, G., and Dusek, U.: Calibration and measurement uncertainties of a continuous-flow cloud condensation nuclei counter (DMT-CCNC): CCN activation of ammonium sulphate and sodium chloride particles in theory and experiment, Atmos. Chem. Phys, 8, 1153–1179, 2008.

Rose, D., Nowak, A., Achtert, P., Wiedensohler, A., Hu, M., Shao, M., Zhang, Y., Andreae, M. O., and Pöschl, U.: Cloud condensation nuclei in polluted air and biomass burning smoke near the mega-city Guangzhou, China – Part 1: Size-resolved measurements and implications for the modeling of aerosol particle hygroscopicity and CCN activity, Atmospheric Chemistry and Physics, 10, 3365–3383, doi:10.5194/acp-10-3365-2010, 2010.

Seinfeld, J. and Pandis, S.: Atmospheric Chemistry and Physics: From Air Pollution to Climate Change, 1998.

Shulman, M., Jacobson, M., Carlson, R., and Synovec, R.: Dissolution behavior and surface tension effects of organic compounds in nucleating cloud droplets, Geophysical Research Letters, 23, 277–280, 1996.

Simon, P. K. and Dasgupta, P. K.: Continuous Automated Measurement of the Soluble Fraction of Atmospheric Particulate Matter, Analytical Chemistry, 67, 71–78, 1995.

Sinnarwalla, A. and Alofs, D.: A cloud nucleus counter with long available growth time, American Meteorological Society, 12, 831–835, 1973.

Sjogren, S., Gysel, M., Weingartner, E., and Alfarra, M.: Hygroscopicity of the submicrometer aerosol at the high-alpine site Jungfraujoch, 3580m asl, Switzerland, Atmos. Chem. Phys, 8, 5715–5729, 2008.

Sorjamaa, R., Raatikainen, T., Henning, S., Bilde, M., and Laaksonen, A.: The role of surfactants in Kohler theory reconsidered, Atmos. Chem. Phys, 4, 2107+2117, 2004.

Sorooshian, A., Brechtel, F. J., Yilin, Weber, R. J., Corless, A., Flagan, R. C., and Seinfeld, J. H.: Modeling and Characterization of a Particle-into-Liquid Sampler (PILS), Aerosol Science and Technology, 40, 396–409, doi:info:doi/10.1080/02786820600632282, 2006.

Squires, P. and Twomey, S.: A comparison of cloud nucleus measurements over central North America and the Caribbean Sea, Journal of the Atmospheric Sciences, 1966.

Stokes, R. and Robinson, R.: Interactions in aqueous nonelectrolyte solutions. I. Solute-solvent equilibria, The Journal of Physical Chemistry, 70, 2126–2130, 1966.

Stolzenburg, M. R. and McMurray, P.: TDMAFIT User' s Manual, Particle Technology Laboratory, Department of Mechanical Engineering, U of Minnesota, Minneapolis, 1988.

Svenningsson, B., Rissler, J., Swietlicki, E., Mircea, M., Bilde, M., Facchini, M., Decesari, S., Fuzzi, S., Zhou, J., Monster, J., and Rosenorn, T.: Hygroscopic growth and critical supersaturations for mixed aerosol particles of inorganic

and organic compounds of atmospheric relevance, Atmospheric Chemistry and Physics, 6, 1937–1952, 2006.

Swietlicki, E., Hansson, H., Hameri, K., and Svenningsson, B.: Hygroscopic properties of submicrometer atmospheric aerosol particles measured with H-TDMA instruments in various environments—a review, Tellus, 60B, 2008.

Topping, D. O., McFiggans, G. B., and Coe, H.: A curved multi-component aerosol hygroscopicity model framework: Part 1 - Inorganic compounds, Atmospheric Chemistry and Physics, 5, 1205–1222, 2005a.

Topping, D. O., McFiggans, G. B., and Coe, H.: A curved multi-component aerosol hygroscopicity model framework: Part 2 - Including organic compounds, Atmospheric Chemistry and Physics, 5, 1223–1242, 2005b.

Twomey, S.: Measurements of natural cloud nuclei, J. Rech. Atmos., 1, 101–105, 1963.

Twomey, S.: Pollution and the planetary albedo, Atmospheric Environment, 1974.

Twomey, S.: Influence of Pollution on Shortwave Albedo of Clouds, Journal of the Atmospheric Sciences, 34, 1149–1152, 1977.

Twomey, S. A.: The Nuclei of Natural Cloud Formation Part II: The Supersaturation in Natural Clouds and the Variation of Cloud Droplet Concentrations, Geofis. Pure Appl., 43, 227–42, 1959.

VanReken, T., Ng, N., and Flagan, R.: Cloud condensation nucleus activation properties of biogenic secondary organic aerosol, Journal of Geophysical Research, 110, 2005.

Varutbangkul, V., Brechtel, F., Bahreini, R., Ng, N., Keywood, M., Kroll, J., Flagan, R., Seinfeld, J., Lee, A., and Goldstein, A.: Hygroscopicity of secondary organic aerosols formed by oxidation of cycloalkenes, monoterpenes, sesquiterpenes, and related compounds, Atmospheric Chemistry and Physics, 6, 2367–2388, 2006.

Virtanen, A., Joutsensaari, J., Koop, T., Kannosto, J., Yli-Pirila, P., Leskinen, J., Makela, J. M., Holopainen, J. K., Poeschl, U., Kulmala, M., Worsnop, D. R.,

and Laaksonen, A.: An amorphous solid state of biogenic secondary organic aerosol particles, Nature, 467, 824–827, doi:10.1038/nature09455, 2010.

Wang, J., Lee, Y., Daum, P., Jayne, J., and Alexander, M.: Effects of aerosol organics on cloud condensation nucleus (CCN) concentration and first indirect aerosol effect, Atmos. Chem. Phys, 8, 6325–6339, 2008.

Wang, J., Cubison, M. J., Aiken, A. C., Jimenez, J. L., and Collins, D. R.: The importance of aerosol mixing state and size-resolved composition on CCN concentration and the variation of the importance with atmospheric aging of aerosols, Atmospheric Chemistry and Physics, 10, 7267–7283, doi: 10.5194/acp-10-7267-2010, 2010.

Wang, S. and Flagan, R.: Scanning electrical mobility spectrometer, Aerosol Science and Technology, 13, 230–240, 1990.

Weber, R. J., Orsini, D., Daun, Y., Lee, Y. N., Klotz, P. J., and Brechtel, F.: A Particle-into-Liquid Collector for Rapid Measurement of Aerosol Bulk Chemical Composition, Aerosol Science and Technology, 35, 718–727, doi: info:doi/10.1080/02786820152546761, 2001.

Wex, H., Hennig, T., Salma, I., Ocskay, R., Kiselev, A., Henning, S., Massling, A., Wiedensohler, A., and Stratmann, F.: Hygroscopic growth and measured and modeled critical super-saturations of an atmospheric HULIS sample, Geophysical Research Letters, 34, L02 818, 2007.

Wex, H., Stratmann, F., Topping, D., and McFiggans, G.: The Kelvin versus the Raoult Term in the Köhler Equation, Journal of the Atmospheric Sciences, 65, 4004–4016, 2008.

Wexler, A. and Clegg, S.: Atmospheric aerosol models for systems including the ions H+, NH4+, Na+, SO42, NO3, Cl, Br, and H2O, Journal of Geophysical Research, 107, 4207–4221, 2002.

Wiedensohler, A.: An approximation of the bipolar charge distribution for particles in the submicron size range, Journal of Aerosol Science, 19, 387–389, 1987.

Williams, P. I.: Construction and validation of a DMPS for aerosol characterisation, Thesis, 1999.

Winklmayr, W., Reischl, G., and Lindner, A.: A new electromobility spectrometer for the measurement of aerosol size distributions in the size range from 1 to 1000 nm, Journal of aerosol science, 22, 289–296, 1991.

Zhou, J., Swietlicki, E., Berg, O., and Aalto, P.: Hygroscopic properties of aerosol particles over the central Arctic Ocean during summer, Journal of Geophysical Research, 106, 111–32,123, 2001.

# 5

# List of publications

## 5.1 Paper I

Draft title: **Evaluation of errors in derived data products from water uptake measurements of atmospheric particulates**

In preparation for submission to Atmospheric Measurement Techniques Discussions.

Manuscript prepared for Atmos. Meas. Tech.
with version 2.3 of the LaTeX class copernicus.cls.
Date: 11 December 2010

# Evaluation of errors in derived data products from water uptake measurements of atmospheric particulates

**M. Irwin**[1], **J. D. Allan**[1,2], **and G. McFiggans**[1]

[1]School of Earth, Atmospheric and Environmental Sciences, University of Manchester, Manchester, UK.
[2]National Centre for Atmospheric Science, University of Manchester, Manchester, UK.

**Abstract.** Methodologies for the propagation of measurement uncertainties associated with the Hygroscopicity Tandem Differential Mobility Analyser and Cloud Condensation Nuclei counter size resolved measurements of aerosol water uptake are presented. Measurement uncertainty has been propagated from raw data to common data products from both instruments; the subsequent errors associated with HTDMA-derived growth factor and CCNc-derived fraction activated, critical supersaturation and critical diameter have been further propagated through to calculations of threshold diameter for activation and number of cloud condensation nuclei, $N_{CCN}$. It is demonstrated how the uncertainties in the precision of measurements from both instruments can be propagated through model parameterisations, allowing for a more informed critical analysis of these commonly reported data products.

## 1 Introduction

Composition and size are the two primary determinants of an aerosol particle's ability to take up water. Simplified descriptions of water uptake are required to allow its straightforward prediction based on measured or modelled composition. In order to probe the efficacy of such models, the accuracy and precision of the measurements must be evaluated, and errors propagated, to ascertain the degree of certainty that can be attributed to each measurement.

Online measurements of aerosol size and water uptake under sub- and supersaturated conditions are becoming more commonplace; the Differential Mobility Particle Sizer (DMPS; Knutson and Whitby, 1975; Williams et al., 2007), Hygroscopic Tandem Differential Mobility Analyser (HTDMA; Rader and McMurray, 1986) and the continuous flow thermal gradient Cloud Condensation Nuclei counter (DMT-CCNc; Roberts and Nenes, 2005) respectively being most widely used techniques.

Reconciliation of independent measurements allows evaluation of our quantitative understanding of water uptake. Sub-saturated aerosol water uptake, a particle's hygroscopicity, can be used in conjunction with number-size aerosol distributions and composition measurements to probe our understanding of physical and chemical processes. For example, Gysel et al. (2007) predicts with good agreement sub-saturated growth from measurements of aerosol composition using the Zdanovskii-Stokes-Robinson (ZSR) mixing rule (Zdanovskii, 1948; Stokes and Robinson, 1966). The review of Swietlicki et al. (2008) summaries HTDMA measurements in various environments, some of which are reconciled with independently measured number-size, mass concentrations and composition (Saxena et al., 1995; Dick et al., 2000; Zhou et al., 2002; Gysel et al., 2004; Aklilu et al., 2006; Rissler et al., 2006; Gysel et al., 2007). Measurements of water uptake in the supersaturated regime, the ability of particles to behave as a cloud condensation nuclei (CCN), can be similarly examined for consistency with respect to independently measured quantities. The number of CCN ($N_{CCN}$) may be predicted from measurements at different supersaturations used in conjunction with aerosol size distributions and measurements of composition (Liu et al., 1996; Covert et al., 1998; Cantrell et al., 2001; Roberts et al., 2003; Broekhuizen et al., 2006).

It is possible to measure $N_{CCN}$ as a function of supersaturation directly with a polydisperse instrumental configuration. However, as the ability of a particle to act as a CCN is also dependent on size, in order to test our understanding of the linkage between composition and hygroscopicity on a process level, both measurements of $N_{CCN}$ as a function of supersaturation and size must be made. The principle of operation is similar to that employed by Dusek et al. (2006) and other studies; size-selected aerosol particles counted at a

*Correspondence to:* G. McFiggans
(gordon.mcfiggans@manchester.ac.uk)

specific supersaturation.

Medina et al. (2007) acknowledge that whilst CCN studies are numerous, a comprehensive CCN climatology is still lacking and as such there is a strong need for CCN reconciliation studies to cover a wide range of seasons and aerosol types. More recently, there have been studies attempting to model the water uptake behaviour of particles using measurements from both the sub- to supersaturated regime (Vestin et al., 2007; Gunthe et al., 2009; Kammermann et al., 2010; Good et al., 2010b). Accurately predicting water uptake for all relative humidities requires multiple parameters to be constrained, which vary as a function of concentration.

Köhler theory (Köhler, 1936) predicts water uptake to an aerosol particle based on the physico-chemical properties (solute mass, activity coefficient, partial molar volume, and number and nature of solute molecules or ions in solution), and works well for inorganic substances such as sodium chloride and ammonium sulphate. However, organic compounds are ubiquitous in the atmosphere and frequently dominate atmospheric aerosol mass concentrations (Kanakidou et al., 2004). This organic fraction is generally poorly characterised at a molecular level. Therefore, simplified representations of the Köhler equation are necessary in order to enable prediction of water uptake to aerosol particles for a variety of compounds by relating water uptake to indeterminate composition. For example the $\kappa$-Köhler (Petters and Kreidenweis, 2007) and $\rho_{ion}$ (Wex et al., 2008) models allow the parameterisation of the results from hygroscopicity instruments such that they can be directly compared. Directly comparing measurements with the use of models such as $\kappa$-Köhler could help constrain these models or even show where measurement techniques need to improve, though caution must be exercised unless the level of certainty from each approach can be assessed.

Monodisperse CCNc measurements can be acquired and analysed by incrementally stepping through dry diameters and/or instrument supersaturation setpoints, where measurements of activated particle number are taken as a function of dry diameter and/or supersaturation, respectively. Results are often reported as the ratio of CCN to condensation nuclei (CN), or total particle concentration as measured by a CPC (e.g. TSI 3010) for a selected size and supersaturation. This ratio is typically referred to as the fraction of CCN activated, $F_A(S, D_0)$. The dry diameter at which $F_A(S, D_0) = 0.5$ is taken to be the threshold dry diameter above which particles will most likely grow into CCN), and is denoted $D_{50,S}$. Similarly, the supersaturation at which $F_A(S, D_0) = 0.5$ is taken to be the critical supersaturation. For simplicity, where CCNc data products are derived from plotting CCN activity against incremental dry diameter or supersaturation measurements, they are denoted 'D-step' and 'S-step' respectively. CCNc measurements, data products and the derivations of $D_{50,S}$ and $S_{c,D0}$ are further discussed in Sections 2 and 3.

The measurement uncertainty associated with the precision of each individual instrument and the effect of these errors on the precision of the derived quantities are investigated in this study enabling significance of any discrepancies in the measurement reconciliation to be assessed. This paper describes a methodology for establishing the magnitude of errors introduced at each stage in the analyses, propagating these errors through the entire reconciliation procedure. Note that this paper only attempts to estimate precisions (expressed as standard errors) intrinsic to the measurements and inversion methods. This paper does not cover issues of accuracy, which will be strongly dependent on the rigour and quality of instrument calibration and operation. However, the methods described in this paper could be employed to propagate estimates of accuracy from the primary measurements through to the derived data products in the same manner as the precision estimates.

Many previous works have assessed the precisions associated with the raw data of both the CCNc and HTDMA instruments. With regards to the HTDMA, the original work of Rader and McMurray (1986) assesses the transfer function of the DMAs as a function of particle number concentration and sampling time. Stolzenburg and McMurry developed the TDMAfit program, with which measured growth factors were assured to fall into well separated log-normally distributed modes and the work of Cubison et al. (2005) was the first to ascribe fitting errors to raw HTDMA data based using the OEM (Optimal Estimation Method) inversion. In addition to the incorporation of a growth factor correction algorithm, (Gysel et al., 2009, and references therein) show that statistical limitations associated with low number concentrations are unavoidable, resulting in an uncertainty of $\Delta N_{poiss} = \sqrt{N}$. Furthermore, the sensitivity of the HTDMA analysis to counting statistics as outlined by Gysel et al. (2009) is explicitly used and propagated through our analysis to final data products. Errors associated with CCNc measurements have also been identified in multiple works. Lance et al. (2006) and Roberts and Nenes (2005) present a flow model describing the dependence of supersaturation on temperature, pressure and flow rate within the DMT-CCNc, describing the errors associated with the thermal conductivity of the column walls. Each of these quantities is logged by the instrument in realtime, and as such the standard error of each quantity can be propagated through analysis procedures to final data products. The study performed by Rose et al. (2008) assessed in detail the errors on CCNc calibrations and measurements, and the impact of these errors on multiple models. As has been previously stated, first order instrumentation errors are associated with particle number concentrations and as such the use of non-laboratory data is key in assessing the magnitude of the errors associated with real life variations in atmospheric particulate matter number concentrations. Rather than repeat the previous work carried out on the instrument-specific functions, or set out to improve measurement uncertainties, a methodology for propagating errors from real atmospheric data through to comparable data products is presented.

It should be noted that this analysis only applies to aerosols of a uniform chemical composition for any given diameter, which is evidenced by a monomodal distribution in the HTDMA-derived growth factor spectra. A discussion and treatment of the impacts of aerosol with multimodal HTDMA-derived growth factor spectra will need to be addressed on a case-by-case basis and is considered in, for example, Irwin et al. (2010).

## 2 Instrumentation

Whilst the methodology described in this paper largely provides a generally-applicable procedural description independent of definitive experimental design, the case studies described herein are reliant on data obtained using a single pairing of instruments run in a configuration described below.

### 2.1 Sub-saturated water uptake

The configuration and operation of the Hygroscopicity Tandem Differential Mobility Analyser (HTDMA) instrument is explained in detail by Cubison et al. (2005), Good et al. (2010a,b) and Irwin et al. (2010). Briefly, polydisperse aerosol is sampled through a charge neutraliser, passed through a diffusion drier and a pseudo-monodisperse particle size selected by a first differential mobility analyser (DMA). The airstream is subjected to a defined relative humidity ($RH$) and the voltage on the central rod of a second DMA is stepped to measure the diameters of all particles after they have grown at the instrument $RH$ (simple schematic shown in Fig. 1a). Typically, six or seven different particle dry diameters are cycled within one hour, depending on the range of growth factors probed. We present HTDMA data for 7 dry diameters in this study; 26, 43, 85, 127, 169, 211, 254 $\mathrm{nm}$.

### 2.2 CCN activity

The CCNc instrument is explained in detail by Roberts and Nenes (2005), with the mode of operation outlined by Good et al. (2010a) and Irwin et al. (2010). Briefly, polydisperse aerosol is sampled through a charge neutraliser, pseudo-monodisperse particle size selected by a DMA (operating with $\leq 10\% RH$ sheath air). The air stream is then split into equal parts, with one half sent directly to a condensation particle counter (CPC, with a bleed-in flow to take the total to 1 $\mathrm{L/min}$) and the other half subjected to a supersaturation ($S$) down the centreline of the main column of the CCNc and counted by an optical particle counter (OPC). The supersaturations are cycled hourly, with 10 minute step increases from a base supersaturation, which is scanned for 20 minutes at the beginning of each hour cycle to allow for temperatures in the column to stabilise after ramping down from the highest setting (simple schematic shown in Fig. 1b).

### 2.3 Instrumental configuration

It is important to assess the magnitude of the errors propagated through analysis with the use of ambient data as, for example, particle counting statistics resulting from low number concentrations or finite averaging times do not influence typical laboratory conditions as much, where higher number concentrations can be sampled for longer, though even laboratory generated aerosol will not be of uniform composition nor constantly generate a polydisperse aerosol of constant number-size distribution.

This paper illustrates the treatment of the errors on data collected during the Convective and Orographically-induced Precipitation Study (2007); further details of the measurement site and the COPS programme are presented in detail by Wulfmeyer et al. (2008). The exact experimental setup is described in detail by Irwin et al. (2010). Briefly, measurements were conducted at a height of 1164m AMSL between 24 June to 18 July 2008 at the Hornisgrinde SuperSite, located in the Western Black Forest in Germany. The field site was a remote moorland area with little vehicle or pedestrian activity.

Air was drawn down a 40 $\mathrm{mm}$ bore, 3 $\mathrm{m}$ high stainless steel stack at a flow rate of 35 $\mathrm{l/min}$, through a cyclone impactor with a 4 $\mu\mathrm{m}$ cut-off, and then into the container to the instrumentation which, excluding the water uptake measurement instrumentation outlined by Irwin et al. (2010), is described in more detail by Jones et al. (2010). A simple schematic describing the scanning procedure of the CCNc and HTDMA is shown in Fig 1.

## 3 Definitions and terminology used in subsequent data analysis

The data from both the HTDMA and coupled DMA-CCNc instruments require significant processing to provide a range of useful data products. The levels of data product and the quantities at each level used in the current paper are summarised in the Glossary (see Table 1).

### 3.1 Primary CCNc data quantities

This section will describe quantities directly measured by the DMA-CCNc instrumentation, which are all logged at a frequency of 1 Hz. Firstly, $\Delta T$ is the reported difference between the wall temperature ($^{\circ}C$) of the column between $T_1$ (top of column) and $T_3$ (bottom of column). A target $\Delta T$ defines the instrument supersaturation for a given flow. The supersaturation setpoint ($S_{set}$; %) is controlled directly by $\Delta T$, where the reported supersaturation for any given measurement is defined as the supersaturation down the centreline of the column (Lance et al., 2006) and is a function of $\Delta T$, pressure ($P$) and flow rate ($Q$). The supersaturation will not be instantaneously established at the entrance to the 0.35 $\mathrm{m}$ column and the flow model of Roberts and Nenes 2005 demon-

strated that the supersaturation is established after between 0.05 and 0.10 m. The dry diameter ($D_0$; nm $\leq$ 20% RH) of the particles is selected by a Vienna design Differential Mobility Analyser (DMA; Winklmayr et al., 1991) and is sized according to their electrical mobility prior to entering the CCNc.

The activated particle number, $N_{S,D_0}$, is the number of activated particles counted by the optical particle counter (OPC) at the bottom of the column of the CCNc. It is dependent on the supersaturation, $S$ and dry diameter, $D_0$. $N_{S,D_0}$ may be represented as a histogram of particle counts in size bins ranging from $0.75-10\mu m$ in 20 bins (measured at top of bin). Particles above $1\mu m$ were considered to have activated, as it is possible that particles below this diameter may have a large, unactivated equilibrium size (Roberts and Nenes, 2005; Lance et al., 2006). A predictable fraction of the particles selected by the DMA will be of a larger size but carrying multiple charges (Wiedensohler, 1987). The reported values for $N_{S,D_0}$ have had a multiple charge correction applied as outlined by Good et al. (2010a). Further to the activated particle number, the total particle number, $N_{D_0}$, is defined as the total number of monodisperse particles counted at a given dry diameter by a Condensation Particle Counter (CPC; TSI model 3010). The reported $N_{D_0}$ is also corrected for multiple charges as outlined by Good et al. (2010a). The ratio of activated to total particles defines the activated fraction of the particles at a given supersaturation ($S$) and dry diameter ($D_0$): $F_A(S, D_0) = \frac{N_{S,D_0}}{N_{D_0}}$.

### 3.2 Secondary CCNc data products

The data products described in this section have been directly derived from those shown in the previous section.

Figure 2a shows an example scan of number concentration against dry diameter, for $S = 0.17\%$. The number concentration reported from the CPC is much higher than that reported by the CCNc at the smallest diameters, as the particles of the smallest sizes have not yet activated into cloud droplets. The ratio of total to activated number can be represented by the fraction activated, shown in Figure 2b. The dry diameter at which 50% of the particles activate for a given supersaturation, $D_{50,S}$, is derived by fitting a sigmoid function, weighted by the magnitude of the uncertainty due to counting statistics, to the plot of $F_A(S, D_0)$ vs $D_0$, as shown in Figure 2b. The point on the sigmoid that corresponds to $F_A(S, D_0)$ = 0.5 is $D_{50,S}$.

Using the same approach, the supersaturation at which 50% of the particles for a given $D_0$ have activated was used to represent the critical supersaturation, $S_{c,D0}$ (e.g. Hoppel, 1979). As with $D_{50,S}$, the critical supersaturation is evaluated from a weighted sigmoidal fit to $F_A(S, D_0)$ data plotted as a function of $S$ for a each dry diameter, as shown in Figure 3b for $D_0$ = 121 nm.

### 3.3 Primary HTDMA data quantities

The HTDMA directly measures the quantities described in this section, which are all logged them at a frequency of 1 Hz. The dry diameter of the reported measurement sized by the first vienna-type DMA (Winklmayr et al., 1991) in the HTDMA instrumentation defines $D_0$ with respect to HTDMA measurements. As with the DMA-CCNc instrument, this measurement is made at less than 15% $RH$ and is therefore considered dry (Cubison et al., 2005). The second Vienna-type DMA of the HTDMA measures the particle diameter after humidification, which defines the wet particle diameter, $D$. The particle is finally counted by the HTDMA's CPC (TSI; 3760A), and $N_{D,RH}$ defines the number concentration as reported for a given dry diameter and relative humidity measurement.

The principle of operation is such that if the aerosol sample relative humidity, $RH$, has not reached equilibrium with the $RH$ of the sheath flow of the DMA, then the dew point sensor (DPS) $RH$ will decrease due to the drying effect of the sample. Therefore, the relative humidity of the measurement is defined as the the relative humidity of the sheath air flow of the second DMA.

### 3.4 Secondary HTDMA data quantities

From the directly measured quantities described in the previous section, it is possible to derive further useful data products. For a given dry diameter and relative humidity measurement particles will grow by different amounts. The growth factor of a particle is defined as the ratio of wet to dry diameter, i.e. $GF_{D_0} = \frac{D}{D_0}$. The number of particles counted at each wet size will determine the HTDMA growth factor probability distribution, $p(GF)$, that will subsequently require correction for variations in relative humidity measurement from the setpoint. The mean of the growth factor probability distribution is calculated by taking the number-weighted mean growth factor of the $p(GF)$ for a given $D_0$ and $RH$, uncorrected for $RH$ variations, and is denoted by $\overline{GF}_{uc}$.

The resolution of the growth factor distribution corrected for fluctuations in the $RH$ of the second DMA column from the target $RH$ (86% for the illustration dataset for COPS) is dependent on the resolution of the analysis used. Cubison et al. (2005) and Gysel et al. (2009) explain the impacts on the growth factor probability density function of the data inversion and retrieval techniques and Good et al. (2010a,b) show an example of the practical application of this, using identical methods to this study. The growth factor correction also takes into account the transfer function of each DMA. The final corrected HTDMA growth factor probability distribution is denoted by $p(GF)_c$. The mean of the corrected growth factor probability distribution is calculated by taking the number-weighted mean growth factor of $p(GF)_c$ for a given $D_0$ and $RH$. The corrected mean growth

factor, $\overline{GF}_{D0,RH,c}$, will accurately represent the growth factor probability distribution if the aerosol is within a single retrieved growth factor bin, but will be a true representative average so long as the distribution is monomodal. As mentioned previously in the introduction, this assessment assumes monomodal aerosol for the purposes of the error propagation, and the effect of aerosol mixing state on measurement reconciliation is explored further by Irwin et al. (2010). Gysel et al. (2009) describes in detail the analysis techniques applied to the HTDMA data set in order to arrive at the final quantities of the growth factor probability distribution and mean growth factor and this shall not be repeated here.

## 4 Identification and quantification of primary CCNc Errors

The primary CCNc data quantities outlined in Section 3.1 each have an associated uncertainty in the precision of their logged values. In this section, we identify this uncertainty for each measurement, so that these errors may be propagated through to the higher level products.

It might be expected that there is an error associated with deviation of the reported temperature associated with changes in flow or pressure down the column. The column temperatures are capable of each controlling the temperature to within $\pm 0.05^{\circ}C$, with a typical temperature variation down the column rarely above $0.3^{\circ}C$.

Since $S$ is controlled solely by the flow-rate of the aerosol stream down the column centreline and the temperature difference down the column, the errors in supersaturation have been calculated from the standard deviation of $\partial T$ for each averaging period. The error associated with the reported pressure of the CCNc column is considered; Rose et al. (2008) show $\partial S/\partial P$ to be 0.00037 $\%/\mathrm{hPa}$. Taking into consideration the effect of the flow rate on supersaturation, Rose et al. (2008) found experimentally $\partial S/\partial Q$ to be 0.038% per 0.1 $\mathrm{Lmin}^{-1}$; less than the $\partial S/\partial Q = 0.061\%$ per 0.1 $\mathrm{Lmin}^{-1}$ reported by the flow model of Roberts and Nenes (2005).

In order to estimate the error in $S$ from the standard deviation of these quantities, the standard deviation ($\sigma$) of each measurement of temperature, flow and pressure ($T, Q$ and $P$ respectively, which are taken to vary independently) is multiplied by its differential value, summed in quadrature and divided by the square root of the number of observations ($N$; number of particles measured during an averaging period) to give the standard error in $S$:

$$\Delta S = \frac{\sqrt{\left(\frac{\partial S}{\partial T}\sigma T\right)^2 + \left(\frac{\partial S}{\partial Q}\sigma Q\right)^2 + \left(\frac{\partial S}{\partial P}\sigma P\right)^2}}{\sqrt{N}} \quad (1)$$

The dependence of $\Delta S$ on $\sqrt{N}$ arises because the instrument detector (the OPC) only samples the conditions when a particle is detected. As $T$, $Q$ and $P$ have been assumed to vary randomly throughout the measurement period, the more particles detected, the more precise the average supersaturation will be.

The range of diameters introduced into the CCNc for a given target diameter is described by the DMA transfer function (Knutson and Whitby, 1975). For this analysis, we have assumed an ideal, triangular transfer function (Knutson and Whitby, 1975), with symmetrical bounds 5% either side of the target dry diameter, $D_T$. One standard deviation of this transfer function is described by $\sigma = c\sqrt{1/6}$, where $c = 0.1D_T$ i.e. the width of the base of the transfer function. When propagating the error associated with the diameter measurement of $D_T$, the standard error of $D_T$ has been used:

$$\Delta D_T = \frac{c\sqrt{(1/6)}}{\sqrt{N}} \quad (2)$$

Once the data has been quality assured, averaged and corrected for multiple charging (Good et al., 2010a), the associated error in deriving the critical supersaturation from an activation curve has been quantified. Unlike the calibration procedure, a maximum of five supersaturations are stepped through in order to generate the activation curve shown in Fig. 3b.

The CCNc and CPC number concentration standard errors (shown by the error bars in Figs. 2 and 3) have been calculated by invoking Poisson statistics as in Eq. 3:

$$\Delta(\sum N) = \sqrt{\frac{\sum N}{Q \sum T}} \quad (3)$$

where $N$ is the number of particles counted, substituted by either CCNc ($N(S, D_0)$) or CPC ($N(D_0)$), $Q$ is the flow rate and $T$ is the sampling time. The uncertainty in $N$ is calculated and then propagated through the multiple charging correction procedure.

The standard error in $F_A(S, D_0)$ has been defined as:

$$\Delta(\sum F_A(S, D_0)) = \quad (4)$$
$$\frac{N(S, D_0)}{N(D_0)} \sqrt{\left(\frac{\Delta(\sum N(S, D_0))}{N(S, D_0)}\right)^2 + \left(\frac{\Delta(\sum N(D_0))}{N(D_0)}\right)^2}$$

## 5 Propagation of primary CCNc errors into secondary data products

Each of the errors associated with the primary quantities have been carried forward into the analysis procedures in order to evaluate the error in derived quantities. The standard error has been propagated through to the following secondary data products as initially outlined in Section 3.2.

### 5.1 Deriving $D_{50,S}$

Previously defined in Section 3.2, $D_{50,S}$ and associated errors are calculated as follows:

$D_{50,S}$ is derived by from D-step CCNc data by plotting $F_A(S, D_0)$ against dry diameter and fitting a sigmoidal curve (Eq. 5) to the data using orthogonal distance regression (ODR) and is weighted according to the associated errors in each axis, using the Igor Pro software package and associated libraries (*ODRPACK95*, Boggs et al., 1989). An example fit is illustrated in Fig. 2b.

$$y = K_0 + \frac{K_1}{1 + \exp\left((x - K_2)/K_3\right)} \quad (5)$$

Where $K_0$ is the base of the sigmoid (held to zero), $K_1$ is the maximum on the sigmoid (unconstrained to minimise effects caused by systematic inaccuracies of either instrument), $K_2$ is the $x$ value at which $y = 0.5$ (in this case, $D_{50,S}$) and $K_3$ is the rate.

In addition, the fitting algorithm outputs a standard error of the $x$ value at $y = 0.5$, shown in Fig. 2 as $\pm$0.767. This error may change depending on the position of $D_{50,S}$; the most successful fit (i.e. those with small errors) would have a $D_{50,S}$ value half way between the smallest and largest selected dry diameters. For each supersaturation, the DMA is used to supply the instrumentation with mobility selected particles ranging from the equivalent dry diameters of 7 $\mathrm{nm}$ to 700 $\mathrm{nm}$. When the derived $D_{50,S}$ approaches these limits, the associated error with the fit increases as the fitting confidence reduces.

### 5.2 Deriving $S_{c,D0}$

S-step data can be used to derived the supersaturation at which 50% of the particles have activated into cloud droplets; the critical supersaturation ($S_{c,D0}$). The fraction of aerosol activated typically increases with increasing supersaturation, ideally until all particles are said to have activated at the highest supersaturation setting. Standard errors show this to not always be the case, with $F_A(S, D_0)$ typically between 0.8 and 1.2 as shown in Fig. 3b. If the measurement and included certainty is greater than 1, then the measurement is treated as erroneous as the CCNc should not be able to count more than the CPC, and any changes in flow are accounted for in the uncertainty.

The sigmoidal function is applied to the multiple charge corrected data using Eq. 5 as discussed in section 5.1. Typically, the sigmoid function is less close to a step function than as seen for deriving $D_{50,S}$ as a result of reduced data frequency.

The associated errors from CCNc and CPC counting statistics, flow and sampling time are propagated through the sigmoidal fit function (Eq. 5), outputting $S_c \pm \sigma$; with errors as described in section 5.1.

## 6 Identification and quantification of primary HTDMA errors

As with the DMA-CCNc instrumentation, the HTDMA primary data products have uncertainty in the precision of the reported values. This section identifies these errors, so that they can be propagated through to higher order data products.

DMA calibrations are outlined in detail in section 4.1 in Good et al. (2010a), including the detailed HTDMA calibration and validation section, 4.2. We have assumed an ideal transfer function for any propagation of the error on this measurement.

The HTDMA instrument is calibrated as outlined by Good et al. (2010a), and data analysed using the TDMAinv procedure described in detail by Gysel et al. (2009). An error simulation forms part of the TDMAinv analysis technique, with the results from the error simulation showing the sensitivity of the inversion result to small changes in the measurement due to added noise (incorporating counting statistics). This helps in, for example, judging whether two peaks in the $p(GF)$ can be attributed to distinct modes or whether the structure of the $p(GF)$ can be reliably attributed to distinct modes or whether they are indistinguishable from instrument noise. This is outlined in detail by Gysel et al. (2009) and is shown in Figs. 4B and C therein.

100 error simulations (Gysel et al., 2009) are performed on $p(GF)$ for each growth factor bin, and the statistical mean of these taken. The standard deviation of the mean 100 simulations was then calculated; an example of which is shown by Fig. 4a and 4b. This standard deviation represents the effects of counting statistics and variability in size measurement, taken as the standard error of this measurement and is denoted by $\sigma_{p(GF)}$.

The $RH$ in DMA2 is monitored by a Dew Point Sensor (DPS; General Eastern Hygro M4/D-2), capable of measuring $RH$ to within $\pm 1.5\%$ relative humidity at around $90\% RH$ (Cubison et al., 2005). As previously stated in 3.3, the sample flow reaches equilibrium with the sheath $RH$ of DMA2, and therefore is taken to be the measurement $RH$.

## 7 Identification and quantification of secondary HTDMA errors

The previously defined standard errors for each primary data product can be propagated through to the secondary data products.

### 7.1 RH Correction

In addition to being subjected to the previously described error simulation analysis, the $p(GF)$ must be corrected for small deviations from the setpoint relative humidity (typically $\pm 2\% RH$ is recommended; Gysel et al., 2009), resulting in $p(GF)_c$ and $\overline{GF}_{D0,RH,c}$, where subscript $c$ denotes '$RH$-corrected'.

This $RH$-corrected mean of the growth factor distribution is propagated through analysis to derive $\kappa$ (and subsequently $N_{CCN}$). The growth factor has an associated error at each dry diameter, due to uncertainty in the precision of the $RH$ measurement as measured by the Dew Point Sensor, as discussed in Section 6.

In the example COPS dataset, due to technical reasons, the HTDMA was set to operate at a target RH of 86%; typically data is collected at 90% RH (Cubison et al., 2005; Duplissy et al., 2009). Uncorrected mean growth factor data, $\overline{GF}_{uc}$, from 84 - 88% RH is corrected to 86% RH:

$$\overline{GF}_{D0,RH,c} = \left(1 + (\overline{GF}_{uc}^{3} - 1)\frac{(1 - RH_m)RH_t}{(1 - RH_t)RH_m}\right)^{\frac{1}{3}} \quad (6)$$

Where $RH_m$ and $RH_t$ are the measured and target $RH$ respectively (i.e. $RH_t = 86\%$ for the data used in this study). A full explanation of the correction applied is described by Gysel et al. (2009).

In order to propagate the error associated with the change in growth factor from this correction, Eq. 6 is differentiated with respect to $RH_m$ to give:

$$\frac{\partial(\overline{GF}_{D0,RH,c})}{\partial(RH_m)} = -\left((\overline{GF}_{uc} - 1)\frac{RH_t}{(1 - RH_t)}\frac{1}{(RH_m)^2}\right)^{-\frac{1}{3}} \quad (7)$$

An example of the magnitude of this error is given in Fig. 4c, and is typically $\leq 3.6\text{x}10^{-4}$ for all sizes.

### 7.2 Summation of HTDMA errors

In order to perform further calculations on the HTDMA data and propagate the independent errors associated with the measurement and retrieval uncertainty, the two resulting errors perviously described are summed in quadrature:

$$\sqrt{\left(\frac{d(GF_{corr})}{d(RH)}0.015\right)^2 + {\sigma_{p(GF)}}^2} \quad (8)$$

Where $\sigma_{p(GF)}$ is the error associated with counting statistics and size variance on $p(GF)$ and 0.015 relates to the 1.5% $RH$ precision error, which accounts for drifts on the timescale of measurement.

Figure 5 shows the total HTDMA standard error for each dry diameter of the COPS data vs $\overline{GF}_{D0,RH,c}$ (mean $RH$-corrected growth factor). The data points are calculated by summing in quadrature (as per Equation 8) the full time series of the example data shown in Figure 4b and 4c. Evident from Figure 5, there is an uncertainty intrinsic to the relative success of the inversion itself for each dry diameter. The success of the $p(GF)$ retrieval is described by the $\chi^2$ parameter (Gysel et al., 2009), which, for this retrieval, is largest for the dry diameters 26, 43 and 254 $\mathrm{nm}$ respectively (further illustrated by the larger $\sigma_{p(GF)}$ derived uncertainty for these three dry diameters shown in Figure 4b). Excluding changes in number concentration and the varying success of the retrieval applicable to ambient data, a size-dependent uncertainty would not be expected. Futhermore, all sizes appear to have apparent minima around a growth factor of 1.1, relating to the intrinsic resolving power of the DMAs used.

It must be noted that no attempt has been made to include variations in flow throughout the HTDMA instrument, as this would need to be included in the error simulation of Gysel et al. (2009). Such modifications are advised to further quantify the uncertainty in precision with HTDMA measurements.

## 8 Theory of application to further products

Rose et al. (2008) review multiple Köhler theory approximations and models frequently used to calculate derived data products from CCNc data. Models that make use of an effective hygroscopicity parameter to allow for direct evaluation of the consistency of HTDMA and CCNc measurements for that particle, assuming that it is the only determining factor of the growth factor and CCN behaviour. It is implicitly assumed that effective hygroscopicity as represented by a single parameter remains constant at all $RH$ at the value at the $RH$ at which it was determined, and that no other factors play a significant role in determining its water uptake behaviour. A particle's water uptake at equilibrium is defined by the Köhler equation (Köhler, 1936; Pruppacher and Klett, 1997) based on physico-chemical properties of the solute:

$$S = a_w \exp K_e \quad (9)$$

Where $S$ is the saturation ratio (= $RH$/100), $a_w$ is the water activity or Raoult term, and $K_e$ is the Kelvin term.

Wex et al. (2008) have defined and used an "ion density" parameter $\rho_{ion} = \phi_s \nu_s \rho_s / M_s$
$\approx i_s \rho_s / M_s$, where $\phi_s$ is the molal or practical osmotic coefficient of the solute, $\nu_s$ is the number of ions per solute molecule, $\rho_s$ is the density of dry solute, $M_s$ is the molar mass of solute and $i_s$ is the vant Hoff factor of the solute.

Petters and Kreidenweis (2007) also defined a hygroscopicity parameter, $\kappa$, that can be used to parameterise the composition dependent water activity of a solution droplet:

$$a_w = \left(1 + \kappa\frac{V_s}{V_w}\right)^{-1} \quad (10)$$

with $V_s$ and $V_w$ being the volumes of the dry solute and of the water in the droplet respectively. Assuming volume additivity and a spherical shape of the dry solute particle and solution droplet, Eq. (10) can be rewritten as:

$$a_w = \frac{D^3 - D_0^3}{D^3 - D_0^3(1 - \kappa)} \quad (11)$$

Substituting $a_w$ from Eq. (11) into the primitive Köhler equation (Eq. 9) leads to:

$$S = \frac{D^3 - D_0^3}{D^3 - D_0^3(1 - \kappa)} \exp\left(\frac{4\sigma_w M_w}{RT\rho_w D}\right) \quad (12)$$

which can be re-written in terms of corrected mean growth factor ($\overline{GF}_{D0,RH,c}$):

$$S = \frac{\overline{GF}^3_{D0,RH,c} - 1}{\overline{GF}^3_{D0,RH,c} - (1-\kappa)} \exp\left(\frac{4\sigma_w M_w}{RT\rho_w D_0 \overline{GF}_{D0,RH,c}}\right) \quad (13)$$

For this study, the $\kappa$-Köhler model is used to derive the following quantities at 293 K and a surface tension of 72.5 $\mathrm{mNm}^{-1}$. It would have been equally possible to evaluate the "ion density" hygroscopicity parameter in the same way and the two parameters are related by the approximation $\rho_{ion} \approx \kappa\rho_w/M_w$, where $\rho_w$ and $M_w$ are the density and molar mass of water respectively.

Expression 12 may be evaluated with a variety of secondary products from the instrumentation previously discussed. Evaluation of $\kappa$ at the dry diameter at which 50% of particles are activated ($D_{50}$) with the corresponding supersaturation denotes the hygroscopicity $\kappa_{D50}$. $\kappa$ may also be derived from the particle critical supersaturation and dry diameter, denoting $\kappa_{Sc}$. $S_{c,D0}$ as derived from the weighted sigmoidal fits to the data is inserted into Eq. 12. A $\kappa$ value is then iteratively found by locating the maximum in $RH$ (identical to $S_{c,D0}$), for a given $D_0$. The hygroscopicity parameter may also be derived from $RH$-corrected, mean subsaturated growth factor directly by inserting $\overline{GF}_{D0,RH,c}$, $D_0$ and $RH$ into Eq. (13), resulting in $\kappa_{GF}$.

Particle predicted critical supersaturation can be derived from hygroscopicity from $RH$-corrected, mean subsaturated growth factor, $\overline{GF}_{D0,RH,c}$. $\overline{GF}_{D0,RH,c}$ is inserted into Eq. 13, resulting in $\kappa_{GF}$. This $\kappa$ is then reinserted into Eq. 13 and the growth factor increased until a maximum in $S$ is achieved. As with traditional Köhler theory, the maximum in $S$ for a given size and composition (expressed by $\kappa$) determines $S_c$ for activation to a cloud droplet (Petters et al., 2007), resulting in $S_{c,GF}$.

The dry diameter above which the particles will absorb water vapour uninhibitedly and experience runaway growth for a given $S$ may also be derived from the $\kappa$-Köhler model, or directly from CCNc measurements. We have termed this diameter the threshold dry diameter for activation, and is denoted by $D_{thres}$. The threshold dry diameter for activation was derived from CCNc measurement via three pathways, two via S-step analysis and one from D-step analysis. It is possible to derive the threshold diameter for activation using S-step data both with and without the use of a hygroscopicity parameter. An array is constructed, for values of $S_{c,D0}$, at 1 $\mathrm{nm}$ and 0.01 $\kappa$ resolution, to find the hygroscopicity parameter associated with a particle of a specific dry diameter and critical supersaturation. This value of $\kappa$ and the supersaturation value of interest (i.e. different values of $S_{set}$ in this paper) are then inserted into Equation 12, and then the dry diameter is increased until the critical supersaturation matches that of the $S_{set}$ value, defining the dry diameter for activation $D_{thres,\kappa,Sc}$. Without the use of the $\kappa$-model, $S_{c,D0} - S_{set}$ can be plotted against $D_0$, where the intercept defines the aerosol physical threshold dry diameter for activation, denoted $D_{thres,Sc}$. Similarly, the most direct way of deriving the threshold diameter for activation is from D-step data, whereby the intercept of the plot $D_{50,S}D_0$ vs $D_0$ is the once more physical threshold diameter for activation, denoted $D_{thres,D50}$.

The threshold dry diameter for activation can also be derived from HTDMA derived $\kappa_{GF}$. As there are 7 dry diameters scanned by the HTDMA, each dry diameter has an associated $\overline{GF}_{D0,RH,c}$ and thus $\kappa$. A threshold dry diameter is calculated for each value of $\kappa_{GF}$ at each dry diameter and supersaturation, and the intercept of this initial derived '$D_{thres}$' is plotted as $D_{thres} - D_0$ vs $D_0$, the intercept of which defines $D_{thres,\kappa,GF}$ (for each probed supersaturation).

An example of graphical derivation and associated errors are further discussed in Section 9.3. The final calculation we present is that of the number of cloud condensation nuclei. For a given supersaturation, $N_{CCN}$ is calculated by integrating the aerosol number-size distribution as measured by the DMPS, from the largest size down to the threshold diameter for activation. It can be evaluated using any of the derived $D_{thres}$ values. However, it must be noted that no competition for water vapour is considered in this calculation, and as such, would not necessarily equate to the cloud droplet number in a real-world situation.

## 9 Quantification of errors in further products

### 9.1 Errors in $\kappa$

The $\kappa$-Köhler model has been used to create a lookup table of $S_c$ as a function of diameter and $\kappa$ (0.01 resolution $\kappa$, 2 $\mathrm{nm}$ resolution $D_0$). $\kappa$ values corresponding to each supersaturation setpoint (i.e. $S_c$) for each derived $D_{50}$ were located in this array, resulting in a $\kappa$ for each measurement. The error cannot be propagated analytically, as no partial derivative of $\kappa$ with respect to $D_{50}$ can be arithmetically derived due to the iterative nature of the function. Instead, this is estimated numerically by calculating $D_{50} \pm \Delta D_{50}$ and taking the corresponding $\kappa$ values (obtained through the lookup table) as $\kappa_{S_c} \pm \Delta\kappa$. The dry diameter $D_0$ and the maximum, minimum and average $S_{c,D0}$ as derived from the fits to the data were inserted into Eq. 12. A $\kappa$ value was then iteratively found by locating the maximum in $RH$ (identical to our $S_c$), for a given $D_0$. Figure 6 shows a short time series of $S_c$ (Fig. 6a) and $\kappa$ (Fig.6b) with their associated errors.

The errors associated with $\kappa_{GF}$ have also been calculated as outlined in section 8 using the above method for the upper and lower bounds of $\overline{GF}_{D0,RH,c}$, defined by the addition and subtraction of the $\kappa_{GF}$ derived from the standard error in growth factor previously calculated, for positive and negative errors respectively.

Figure 7 shows $\kappa_{GF}$ vs $\kappa_{Sc}$ based on the COPS dataset. $\kappa_{GF}$ and $\kappa_{Sc}$ do not always agree, and the error of $\kappa_{Sc}$ is typically larger than that of $\kappa_{GF}$ for a given observation. $\kappa_{Sc}$ has better agreement with $\kappa_{GF}$ for increasing dry diameters; which may be due to the size and supersaturation range measured by the CCNc. Figure 8 shows the HTDMA predicted $S_{c,GF}$ and CCNc derived $S_{c,D0}$ as a function of dry diameter. The solid black lines represent the bounds of the CCNc supersaturation settings (i.e. 0.11% and 0.80%). The ADDEM derived critical supersaturation for ammonium sulphate is shown as a red dashed line on the figure. Ambient continental aerosol is not expected to be more hygroscopic than ammonium sulphate, and so few data are found below 40 nm from the CCNc S-step analysis. At $D_0 = 43$ nm, data for $S_{c,GF}$ resides either side of the 0.80% upper limit of the CCNc measurement. This same issue is apparent at 85 nm and at the lower $S_{set}$ bound for 169, 211 and 254 nm. Should the CCNc $S_{set}$ range be increased to below 0.11% and above 0.80%, it is likely that $S_{c,D0}$ would be derived for these regions, just as the HTDMA predicts. This instrumental limit means that $S_{c,D0}$ can only be derived for particles with $S_{set0} < S_{c,D0} < S_{set4}$, which will impact on the reconciling ability of S-step CCN analysis with HTDMA data products. This issue is further discussed in the project-dedicated full analysis by Irwin et al. (2010).

### 9.2 Errors in $S_{c,GF}$

It is possible to derive particle critical supersaturation from its derived $\kappa$ value. For HTDMA data, this is done by calculating $\kappa$ for a given $D_0$ and $\overline{GF}_{D0,RH,c}$, then using this $\kappa$ to predict the critical supersaturation of this given dry diameter. It is possible to display the $RH$ corrected mean hygroscopic growth factor as a function of derived particle critical supersaturation, as shown by Figure 9. The critical supersaturation derived from by $\kappa$-Köhler model is shown as solid circles. We have shown how the model is sensitive to changes in surface tension, with smaller circles representing a decrease in surface tension from that of water ($\sigma$ = 72.5 $\mathrm{nNm}^{-1}$). Particle dry diameter is represented through changes in colour, shown in the legend. For reference, the hygroscopic growth factors and critical supersaturations as derived by the ADDEM model (Topping et al., 2005) are also shown. The critical supersaturation as derived directly from CCNc measurement, $S_{c,D0}$ is plotted against $RH$ corrected mean growth factors measurements from the same time periods and are shown as crosses. The darkest crosses are data where the $RH$ corrected mean growth factor is within 5% of the peak growth factor (i.e. the growth factor bin containing the highest number of counts). By doing this, there seems to be no clear indication that mixing state is responsible for the apparent disagreement between HTDMA and CCNc $S_{c,D0}$. The different values of surface tension to that of initial run (that of water); show that an unrealistic suppression in surface tension would be required to account for the observed disagreement, as the CCNc derived $S_{c,D0}$ does not systematically fall within the box and whisker plots, which show the median and respective percentiles of the $\kappa$-Köhler derived critical supersaturation. Agreement between the methods does improve with particle size, however HTDMA growth factor errors are approximately $0.031 \pm 0.004$ across the size range, but CCNc $S_{c,D0}$ errors vary from 0.039 at 43 nm to 0.152 at 214 nm. This increase in $S_{c,D0}$ error with increasing size may be due to both a reduction in particle concentrations at larger sizes and the increasing likelihood that particle critical supersaturations will reduce beyond the lowest $S$ setting the larger they become.

### 9.3 Errors in $D_{thres}$

The $\kappa$ values derived from the $S_c$ analysis were inserted into the $\kappa$-Köhler equation (12) in order to derive the threshold diameter for activation for each supersaturation scan for the experiment. The the upper and lower values for $\kappa_{Sc}$ were propagated through to upper and lower bounds of $D_{thres,\kappa,Sc}$. An example DMPS number-size distribution with the threshold diameters from each method is shown in Figure 10. As there are 7 HTDMA dry diameters scanned, each dry diameter has an associated $\overline{GF}_{D0,RH,c}$ and thus $\kappa$. In order to calculate a single quantity; in this case, the threshold dry diameter for activation ($D_{thres,\kappa,GF}$), each derived $D_{thres}$ for each $D_0$, with errors, is plotted on a graph of $D_{thres} - D_0$ vs $D_0$; shown in Fig. 11. The data is linearly interpolated between the two data points straddling the zero line, and the intercept defines HTDMA $D_{thres,\kappa,GF}$. The standard errors of $D_{thres}$ are propagated through to $D_{thres,\kappa,GF}$ arithmetically.

As previously discussed, $D_{thres}$ can be directly evaluated as $D_{50}$ along with the upper and lower bounds from the error in the fit (Fig. 2) propagated through to provide the maximum, average and minimum threshold diameters for activation. Figure 12 shows the final derived $D_{thres,\kappa,GF}$ vs $D_{thres,D50}$. Typically, as particle size increases, less supersaturation is required to activate into cloud droplets. The $D_{thres,D50}$ analysis shows strongest agreement with $D_{thres,\kappa,GF}$ at the lowest supersaturation whereas a weaker agreement is shown at higher supersaturations, where the HTDMA shows a less hygroscopic aerosol (inferred from the larger threshold dry diameter). As previously described $D_{thres,\kappa,GF}$ is calculated as shown by Figure 11, whereby threshold diameters for activation are calculated from values of $\kappa$ for each supersaturation settings and dry diameter, to which a straight line is plotted to infer $D_{thres,\kappa,GF}$. Inherent to this procedure, is a further loss of some of individual hygroscopicity characteristics at each dry diameter studied. As shown by Figure 7, $\kappa$ increases with increasing dry diameter for HTDMA data but decreases for CCNc data. Therefore, taking a pseudo-averaged value of $\kappa$ from HTDMA in this manner leads to the CCNc data showing better agreement at the larger dry diameters ($D_0 > 169$ nm), where derived aerosol hygroscopicity from the HTDMA is higher than from

the CCNc (data for 169 $\mathrm{nm}$ sits the other side of the 1:1 line than for smaller dry diameters), resulting in the correlations shown in Figure 12.

For each mobility selected size, $S_{c,D0} - S_{set}$ vs $D_0$ is plotted, with error bars (derived from fitting coefficients) in order to derive a physical, threshold diameter for activation of the aerosol. The point at which the line crosses the zero line is defined as our nominal threshold diameter from $S_c$; in the same manner as shown in Fig. 11. The error at the point of intercept is arithmetically propagated from the errors associated with the derivation of $S_c$ (i.e. confidence of the fit), deriving $D_{thres,S_c}$.

### 9.4 Errors in $N_{CCN}$

The number of cloud condensation nuclei ($N_{CCN}$) are calculated using the derived $D_{thres}$ and upper and lower bounds as calculated either by propagating errors (HTDMA, S-step analyses) or the fitting error from D-step analysis by numerically integrating the DMPS $dNd\log D_p$ number-size distribution with respect to $logD_p$ using the trapezium rule.

An example of the integration of the DMPS number-size distribution is shown in Fig. 10, for a scan at a supersaturation of 0.11%. Most notably, from D-step analysis, the upper and lower bounds are much closer to that of the derived HTDMA and $S_c$ threshold diameters. For the $S_c$ analysis, the large spread of diameters is due to the error in fitting the sigmoid function to only 5 data points. A plot of $N_{CCN}$ derived from both HTDMA and $D_{50}$ for COPS is shown in Fig. 13.

The averaging period must be decided on a case by case basis. For this project, we present data on an hourly time base; consisting of typically 7 HTDMA scans (7 dry diameters every hour), a single CCNc S-scan (one diameter each hour, for 5 supersaturations) and 5 CCNc D-scans (5 supersaturations each hour, multiple dry diameters). If there is a change in particle composition or number concentration over the averaging period, this will be manifested as an increase in reported error, due to the reduced quality of the ODR fits. This error will be reduced with longer averaging times, but this will be at the cost of temporal resolution.

For example, comparing $\kappa_{D50}$ with $\kappa_{Sc}$, it can be seen that the two data products should be comparable and do broadly agree as shown in Fig. 15. The D-step analysis would appear to be the more precise method because there is less scope for variations in composition during the shorter averaging time. There is some disagreement, which stems from the fact that the S-scans covers a longer sampling period and as such will be more affected by variations in composition. However, the S-step of operation will be more representative of a longer period of time, so will be ultimately more accurately reflecting the aerosol composition during a given hour.

The amount of error introduced will also depend on the sampling conditions and is therefore considered outside the scope of this paper. We have therefore assumed that the size distribution does not change significantly during the hour in which we derive $D_{thres}$ from each method, but the potential impact of the DMPS size distribution on $N_{CCN}$ is explored in Fig. 14.

As can be seen in Fig. 13, $N_{CCN}$ varies between 0 and around 4000, depending on supersaturation. As shown previously by Fig. 12, the results from the lowest supersaturation show the best agreement, with the largest errors associated with the $N_{CCN}$ at the highest supersaturation.

The shape of the number-size distribution will ultimately affect how many particle may be considered $N_{CCN}$ for each measurement point, as can be seen by the spread of the data. Figure 14 shows the average DMPS distribution, with the standard deviation of dNdLogDp at each dry diameter. In addition, two example single scan distributions have been appended to the graph in order to show the magnitude of some of the deviations from this mean distribution. Subsequently, in averaging the entire size distribution, a lot of information is lost regarding the $N_{CCN}$ throughout the campaign, as depending on the size and magnitude of the size distribution, the potential cloud droplet number concentration derived from each analysis technique could vary by an order of magnitude.

## 10 Discussion and Conclusions

We present a rigorous and robust method of repeatedly propagating the associated instrumental measurement uncertainties through to model application. Previous work has demonstrated examples of the instrument analysis techniques used Good et al. (2010a), including calibrations in order to verify performance. This work follows on from analysis, such that a suite of instruments can have their accuracy and precision variabilities carried forward into either direct comparisons or in order to test model suitability.

There have been many previous studies involving both HTDMA and CCN instruments, and the number of studies attempting to reconcile the two instruments using models will surely increase with time. In order to aid the discussions and conclusions of the findings of these reconciliation studies and the suitability of models, the propagation of errors allows the community to distinguish between measurement precision uncertainty and limitations of a model.

Just as measurements are always performed with calibrations in order to ensure reliable measurement, the errors must too be propagated so that the final results allow a finite amount of certainty in their interpretation.

We have demonstrated the propagation of instrumental error through to calculations of $N_{CCN}$, though many studies will have different end products ($\kappa$, $\rho_{ion}$, $D_{thres}$ etc, depending on applicability). As previously mentioned in Section 9.4, the error associated with changes in the size distribution over the averaging period must be treated on a case by case basis, and is only provided here for example. The errors associated with each derived product will be reduced with in-

creasing averaging time due to the increase in the number of measurement events. Figure 16 shows the propagated error with respect to the derived aerosol hygroscopicity, $\Delta\kappa_{S_c,D0}$, against averaging time for two time periods, selected for their difference in mean total number concentration during the COPS project. As would be expected, increasing the averaging time from 20 seconds for each $D_0$ (equivalent to 1 hour of $\kappa_{S_c,D0}$ measurement) to 400 seconds (equivalent to 20 hours of $\kappa_{S_c,D0}$ measurement), results in a $\Delta\kappa_{S_c,D0}$ reduction from 0.20 to below 0.05 for the low number regime (Sample 1; $\overline{N} \sim 1000$) and from 0.10 to below 0.05 for the high number regime (Sample 2; $\overline{N} \sim 3000$). However, depending on the application of the products, a shorter averaging time may be more desirable (such as when studying the variability in composition throughout a 24 hour period). This was previously alluded to by Figure 15, where it was shown that aerosol composition may change markedly throughout even the most basic averaging periods.

In addition, when comparing the CCNc and HTDMA, special care must be taken in comparing any data for which the CCNc may not have full supersaturation coverage. Figure 8 shows that the $S$ range of 0.11% - 0.80% only covers $S_c$ at around 120-130 $\mathrm{nm}$, as sizes $\leq 120$ $\mathrm{nm}$ seem to hit a ceiling (above which the HTDMA predicts their should be $S_c$ values for these particles, and the opposite for $D_0 \geq 130$ $\mathrm{nm}$. The error from sigmoidal fits to S-step CCNc data could be reduced by scanning through a higher number of $S_{set}$ values than the CCNc software currently permits. If possible, a wide-range high step S-step configuration would improve the derivation of critical supersaturation for a wider-range of dry diameters. However, for CCNc instruments running through a single $S_{set}$ each hour, we advise D-step data analysis in order to compare HTDMA and CCNc data across multiple supersaturations and dry diameters.

*Acknowledgements.* The UK Convective and Orographically-induced Precipitation Study (UK-COPS) was funded by the National Environmental Research Council (NERC) (NE/E016200/1) and NERC Ph.D Studentship of Martin Irwin (NER/S/A/2006/14036).

## References

Aklilu, Y., Mozurkewich, M., and Prenni, A.: Hygroscopicity of particles at two rural, urban influenced sites during Pacific 2001: Comparison with estimates of water uptake from particle composition, Atmospheric Environment, 40, 2650–2661, 2006.

Boggs, P., Donaldson, J., Byrd, R., and Schnabel, R.: Algorithm 676: ODRPACK: software for weighted orthogonal distance regression, ACM Transactions on Mathematical Software (TOMS), 15, 364, 1989.

Broekhuizen, K., Chang, R., Leaitch, W., and Li, S.: Closure between measured and modeled cloud condensation nuclei (CCN) using size-resolved aerosol compositions in downtown Toronto, Atmospheric Chemistry and Physics Discussions, 6, 2006.

Cantrell, W., Shaw, G., and Cass, G.: Closure between aerosol particles and cloud condensation nuclei at Kaashido Climate Observatory, Journal of Geophysical Research, 106, 28,711–28,718, 2001.

Covert, D., Gras, J., and Wiedensohler, A.: Comparison of directly measured CCN with CCN modeled from the number-size distribution in the marine boundary layer during ACE I at Cape Grim, Tasmania, Journal of Geophysical Research, 103, 16,597–16,608, 1998.

Cubison, M. J., Coe, H., and Gysel, M.: A modified hygroscopic tandem DMA and a data retrieval method based on optimal estimation, Journal of Aerosol Science, 36, 846–865, 2005.

Dick, W., Saxena, P., and McMurry, P.: Estimation of water uptake by organic compounds in submicron aerosols measured during the Southeastern Aerosol and Visibility Study, Journal of Geophysical Research-Atmospheres, 105, 1471–1479, 2000.

Duplissy, J., Gysel, M., Sjogren, S., Meyer, N., Good, N., Kammermann, L., Michaud, V., Weigel, R., dos Santos, S. M., and Gruening, C.: Intercomparison study of six HTDMAs: results and general recommendations for HTDMA operation, Atmospheric Measurement Techniques, 2, 363–378, 2009.

Dusek, U., Frank, G., Hildebrandt, L., Curtius, J., Schneider, J., Walter, S., Chand, D., Drewnick, F., Jung, D., Borrmann, S., and Andreae, M. O.: Cloud-Nucleating Ability of Aerosol Particles Size Matters More Than Chemistry for Cloud-Nucleating Ability of Aerosol Particles, Science, 312, 1375–1378, 2006.

Good, N., Coe, H., and McFiggans, G.: Instrumentational operation and analytical methodology for the reconciliation of aerosol water uptake under sub-and supersaturated conditions, Atmospheric Measurement Techniques Discussions, 3, 359–403, 2010a.

Good, N., Topping, D., Allan, J., Flynn, M., Fuentes, E., Irwin, M., Williams, P., Coe, H., and McFiggans, G.: Consistency between parameterisations of aerosol hygroscopicity and CCN activity during the RHaMBLe Discovery cruise, Atmos. Chem. Phys., 10, 3189–3203, 2010b.

Gunthe, S., King, S., Rose, D., and Chen, Q.: Cloud condensation nuclei in pristine tropical rainforest air of Amazonia: size-resolved measurements and modeling of atmospheric aerosol composition and CCN activity, Atmospheric Chemistry and Physics Discussions, pp. 3811–3870, 2009.

Gysel, M., Weingartner, E., Nyeki, S., Paulsen, D., Baltensberger, U., Galambos, I., and Kiss, G.: Hygroscopic properties of water-soluble matter and humic-like organics in atmospheric fine aerosol, Atmospheric Chemistry and Physics, 4, 35–50, 2004.

Gysel, M., Crosier, J., Topping, D. O., Whitehead, J., Bower, K. N., Cubison, M. J., Williams, P. I., Flynn, M. J., McFiggans, G. B., and Coe, H.: Closure study between chemical composition and hygroscopic growth of aerosol particles during TORCH2, Atmospheric Chemistry and Physics, 7, 6131–6144, 2007.

Gysel, M., McFiggans, G., and Coe, H.: Inversion of tandem differential mobility analyser (TDMA) measurements, Journal of aerosol science, 40, 134–151, 2009.

Hoppel, W.: Measurement of the size distribution and CCN supersaturation spectrum of submicron aerosols over the ocean, J. atmos. Sci, 36, 2006–2015, 1979.

Irwin, M., Good, N., Crosier, J., Choularton, T. W., and McFiggans, G.: Reconciliation of measurements of hygroscopic growth and critical supersaturation of aerosol particles in Central Germany, Atmospheric Chemistry and Physics Discussions, 2010.

Kammermann, L., Gysel, M., and Weingartner, E.: Subarctic atmospheric aerosol composition: 3. Measured and modeled properties of cloud condensation nuclei, Journal of Geophysical Research, 115, 2010.

Kanakidou, M., Seinfeld, J., Pandis, S., Barnes, I., Dentener, F., Facchini, M., Dingenen, R. V., Ervens, B., Nenes, A., and Nielsen, C.: Organic aerosol and global climate modelling: a review, Atmospheric Chemistry and Physics Discussions, 4, 5855–6024, 2004.

Knutson, E. and Whitby, K.: Aerosol classification by electric mobility: apparatus, theory, and applications, Journal of Aerosol Science, 6, 443–451, 1975.

Köhler, H.: The nucleus in and the growth of hygroscopic droplets, Transactions of the Faraday Society, 32, 1152–1161, doi:DOI:10.1039/TF9363201152, 1936.

Lance, S., Medina, J., Smith, J., and Nenes, A.: Mapping the operation of the DMT continuous flow CCN counter, Aerosol Science and Technology, 40, 242–254, 2006.

Liu, P. S. K., Leaitch, W. R., Banic, C. M., Li, S. M., Ngo, D., and Megaw, W. J.: Aerosol observations at Chebogue Point during the 1993 North Atlantic Regional Experiment: Relationships among cloud condensation nuclei, size distribution, and chemistry, Journal of Geophysical Research, 101, 28 971–28,990, 1996.

Medina, J., Nenes, A., Sotiropoulou, R., and Cottrell, L.: Cloud condensation nuclei closure during the International Consortium for Atmospheric Research on Transport and Transformation 2004 campaign: Effects of size-resolved composition, J. Geophys. Res, 112, D10S31, 2007.

Petters, M. and Kreidenweis, S.: A single parameter representation of hygroscopic growth and cloud condensation nucleus activity, Atmospheric Chemistry and Physics, 7, 1961–1971, 2007.

Pruppacher, H. and Klett, J.: Microphysics of Clouds and Precipitation, vol. 18, Kluwer Acad., Nor- well, Mass., 1997.

Rader, D. and McMurray, P.: Application of the Tandem Differential Mobility Analyser to Sudies of Droplet Growth or Evaporation, Journal of Aerosol Science, 17, 771–787, 1986.

Rissler, J., Vestin, A., Swietlicki, E., Fisch, G., Zhou, J., Artaxo, P., and Andreae, M.: Size distribution and hygroscopic properties of aerosol particles from dry-season biomass burning in Amazonia, Atmospheric Chemistry and Physics, 6, 471–491, 2006.

Roberts, G., Nenes, A., and Seinfeld, J.: Impact of biomass burning on cloud properties in the Amazon Basin, J. Geophys. Res., 2003.

Roberts, G. C. and Nenes, A.: A continuous-flow streamwise thermal-gradient CCN chamber for atmospheric measurements, Aerosol Science and Technology, 39, 206–221, 2005.

Rose, D., Gunthe, S., Mikhailov, E., Frank, G., and Dusek, U.: Calibration and measurement uncertainties of a continuous-flow cloud condensation nuclei counter (DMT-CCNC): CCN activation of ammonium sulphate and sodium chloride particles in theory and experiment, Atmos. Chem. Phys, 8, 1153–1179, 2008.

Saxena, P., Hildemann, L., McMurray, P., and Seinfeld, J. H.: Organics Alter Hygroscopic Behaviour of Atmospheric Particles, Journal of Geophysical Research, 100, 18 755–18 770, 1995.

Stokes, R. and Robinson, R.: Interactions in aqueous nonelectrolyte solutions. I. Solute-solvent equilibria, The Journal of Physical Chemistry, 70, 2126–2130, 1966.

Swietlicki, E., Hansson, H., Hameri, K., and Svenningsson, B.: Hygroscopic properties of submicrometer atmospheric aerosol particles measured with H-TDMA instruments in various environments—a review, Tellus, 60B, 2008.

Topping, D. O., McFiggans, G. B., and Coe, H.: A curved multicomponent aerosol hygroscopicity model framework: Part 1 - Inorganic compounds, Atmospheric Chemistry and Physics, 5, 1205–1222, 2005.

Vestin, A., Rissler, J., Swietlicki, E., and Frank, G.: Cloud-nucleating properties of the Amazonian biomass burning aerosol: Cloud condensation nuclei measurements and modeling, Journal of Geophysical Research, 112, D14 201, 2007.

Wex, H., Stratmann, F., Topping, D., and McFiggans, G.: The Kelvin versus the Raoult Term in the Köhler Equation, Journal of the Atmospheric Sciences, 65, 4004–4016, 2008.

Wiedensohler, A.: An approximation of the bipolar charge distribution for particles in the submicron size range, Journal of Aerosol Science, 19, 387–389, 1987.

Williams, P., McFiggans, G., and Gallagher, M.: Latitudinal aerosol size distribution variation in the Eastern Atlantic Ocean measured aboard the FS-Polarstern, Atmospheric Chemistry and Physics, 7, 2563–2573, 2007.

Winklmayr, W., Reischl, G., and Lindner, A.: A new electromobility spectrometer for the measurement of aerosol size distributions in the size range from 1 to 1000 nm, Journal of aerosol science, 22, 289–296, 1991.

Wulfmeyer, V, Behrendt, A., Bauer, H., Kottmeier, C., Corsmeier, U., Blyth, A., Craig, G., Schumann, U., Hagen, M., Crewell, S., Girolamo, P. D., Flamant, C., Miller, M., Montani, A., Mobbs, S., Richard, E., Rotach, M., Arpagaus, M., Russchenberg, H., Schlüssel, P., König, M., Gärtner, V., Steinacker, R., Dorninger, M., Turner, D., Weckwerth, T., Hense, A., and Simmer, C.: A research and Development Project of the World Weather research Program for Improving Quantitative Precipitation Forecasting in Low-Mountain regions, American Meteorological Society, 89, 1477–1486, 2008.

Zdanovskii, A.: New methods for calculating solubilities of electrolytes in multicomponent systems, Zhur. Fiz. Khim., 22, 1475–1485, 1948.

Zhou, J., Swietlicki, E., Hansson, H., and Artaxo, P.: Submicrometer aerosol particle size distribution and hygroscopic growth measured in the Amazon rain forest during the wet season, J. Geophys. Res, 107, 8055, 2002.

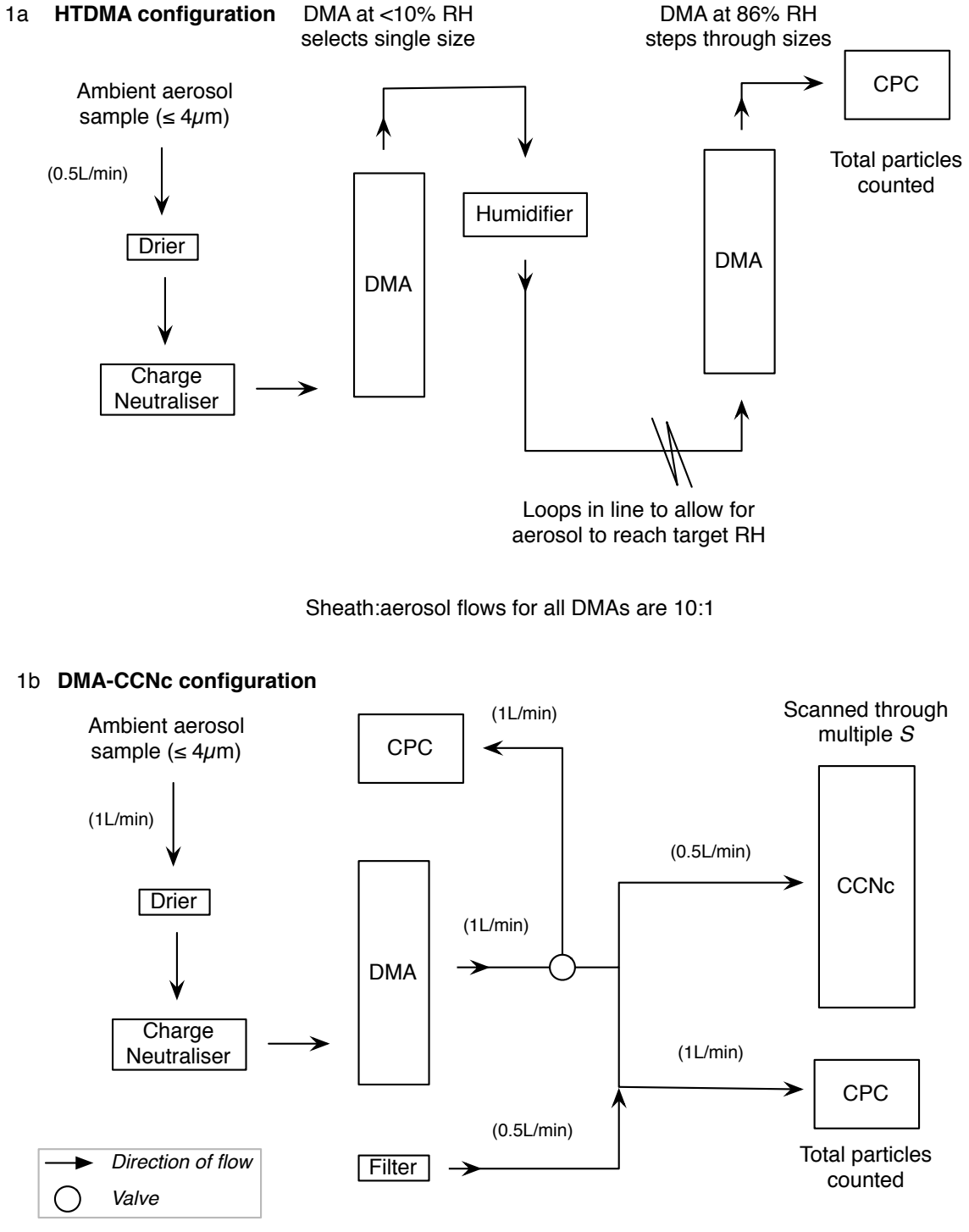


**Fig. 1.** 1a: Simple schematic showing the HTDMA. 1b: Simple schematic of the CCNc setup used for the experiment..

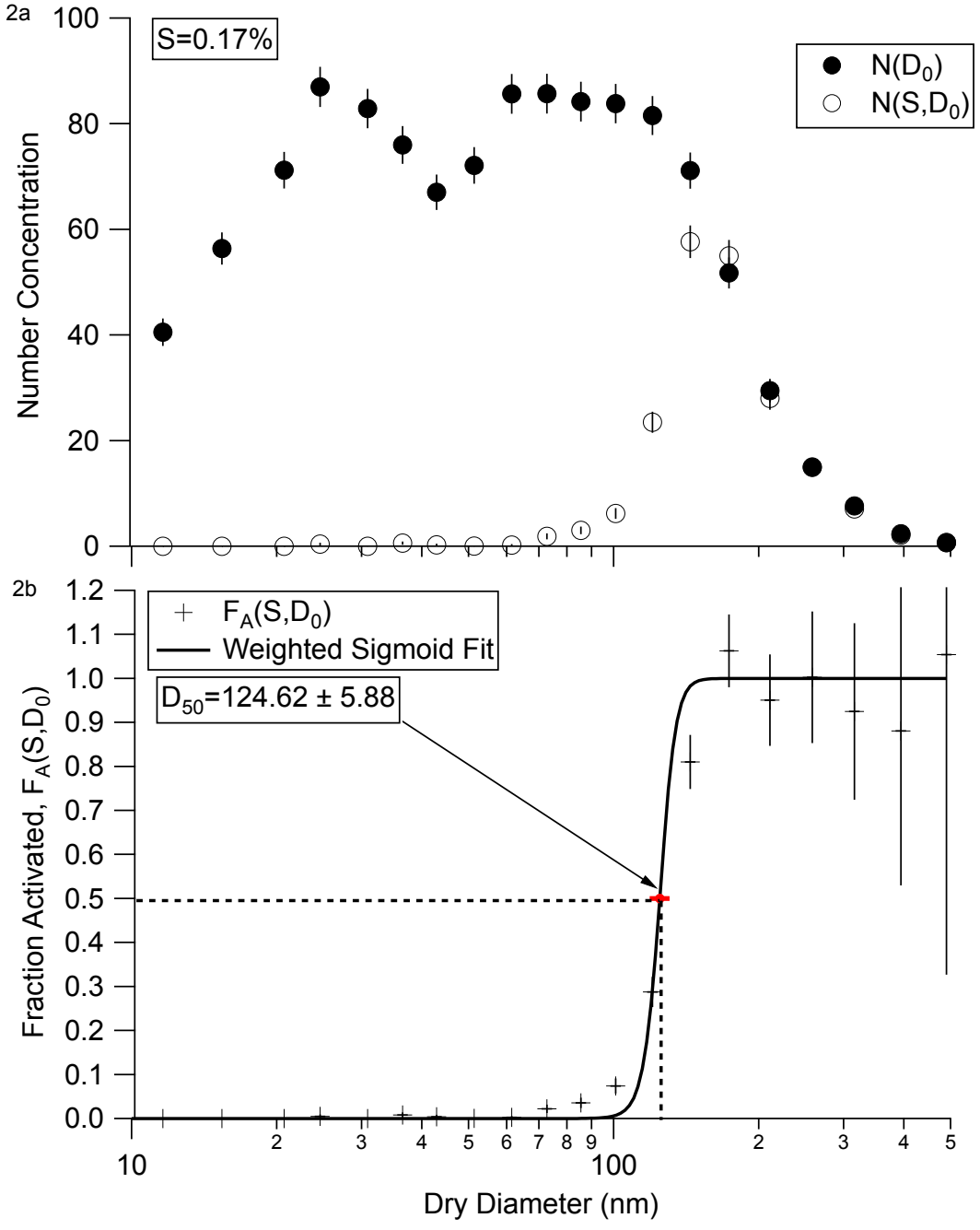


**Fig. 2.** 2a: An example of Number vs. Dry diameter for a supersaturation scan at 0.17%. 2b shows the Fraction Activated, $F_A(S, D_0)$, and the derived $D_{50,S}$. Error bars represent the standard error, calculated and propagated from the parameters defined in Section 3.1.

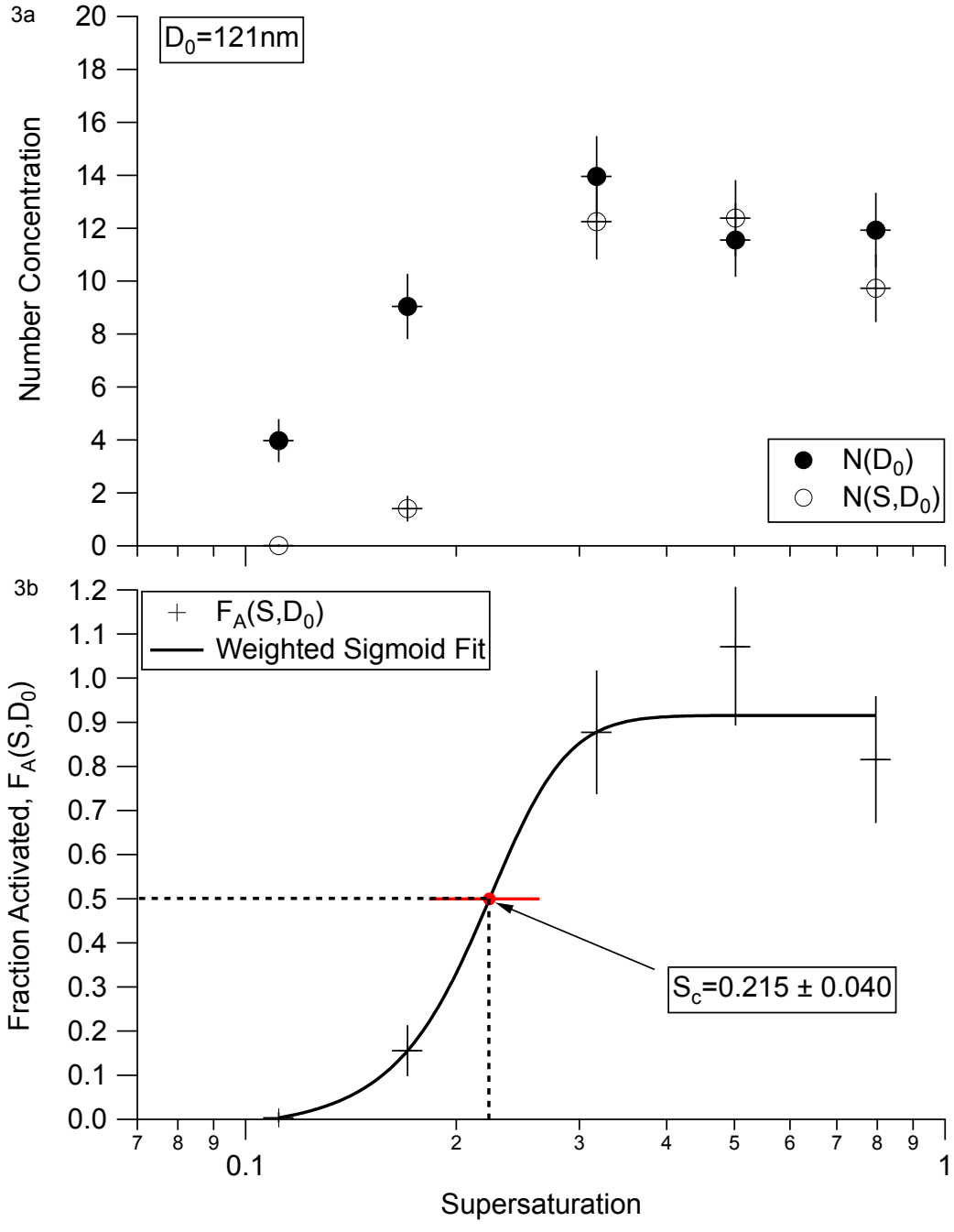


**Fig. 3.** 3a: An example of Number vs. Supersaturation for a dry diameter of 121nm. 3b shows the Fraction Activated, $F_A(S, D_0)$, and the derived critical supersaturation, $S_{c,D0}$. Error bars represent the standard error, calculated and propagated from the parameters defined in Section 3.1.

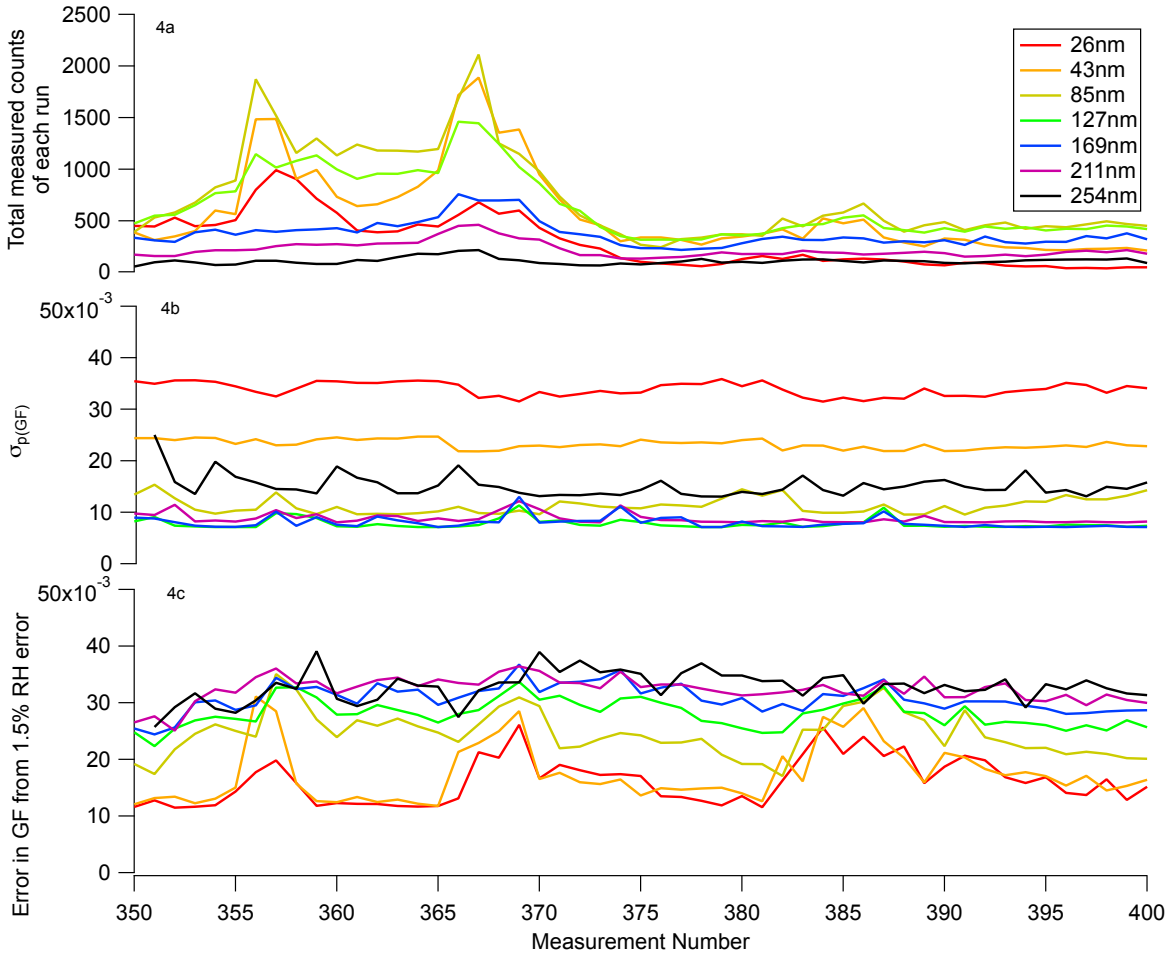


**Fig. 4.** 4a) The total number of counts for each run 4b) An example of the error associated with the Error Simulation, $\sigma_{p(GF)}$ 4c) An example of the error associated with the growth factor correction applied to the data. Colours denote the measurement dry diameter.

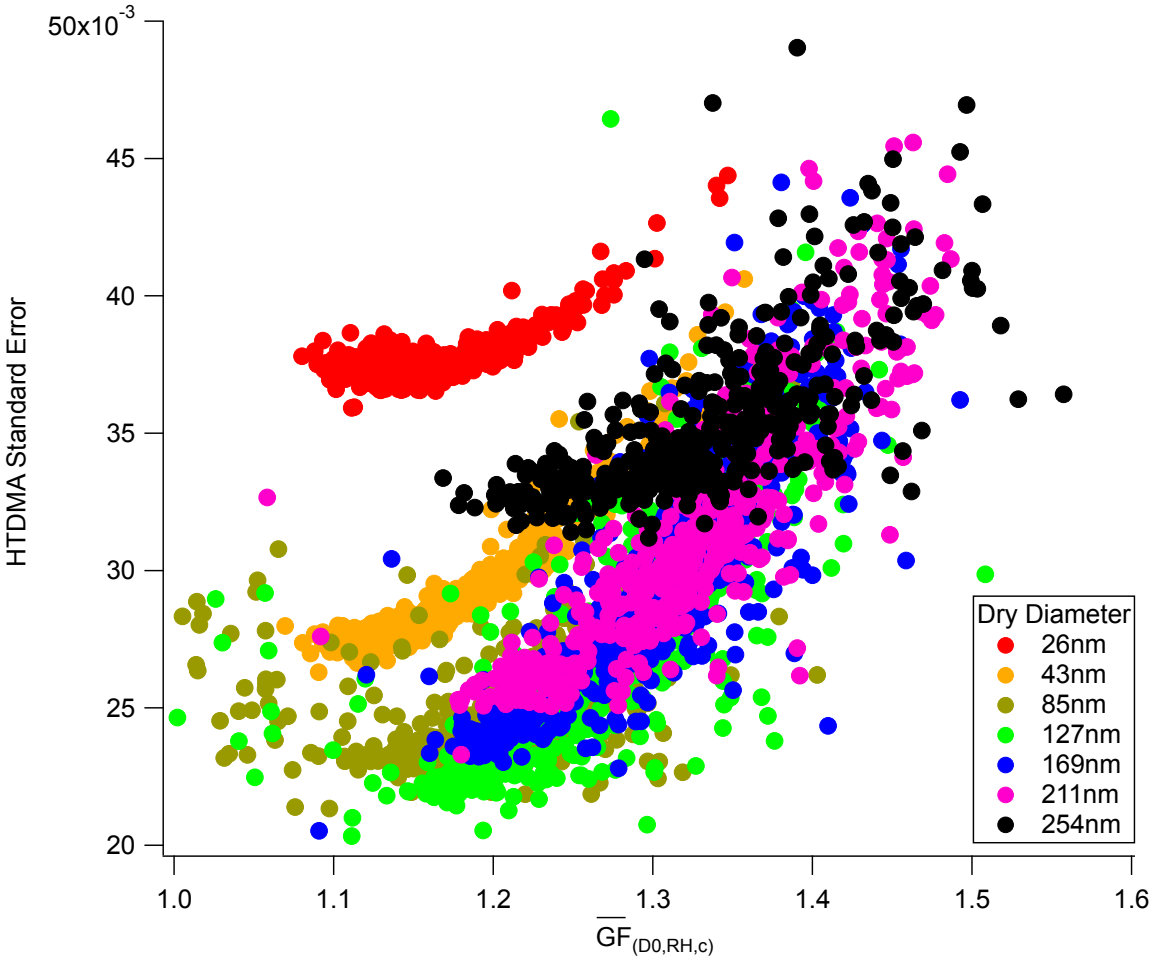


**Fig. 5.** The total HTDMA standard error for each dry diameter (see legend) vs $\overline{GF}_{D0,RH,c}$ (mean $RH$-corrected growth factor). For each size, the error typically increases with increasing growth factor.

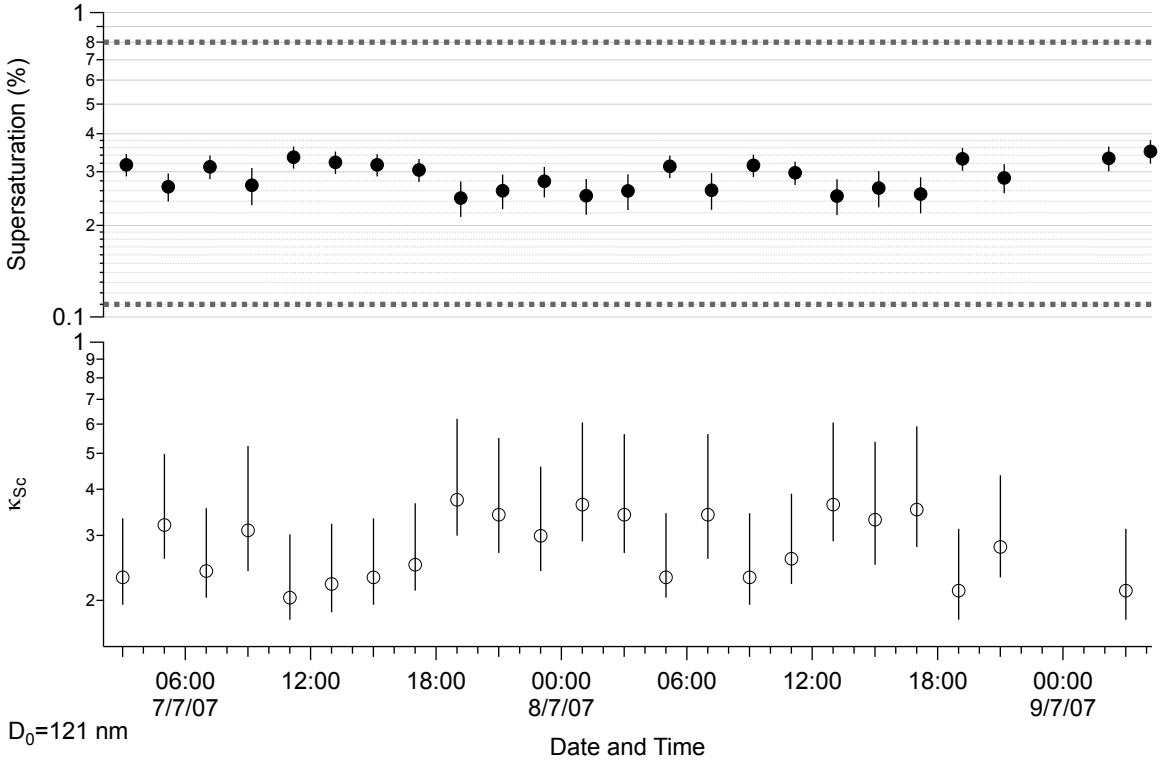


**Fig. 6.** 6a: An example of a series of derived critical supersaturations for the dry diameter 121 $\mathrm{nm}$, including positive and negative error from the fitting of the error-weighted sigmoidal function. 6b: The derived $\kappa_{Sc}$ values, with the error bars illustrating the maximum and minimum in $\kappa_{Sc}$ from the respective $S_{c,D0}$ errors.

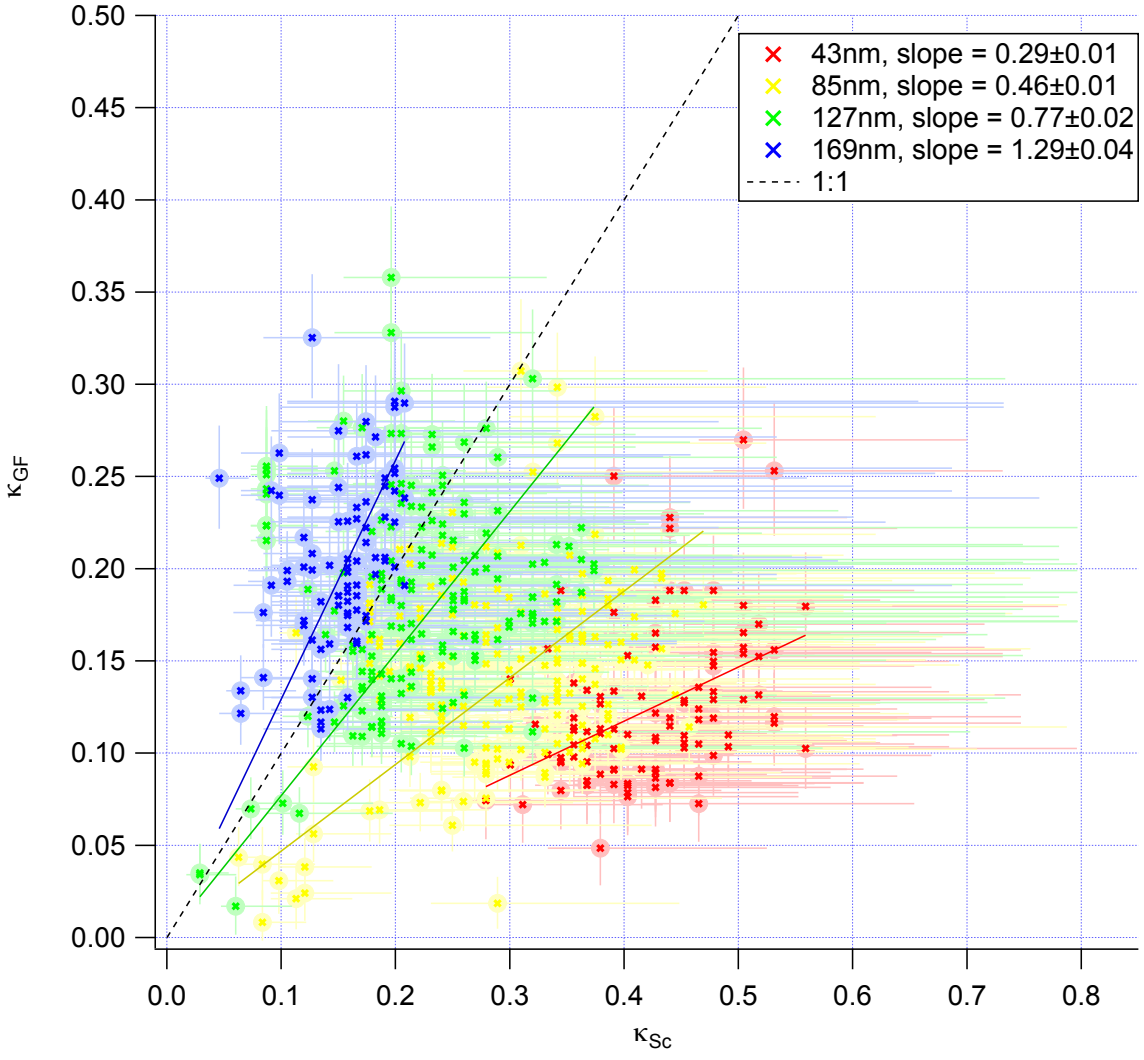


**Fig. 7.** $\kappa_{GF}$ vs $\kappa_{Sc}$, with upper and lower bounds given by their respective errors. The best agreement is at 127 $\mathrm{nm}$. There is typically more error at each size associated with the error derived from the CCNc.

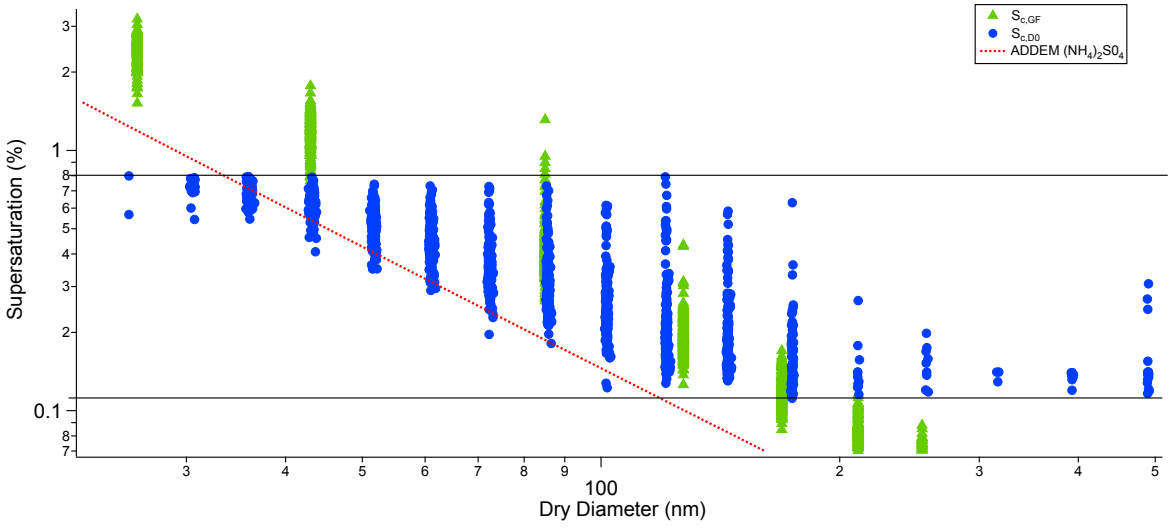


**Fig. 8.** HTDMA predicted $S_{c,GF}$ and CCNc S-scan derived $S_{c,D0}$ plotted against dry diameter. The CCNc maximum and minimum supersaturation settings are shown in black. The HTDMA predicted $S_c$ far extends beyond the measurement ability of the CCNc, with only particles at $\sim$127 $\mathrm{nm}$ bounded completely in supersaturation space.

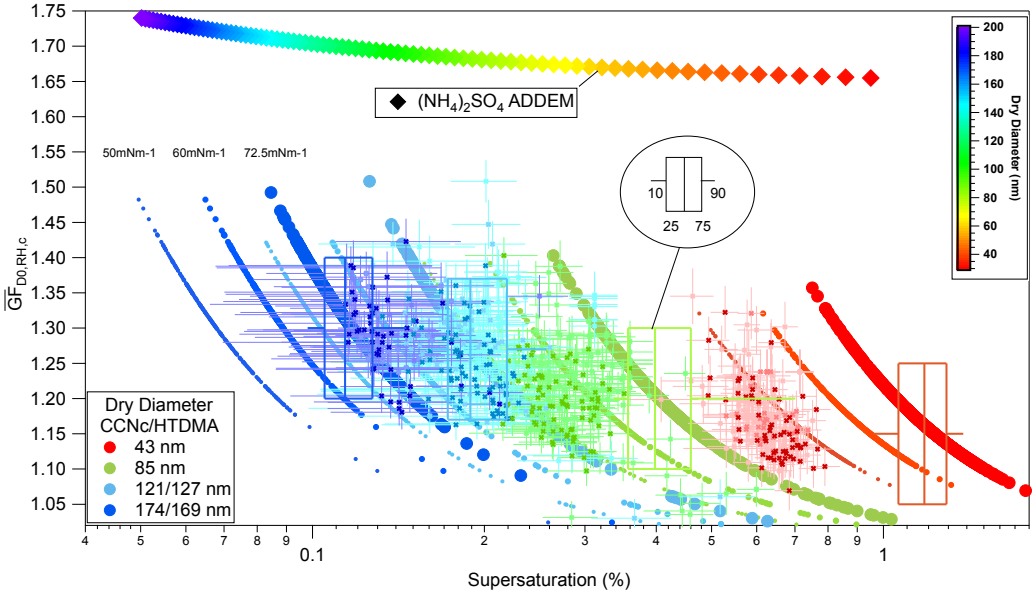


**Fig. 9.** A figure showing HTDMA mean growth factor against predicted $S_c$ (solid circles). CCNc derived $S_c$ is also plotted as crosses, with darker data points representing data in which the mean growth factor is within 5% of the peak growth factor bin (a guide for mixing state).

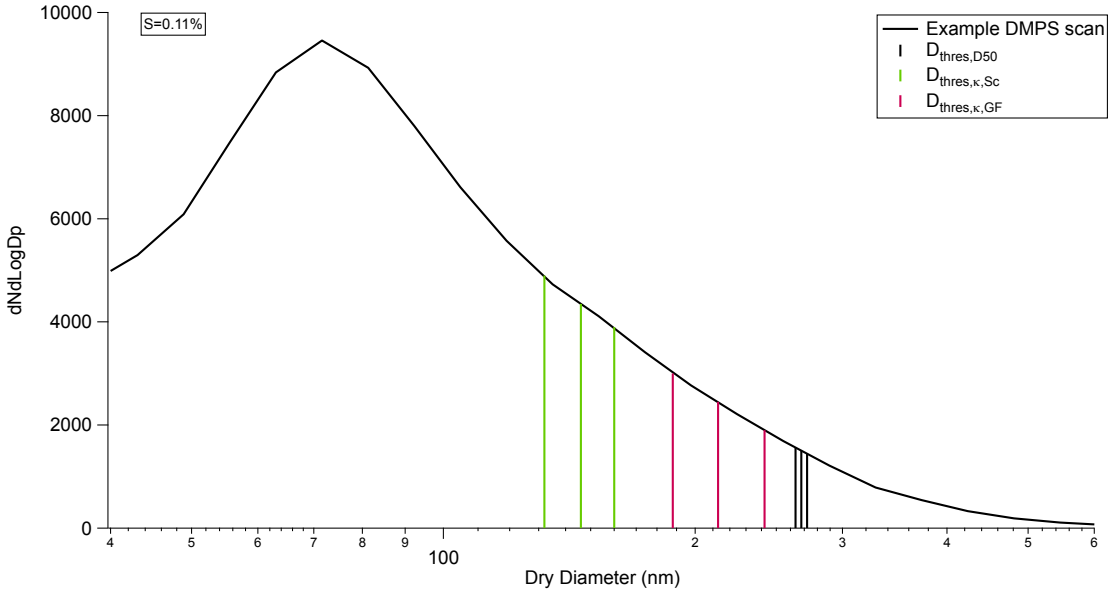


**Fig. 10.** A plot showing an example DMPS number-size distribution, with markings for minimum, mean and maximum derived threshold dry diameters for activation for each analysis method.

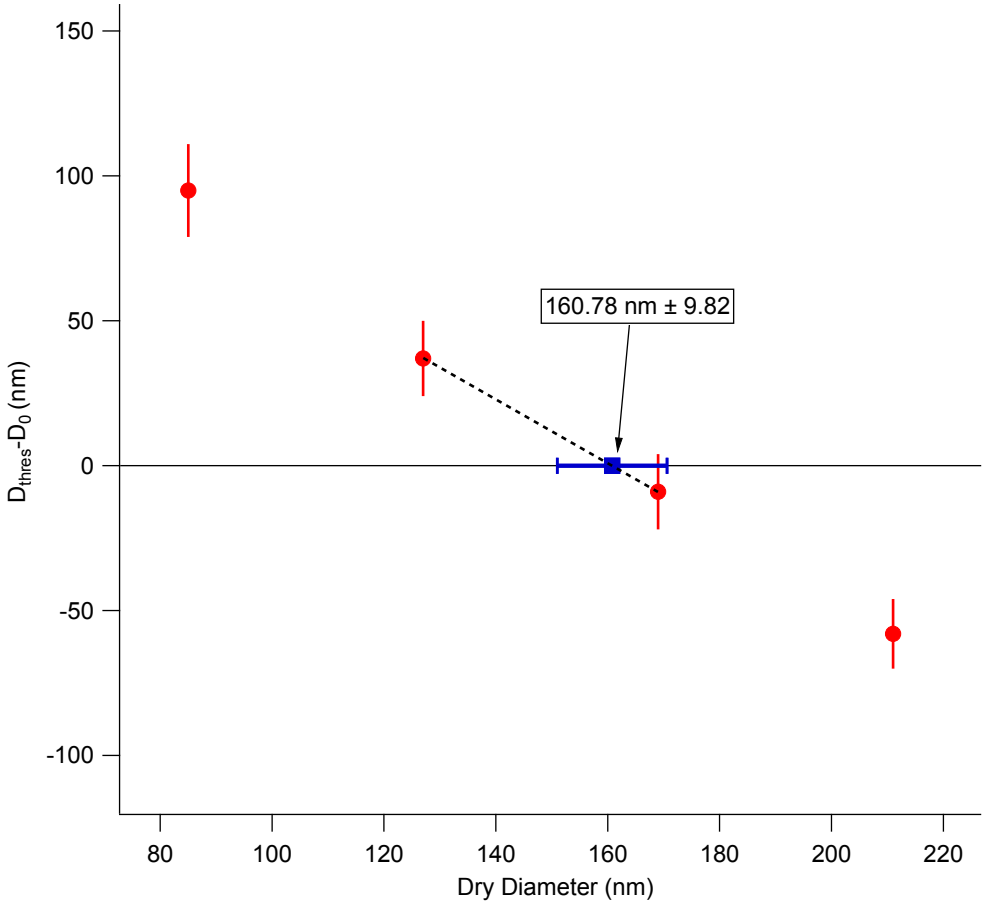


**Fig. 11.** HTDMA derived $D_{thres} - D_0$ vs $D_0$. The two data points straddling the zero line are linearly interpolated between, with the intercept defining the HTDMA $D_{thres,\kappa,GF}$.

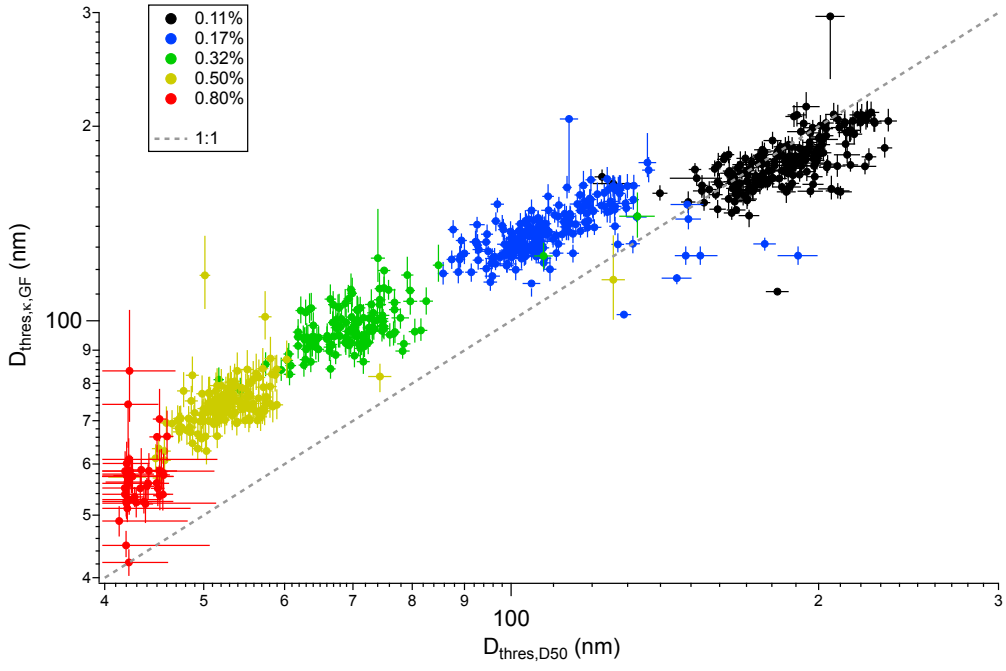


**Fig. 12.** $D_{thres,\kappa,GF}$ vs $D_{thres,D50}$ as a function of supersaturation. Best agreement is shown at the lowest supersaturation, with measurements at the highest supersaturation setting dominated by error.

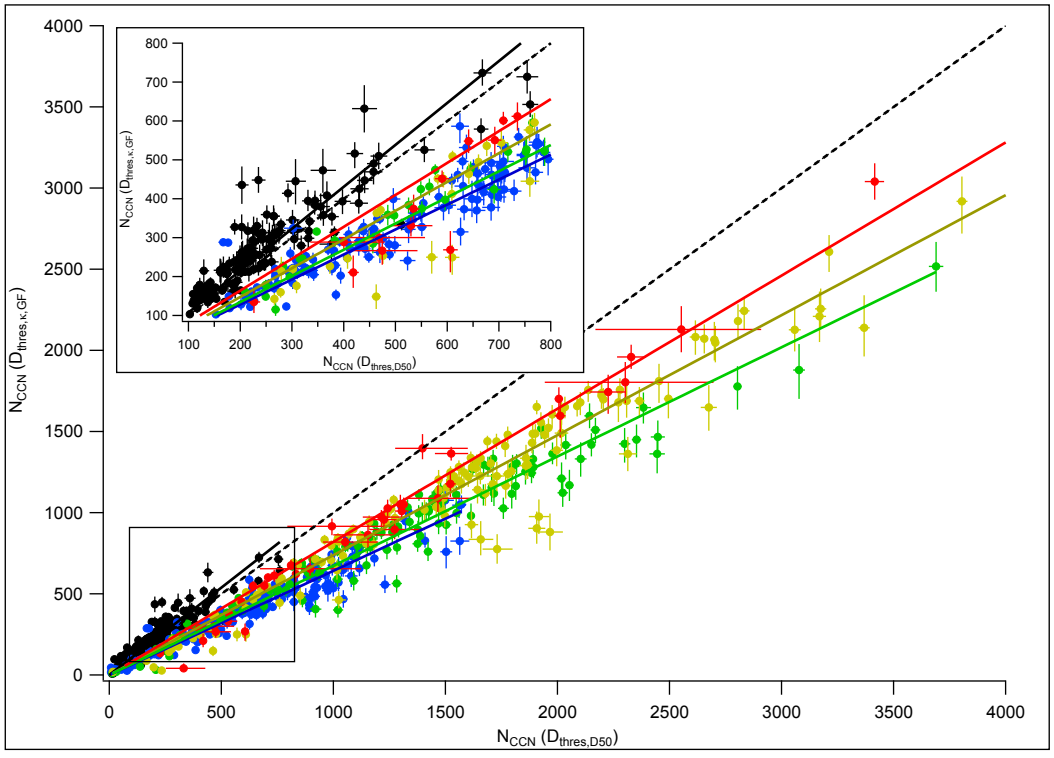


**Fig. 13.** A plot showing the individual $N_{CCN}$ results from HTDMA and $D_{50}$ analysis, at each measurement supersaturation. Inset highlights the agreements and discrepancies in the low number regime.

**Table 1.** Glossary of terms

| | |
|---|---|
| $\Delta T$ | Wall temperature $T3$-$T1$ difference down the CCNc column |
| $S$ | Supersaturation |
| $P$ | Pressure |
| $Q$ | Flow down the CCNc column |
| $D_0$ | Dry particle diameter |
| $N_{S,D0}$ | Activated particle number at $S$ and $D_0$ |
| $N_{D_0}$ | Total particle number |
| $F_A(S, D_0)$ | Fraction of particles activated |
| $D_{50,S}$ | Diameter at which 50% of particles activate |
| $S_{c,D0}$ | Critical supersaturation |
| $D$ | Wet particle diameter |
| $RH$ | Measured relative humidity |
| $p(GF)$ | Uncorrected growth factor probability distribution |
| $p(GF)_c$ | Corrected growth factor probability distribution |
| $\overline{GF}_{uc}$ | Uncorrected mean growth factor |
| $\overline{GF}_{D0,RH,c}$ | Corrected mean growth factor |
| $\kappa_{D50}$ | Hygroscopicity parameter derived from $D_{50,S}$ |
| $\kappa_{Sc}$ | Hygroscopicity parameter derived from $S_{c,D0}$ |
| $\kappa_{GF}$ | Hygroscopicity parameter derived from $\overline{GF}_{D0,RH,c}$ |
| $S_{c,GF}$ | $S_c$ derived from $\kappa_{GF}$ |
| $D_{thres,\kappa,Sc}$ | Threshold diameter for activation derived from $\kappa_{Sc}$ |
| $D_{thres,\kappa,GF}$ | Threshold diameter for activation derived from $\kappa_{GF}$ |
| $D_{thres,Sc}$ | Threshold diameter for activation derived from $S_{c,D0}$ |
| $D_{thres,D50}$ | Threshold diameter for activation derived from $D_{50,S}$ |
| $N_{CCN}$ | Number of cloud condensation nuclei |

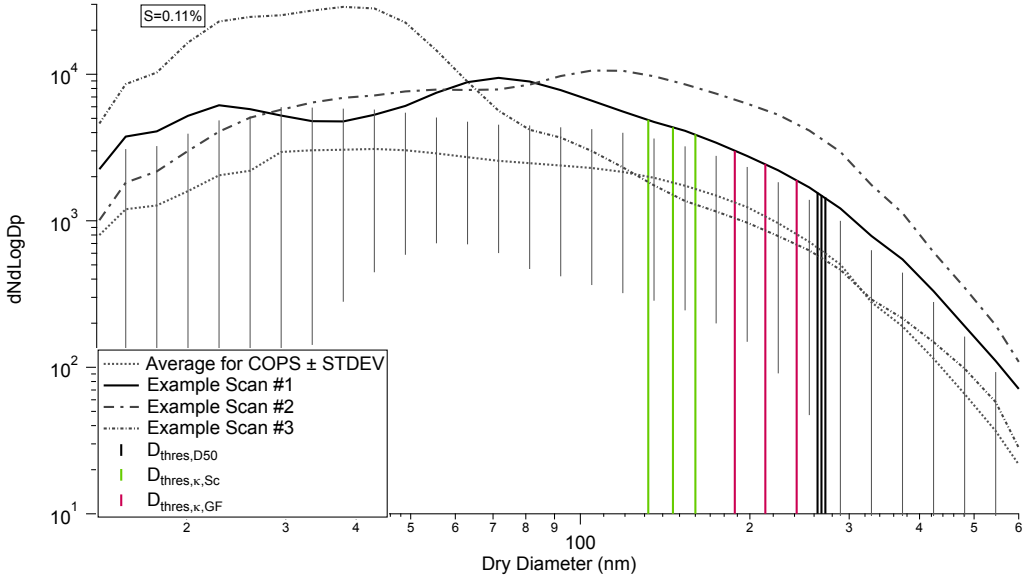


**Fig. 14.** A plot showing the average DMPS number-size distribution for COPS, with standard deviation. In addition to markings for minimum, mean and maximum derived threshold diameters for activation $D_{thres}$ for each analysis method, are two example scans showing how averaging the size distribution across multiple days results in a high loss of detail. There will be considerable variation in NCCN derived from the average when compared to NCCN from single scans due to the position and magnitude of the mode(s).

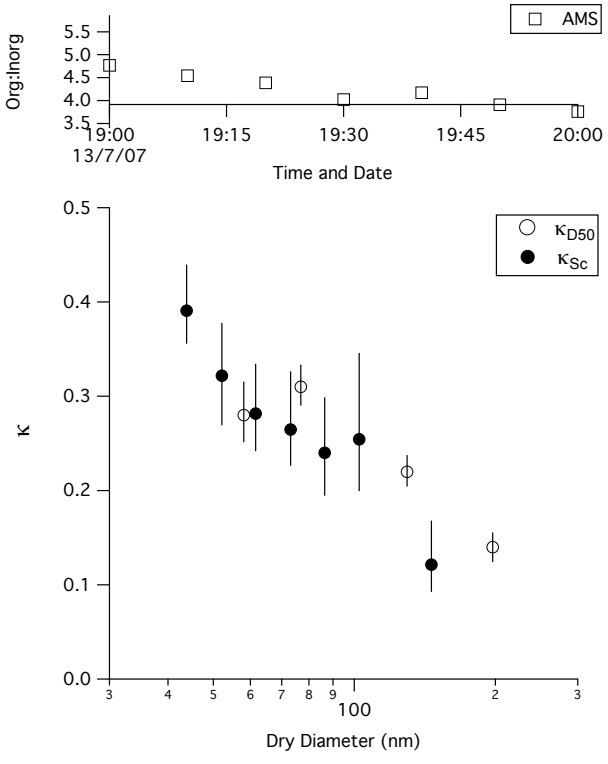


**Fig. 15.** Changes in the organic:inorganic ratio as measured by the AMS during an hour of CCNc size-resolved measurements from which $\kappa_{Sc}$ and $\kappa_{D50}$ are derived.

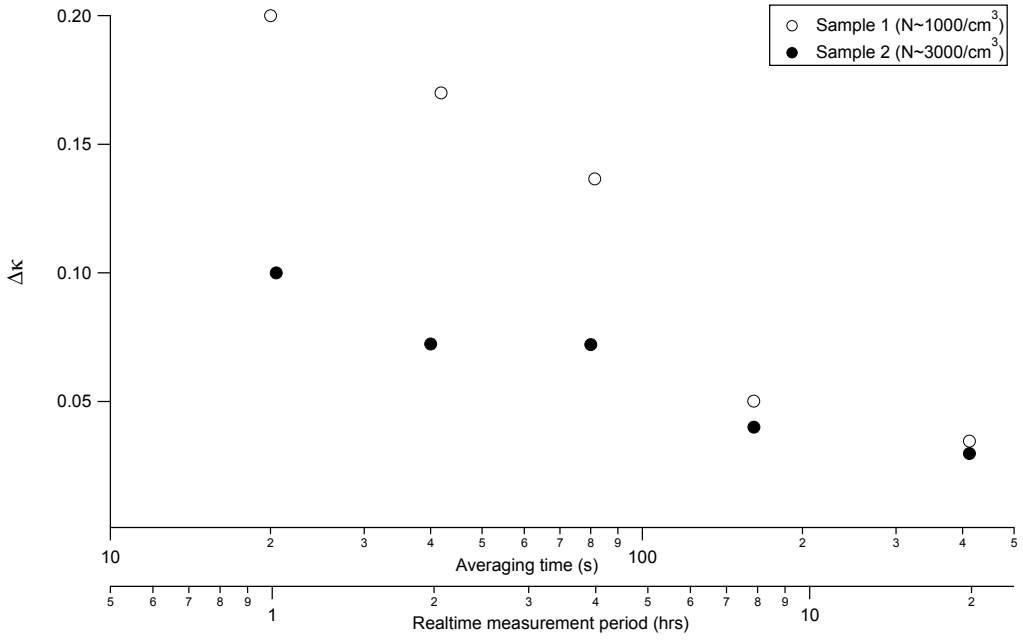


**Fig. 16.** $\Delta\kappa$ plotted as a function of averaging time. The second horizontal axis shows the corresponding timebase of the $\kappa$ measurement. Data from each $D_0$ is originally sampled for 20 seconds and averaged, for each $S$ (of which there are six every ten minutes), resulting in a 1 hour "measurement period".

## 5.2 Paper II

**Reconciliation of measurements of hygroscopic growth and critical supersaturation of aerosol particles in central Germany**

Published in Atmospheric Chemistry and Physics.

Irwin, M., Good, N., Crosier, J., Choularton, T. W., and McFiggans, G. Reconciliation of measurements of hygroscopic growth and critical supersaturation of aerosol particles in Southwest Germany. Atmos. Chem. Phys. (2010) vol. 10 pp. 11737-11752

Atmos. Chem. Phys., 10, 11737–11752, 2010
www.atmos-chem-phys.net/10/11737/2010/
doi:10.5194/acp-10-11737-2010


Atmospheric Chemistry and Physics

# Reconciliation of measurements of hygroscopic growth and critical supersaturation of aerosol particles in central Germany

**M. Irwin**[1], **N. Good**[1], **J. Crosier**[1,2], **T. W. Choularton**[1], **and G. McFiggans**[1]

[1]School of Earth, Atmospheric and Environmental Sciences, University of Manchester, Manchester, UK
[2]National Centre for Atmospheric Science, University of Manchester, Manchester, UK

Received: 31 May 2010 – Published in Atmos. Chem. Phys. Discuss.: 12 July 2010
Revised: 28 November 2010 – Accepted: 6 December 2010 – Published: 10 December 2010

**Abstract.** Aerosol physical, chemical and hygroscopic properties were measured in a range of airmasses during COPS (Convective and Orographically-induced Precipitation Study) ground-based in June and July of 2007 at the Hornisgrinde mountain site in the Black Forest, Southwest Germany. Non-refractory aerosol composition was measured with an Aerosol Mass Spectrometer, simultaneous to hygroscopic growth factors at 86% relative humidity and CCN activity measurements for particles of dry ($< 20\%$) diameters 27 to 217 nm, with particle water uptake exhibiting substantial variability with time and with particle size.

Variability in the measurements of hygroscopic growth factor and critical supersaturation for particles of similar sizes indicates significant compositional impact on particle water affinity. Critical supersaturation prediction using a single parameter hygroscopicity approximation derived from measured HTDMA mean growth factors deviate, beyond measurement uncertainties, from critical supersaturations derived from CCN measurements. These led to differences averaging around 35% in the number of CCN ($N_{CCN}$) for the most reliable measurements depending on averaging methodology, often very much larger for individual time periods. This indicates aspects of water uptake behaviour unresolved in this experiment by the single parameter representation which, depending on its origin, may have important consequences on its generalised use.

*Correspondence to:* G. McFiggans
(gordon.mcfiggans@manchester.ac.uk)

## 1 Introduction

Atmospheric aerosol plays a key role in a number of important climate processes, commonly classified into direct effects (scattering and absorbing radiation; McCormick and Ludwig, 1967; Haywood and Boucher, 2000) and indirect effects (radiative effects that result from modifying the reflectivity, abundance, persistence and other cloud properties). The Intergovernmental Panel on Climate Change (IPCC) Fourth Assessment Report has attributed the largest uncertainty in radiative forcing to that of the aerosol indirect effect (Forster et al., 2007). The first indirect effect, the cloud albedo effect, occurs because differences in the number of cloud condensation nuclei ($N_{CCN}$) alter the reflectivity of clouds (Twomey, 1977). Aerosol particles also have effects on cloud longevity and the initiation or delay of precipitation through increased $N_{CCN}$, which are some of the secondary indirect effects on climate (Albrecht, 1989; Lohmann and Feichter, 2005; Andreae and Rosenfeld, 2008). Uncertainty in $N_{CCN}$ is central to the uncertainty in the aerosol indirect effects.

The ability for a particle to act as a CCN depends on its size and composition. Particles of a dry diameter less than 40 nm are unlikely to activate into cloud droplets regardless of composition and sufficiently large particles will most probably contain enough soluble material to activate under all reasonable atmospheric supersaturations (McFiggans et al., 2006). If a particle's composition is known, then its water uptake at equilibrium can be modelled using the Köhler equation (Köhler, 1936; Rogers and Yau, 1989; Pruppacher and Klett, 1997; Seinfeld and Pandis, 1998) based on physicochemical properties of the solute:

Published by Copernicus Publications on behalf of the European Geosciences Union.

$$S = a_w \exp K_e \quad (1)$$

where $S$ is the saturation ratio (=RH/100), $a_w$ is the water activity or Raoult term, and $K_e$ is the Kelvin term.

The Köhler equation can be envisaged as the competition between two effects, namely the Raoult effect and Kelvin effect. The Raoult effect is defined by the water activity and drawing water into the growing droplet by virtue of the soluble material therein. The Kelvin effect is defined by the resistance to growth resulting from the increased saturation vapour pressure of water with increasing curvature of smaller particles by virtue of the energy associated with the creation of the droplet surface. The Köhler equation is dominated by the water activity when significantly below saturation and the Kelvin term increases in importance approaching the point of activation. The relative importance of the terms in the Köhler equation is explored systematically in Wex et al. (2008).

The atmospheric aerosol is comprised of substantial amounts of organic material (Kanakidou et al., 2005; Hallquist et al., 2009), which may suppress surface tension (Facchini et al., 2000; McFiggans et al., 2005, 2006; Weingartner et al., 2004). Since the surface tension enters into the Köhler equation through the Kelvin term and it is known that organic components may reduce the surface tension of their aqueous solutions, it has been assumed that organic components may play a role in determining cloud activation (e.g. Novakov and Penner, 1993; Saxena et al., 1995; Shulman et al., 1996; Abdul-Razzak and Ghan, 2004). A change in surface tension would play a more important role as the saturation ratio increases (Wex et al., 2008), thus it has been argued that the incorporation of organic material into existing inorganic particles may substantially reduce the supersaturation required to activate an aerosol particle into a cloud droplet (its critical supersaturation, $S_c$). Such an effect would result in an increase in the number of CCN by impacting on the Kelvin term, whilst not significantly influencing subsaturated growth factor through impacts on the number of soluble molecules, affecting the Raoult term. However, bulk to surface partitioning has recently been postulated as occurring within a more detailed description of the surface chemistry which can increase the critical supersaturation required for activation by changing concentration gradients approaching the surface (Sorjamaa et al., 2004; Kokkola et al., 2006; Topping et al., 2007) acting to offset the reduction in $S_c$ predicted to result from reduced surface tension.

A current challenge is to demonstrate the quantitative understanding of atmospheric aerosol behaviour under sub- and supersaturated conditions and the relationship between the two regimes. Multiple field studies from around the world utilising a variety of modelling techniques have compared sub- and supersaturated measurements and model predictions (e.g. Broekhuizen et al., 2006 and references to CCN closure studies in McFiggans et al., 2006 and e.g. Medina et al., 2007; Petters and Kreidenweis, 2007, and references therein) with varying degrees of success. The latter reference presented the $\kappa$-Köhler model, making use of a single parameter $\kappa$ to describe particle hygroscopicity at any humidity. This approach can demonstrably reconcile sub- and supersaturated behaviour of inorganic salts such as sodium chloride within experimental uncertainty, and the use of $\kappa$ to describe the hygroscopicity of ambient aerosol populations has been explored previously (Andreae and Rosenfeld, 2008; Gunthe et al., 2009).

In this study we use the $\kappa$-Köhler model to interpret data from both sub- and supersaturated regimes measured at a continental forest site with strong topographical and convective influences on cloud formation, aiming to reconcile particle water uptake in the two regimes.

## 2 Experimental methodology

### 2.1 Sampling Site and measurement platform

Measurements were conducted from 24 June to 18 July 2008 as part of the Convective and Orographically forced Precipitation Study (COPS) at the Hornisgrinde SuperSite (48°36′0″ N, 8°12′0″ E), which is located in the Western Black Forest in Germany. The Hornisgrinde Mountain is at a height of 1164 m a.b.s.l. and the moorland area at the summit of the Hornisgrinde is a nature reserve with pedestrian access and little vehicle activity. Further details of the measurement site and the COPS programme are presented in detail by Wulfmeyer et al. (2008).

Air was drawn down a 40 mm bore, 3 m high stainless steel stack at a flow rate of 35 l/min, through a cyclone impactor with a 4 $\mu$m cut-off, and then into the container to the instrumentation which, excepting the water uptake measurement instrumentation outlined in Sects. 2.2 and 2.3, is described in more detail by Jones et al. (2010).

### 2.2 Sub-saturated water uptake measurement

A Hygroscopicity Tandem Differential Mobility Analyser (HTDMA; Cubison et al., 2005; Gysel et al., 2007) was used to measure the hygroscopic growth factor distributions at 86% relative humidity (RH) of particles with dry diameters ($D_0$); 27, 43, 85, 127, 169, 211 and 254 nm. The hygroscopic growth factor of a particle is defined as the ratio of wet (86% RH) to dry (< 20% RH) particle diameter. To ensure the HTDMA instrument was measuring reliably, the instrument was calibrated as described in Good et al. (2010a). Briefly, the laminar flow elements and pressure transducers controlling flow through the Differential Mobility Analysers (DMAs) were calibrated using a bubble flowmeter and the DMAs were size-calibrated using NIST-traceable polystyrene latex spheres (PSLs) as outlined by Good et al. (2010a). The RH and temperature sensors within the instrument were calibrated and continuously referenced against a dew point hydrometer (Cubison et al., 2005). Dry (RH $\leq$ 20%) scans were performed at weekly intervals to ensure that both the DMAs were in agreement, to monitor the width of the DMA transfer functions, to measure the offset between the two

DMAs as well as any temporal trend (Gysel et al., 2009; Good et al., 2010a). The HTDMA system was calibrated with dried, charge-neutralised 150 nm ammonium sulphate and sodium chloride ($\geq$ 99.5%, Sigma Aldrich) such that the RH of the second DMA was increased slightly beyond the measurement range (to typically greater than 90% RH). Both deliquescence and effloresced points for both salts are measured by the HTDMA and verified against the ADDEM model (Topping et al., 2005).

The first DMA was used to select dry particle size with dry sheath air and a residence time of ~60 s was included between the humidifier and the second DMA (Cubison et al., 2005; Gysel et al., 2007). The second DMA was operated with both sheath and aerosol flows at a target RH of 86%, as due to unforeseen circumstances the instrument struggled to reach 90% RH whilst sampling ambient aerosol, and the decision was made to sample at a lower RH with greater stability. The target of 86% RH was reached for the majority of the experiment with variability between 84–88% RH. The second DMA voltage (and thus mobility diameter) was stepped through each $D_0$ to measure the raw particle diameter growth factor distribution. These raw data were inverted to account for the HTDMA instrument function using the TDMAinv algorithm along with the associated analysis and quality assurance procedures described by Gysel et al. (2009).

Further to inversion, data measured between 84%–88% RH were corrected to 86% RH using Eq. (S1) in the Supplement, and an error simulation showing the sensitivity of the inversion result to small changes in measurement was performed as described by Gysel et al. (2009). The results of the error simulation and the propagation of measurement uncertainty as standard errors are described in Sect. 1.1 of the Supplement. From the analysis and error propagation, the mean of the particle growth factor probability distribution ($p$(GF); the probability distribution of the aerosol particle having a specific growth factor) becomes the corrected mean growth factor, $\overline{\mathrm{GF}}_{D_0,\mathrm{RH,c}}$.

### 2.3 Droplet activation measurement

A Droplet Measurement Technologies (DMT) Cloud Condensation Nucleus counter (CCNc; Roberts and Nenes, 2005) was used to probe the activation behaviour of the sampled particles. The CCNc instrumental configuration was alternated between sampling poly-disperse and monodisperse aerosol. To generate a monodisperse aerosol, dried (RH < 20%) polydisperse aerosol was charge equilibrated then size selected in a DMA. This monodisperse aerosol was then split between the CCNc and a 3010 TSI Condensation Particle Counter (CPC) with the sample line lengths from the DMA to the CPC inlet and top of the CCNc column matched in order to ensure line losses were equal. The DMA operated at an aerosol flow rate of 1 Lmin$^{-1}$ (10:1 with sheath flow), the CCNc operated at 0.5 Lmin$^{-1}$, the CPC at 1 Lmin$^{-1}$ with 0.5 Lmin$^{-1}$ from the DMA and 0.5 Lmin$^{-1}$ from a filtered air supply. All sample flows were ensured to be the same and were calibrated and checked daily with a bubble flow meter. For each mobility-selected size, the ratio of CCN to CPC concentration defines the activated fraction at a given supersaturation. Particles just below their critical supersaturation may have a large unactivated equilibrium size that can be of the same order as activated droplets ($\approx$1 $\mu$m, Lance et al., 2006) and particles were judged to have activated when detected by the OPC in the CCNc at diameters above 1 $\mu$m. The fraction of the particles at a given supersaturation ($S$) and dry diameter ($D_0$) that have activated into cloud droplets is defined as $F_\mathrm{A}(S, D_0) = N(S, D_0)/N(D_0)$ where $N(S, D_0)$ is the number of activated particles counted by the CCNc and $N(D_0)$ is the number of condensation nuclei (CN).

Perfectly monodisperse internally mixed particles would all activate at a single discrete supersaturation such that 100% of the particles would be unactivated at an infinitesimally lower supersaturation, but activated at an infinitesimally higher value. In reality, the monodisperse selection will be of finite dispersion with broadening defined by the DMA transfer function. In addition, as found by Rose et al. (2008) there is an indeterminate contribution to the "system transfer function" such that deviation in the observed CCN spectrum from a step change in the activated fraction does not result from the ideal transfer function of the DMA alone.

Assuming that the DMA transfer function is symmetrical about the selected dry mobility, the supersaturation at which 50% of the particles have activated into cloud droplets for a given dry diameter, was directly interpreted as representing the critical supersaturation for activation, denoted $S_{\mathrm{c},D_0}$ and derived by fitting a sigmoidal function to $F_\mathrm{A}(S, D_0)$ vs. $S_\mathrm{set}$, as described in Sect. 1.2 in the Supplement, and hereafter referred to as S-step analysis. Variations in the hygroscopicity of particles of the same $D_0$ may lead to further spectral broadening, affecting the interpretation of $S_{\mathrm{c},D_0}$. The impacts of such deviations from an internally-mixed particle population is discussed later. In addition to deriving particle critical supersaturation through S-step analysis, fitting the sigmoid function to a plot of $F_\mathrm{A}(S, D_0)$ vs. $D_0$ defines D-step analysis, from which the diameter at which 50% of the particles activated into cloud droplets was derived at each supersaturation; $D_{50,\mathrm{S}}$. The sigmoidal function is identical for both S-Step and D-step analyses, described in Sect. 1.2 in the Supplement.

The DMA supplying the CCNc performed a full cycle of sequential steps of values of $D_0$ every 7 min, with a 3 min settling period before each 7 min sequence (to allow temperatures in the CCNc column to stabilise), resulting in 10 min size distributions. Simultaneously, the CCNc would step through 5 different values of $S_\mathrm{set}$ every hour, remaining at each supersaturation for 10 min, with lowest supersaturation scan repeated twice at the beginning of each hour to allow for the temperature to stabilise down the column. Therefore, every 10 min, a full cycle of $D_0$ steps were performed and every hour, a full cycle of $S_\mathrm{set}$ steps were performed.

The benefit of S-step analysis is that the critical supersaturation for multiple dry diameters is measured on an hourly basis. However, D-step analysis typically has a smaller associated fitting error resulting from the increase in the number of data points used in each sigmoidal fit (20 $D_0$ for each of the five supersaturations; see Sect. 1.2 in the Supplement). The single hygroscopicity parameter $\kappa$ may be derived from either S-step or D-step analysis. However, the error associated with the calculation of $\kappa$ cannot be propagated as the the $\kappa$-model cannot be solved numerically or analytically, and as such the uncertainty in $\kappa$ is simply propagated through as a standard error from the sigmoidal fit, resulting in maximum and minimum values of $\kappa$, described in Sect. 2.5. The number of CCN ($N_{CCN}$) for a given dry diameter and supersaturation can be calculated from both S-step and D-step approaches and the aerosol number-size distributions as described in Sect. 3.6.

CCN instrument calibration involved the sampling of nebulised, dried, charge-equilibrated, and size-selected ammonium sulphate ($\geq 99.5\%$, Sigma Aldrich) and sodium chloride ($\geq 99.5\%$, Sigma Aldrich) aerosol particles with a TSI 3010 CPC and the CCNc. The measured $S_c$ was plotted against the predicted $S_c$ of ammonium sulphate particles of the same dry diameter as calculated using the ionic interaction model within the Aerosol Diameter Dependent Equilibrium Model (ADDEM; Topping et al., 2005). A $\Delta T$ dependent calibration factor was applied such that the calibrated supersaturation setpoints were 0.11%, 0.17%, 0.32%, 0.50% and 0.80% (the supersaturation range was increased from 0.11%, 0.17%, 0.28%, 0.35% and 0.65% after the first week, 25 June–3 July, after reviewing the aerosol activation behaviour).

The number fraction of particles with multiple charges at $F_A(S, D_0) = 0.5$ of the calibration aerosol were found to be negligible due to the shape of the distribution. Nevertheless, the dataset was corrected for the effects of multiply charged particles in standard DMPS procedure, using the charging probability coefficients found by Wiedensohler (1987) as reported by Good et al. (2010a). As the container was air conditioned to $20\,^{\circ}C \pm 2\,^{\circ}C$, the set point supersaturations corresponded to a near-constant $\Delta T$ and thus absolute $T$, ensuring validity of the calibration. In addition to calibrations, uncertainty in the measurements have been propagated through the data analysis as described in previously, in the Supplement. Hourly switching of the DMA-CCNc instrumentation between polydisperse and monodisperse operation continued throughout the project, as the DMPS made use of two DMA columns, compared to the sole DMA used in the DMA-CCNc configuration. When the CCNc was running in poly-disperse mode, the CPC was used in the Differential Mobility Particle Sizer (DMPS; Williams et al., 2007) instrument. During monodisperse operation, the DMA supplied the CCNc and CPC as outlined above. Only results from this latter mode of operation are presented here.

A more complete description of the calibration, quality assurance procedures carried out for the two instruments is presented by Good et al. (2010a) and additional information on the error propagation can be found in the Supplement.

### 2.4 Aerosol composition

A High-Resolution Time-of-Flight Aerosol Mass Spectrometer (HR-ToF-AMS, Aerodyne Research Inc.) was used to probe non-refractory aerosol particle composition (DeCarlo et al., 2006). The instrument was operated with a heater temperature of approximately 550 °C and is capable of measuring particles from 40 nm–700 nm vacuum aerodynamic diameter (DeCarlo et al., 2004). The mass size distribution of the aerosol particles was measured in particle mode. The collection efficiency used for the COPS data was 0.5, which is consistent with results from laboratory (Matthew et al., 2008) resulting in broad agreement with the integrated submicron volume time series from the DMPS (i.e. within 20% using an organic density of $1.4\,gm^{-3}$).

### 2.5 Predicting $S_c$ from measured HTDMA $GF_D$

The $\kappa$-Köhler model represents water activity ($a_w$) in terms of a constant ($\kappa$) within the primitive Köhler equation (Eq. 1) assuming a constant value for surface tension within the kelvin term:

$$S = \frac{D^3 - D_0^3}{D^3 - D_0^3(1-\kappa)} \exp\left(\frac{4\sigma_w M_w}{RT\rho_w D}\right) \quad (2)$$

Where $D$ is the droplet diameter at the given RH, $D_0$ is dry particle diameter, $\sigma_w$ is the surface tension of water, $M_w$ is the molecular weight of water, $R$ is the universal gas constant, $T$ is the droplet temperature and $\rho_w$ is the density of water.

To examine the applicability of the $\kappa$-Köhler approach taken by Petters and Kreidenweis (2007), $\kappa$ is derived from measured HTDMA-determined values of the hygroscopic diameter growth factor. Substituting $GF_{D_0,RH}$ into Eq. (2), the $\kappa$-Köhler equation for a defined RH becomes:

$$RH = \frac{GF_{D_0,RH}^3 - 1}{GF_{D_0,RH}^3 - (1-\kappa)} \exp\left(\frac{4\sigma_w M_w}{RT\rho_w D_0 GF_{D_0,RH}}\right) \quad (3)$$

The critical supersaturation predicted from the HTDMA, denoted $S_{c,GF}$, is predicted for a given droplet diameter using Eq. (3) with $\kappa_{GF}$ (i.e. $\kappa$ derived from HTDMA measurements of hygroscopic Growth Factor) and incrementally increasing the growth factor until the relative humidity starts to decrease. As with traditional Köhler theory, the maximum in $S$ for a given size and composition (expressed by $\kappa$) determines $S_c$ for activation to a cloud droplet (Petters et al., 2007).

### 2.6 Error analysis

In order to investigate whether the sub- and supersaturated water uptake behaviour can be reconciled within the

measurement uncertainty, it is necessary to propagate the errors associated with each step in the analysis into each level of data product. A description of the uncertainty analysis and error propagation is provided in Sects. 1.1–1.3.3 in the Supplement.

Briefly, the measurements of both the CCNc and HTDMA have been broken down into primary and secondary data quantities, with the measurement uncertainty at each stage quantified as standard error. Equation (S4) in the Supplement shows the fitting function used to derive $S_{c,D_0}$ and $D_{50,S}$. The function outputs a standard error, which is used to calculate maximum and minimum values of $S_{c,D_0}$ and $D_{50,S}$. Similarly, the error defined by Eq. (S3) in the Supplement defines the standard error in $GF_{D_0,RH,}$, providing a maximum and minimum $GF_{D_0,RH,}$. These standard errors have been propagated through to higher order data products in order to better interpret the results of any comparison or the conclusions drawn.

## 3 Results and analysis

### 3.1 Meteorological conditions

For the majority of the experiment, the wind originated from west of southwest, flowing up the valley (see Fig. S2 in the Supplement). Throughout the experiment the measurement site was frequently within cloud, with ambient RH sensors saturating at 100% (Fig. S3 in the Supplement). No-cloud conditions often resulted from cloud base rising well above the measurement platform. The beginning of the measurement period (24 June–28 June) was characterised by cloud cover and some rainfall. The period of 29 June–2 July was mostly clear, with a distinct cloud event on the 30 June. The site was in cloud from 2–6 July, and again from 9–14 July. The final days of the measurement were characterised by clear, sunny days and low RH. Cloudy and no-cloud sampling periods were distinguished according to aerosol number concentrations as measured by a GRIMM Optical Particle Counter ($0.3\,\mu m \leq D \leq 20\,\mu m$ in conjunction with ambient RH data (GRIMM concentration $\leq 100\,L^{-1}$ and RH $\geq 95\%$). These periods have been broadly approximated for contiguous representation and are described in Table 1. "Cloud periods" are denoted "CP" and "No-cloud" periods denoted "NC". Jones et al. (2010) have further detailed the meteorological conditions with the use of cloud camera data for their analysis.

During cloud periods, accumulation mode particle concentrations were low. This would be expected because of the activation of particles larger than the threshold dry size for activation forming droplets larger than the inlet cyclone cut of $4\,\mu m$. There were periods when high concentrations of particles ($1000\,cm^{-3}$) of $D_0 \leq 20\,nm$ were observed in both cloudy and no-cloud periods. Each no-cloud period was characterised by high concentrations of particles with $D_0 \geq 30\,nm$ a matter of hours after the RH dropped to below 80%, with the distribution exhibiting apparent growth over the course of the day to an average $D_0$ of 100 nm (Fig. S3 in the Supplement). It is apparent that there was a significant dynamical evolution of the observed aerosol throughout the experiment.

**Table 1.** Time and date for "cloud periods" (CP) and "no-cloud" (NC) periods as defined by RH and GRIMM measurements, and the Organic:Sulphate ratio for each period.

| Name | Start | End | Org:Sulphate |
|---|---|---|---|
| CP1 | 25/06/2007 12:00 | 28/06/2007 16:00 | 2.251 |
| NC1 | 28/06/2007 16:00 | 02/07/2007 22:00 | 2.491 |
| CP2 | 02/07/2007 22:00 | 06/07/2007 15:00 | 2.522 |
| NC2 | 06/07/2007 15:00 | 08/07/2007 15:00 | 2.903 |
| CP3 | 08/07/2007 15:00 | 13/07/2007 11:00 | 3.635 |
| NC3 | 13/07/2007 11:00 | 18/07/2007 11:30 | 5.522 |
| CP4 | 18/07/2007 11:30 | 22/07/2007 13:00 | 2.830 |
| NC4 | 22/07/2007 13:00 | 23/07/2007 16:00 | 1.346 |

### 3.2 Aerosol composition

The organic:sulphate mass ratio, as diagnosed from the HR-ToF-AMS, averaged 3:1 over the course of the project, with significant variability (see Fig. S3 in the Supplement). The organic:sulphate ratio tracks the organic:inorganic ratio well, with the majority of the variation in the organic:inorganic ratio coming from the variation in the sulphate component. Cloud periods are characterised by low accumulation mode number concentrations and lower mean organic:sulphate ratio (largely driven by enhanced sulphate loading), primarily seen in the second and fifth cloud periods, CP2 and CP5. A significant deviation from the mean was observed during the third no-cloud period, NC3, during which the organic:sulphate ratio was highly variable with peak ratio in excess of 8:1 and minima around 1:1. This highly variable period was followed by a more quiescent period and a reduction to the campaign mean ratio of 3:1 from the 17 July onwards. It should be noted that the meteorological influences on the aerosol composition were complex. All things being equal, one might expect sulphate aerosol to be preferentially scavenged by cloud and hence the organic to sulphate ratio to be enhanced in interstitial aerosol particles sampled under cloudy conditions. This was not clearly observed during COPS and the organic to sulphate ratio was frequently enhanced during no-cloud conditions. This was particularly noticeable during NC3. Prior to NC3, the cloud had been clearly advective and large-scale, with the possibility of large-scale in-cloud sulphate production leading to comparatively low organic:sulphate ratio. In contrast, the temperature (shown in the top panel of Fig. S3 in the Supplement) from this period onwards was warmer than before and the clear-sky conditions were conducive to biogenic organic aerosol

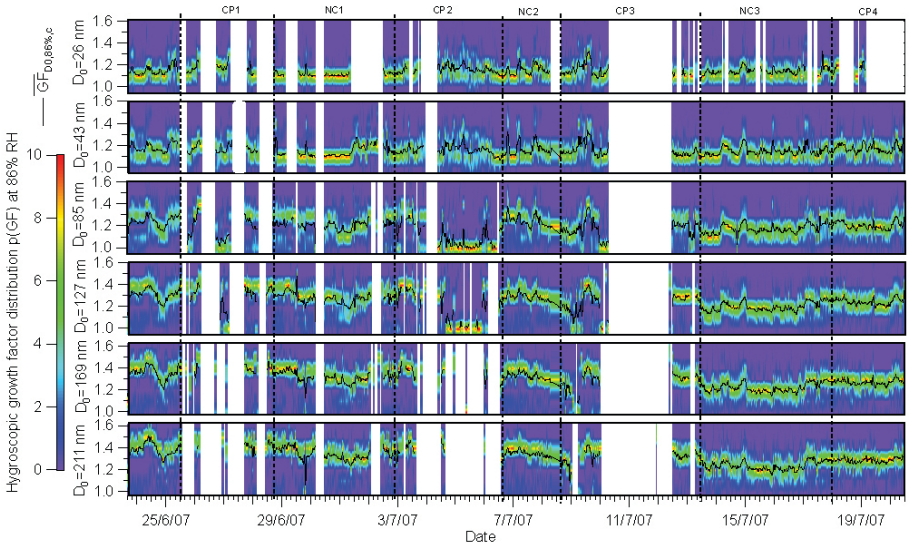


**Fig. 1.** Measured HTDMA hygroscopic growth factor probability distribution, $p$(GF), as a function of time. The HTDMA growth factor distribution is typically well represented by the mean growth factor, $\overline{\mathrm{GF}}_{D_0,86\%,\mathrm{c}}$. However, there is an increasing prominence of bimodality seen with an increase of size (see Fig. S6 in the Supplement).

formation that may have led to the increased organic:sulphate ratio (Jones et al., 2010).

The AMS cannot detect refractory components and such there are no measurements of dust, black carbon or sea-salt. Variations in any of these components would alter particulate composition and thus hygroscopicity with less hygroscopic components such as dust and black carbon and more hygroscopic components such as sea-salt influencing particle growth factor and critical supersaturation for given dry diameters, though the AMS cannot be used to probe the magnitude of each component. Black carbon was measured by a Multi-Angle Absorption Photometer (MAAP), and analysis of the data showed no distinct correlation between the measured amounts of BC and aerosol hygroscopicity and derived products such as $\kappa$ from HTDMA or CCNc as there was too little BC measured to affect the hygroscopic growth factor distrubutions. Dust and seasalt composition were not directly measured (though dust can be inferred from OPC measurements, aerosol hygroscopicity did not change greatly with the magnitude of the aerosol coarse mode and sea-salt is unlikely important in the COPS region). Aerosol composition during COPS is further discussed by Jones et al. (2010).

### 3.3 Hygroscopic behaviour in the sub-saturated regime

Growth factor probability densities were measured as described in Sect. 2.2 and are shown in Fig. 1 with a time resolution of 1h. For the majority of the measurement period a strong influence of particle size on hygroscopic growth is observed with the mean hygroscopic growth factor ($\overline{\mathrm{GF}}_{D_0,\mathrm{RH,c}}$) increasing from an average of 1.15 at 26 nm to 1.35 at 211 nm. For the majority of the experiment, the mean growth factor represents well the modal growth factor for each measured size, though at times there is increased bimodality at dry diameters greater than 127 nm. At all sizes, there is a fraction of the particles with low hygroscopicity (growth factor of ~1.15, similar to the mean seen at the lowest dry diameter, $D_0 = 26$ nm) though with considerably reduced relative contribution at larger sizes. When the concentrations of the less hygroscopic mode are higher (NC1, NC2, CP3) the mean growth factor is reduced by up to 0.05 from the peak in the $p$(GF), invariably found in the main, more hygroscopic mode.

The aerosol sampled during cloudy periods were, somewhat counter-intuitively, characterised by a low organic:sulphate ratio (as mentioned in Sect. 3.2 above), and this increase in relative sulphate is consistent with the slightly higher mean growth factors during these periods. Out of cloud mean growth factors tend to be lower in comparison, consistent with the increased mass fraction of organics, with a typical organic:sulphate ratio of $\geq$4:1.

### 3.4 Measurements of cloud activation behaviour

The fraction of aerosol activated, $F_{\mathrm{A}}(S, D_0)$, typically increases with both dry diameter and supersaturation as shown in Fig. 2. Towards the latter part of the first half of the experiment, it was noted that the supersaturation settings $S_{\mathrm{set}}$ of 0.65% was not activating all of the aerosol size distribution. The measurement range was increased to a ceiling of $S_{\mathrm{set}} = 0.80\%$ as to improve the derivation of $S_{\mathrm{c},D_0}$ for $D_0$ below 100 nm. At the lowest supersaturation (0.11%) only sizes with $D_0$ over 200 nm activate for the majority of the measurement period. As is expected, $F_{\mathrm{A}}(S, D_0)$ increases with

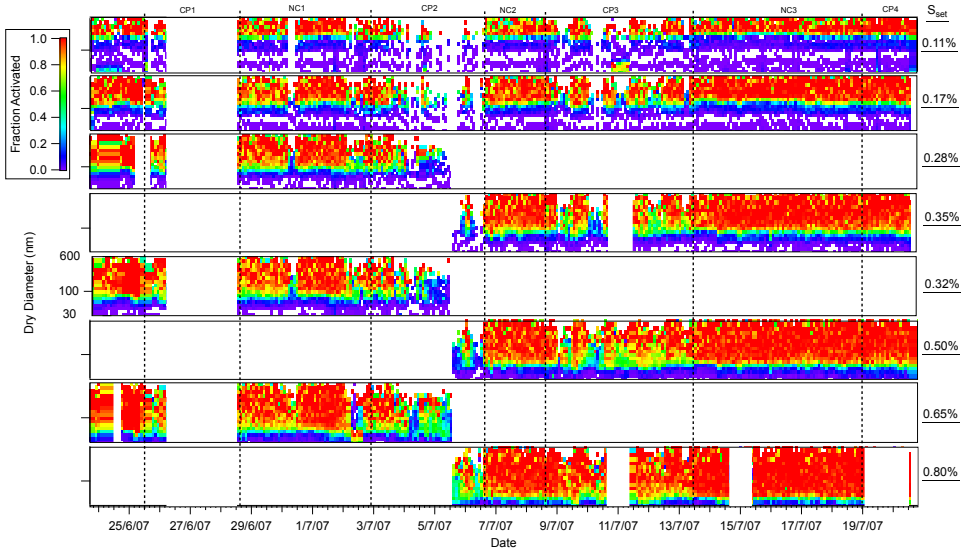


**Fig. 2.** Fraction of CCN activated against time, for each supersaturation setting. The fraction of aerosol activated typically increases with dry diameter and supersaturation. The decision was made during CP2 to increase the upper limit of the supersaturation setting ($S_{\text{set}}$) from 0.65% to 0.80%, in an attempt to activate more of the aerosol below 100 nm.

increasing supersaturation, until at the highest supersaturation (0.80%) almost all particles activate. For the majority of the experiment, each supersaturation could be characterised with a "threshold dry diameter" above which all particles activate.

Though variations throughout the experiment are evident in the activated fraction at each supersaturation (Fig. 2), these do not systematically vary with changes in the ratio of organic to sulphate mass loading (Fig. S3 in the Supplement). However CP2, NC2 and CP3 show some variability in $F_{\text{A}}(S, D_0)$, but these periods are also characterised by low temporal resolution due to low number concentrations (averaged number concentration of less than 5 particles detected at each $D_0$) between $50\,\text{nm} \leq D_0 \leq 200\,\text{nm}$. CP3 is characterised by an increase in $F_{\text{A}}(S, D_0)$ across the size distribution, which may be expected as the threshold diameter for activation at a given supersaturation would increase when sampling from within a cloud, as the instrument would then be sampling interstitial particles which have not activated into cloud droplets. In addition, the organic:sulphate ratio (Fig. S3 in the Supplement) is somewhat higher for CP3 than for other cloud periods. The large difference between NC3 and CP4 in terms of the organic:sulphate ratio (10:1 down to 1:1, Fig. S3 in the Supplement) is not reflected in the activation ability of the aerosol across the size distribution. This is considered further in Sect. 3.6. It should be noted that size resolved measurements were unavailable at high time resolution and hence any systematic difference may be masked by time or size averaging of the composition.

Figure 3 shows a contour plot of derived $S_{\text{c},D_0}$ for the entire project as described in Sect. 2.3. The supersaturation range 0.11%–0.65% was increased as previously described to 0.11%–0.80%. This increased data range typically reduced fitting errors and allowed for the derivation of $S_{\text{c},D_0}$ for smaller particle sizes; illustrated by the inclusion of $S_{\text{c},D_0}$ for $50\,\text{nm} < D_0$ (Fig. 3). Whilst some variation in $S_{\text{c},D_0}$ is evident between cloud and no-cloud periods and is consistent with the variation in activated fraction, no systematic difference was found between high and low organic to sulphate periods and $S_{\text{c},D_0}$.

Whilst size resolved measurements were unavailable at high time resolution AMS compositional data was converted from vacuum aerodynamic diameter to mobility diameter using the methods described in DeCarlo et al. (2004) and assuming a typical density for aged organics of $1400\,\text{kg}\,\text{m}^{-3}$ (Alfarra et al., 2006; Sjogren et al., 2008) and averaged over the periods of high and low organic to sulphate ratios. Particles over 100 nm have an increased organic to sulphate content with a peak at around 300 nm which was above the dry diameter range for HTDMA growth factor measurements and the derivation of critical supersaturation from CCNc measurements during this experiment (see Fig. S4 in the Supplement). Though $F_{\text{A}}(S, D_0)$ data exists for dry diameters above 300 nm, it is not possible to derive $S_{\text{c},D_0}$ from this data, as the fraction of aerosol activated is almost always over 0.5 at the lowest $S_{\text{set}}$.

### 3.5 Reconciliation of the hygroscopicity and droplet activation measurements

For each dry diameter measured, values of $\kappa$ were calculated by inserting $\overline{\text{GF}}_{D_0,86\%,\text{c}}$ data into Eq. (2). The derived $\kappa$ value and $\overline{\text{GF}}_{D_0,86\%,\text{c}}$ were held constant whilst the RH was increased until reaching a maximum, thereby obtaining

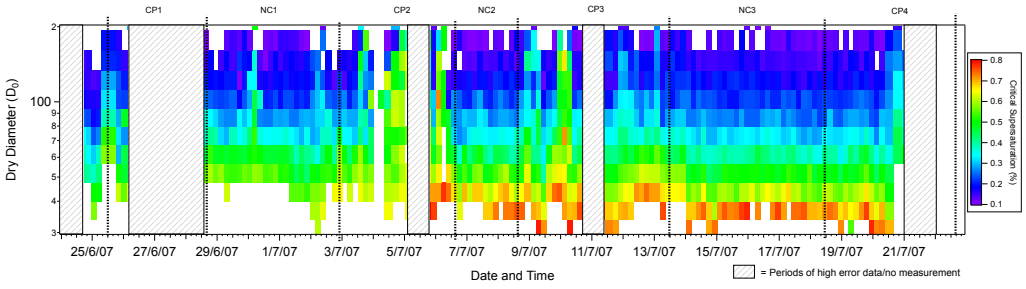


**Fig. 3.** Time series of $S_{c,D_0}$ for the duration of the experiment. Larger particles typically require less supersaturation to activate and thus have a lower $S_{c,D_0}$. Some variation in $S_{c,D_0}$ is apparent, but does not correspond strongly to changes in the AMS organic:sulphate ratio.

$S_{c,GF}$ for each dry diameter. $\kappa$ values were evaluated at a constant assumed surface tension equal to that of pure water (72.5 mNm$^{-1}$ at 298 K) in addition to a range of suppressed $\sigma$ values, neglecting surface-to-bulk partitioning.

$S_{c,D_0}$ was calculated from CCNc data, where possible, in the same fashion as outlined in Sect. 2.3 and in Sect. 1.2 of the Supplement. Calculations of $S_{c,D_0}$ were not possible for $D_0 \leq 30$ nm or $D_0 \geq 200$ nm as the critical supersaturation of the aerosol at these sizes was outside of the supersaturation range measured by the instrumentation.

$\overline{GF}_{D_0,86\%,c}$ is plotted against both $S_{c,GF}$ (circles) and $S_{c,D_0}$ (crosses) for the size range $20\,nm \leq D_0 \leq 200\,nm$ and is shown in Fig. 4. The box plots in Fig. 4 show the median, 25th and 75th percentiles of the model predicted critical supersaturation, $S_{c,GF}$, using the range of mean growth factor measured at the size denoted by colour and the whiskers denote the 10th and 90th percentiles of these predictions. The growth factors for ammonium sulphate are also plotted against their respective $S_{c,D_0}$ for comparison. The coloured circles indicate the predicted $S_{c,GF}$ for a given growth factor (and assumed surface tension, $\sigma$) for guidance. The crosses represent the measured data pairs of mean growth factor $\overline{GF}_{D_0,86\%,c}$ and $S_{c,D_0}$, with the particle dry diameter represented by its colour. The error bars show the standard error associated with each data point; propagated from primary data quantities as described previously. $\kappa$-Köhler evaluation of HTDMA growth factor and CCNc S-step data assuming a surface tension of water and a temperature of 298 K, shows that for $D_0 = 43$ nm and 85 nm there is a clear tendency for the model to over-predict $S_{c,GF}$, with $S_{c,D_0}$ falling far outside of the box plots beyond the measurement uncertainty, indicating an inability of the model to predict critical supersaturation at these sizes within instrumental uncertainties. At 121/127 nm, better agreement between model and measurement is seen, but still with a slight bias towards overpredicting the critical supersaturation. At $D_0$ of 174/169 nm similar agreement between model and measurement is seen, but with the bias reversing and underpredicting critical supersaturation. All data points have been ascribed a transparency according to the degree of multimodality in the growth factor distribution using the difference between $\overline{GF}_{D_0,86\%,c}$ and the peak in $p$(GF) as a qualitative indicator. The solid crosses represent points where these values deviate by less than 5%, intermediate transparency points for between 5 and 10% deviation and the most transparent values for points where the mean and peak growth factors deviate by more than 10%. It can be seen that an almost identical trend is followed irrespective of the multimodal nature of the distribution with the best agreement at the largest sizes. So, even when nominally monomodal ($\overline{GF}_{D_0,86\%,c}$ within 5% of the peak in $p$(GF), reconciliation of sub- and supersaturated measurements at $D_0 = 43$ nm or 85 nm are not achieved within measurement uncertainty.

Hygroscopicity parameters derived from the sub- and supersaturated water uptake measurements, $\kappa_{S_c}$ and $\kappa_{GF}$ were calculated (using the surface tension of water, $\sigma = 72.5\,mNm^{-1}$, and temperature 298 K) and are plotted in Fig. 5 with their associated errors (as described in Sect. 2.6). These data are further tabulated in Tables 2 and 3, where $\kappa$ values have been sectorised according to the organic:sulphate ratio. The greatest discrepancy is observed at smaller particle sizes, with $\kappa_{S_c}$ systematically greater than $\kappa_{GF}$ and well outside measurement uncertainty. The $\kappa$-values move into closer agreement with increasing size, until at 169 nm diameter, the average $\kappa_{GF}$ is slightly greater than the $\kappa_{S_c}$.

No size-dependent systematic difference was found between the HTDMA and CCNc derived critical supersaturation of particles with different organic to sulphate ratios. Figure 6 shows the HTDMA derived and CCNc derived critical supersaturations, coloured according to their organic:sulphate ratio. The left panel of Fig. 6 shows that for the larger sizes of 127 nm and above, the critical supersaturation as predicted from hygroscopicity parameterisation of the HTDMA data is higher during periods of a high organic to sulphate ratio, than when sulphate dominated. However, this is not consistent at all sizes, and when comparing to the critical supersaturations as derived from CCNc data, there is no clear relationship between particle composition and water affinity.

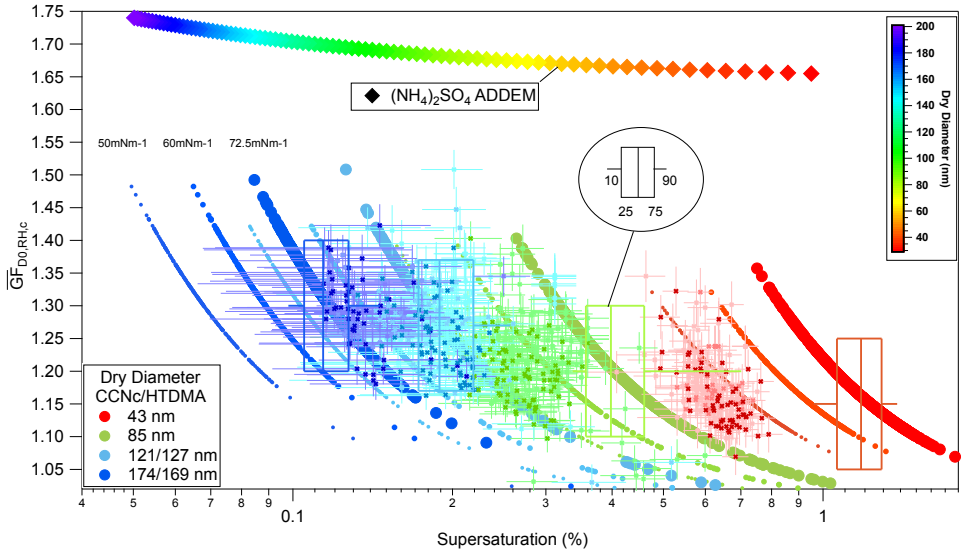


**Fig. 4.** $\overline{\mathrm{GF}}_{D_0,\mathrm{RH,c}}$ plotted against derived critical supersaturation for HTDMA dry diameters 43 nm $\leq D_0 \leq$ 169 nm. The crosses represent measured data and the circles of increasing diameter represent predictions from the model with three surface tensions; 50 mNm$^{-1}$, 60 mNm$^{-1}$ and 72.5 mNm$^{-1}$ respectively. Error bars are shown in both axis representing the uncertainty in the measured growth factor, and derived $S_{\mathrm{c},D_0}$.

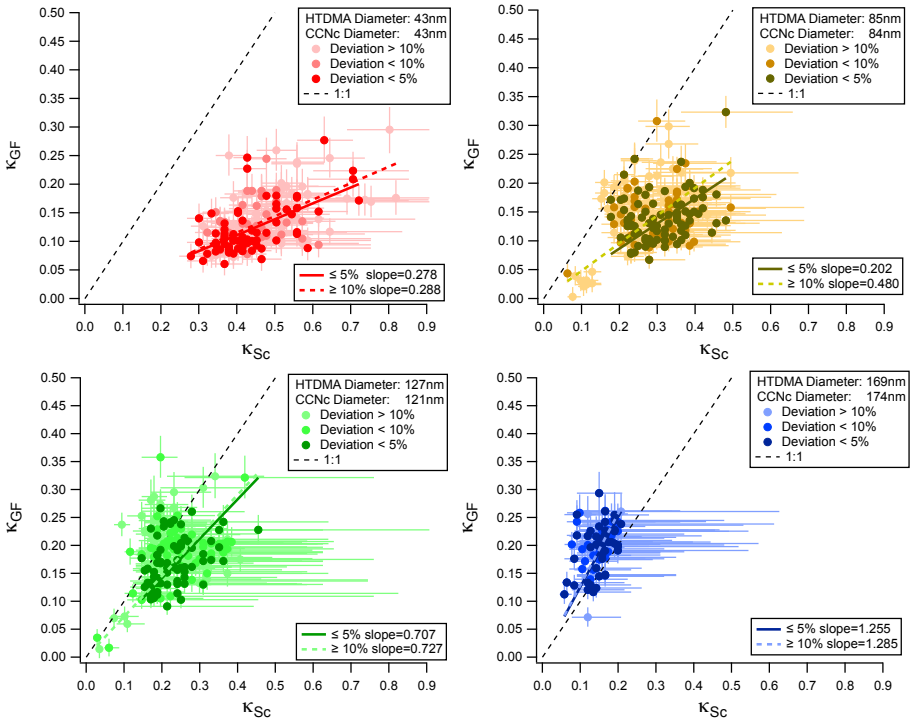


**Fig. 5.** $\kappa_{\mathrm{GF}}$ plotted against $\kappa_{S_c}$ for the CCN dry diameters closest to those of the measured by the HTDMA. The data is colour weighted according to the proximity of the peak of the growth factor relative to that of the mean growth factor, with the most solid colours representing a deviation below 5%.

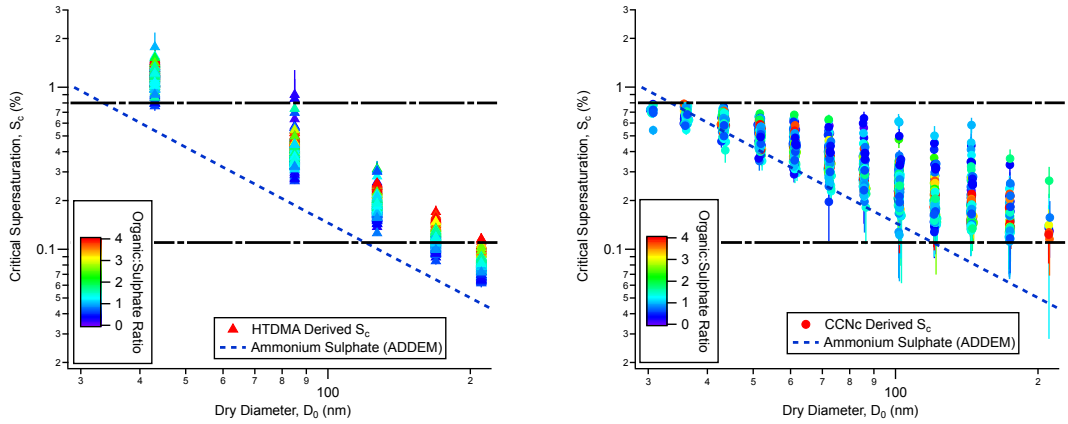


**Fig. 6.** Left panel: a graph showing $S_{c,GF}$ vs. $D_0$, coloured according to organic:sulphate ratio. Right panel: a graph showing $S_{c,D_0}$ vs. $D_0$, coloured according to organic:sulphate ratio. The black dashed line represents the upper and lower values of the supersaturation setting of the CCNc.

Though the mean $\kappa$ for both CCNc and HTDMA data appear to vary ($\overline{\kappa}_{Sc} = 0.292 \pm 0.128$, $\overline{\kappa}_{GF} = 0.181 \pm 0.056$) with increased relative sulphate contribution, possibly indicating a slightly more hygroscopic aerosol than when the organic:sulphate ratio is high ($\overline{\kappa}_{Sc} = 0.283 \pm 0.069$, $\overline{\kappa}_{GF} = 0.142 \pm 0.036$; Tables 2 and 3), the variability of $\kappa$ is too large to draw any firm conclusions. The total aerosol organic fraction is an average across all dry diameters, and the size-resolved AMS composition campaign average (Fig. S4 in the Supplement) show a markedly higher organic fraction at sizes greater than 100 nm in both periods of low and high organic fraction. This will most likely contribute to the lack of difference in aerosol hygroscopic growth factor during these periods (Tables 2 and 3), as the relative organic mass fraction at each dry diameter appears to influence their measured hygroscopicity and subsequently derived critical supersaturation, $S_{\kappa,GF}$ (Fig. 6).

In numerous cases, the mean growth factor either matches the peak value or is too close for an error bar to be visible but there are cases for which the mean growth factor deviates, typically to lower values, from the peak of the hygroscopic mode due to a background of less hygroscopic particles. Even when screening for bimodality, the $\kappa$-Köhler model fails to accurately predict the CCNc derived $S_{c,D_0}$, and the decrease in the discrepancy between model and measurement with larger particle size cannot be solely due to the previously discussed increase in hygroscopic bimodality of the aerosol at larger sizes. It can be seen from the lack of difference between points of varying transparency that the bimodality in aerosol mixing state with respect to growth factor cannot be the only reason for the discrepancy in the HTDMA and CCNc derived $\kappa$-values.

The aerosol sample airflow is dried through the use of a counterflow nafion drier, before entering both the CCNc and HTDMA. The RH of the aerosol sample flow after the drying process, will be between the RH before drying (ambient RH) and the RH of the counterflow in the drier (around RH = 2% from the compressed air supply). In the drying process, aerosol particles will lose water to the gaseous phase (and thus reduce in size) as the particle airflow attempts to reach equilibrium with the dry sheath air flow. In addition, any volatile or semi-volatile compounds can start to evaporate from the aqueous to the gaseous phase. The emerging aerosol sample flow is therefore a mix of relatively dry particulate matter and a gaseous mixture of water vapour and other semi-volatile compounds (inorganic and organic). Initially, this mixture will be further diluted through the first DMA, but after a few scans (circa 1 h), the DMA sheath flow will have also reached equilibrium with the aerosol flow assuming the composition does not change in this time, with both containing similar amounts of components in the gaseous phase. In the HTDMA, after size-selection, the aerosol flow passes through the humidification system, which will grow the particle as water vapour and other gaseous components condense onto the particles. The second DMA (at the RH of the aerosol flow) then sequentially steps through voltages, determining the new particle diameters and thus the growth factor can be calculated. Since the initial drying procedure will not completely dry the particles, a small overestimation of $D_0$ will result, hence leading to an underestimation of the measured growth factor even if equilibrium is reached in the humidification section. This is in addition to any further underestimation in growth factor that would result from a perfectly dry aerosol not reaching equilibrium in the humidification section of the instrument (discussed further below).

For example, it has been shown that hygroscopic growth factor measurements of compounds containing nitrate are sensitive to instrument residence time (e.g. Gysel et al., 2007), and generally there was little nitrate seen during the COPS ground measurements. However, there were a few instances later on in the project when higher concentrations of $NO_3^-$ were observed. The air mass trajectories for

**Table 2.** $\kappa$ values for both HTDMA and CCN data, split by an organic:sulphate ratio of $\leq$ 4:1. $D_0$ is particle dry diameter and $\sigma$ is the standard deviation.

| $D_0$ | $\kappa_{S_c}$ | $\sigma$ | $\kappa_{GF}$ | $\sigma$ |
|---|---|---|---|---|
| 26 nm | | | 0.137 | 0.046 |
| 43 nm | 0.464 | 0.099 | 0.129 | 0.045 |
| 85 nm | 0.269 | 0.100 | 0.147 | 0.052 |
| 121/127 nm | 0.211 | 0.096 | 0.187 | 0.057 |
| 174/169 nm | 0.133 | 0.051 | 0.213 | 0.052 |
| 211 nm | | | 0.231 | 0.055 |

**Table 3.** $\kappa$ values for both HTDMA and CCN data, split by an organic:sulphate ratio of $\geq$ 4:1. $D_0$ is particle dry diameter and $\sigma$ is the standard deviation.

| $D_0$ | $\kappa_{S_c}$ | $\sigma$ | $\kappa_{GF}$ | $\sigma$ |
|---|---|---|---|---|
| 26 nm | | | 0.139 | 0.036 |
| 43 nm | 0.430 | 0.104 | 0.084 | 0.042 |
| 85 nm | 0.203 | 0.118 | 0.090 | 0.057 |
| 121/127 nm | 0.131 | 0.112 | 0.128 | 0.072 |
| 174/169 nm | 0.102 | 0.062 | 0.155 | 0.055 |
| 211 nm | | | 0.165 | 0.069 |

these events were different to the other periods (slower wind speeds and thus local influence from nearby valley), and a ZSR calculation showed that the HTDMA was most likely not seeing this $NO_3^-$. During COPS, the largest amounts of nitrate were measured on 19 July, incidentally a date marking the end of HTDMA measurements.

Further to the effects of evaporative equilibration in the particle pre-drying section, there are potential kinetic limitations to particle growth. After drying, any particles that are still in the aqueous phase may have different growth rates compared to those in a crystalline solid or glassy state, as a result of differences in the diffusion coefficient in the condensed phase. As the particle initially enters the humidification section, the high RH gaseous mixture within the sheath flow will start to condense onto the surface of the particle, which may not be exactly representative of the composition of the entire particle. As it takes longer for the molecules to diffuse through a solid particle compared to an aqueous one, any compositional influences of water uptake can encounter kinetic limitation to the rate of diffusion of the various compounds within the particle and of the diffusion of water into the particle. That is to say, that the particle will pass through the humidification system before all components of the particle in the solid phase are exposed to water molecules. Such limitation through increased viscosity and reduced diffusion in amorphous solid particles may be thought to be likely in the atmosphere following their discovery in chamber secondary organic aerosol systems Virtanen et al. (2010).

Good et al. (2010b) showed how HTDMA humidification residence time could not be linked directly to aerosol hygroscopicity in multiple chamber experiments involving organic compounds. These finding may indicate that, if non-equilibrium behaviour is responsible for any variability, it would most likely be in the drying section for these particular aerosol systems.

It should be noted that similar drying effects and impacts of semi-volatile component evaporation and condensation can take place in the monodisperse CCNc configuration used here, providing further potential sources of discrepancies when reconciling HTDMA and CCNc data.

### 3.6 Number of CCN

For each supersaturation, assuming internal mixing with respect to CCN activity, the aerosol will have a corresponding threshold dry diameter above which the aerosol particles activate into cloud droplets. It is possible to estimate the maximum $N_{CCN}$ at the given supersaturation by integrating the DMPS size distribution from the largest diameter bin to this threshold diameter. This provides an upper limit to cloud droplet number, but the competition between droplets for water vapour during the activation and growth process reduces the available supersaturation and cloud droplet number is normally substantially lower. Variation in droplet number is damped by this process and is lower than variation in CCN.

The threshold dry diameter for activation were derived from CCNc measurement via three methods, two via S-step analysis and one from D-step analysis.

The threshold dry diameter for activation can be calculated from the S-step products $S_{c,D_0}$ and $\kappa_{S_c}$. The first method does not require the hygroscopicity parameter and is found by plotting $S_{c,D_0} - S_{set}$ against $D_0$, defining the intercept (simply where $D_0 = S_{set}$) as the physical threshold dry diameter for activation. Connecting the two points either side of $S_{c,D_0} - S_{set} = 0$ by a straight line, $D_{thres(Sc)}$ is determined, as shown in Fig. S5 in the Supplement. A clear benefit of this method is that fewer calculations are performed, thus not increasing the propagated errors further. However, a significant drawback is that this technique only works for interim supersaturations. Alternatively, the threshold diameter for activation can be derived from $\kappa_{S_c}$ through the use of a $\kappa$ lookup table at 1 nm and $0.01\kappa$ resolution. The $\kappa$ value is then inserted into Eq. (3) and for a given $S_{set}$ (effectively $S_c$), the threshold dry diameter for activation can be calculated, defined as $D_{thres(\kappa,Sc)}$. Additionally, using D-step analysis, the threshold dry diameter for activation has been derived by plotting $D_{50,S} - D_0$ vs. $D_0$, where again, the intercept represents the physical threshold dry diameter for activation of the aerosol, denoted $D_{thres(D_{50})}$.

The threshold dry diameter for activation can also be derived from $\kappa_{GF}$. As there are 7 dry diameters scanned by the HTDMA, each dry diameter has an associated $\overline{GF}_{D_0,RH,c}$ and

thus $\kappa$. A threshold dry diameter is calculated for each $\kappa_{GF}$ at each $D_0$ and $S_{set}$, and the intercept of $D_{thres} - D_0$ vs. $D_0$ defines $D_{thres(\kappa,GF)}$ at each $S_{set}$.

The $N_{CCN}$ calculation is most sensitive to the threshold diameter for activation around the peak of the aerosol size distribution, and is heavily dependent on the position and breadth of this peak. Out of cloud measurements were typically characterised by a monomodal distribution with a peak around 100 nm and with typical threshold dry activation diameters between 40 nm and 180 nm, the difference in $N_{CCN}$ is affected greatly by this mode. Figure 7a shows the largest difference in single hygroscopicity parameter derived $N_{CCN}$ occurs at the lowest supersaturation (0.11%). Even though the mean difference in the threshold dry diameter is 12% ($D_{thres(GF)} = 182$ nm, $D_{thres(\kappa,S_c)} = 163$ nm), the difference in $N_{CCN}$ is 40%. For all supersaturations, the disagreement between the predictions of $N_{CCN}$ is greater than 30%. In contrast, Fig. 7b shows the smallest difference in $N_{CCN}$ between $D_{thres(\kappa,GF)}$ and $D_{thres(D_{50,S})}$ at the lowest supersaturation. This is due to the increased proximity of $D_{thres(\kappa,GF)} = 182$ nm, $D_{thres(D_{50,S})} = 184$ nm. Excluding the measurement at the lowest supersaturation, the results follow a similar pattern as seen in Fig. 7. It can be seen that the discrepancies are usually outside the attributable errors and cannot be easily reconciled.

## 4 Discussion

The degree of success of each reconciliation method is shown in Fig. 7, represented by the slopes of the linear regression fits to the data. The degree of agreement is dependent on the analytical methods for CCNc data, with the $\kappa$-model showing the weakest overall agreement (most notably at lower supersaturations, as shown by Fig. 5) compared to the better agreement shown for data analysed without invoking the $\kappa$-model. Though it is useful to calculate $\kappa$ values from both CCNc and HTDMA data for comparison, the more direct analysis (i.e. D-step analysis) allows the threshold dry diameter for activation to be known directly from measurement and is therefore not subjected to model approximations in the same manner. Furthermore, as the threshold diameter for activation cannot be calculated from S-step analysis (i.e. $S_{c,D_0}$) data for the highest and lowest supersaturations, the best overall reconciliation between HTDMA data and CCNc data, are for CCNc products derived via D-Step analysis, without the use of the $\kappa$-model (i.e. $D_{50,S}$), as shown by Fig. 7.

The best overall reconciliation between HTDMA data and CCNc data, are for the D-step CCNc products derived without the use of the $\kappa$-model (e.g. $D_{50,S}$), as shown by Fig. 7. Agreement is strongest most notably at the lowest supersaturation setting; where activation diameters are typically mid-range of the DMPS size-distribution (improving fitting statistics). Reconciliation between the HTDMA and CCNc using the hygroscopicity parameter $\kappa$ results in the weakest overall agreement. Figure 5 shows that only for the 127/121 nm and 169/174 nm measurements do values of $\kappa$ approach the 1:1 line; though the error associated with $\kappa_{S_c}$ reduces the confidence in conclusions drawn from this agreement.

However, it must be noted that at both the lowest and highest supersaturations, the number of data points generated from S-step analysis is lower than at intermediate supersaturations as fitting is only successful if $S_{min} \leq S_c \leq S_{max}$, and as such the results are biased towards values where critical supersaturation for a threshold diameter for activation is bounded by $S_{set}$. This is further illustrated by Fig. 6; the predicted critical supersaturations for all sizes, with the exception of 127 nm, have points which fall outside of the $S_{set}$ range. This creates an artificial floor and ceiling to the critical supersaturation data derived from the CCNc, and even at 121 nm, some of the derivations lead to uncertainty falling outside of this range. This may explain why at 121/127 nm the $\kappa$ values derived from each instrument show best agreement (Fig. 5), and also go some way to explain how the size dependence of $\kappa_{S_c}$ is reversed to that of the HTDMA (Tables 2 and 3).

The segregation of the data into single mode (mean growth factor $\leq$5% of the peak bin), and multi-mode (mean growth factor $\geq$10% of the peak bin) could not explain the disagreement between the two instruments. No clear influence of mixing state was found when comparing the derived hygroscopicity parameters from both instruments (Fig. 5).

This study was performed with the assumption that the growing cloud droplets have a surface tension equal to that of water (72.5 mNm$^{-1}$ at 298 K) at the point of activation. The model represents the measured critical supersaturations at 174/169 nm well, using a surface tension of 72.5 mNm$^{-1}$ (Fig. 4). In order to bring the model predictions into agreement with the measured CCN activity for the dry diameters of 121/127 nm and below, surface tensions ranging from 50 mNm$^{-1}$ to 70 mNm$^{-1}$ must be assumed, with the smallest sizes requiring the smallest surface tension. It is not clear that any atmospherically reasonable organic compounds at the concentration found at the point of activation can be responsible for the apparent large surface tension suppressions required to reconcile the data. Furthermore, if the influences of organic compounds on surface tension were important, the critical supersaturation would be lowered with an increasing amount of organic matter, offsetting the increase of $S_{c,D_0}$ expected from a reduction of inorganic matter, potentially leading to a cancellation of effects and no clear relationship.

Surface tensions of multicomponent mixtures are not readily predictable even in bulk solutions (Topping et al., 2005). Bulk to surface partitioning has been postulated as a potentially important phenomena which can increase the predicted critical saturation ratio required for droplet activation through removal of material used to calculate the Raoult term in the Köhler equation (Eq. 1). Neglecting bulk-to-surface partitioning has been shown to result in an underestimation of $S_c$ (Sorjamaa et al., 2004; Kokkola et al., 2006) and that

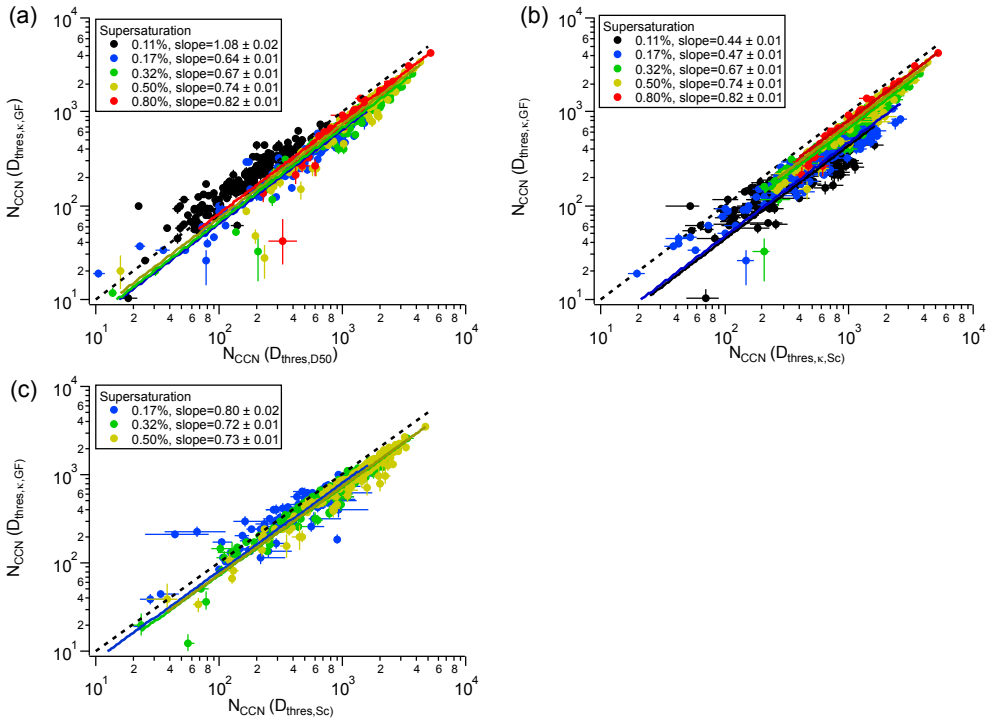


**Fig. 7.** The number of cloud condensation nuclei ($N_{CCN}$) as predicted from HTDMA derived $\kappa$-Köhler analysis plotted against **(a)** $N_{CCN}$ derived from D-step ($D_{50,S}$) analysis, **(b)** $N_{CCN}$ derived from $\kappa_{S_c}$ analysis, **(c)** $N_{CCN}$ derived from S-step ($S_{c,D_0}$) analysis. Where possible, the calculations were preformed for the five supersaturation settings. The error bars are the upper and lower bounds in $N_{CCN}$ given as a result of the propagation of errors through the analysis procedure. The best fit lines have been plotted using orthogonal distance regression and are weighted according to error.

the smaller the particle, the greater the effect of surface to bulk partitioning (Sorjamaa et al., 2004). However, for this study all calculations have neglected the partitioning of material between a bulk and surface layer. An overestimation of $S_c$ is seen for all sizes below 121/127 nm, above which better agreement is seen between the predicted $S_c$ and measured $S_c$, indicating that if the effects of bulk to surface partitioning were to be included, predicted $S_c$ would further deviate from measured $S_c$.

Segregating the data into periods of high and low sulphate to organic ratio (Fig. S3 in the Supplement and even using size resolved AMS data (Fig. S4 in the Supplement) resulted in no systematic improvement or degradation to the agreement between the predicted and measured data (Fig. 4). Whilst the model leads to better agreement for sizes of 121/127 nm and above (Fig. 4), the reason for the apparent agreement is unclear. The influence of bimodality on the mean growth factor cannot explain the difference between $\kappa_{GF}$ and $\kappa_{S_c}$, as strongly monomodal aerosol does not conclusively show this to be the reason behind the apparent discrepancy (Fig. 5). As the AMS-derived composition is governed by the composition of relatively large particles, the fact that the hygroscopicity of relatively small particles ($<$ 127 nm) did not correlate with the AMS-derived organic:sulphate ratio is not contradictory. Indeed, in the case of relatively large particles ($>$ 127 nm), some relationship between the HTDMA growth factor data and organic:sulphate ratio was observed (as previously shown in Fig. 6, with HTDMA data represented by $S_{c,GF}$). It is worth noting that an internally mixed aerosol will appear to be well represented by the mean growth factor, and a spectrum of compositions may appear as one broad mode. This would be lost within the CCNc data as the resolution of the instrument would not pick out these particles of varied composition. In theory, this broadens the ideal step function in activation space of the CCNc, yet with only 5 supersaturations for each $D_0$, the fitted sigmoid function is reasonably broad initially and a spread of compositions would not be resolved in this manner.

The $\kappa$-Köhler model takes a snapshot of the aerosol behaviour at a specific RH, assuming the system to be in equilibrium, and extrapolates these properties to the maximum point in the Köhler curve. The application of the same $\kappa$ assumes the same degree of non-ideality (same activity coefficient of water) at the point of sub-saturated measurement and the critical point of the Köhler curve. Departure from this and from the assumptions of equilibrium (no kinetic limitations to evaporation on drying or growth by recondensation of material at high RH), will manifest themselves as disagreement in reconciliation studies. As previously discussed, the residence time of the sample aerosol on

drying and humidification within the HTDMA will impact on measured particle growth factor. Similarly for the CCNc, the residence time of the sample aerosol in the drying prior to the DMA size selection may impact on the derived critical supersaturation. Though the role of surface-active compounds at the point of activation remains unclear, we have illustrated that an unrealistically low surface tension of 50 $mNm^{-1}$ is required for HTDMA and CCNc measurements to agree. It is possible that kinetic limitations to condensation of water in humidification and evaporative departure from equilibrium in drying may substantially contribute to the disagreements shown in Figs. 4, 5 and 7.

## 5 Conclusions

Measurements of aerosol hygroscopic growth, CCN activity, and composition were made simultaneously and have been used to probe the applicability of a single parameter representation of aerosol water uptake. It was found that changes in the organic:sulphate ratio did result in variations in aerosol hygroscopicity at 86% RH but no systematic variation in the CCN activity of the aerosol was found. Periods of measurement conducted "in cloud" were typically characterised by low number concentrations (averaged number concentration of less than 5 particles detected at each $D_0$), a lower organic:sulphate ratio and a higher hygroscopic mean growth factor. "no-cloud" periods were characterised by higher aerosol concentrations across the size range, an increased organic:sulphate ratio and a lower hygroscopic mean growth factor. Whilst variations in the CCN fraction are evident they could not be directly linked to changes in composition, in part due to the variations in mixing state of the aerosol during different periods.

Corrected mean growth factors at 86% RH as measured by the HTDMA at multiple $D_0$ were used to derive the hygroscopicity parameter $\kappa$. The $\kappa$-Köhler model was used to predict both critical supersaturations and threshold diameters for activation from the data. Critical supersaturation was derived as a function of dry diameter by the CCNc and was compared to the HTDMA $\kappa$-model derived critical supersaturation with varying results. When comparing $\kappa$ derived products from each instrument, the discrepancy appears largest for the most atmospherically relevant supersaturations with the most significant difference being a 56% difference in $N_{CCN}$ at the lowest supersaturation (0.11%), with higher supersaturations (0.17–0.80%) resulting in less difference between prediction and measurement (53%–18%), shown in Fig. 7.

CCNc data was also analysed without the use of the hygroscopicity parameter $\kappa$, but in terms of the threshold dry diameter for activation from both S-step and D-step analyses. The D-step analysis had the best agreement with the HTDMA derived $N_{CCN}$ at the lowest supersaturation with an 8% difference, but for the rest of the supersaturation range there was a decreasing over-estimate with supersaturation (26%–18%). Data which falls closest to the centre of the ranges of dry diameter selection and supersaturation are less susceptible to bias from instrument limitations and as such generated more data points with reduced standard error than those made at the limits of the CCN instrument. From the S-step analysis, the threshold diameter of the aerosol was derived directly from $S_{c,D_0}$ by plotting the intercept of $S_{c,D_0} - S_{set}$ vs. $S_{set}$. Whilst this method could only derive $D_{thres,Sc}$ for the latter-half interim supersaturations of 0.17%, 0.32% and 0.50%, there is only between 20–27% over estimation when compared to the HTDMA derived $N_{CCN}$.

Measurement uncertainty has been propagated through to derived products for each calculation presented in the paper. The inclusion and propagation of these errors has allowed an assessment on the reconciliation ability of the instruments to take place. The disagreement between the derived products is far outside instrument uncertainty and as such, attempts have been made to uncover the reason for this disagreement. Mixing state has not resulted in clear, systematic differences between the products and neither has the segregation of the data into periods dominated by sulphate or organic composition. It is clear, is that the predicted critical supersaturation from HTDMA data ($S_{c,GF}$) will shows best agreement with the derived critical supersaturation from the CCNc ($S_{c,D_0}$) at a dry diameter range that activates mostly within the measured $S_{set}$ range; a trend that follows for all derived products. Should particles of a given diameter have critical supersaturations that cannot be derived by the CCNc but can be predicted by the HTDMA, results will surely diverge.

Whilst the $\kappa$-Köhler model has been shown to work for a variety of different compositions (Petters and Kreidenweis, 2007, 2008) and previous $\kappa$-Köhler closure attempts ambient CCNc and HTDMA measurements have shown agreement to within approximately 20% (Carrico et al., 2008), it appears not to be the case for the ambient measurements in this study unless surface properties are changed, probably unrealistically. In addition, the inclusion of bulk to surface partitioning would lead to an increased discrepancy between the derived values of $S_c$, illustrating a possible need for caution in the generalised application of this single parameter approximation in ambient atmospheric studies until reasons for the highlighted discrepancies are understood. Obviously the use of $\kappa$ values differing by as much as those derived from our HTDMA and CCN measurements in this study would result in differences in predicted aerosol indirect effects corresponding to the significant difference in $N_{CCN}$ as reported.

**Supplementary material related to this article is available online at: http://www.atmos-chem-phys.net/10/11737/2010/acp-10-11737-2010-supplement.pdf**.

*Acknowledgements*. The UK Convective and Orographically-induced Precipitation Study (UK-COPS) was funded by the National Environmental Research Council (NERC) (NE/E016200/1) and NERC Ph.D Studentship of Martin Irwin (NER/S/A/2006/14036). The authors wish to thank Michael Flynn and Keith Bower for their assistance in the field.

Edited by: M. C. Facchini

## References

Abdul-Razzak, H. and Ghan, S. J.: Parameterization of the influence of organic surfactants on aerosol activation, J. Geophys. Res.-Atmos., 109, D03205, 10.1029/2003JD004043, 2004.

Albrecht, B.: Aerosols, cloud microphysics, and fractional cloudiness, Science, 245, 1227–1230, 1989.

Alfarra, M. R., Paulsen, D., Gysel, M., Garforth, A. A., Dommen, J., Prévôt, A. S. H., Worsnop, D. R., Baltensperger, U., and Coe, H.: A mass spectrometric study of secondary organic aerosols formed from the photooxidation of anthropogenic and biogenic precursors in a reaction chamber, Atmos. Chem. Phys., 6, 5279–5293, doi:10.5194/acp-6-5279-2006, 2006.

Andreae, M. and Rosenfeld, D.: Aerosol-cloud-precipitation interactions. Part 1. The nature and sources of cloud-active aerosols, Earth Sci. Rev., 89, 13–41, 2008.

Broekhuizen, K., Chang, R. Y.-W., Leaitch, W. R., Li, S.-M., and Abbatt, J. P. D.: Closure between measured and modeled cloud condensation nuclei (CCN) using size-resolved aerosol compositions in downtown Toronto, Atmos. Chem. Phys., 6, 2513–2524, doi:10.5194/acp-6-2513-2006, 2006.

Carrico, C. M., Petters, M. D., Kreidenweis, S. M., Collett, J. L., Engling, G., and Malm, W. C.: Aerosol hygroscopicity and cloud droplet activation of extracts of filters from biomass burning experiments, J. Geophys. Res., 113, D08206, 10.1029/2007JD009274, 2008.

Cubison, M. J., Coe, H., and Gysel, M.: A modified hygroscopic tandem DMA and a data retrieval method based on optimal estimation, J. Aerosol Sci., 36, 846–865, 2005.

Decarlo, P., Slowik, J., Worsnop, D., Davidovits, P., and Jimenez, J.: Particle Morphology and Density Characterization by Combined Mobility and Aerodynamic Diameter Measurements. Part 1: Theory, Aerosol Sci. Technol., 38, 1185–1205, 10.1080/027868290903907, 2004.

DeCarlo, P., Kimmel, J., Trimborn, A., Northway, M., Jayne, J., Aiken, A., Gonin, M., Fuhrer, K., Horvath, T., Docherty, K., Worsnop, D., and Jimenez, J. L.: Field-Deployable, High-Resolution, Time-of-Flight Aerosol Mass Spectrometer, Anal. Chem., 78, 8281–8289, 2006.

Facchini, M. C., Decesari, S., Mircea, M., Fuzzi, S., and Loglio, G.: Surface tension of atmospheric wet aerosol and cloud/fog droplets in relation to their organic carbon econtent and chemical composition, Atmos. Environ., 33, 4853–4857, 2000.

Forster, P., Ramaswamy, V., Artaxo, P., Berntsen, T., Betts, R., Fahey, D., Haywood, J., Lean, J., Lowe, D., Myhre, G., Nganga, J., Prinn, R., Raga, G., Schulz, M., and Dorland, R. V.: Changes in Atmospheric Constituents and in Radiative Forcing. In: Climate Change 2007: The Physical Science Basis. Contribution of Working Group I to the Fourth Assessment Report of the Intergovernmental Panel on Climate Change, 2007.

Good, N., Coe, H., and McFiggans, G.: Instrumentational operation and analytical methodology for the reconciliation of aerosol water uptake under sub- and supersaturated conditions, Atmos. Meas. Tech., 3, 1241–1254, doi:10.5194/amt-3-1241-2010, 2010a.

Good, N., Topping, D. O., Duplissy, J., Gysel, M., Meyer, N. K., Metzger, A., Turner, S. F., Baltensperger, U., Ristovski, Z., Weingartner, E., Coe, H., and McFiggans, G.: Widening the gap between measurement and modelling of secondary organic aerosol properties?, Atmos. Chem. Phys., 10, 2577–2593, doi:10.5194/acp-10-2577-2010, 2010b.

Gunthe, S. S., King, S. M., Rose, D., Chen, Q., Roldin, P., Farmer, D. K., Jimenez, J. L., Artaxo, P., Andreae, M. O., Martin, S. T., and Pöschl, U.: Cloud condensation nuclei in pristine tropical rainforest air of Amazonia: size-resolved measurements and modeling of atmospheric aerosol composition and CCN activity, Atmos. Chem. Phys., 9, 7551–7575, doi:10.5194/acp-9-7551-2009, 2009.

Gysel, M., Crosier, J., Topping, D. O., Whitehead, J. D., Bower, K. N., Cubison, M. J., Williams, P. I., Flynn, M. J., McFiggans, G. B., and Coe, H.: Closure study between chemical composition and hygroscopic growth of aerosol particles during TORCH2, Atmos. Chem. Phys., 7, 6131–6144, doi:10.5194/acp-7-6131-2007, 2007.

Gysel, M., McFiggans, G., and Coe, H.: Inversion of tandem differential mobility analyser (TDMA) measurements, J. Aerosol Sci., 40, 134–151, 2009.

Hallquist, M., Wenger, J. C., Baltensperger, U., Rudich, Y., Simpson, D., Claeys, M., Dommen, J., Donahue, N. M., George, C., Goldstein, A. H., Hamilton, J. F., Herrmann, H., Hoffmann, T., Iinuma, Y., Jang, M., Jenkin, M. E., Jimenez, J. L., Kiendler-Scharr, A., Maenhaut, W., McFiggans, G., Mentel, Th. F., Monod, A., Prévôt, A. S. H., Seinfeld, J. H., Surratt, J. D., Szmigielski, R., and Wildt, J.: The formation, properties and impact of secondary organic aerosol: current and emerging issues, Atmos. Chem. Phys., 9, 5155–5236, doi:10.5194/acp-9-5155-2009, 2009.

Haywood, J. and Boucher, O.: Estimates of the direct and indirect radiative forcing due to tropospheric aerosols: A review, Rev. Geophys., 38, 513–543, 2000.

Jones, H. M., Crosier, J., Russell, A., Irwin, M., Flynn, M., Choularton, T., Coe, H., and McFiggans, G.: In-situ aerosol measurements taken during the 2007 COPS field campaign at the Hornisgrinde ground site, Q. J. Roy. Meteorol. Soc., in press, 2010.

Kanakidou, M., Seinfeld, J. H., Pandis, S. N., Barnes, I., Dentener, F. J., Facchini, M. C., Van Dingenen, R., Ervens, B., Nenes, A., Nielsen, C. J., Swietlicki, E., Putaud, J. P., Balkanski, Y., Fuzzi, S., Horth, J., Moortgat, G. K., Winterhalter, R., Myhre, C. E. L., Tsigaridis, K., Vignati, E., Stephanou, E. G., and Wilson, J.: Organic aerosol and global climate modelling: a review, Atmos. Chem. Phys., 5, 1053–1123, doi:10.5194/acp-5-1053-2005, 2005.

Köhler, H.: The nucleus in and the growth of hygroscopic droplets, Trans. Faraday Soc., 32, 1152–1161, 10.1039/TF9363201152, 1936.

Kokkola, H., Sorjamaa, R., Peräniemi, A., Raatikainen, T., and Laaksonen, A.: Cloud formation of particles containing humic-like substances, Geophys. Res. Lett., 33, L10816, 10.1029/2006GL026107, 2006.

Lance, S., Medina, J., Smith, J., and Nenes, A.: Mapping the operation of the DMT continuous flow CCN counter, Aerosol Sci. Technol., 40, 242–254, 2006.

Lohmann, U. and Feichter, J.: Global indirect aerosol effects: a review, Atmos. Chem. Phys., 5, 715–737, doi:10.5194/acp-5-715-2005, 2005.

Matthew, B. M., Middlebrook, A., and Onasch, T.: Collection Efficiencies in an Aerodyne Aerosol Mass Spectrometer as a Function of Particle Phase for Laboratory Generated Aerosols, Aerosol Sci. Technol., 42, 884–898, 10.1080/02786820802356797, 2008.

McCormick, R. and Ludwig, J.: Climate modification by atmospheric aerosols, Science, 156, 1358–1359, 1967.

McFiggans, G., Alfarra, M., Allan, J., Bower, K., and Coe, H.: Simplification of the representation of the organic component of atmospheric particulates, Faraday Discuss., 130, 341-362, 2005.

McFiggans, G., Artaxo, P., Baltensperger, U., Coe, H., Facchini, M. C., Feingold, G., Fuzzi, S., Gysel, M., Laaksonen, A., Lohmann, U., Mentel, T. F., Murphy, D. M., O'Dowd, C. D., Snider, J. R., and Weingartner, E.: The effect of physical and chemical aerosol properties on warm cloud droplet activation, Atmos. Chem. Phys., 6, 2593–2649, doi:10.5194/acp-6-2593-2006, 2006.

Medina, J., Nenes, A., Sotiropoulou, R., and Cottrell, L.: Cloud condensation nuclei closure during the International Consortium for Atmospheric Research on Transport and Transformation 2004 campaign: Effects of size-resolved composition, J. Geophys. Res, 112, D10S31, 10.1029/2006JD007588, 2007.

Novakov, T. and Penner, J.: Large contribution of organic aerosol to cloud condensation nuclei concentrations, Nature, 365, 823–826, 1993.

Petters, M. D. and Kreidenweis, S. M.: A single parameter representation of hygroscopic growth and cloud condensation nucleus activity, Atmos. Chem. Phys., 7, 1961–1971, doi:10.5194/acp-7-1961-2007, 2007.

Petters, M. D. and Kreidenweis, S. M.: A single parameter representation of hygroscopic growth and cloud condensation nucleus activity – Part 2: Including solubility, Atmos. Chem. Phys., 8, 6273–6279, doi:10.5194/acp-8-6273-2008, 2008.

Petters, M., Prenni, A. J., Kreidenweis, S. M., and DeMott, P. J.: On Measuring the Critical Diameter of Cloud Condensation Nuclei Using Mobility Selected Aerosol, Aerosol Sci. Technol., 41, 907–913, 2007.

Pruppacher, H. and Klett, J.: Microphysics of Clouds and Precipitation, vol. 18, Kluwer Acad., Norwell, Mass., 1997.

Roberts, G. C. and Nenes, A.: A continuous-flow streamwise thermal-gradient CCN chamber for atmospheric measurements, Aerosol Sci. Technol., 39, 206–221, 2005.

Rogers, R. R. and Yau, M. K.: A Short Course in Cloud Physics, Butterworth-Heinemann; 3rd edition, January 15, 1989.

Rose, D., Gunthe, S. S., Mikhailov, E., Frank, G. P., Dusek, U., Andreae, M. O., and Pöschl, U.: Calibration and measurement uncertainties of a continuous-flow cloud condensation nuclei counter (DMT-CCNC): CCN activation of ammonium sulfate and sodium chloride aerosol particles in theory and experiment, Atmos. Chem. Phys., 8, 1153–1179, doi:10.5194/acp-8-1153-2008, 2008.

Saxena, P., Hildemann, L., McMurray, P., and Seinfeld, J. H.: Organics Alter Hygroscopic Behaviour of Atmospheric Particles, J. Geophys. Res., 100, 18755–18770, 1995.

Seinfeld, J. and Pandis, S.: Atmospheric Chemistry and Physics: From Air Pollution to Climate Change, 1998.

Shulman, M., Jacobson, M., Carlson, R., and Synovec, R.: Dissolution behavior and surface tension effects of organic compounds in nucleating cloud droplets, Geophys. Res. Lett., 23, 277–280, 1996.

Sjogren, S., Gysel, M., Weingartner, E., Alfarra, M. R., Duplissy, J., Cozic, J., Crosier, J., Coe, H., and Baltensperger, U.: Hygroscopicity of the submicrometer aerosol at the high-alpine site Jungfraujoch, 3580 m a.s.l., Switzerland, Atmos. Chem. Phys., 8, 5715–5729, doi:10.5194/acp-8-5715-2008, 2008.

Sorjamaa, R., Svenningsson, B., Raatikainen, T., Henning, S., Bilde, M., and Laaksonen, A.: The role of surfactants in Khler theory reconsidered, Atmos. Chem. Phys., 4, 2107–2117, doi:10.5194/acp-4-2107-2004, 2004.

Topping, D. O., McFiggans, G. B., and Coe, H.: A curved multicomponent aerosol hygroscopicity model framework: Part 1 – Inorganic compounds, Atmos. Chem. Phys., 5, 1205–1222, doi:10.5194/acp-5-1205-2005, 2005.

Topping, D. O., McFiggans, G. B., Kiss, G., Varga, Z., Facchini, M. C., Decesari, S., and Mircea, M.: Surface tensions of multicomponent mixed inorganic/organic aqueous systems of atmospheric significance: measurements, model predictions and importance for cloud activation predictions, Atmos. Chem. Phys., 7, 2371–2398, doi:10.5194/acp-7-2371-2007, 2007.

Twomey, S.: Influence of Pollution on Shortwave Albedo of Clouds, J. Atmos. Sci., 34, 1149–1152, 1977.

Virtanen, A., Joutsensaari, J., Koop, T., Kannosto, J., Yli-Pirila, P., Leskinen, J., Makela, J. M., Holopainen, J. K., Poeschl, U., Kulmala, M., Worsnop, D. R., and Laaksonen, A.: An amorphous solid state of biogenic secondary organic aerosol particles, Nature, 467, 824–827, 10.1038/nature09455, 2010.

Weingartner, E., Sjögren, S., Cozic, J., Verheggen, B., Baltensberger, U., Alfarra, M. R., Bower, K. N., Flynn, M. J., Gysel, M., and Coe, H.: Hygroscopic properties and chemical composition of aerosol particles at the high alpine site Jungfraujoch, J. Aerosol Sci., 35, S135–S136, 2004.

Wex, H., Stratmann, F., Topping, D., and McFiggans, G.: The Kelvin versus the Raoult Term in the Köhler Equation, J. Atmos. Sci., 65, 4004–4016, 2008.

Wiedensohler, A.: An approximation of the bipolar charge distribution for particles in the submicron size range, J. Aerosol Sci., 19, 387–389, 1987.

Williams, P. I., McFiggans, G., and Gallagher, M. W.: Latitudinal aerosol size distribution variation in the Eastern Atlantic Ocean measured aboard the FS-Polarstern, Atmos. Chem. Phys., 7, 2563–2573, doi:10.5194/acp-7-2563-2007, 2007.

Wulfmeyer, V, Behrendt, A., Bauer, H., Kottmeier, C., Corsmeier, U., Blyth, A., Craig, G., Schumann, U., Hagen, M., Crewell, S., Girolamo, P. D., Flamant, C., Miller, M., Montani, A., Mobbs, S., Richard, E., Rotach, M., Arpagaus, M., Russchenberg, H., Schlüssel, P., König, M., Gärtner, V., Steinacker, R., Dorninger, M., Turner, D., Weckwerth, T., Hense, A., and Simmer, C.: A research and Development Project of the World Weather research Program for Improving Quantitative Precipitation Forecasting in Low-Mountain regions, American Meteorological Society, 89, 1477–1486, 2008.

## 5.3 Paper III

Draft Title: **Size-resolved aerosol water uptake and cloud condensation nuclei measurements as measured above a Southeast Asian rainforest during OP3**

In preparation for submission to Atmospheric Chemistry and Physics.

Manuscript prepared for Atmos. Chem. Phys.
with version 2.3 of the LaTeX class copernicus.cls.
Date: 15 December 2010

# Size-resolved aerosol water uptake and cloud condensation nuclei measurements as measured above a Southeast Asian rainforest during OP3

**M. Irwin[1], N. Robinson[1], J. Allan[1,2], H. Coe[1], and G McFiggans[1]**

[1]School of Earth, Atmospheric and Environmental Sciences, University of Manchester, Manchester, UK.
[2]National Centre for Atmospheric Science, University of Manchester, Manchester, UK.

**Abstract.** The influence of the properties of fine particles on the formation of clouds and precipitation in the tropical atmosphere is of primary importance to their impacts on radiative forcing and the hydrological cycle. Measurements of aerosol number size distribution, hygroscopicity in both sub- and supersaturated regimes and composition were taken between March and July 2008 in the tropical rainforest in Borneo, Malaysia, marking the first study of this type in an Asian tropical rainforest. Hygroscopic growth factors (GF) at 90% relative humidity (RH) for the dry diameter range $D_0 = 32 - 258$ nm, supersaturated water uptake behaviour for the dry diameter range $D_0 = 20 - 300$ nm and aerosol chemical composition were simultaneously measured using a Hygroscopicity Tandem Differential Mobility Analyser (HTDMA), a Droplet Measurement Technologies Cloud Condensation Nuclei counter (CCNc) and an Aerodyne Aerosol Mass Spectrometer (AMS) respectively.

The derived hygroscopicty parameter $\kappa$ ranged from between $0.05-0.37$ for the supersaturation range $0.11-0.73\%$ compared to those between $0.17 - 0.37$ for measurements performed at a relative humidity of 90%. In contrast, results from a study with similar methodology performed in the Amazon basin report more similar values for $\kappa$, indicating that the aerosol as measured from both sites shows similar hygroscopic properties. However, the derived number of cloud condensation nuclei ($N_{CCN}$) were much higher than those measured in the Amazon, due to the higher particle number concentrations in the rainforests of Borneo. This first contrast between the two environments may be of substantial importance in describing the impacts of particles in the tropical atmosphere.

*Correspondence to:* G. McFiggans
(g.mcfiggans@manchester.ac.uk)

## 1 Introduction

Of all the components of anthropogenic forcings, the complex interactions between atmospheric aerosols and cloud formation, properties and lifetime, collectively termed the 'aerosol indirect effects' have been identified as having the greatest range of uncertainty (Forster et al., 2007). Cloud condensation nuclei (CCN) are the subset of the atmospheric aerosol which have the ability to nucleate cloud droplets in the presence of a water supersaturated air mass. The number of CCN may indirectly influence the radiative balance of the atmosphere by changing the number of cloud droplets, in turn changing the albedo, longevity and precipitation patterns of clouds (Twomey, 1977; Albrecht, 1989; Lohmann and Feichter, 2005 and Feichter et al., 2004; Andreae and Rosenfeld, 2008). A greater understanding of the CCN activation behaviour of the ambient aerosol distribution will improve predictions and further reduce this uncertainty.

The majority of land-based CCN studies report measurements from both moderately polluted continental regions and the marine environment, often in the mid-latitudes. The number of studies conducted in tropics is very low at present, with most limited to Amazonia, where Roberts et al. (2001, 2002, 2003); Andreae et al. (2004); Rissler et al. (2006); Vestin et al. (2007); Freud et al. (2008); Gunthe et al. (2009) classified the Amazonian aerosol as almost "marine"; with CCN concentrations and activation properties closer to that of sea salt than would be expected for continental regimes. More recently, Chen et al. (2009) segregated periods of measurement from within the Amazon rainforest into in-Basin and out-of-Basin, where out-of-basin periods were characterised by aged organic material delivered by long range transport. Roberts et al. (2001) show that low CCN concentrations and high CCN to condensation nuclei (CN) ratios over the unpolluted Amazon Basin resemble conditions previously reported from marine environments, though it is noted that similar CCN and CN concentrations prevail in both marine and

continental regions in spite of the differences in aerosol composition.

Ambient aerosol particles contain a vast number of compounds, almost all in the organic fraction, many of which are unknown (Goldstein and Galbally, 2007; Hallquist et al., 2009). Natural volatile organic compounds (VOC) such as isoprene, monoterpenes and sesquiterpenes as well as anthropogenically-associated aromatic VOCs have been found to be precursors to secondary organic aerosol (SOA), which form when precursor species react with oxidants such as hydroxyl radicals, ozone and nitrogen oxides (Kanakidou et al., 2004). It has also been reported that in remote forested locations biogenic secondary organic aerosol (SOA) plays an important role in the growth of new particles (Allan et al., 2006; Laaksonen et al., 2008; Tunved et al., 2006). Claeys et al. (2004) and Henze and Seinfeld (2006) have shown the formation of secondary organic aerosol through photooxidation of isoprene in the ambient atmosphere, and Robinson et al. (2010a) found evidence for isoprene SOA formation being important at this site. Isoprene is emitted in high quantities in rainforests and represents 38% of the Earth's Non-Methane Hydrocarbon (NMHC) budget (Hallquist et al., 2009), which could potentially change the CCN ability of particles through changes in overall bulk and/or surface composition and water affinity (Facchini et al., 2000; McFiggans et al., 2005, 2006).

Further to the aforementioned CCN studies, aerosol subsaturated water uptake has only been measured in the Amazonian regions of the tropics, where data from hygroscopicity tandem differential mobility analyser (HTDMA) experiments were used to predict aerosol CCN activity under supersaturated conditions (Zhou et al., 2002; Rissler et al., 2004, 2006; Vestin et al., 2007; Gunthe et al., 2009). Such reconciliation studies allow for comparisons with similar marine and continental reconciliation studies, probing our understanding of particle water uptake for a variety of different aerosol number-size distributions and compositions. Changes to a particle's physicochemical properties will change its propensity to behave as a CCN, which is discussed in detail by McFiggans et al. (2006). Organic molecules may influence both the Raoult and Kelvin terms of the Köhler equation by their effect on both water activity and surface tension respectively. VanReken et al. (2005) found a decreasing hygroscopicity in the supersaturated regime with aging time for SOA from biogenic precursors, whereas Duplissy et al. (2008) found an increasing hygroscopicity with aging time in both sub- and supersaturated regimes. Duplissy et al. (2008) went on to further demonstrate how, within error, the aerosol growth factor measurements and CCN activity of chamber-produced SOA can be reconciled with the use of the hygroscopicity parameter $\kappa$ from the semi-empirical $\kappa$-Köhler theory of Petters and Kreidenweis (2007), although Good et al. (2010c), using data from the same experiment, demonstrated that the ability to reconcile the measurements depended on the instrument used for the sub-saturated measurement. Previous reconciliation studies have found that when the aerosols were not strongly influenced by anthropogenic sources and contained low organic content, better agreements between the predicted and measured number of CCN ($N_{CCN}$) were observed (Liu et al., 1996; Chuang et al., 2000; Roberts et al., 2002; Snider et al., 2003; Broekhuizen et al., 2006; Rissler et al., 2006; Medina et al., 2007).

In order to better understand the role of particle size and composition on particle water uptake ability and thus the CCN potential, size-resolved ambient measurements are becoming increasingly common (e.g. Wang et al., 2008; Shinozuka et al., 2009; Good et al., 2010b; Dusek et al., 2010; Pringle et al., 2010). During the "Oxidant and particle photochemical processes above a South-East Asian tropical rainforest" (OP3) project (Hewitt et al., 2010), size-resolved aerosol water uptake in both the sub- ($RH < 100\%$) and supersaturated ($RH > 100\%$) regimes were measured for the first time in the Bornean rainforest. To link aerosol behaviour and air mass origin, we use a classification based on air mass history discussed by Robinson et al. (2010b), who used this approach to show the influence of marine and terrestrial back trajectories using a method consistent with the in- and out-of-basin Amazonian study of Chen et al. (2009). The comparison of air mass origin to the study of aerosol water uptake behaviour as measured in this tropical rainforest is the first measurement of this type, allowing aerosol cloud forming potential in this region to be better quantified.

## 2 Methodology

### 2.1 Measurement Location and Sampling

The OP3 project was carried out during March through July 2008 at the Global Atmospheric Watch (GAW) station at Bukit Atur in the Danum Valley Conservation Area (location: 04° 58' 53" N, 117° 50' 37" E, elevation 426m AMSL). This study focuses on the measurement period OP3-III; 03 July through 20 July after setup and calibrations. For further information regarding the duration, location, meteorology, and weather of the project and for an overview of all measurements, please see Hewitt et al. (2010).

Instrumentation was located inside an air-conditioned shipping container beneath the Global Atmospheric Watch (GAW) station, at the top of the Bukit Atur ridge in a small clearing above the forest canopy (with top of the canopy reaching $30\ \mathrm{m}$ up the $100\ \mathrm{m}$ tall GAW tower). Air was sampled from a common inlet system with an intake located at $30\ \mathrm{m}$ up the centre of the GAW tower. Air was drawn down a solar insulated $28\ \mathrm{m}$, $15\ \mathrm{cm}$ diameter plastic inlet stack with a flow rate of 1500 litres per minute ( $\mathrm{l/min}$). At the bottom of this pipe, air was isokinetically subsampled from the centre of the flow at $35\ \mathrm{l/min}$ and this air was then dried using a 780 tube nafion drier operating with a dry air counterflow. After the drier, the sample air was decelerated to obtain

laminar flow conditions and distributed to instrumentation in the container using an isokinetic sub-sampling system.

### 2.2 CCN Measurements

CCN concentrations as a function of dry diameter ($D_0$, $RH < 20\%$) and supersaturation were measured using the continuous flow thermal-gradient Cloud Condensation Nuclei counter (DMT-CCN counter, Roberts and Nenes, 2005) and were used to derive particle critical supersaturation, $S_{c,D0}$, and threshold dry diameter for activation, $D_{50,S}$. The CCN counter was operated in parallel to a condensation nucleus (CN) counter (TSI - 3010) downstream of a scanning mobility particle sizer (SMPS, TSI - 3080, DMA column 3081). The SMPS was stepped discretely through dry diameters from 20 $\mathrm{nm}$ to 300 $\mathrm{nm}$, referred to hereafter as D-step. This allowed simultaneous measurement of CCN and CN number-size distributions whilst avoiding smearing of sizes whilst scanning the voltage on the SMPS central rod. A settling time of 180 seconds before sizing allowed the stabilisation of temperatures within the CCN counter, with each mobility scan spanning around 12 seconds to increase data yield. The CCN counter stepped through 5 calibrated supersaturations (0.11%, 0.18%, 0.37%, 0.48% and 0.73%; calibrations described below) repeatedly at 10 minute intervals, referred to hereafter as S-step, with the first set point duplicated at the beginning of the scan to allow temperatures within the column to stabilise further, giving a 1 $\mathrm{hr}$ time resolution for this measurement. The CCN and CN number-size distributions were corrected for multiple charge events using the probability coefficients specified in Wiedensohler (1987).

The CCN counter was calibrated using nebulised monodisperse sodium chloride and ammonium sulphate ($>$ $99.95\%$ Sigma Aldrich) aerosol. The shape of the size distribution from the nebuliser is such that multiple charging probabilities are extremely low, and as consequence no charge correction was needed. The calibration aerosol is nebulised, dried, size selected using the differential mobility analyser of the SMPS and split between the CCN counter and CN counter. In total, 20 dry diameters were stepped through between 20 $\mathrm{nm}$ and 220 $\mathrm{nm}$, though complications due to software malfunction increased the lower limit to 45 $\mathrm{nm}$. The fraction of aerosol activated at a given supersaturation and dry diameter, $F_A(S, D_0)$, was measured as a function of the temperature gradient down the column at selected dry diameters. Assuming the system to have a symmetrical transfer function, the data were fitted with an error-weighted sigmoidal function and the temperature gradient at which $F_A(S, D_0)$ = 50% was determined, and interpreted as the critical supersaturation if plotted against supersaturation setpoints ($S_{set}$) or as the threshold dry diameter for activation, $D_{50,S}$, if plotted against $D_0$ (S-step and D-step analysis respectively, explained in Sect. 1 of the Supplement). The supersaturation was then calibrated to agree with the theoretical critical supersaturation calculated using ADDEM (Topping et al., 2005). The CCN counter was operated with an inlet temperature of $\sim 20^{\circ}C$ for the duration of the experiment. This methodology of measurement is consistent with those described by Good et al. (2010a) and Irwin et al. (2010), and is summarised in the Supplement.

### 2.3 Hygroscopic Growth Factor Measurements

Hygroscopic growth factor probability distributions, $p(GF)$, were measured as a function of six dry ($RH < 20\%$) diameters ($D_0$ = 32 $\mathrm{nm}$, 53 $\mathrm{nm}$, 104 $\mathrm{nm}$, 155 $\mathrm{nm}$, 207 $\mathrm{nm}$ and 258 $\mathrm{nm}$) at 90% relative humidity (RH) by a hygroscopicity tandem differential mobility analyser (HTDMA) with 1 $\mathrm{hr}$ time resolution. A dry aerosol mobility is selected by the first DMA which is then humidified to 90% RH and sized again using a second DMA, which steps through voltages, giving a size distribution of the humidified aerosol. The growth factor is defined as the particle diameter at a given $RH$, $D$, divided by its dry diameter, $D_0$. The HTDMA used in this study was the modified version shown by Good et al. (2010a), which was principally described by Cubison et al. (2005). Following quality assurance, the HTDMA data was inverted using the multi-triangle inversion described by Gysel et al. (2009), resulting in the growth factor probability distribution, $p(GF)$. Instrumental errors (e.g. precision of $RH$ measurement) were propagated through to derived data products (such as the single hygroscopicity parameter $\kappa$) as described in the Supplement.

### 2.4 Other measurements

Non-refractory aerosol particle composition was measured by a High-Resolution Time-of-Flight Aerosol Mass Spectrometer (HR-ToF-AMS, Aerodyne Research Inc,; DeCarlo et al., 2006; Canagaratna et al., 2007). The instrument was operated with a heater temperature of approximately $550^{\circ}C$ and is capable of measuring particles from 40 $\mathrm{nm}$ - 700 $\mathrm{nm}$ vacuum aerodynamic diameter (Jayne et al., 2000; Liu et al., 1995a,b). The mass size distribution of the aerosol particles was monitored by measuring the mass as a function of flight time of the sampled particles in vacuum. Standard data analysis techniques were applied (Allan et al., 2003). The collection efficiency used for the OP3 data was 0.5, which is consistent with results from the laboratory (Matthew et al., 2008) and results in good agreement with the integrated submicron volume time series from the DMPS, assuming sphericity and the densities measured by Cross et al. (2007).

Aerosol number-size distributions between 20 $\mathrm{nm}$ and 700 $\mathrm{nm}$ were measured by a differential mobility particle analyzer (DMPS; Williams et al., 2007). A complete mobility scan was performed every 10 minutes.

### 2.5 Air Mass Classification

Data from the final OP3 campaign, OP3-III which spanned 23 June - 23 July, are presented as this period had the most

complete data coverage (for a list of the campaigns see Hewitt et al., 2010).

A backwards air mass trajectory analysis was performed for the OP3 campaign, and is detailed by Robinson et al. (2010b). In this case, back trajectories were calculated from ECMWF wind fields (BADC, 2009). One trajectory per hour was generated for the whole of the OP3 project, with any trajectories that impacted with the ground discarded. All analysis in this paper is segregated using the back trajectory analysis performed with 950 $\mathrm{hPa}$ data. OP3 has been segregated into five distinct periods of influence defined by different air mass (Fig. S1 in the Supplement), defined by back-trajectory cluster analysis and as such the nomenclature is a qualitative guide, rather than assuring the certainty of air mass origin.

During OP3-III, 4 of the 5 air mass sectors were observed; with the Marine and Terrestrial periods dominating the sectorisation (Fig. 1a). The four day Terrestrial period is characterised by a relatively high organic:sulphate ratio (Fig. 1b) when compared to the rest of OP3-III. In contrast, the observed organic:sulphate ratio is much lower during the Marine period ($< 2:1$). No hygroscopicity data were collected during air masses designated to be of 'coastal' origin during OP3-III, and only around 24 hours worth of data were attributed to the Westerly and Northeasterly back trajectories respectively (Fig. 1a).

## 3 Results

### 3.1 Aerosol composition and size distributions

The number-size distribution for the campaign was characterised by a broad monomodal Aitken mode peak between 40 $\mathrm{nm}$ and 70 $\mathrm{nm}$, with occasional high particle concentrations below this diameter (Fig. 1c). Whitehead et al. (2010) present an overview of the aerosol dynamics and size distributions in an Optical Particle Counter (OPC) study representing the accumulation mode. Briefly, from the above canopy measurements it was found that the coarse mode aerosol did not contribute to the number-size distribution, as the number concentrations were extremely low above diameters of 300 $\mathrm{nm}$. Particle number concentrations were typically higher across the entire size distribution between late evening (1800hrs local time) and early morning (0300hrs local time), which may be linked to the collapse of the boundary layer to below the measurement site.

The high organic:sulphate ratio seen during 4 July to 5 July of the Terrestrial period, is characterised by relatively low number concentrations at all sizes. From the latter half of 5 July through 7 July, the organic:sulphate ratio is seen to decrease and the particle number concentration between 20 $\mathrm{nm}$ and 100 $\mathrm{nm}$ increase, after which the period is attributed to the Unclassified sector, before switching to Marine. The Marine period has a relatively low and stable organic:sulphate ratio ranging from $0.25 - 2$, though the particle concentration is seen to vary quite dramatically across the number-size distribution. Most notably, the first half of the Marine period (8 July through 12 July) is characterised by an overall low particle concentration above 70 $\mathrm{nm}$, with a peak in the number-size distribution around 40 $\mathrm{nm}$. 10 July is characterised by a higher than average organic:sulphate ratio, which peaks at midday, followed by very high particle concentrations $< 40$ $\mathrm{nm}$. The latter half of 12 July is characterised by very high particle concentrations between 20 $\mathrm{nm}$ and 110 $\mathrm{nm}$. Similar behaviour is exhibited on the evening of 12 July and less so on the afternoon of 13 July, though for a much shorter period of time in each case. 14 July is shown to have much lower particle concentrations across the size range. The Marine period from midday on 17 July through 19 July is characterised by a slightly higher organic:sulphate ratio than the earlier Marine period (from $0.44 - 2.2$), and number concentrations are much higher at sizes $> 40$ $\mathrm{nm}$.

### 3.2 Activable fraction of particles

Fig. 1c shows the substantial diurnal variability in particle concentrations as a function of size. Typically, higher particle number between 50 $\mathrm{nm}$ and 200 $\mathrm{nm}$ was observed during the day. Fig. 2 shows the Fraction Activated, $F_A(S, D_0)$, of aerosol at each CCNc calibrated supersaturation setting, $S_{set}$, as a function of particle dry diameter, $D_0$. The open circles represent the average $F_A(S, D_0)$ during the day (0600 - 1800hrs) and the solid circles the night-time average showing no significant difference in activation behaviour; the solid line represents the average $F_A(S, D_0)$ for the entire measurement period at each supersaturation, with the error bars showing the standard deviation. There is an apparent departure from the monotonic trend in the fraction activated for the three highest supersaturations with particles below 100 $\mathrm{nm}$ appearing to activate more readily than those just above 100 $\mathrm{nm}$. Owing to low mass loadings, there are no size-resolved composition data from the AMS available, though the aerosol growth factor and mixing state (shown by HTDMA measurements) will allow for an interpretation of aerosol composition at each size (see Sect. 3.4 for the results of HTDMA measurements).

The particle activation data were further split into the Terrestrial and Marine periods; the temporal resolution of the other periods was too low to sectorise effectively. As for the entire dataset, day and night activation behaviour for both Marine and Terrestrial did not differ significantly. These data were further screened for periods of external mixing; the CCNc data were segregated into 5 discrete bins by using $\sqrt{D_0 * D_1}$ for the lower bin edge and $\sqrt{D_1 * D_2}$ for the upper bin edge of the HTDMA dry diameters. Then, only data where the mean growth factor at 90% $RH$ deviated less than 5% from the peak growth factor bin (i.e. the bin of highest particle number) were retained. Fig. 3 shows the fraction of aerosol activated as a function of particle dry diameter. The grey dashed lines indicate the average $F_A(S, D_0)$ of

the Marine and Terrestrial clusters, with the coloured lines indicating the $F_A(S, D_0)$ during periods where the mean growth factor was within 5% deviation of the peak growth factor, for each $S_{set}$. Both clusters exhibit similar trends; particle activation increasing with an increase in supersaturation. Though the external mixture screened data shows some small differences to each sector's mean $F_A(S, D_0)$, as Fig. 2 has shown, this is well within measurement variability. The previously noted departure from monotonic trend across the size range is consistent in each case; at supersaturations above 0.37% ($S_{set2}$), which has the smallest overall standard error, see Fig. S2 in the Supplement, particles of 80 to 90 $\mathrm{nm}$ diameter activate more readily than particles of 100 to 120 $\mathrm{nm}$ in both clusters, indicating more soluble material at the smaller sizes, with the deviation from monotonic behaviour more pronounced in the marine cluster. Overall, particles from the Terrestrial sector activate less readily than those from the Marine sector.

### 3.3 Particle critical supersaturation

The particle critical supersaturation (the supersaturation above which a particle of dry diameter $D_0$ will experience runaway growth into a cloud droplet, denoted $S_{c,D0}$) has been derived for the ambient dry particle size range 65 $\mathrm{nm}<$ $D_0 < 210$ $\mathrm{nm}$. Data outside this range were dominated by large uncertainty, since particles with critical supersaturation close to the CCNc maximum and minimum $S_{set}$ will be constraining the sigmoidal fit with few data on one side or the other of $F_A(S, D_0)$ = 50%, increasing the uncertainty of the fit. Such data are removed during the quality assurance process. This does not substantially limit the data analysis since it is the size range that will almost certainly span the threshold dry diameter for droplet activation at reasonable atmospheric updraught speeds and ambient supersaturations (e.g. $S_{max} <\approx 0.2\%$ for a more hygroscopic aerosol, where the Amazonian study of Reutter et al. (2009) found the variability of initial cloud droplet number concentration in convective clouds to be mostly dominated by the variability of updraft velocity and aerosol particle number concentration in the accumulation mode).

The Terrestrial cluster has a slightly higher activated fraction at the highest supersaturation (0.73%) between 80 to 90 $\mathrm{nm}$ than at the larger dry diameters of 100 to 120 $\mathrm{nm}$ as shown in Fig. 3. However, as the activated fraction increases at lower supersaturations for the same diameters the derived critical supersaturation will increase, though the error associated with the sigmoid fit will be larger. Similarly for the Marine sector, $F_A(S, D_0)$ data at 0.48% and 0.73% both decrease between 80 to 110 $\mathrm{nm}$ which have a greater influence over the sigmoidal function and do in fact decrease the critical supersaturation. The critical supersaturation data are presented in Table. 1 for both sectors for the measured size distribution.

Figure. 4 shows how the peaks in the organic:sulphate ratio are tracked well by the particle critical supersaturation, and the reduced relative organic content seen during the Marine period is characterised by a reduction in the critical supersaturation (this may be expected if the particles can indeed be attributed to be of marine origin with higher relative sulphate or sea salt content).

The $S_{c,D0}$ data was sectorised for Marine and Terrestrial back trajectories, the results of which are shown in Table. 1. There is less variability in $S_{c,D0}$ during the Terrestrial period (denoted by $\sigma$), and there is an overall higher organic:sulphate ratio during this period (Fig. 4). The particles attributed to the Marine sector are easier to activate, requiring a lower supersaturation at all sizes until almost all particles are activated over $D_0 = 200$ $\mathrm{nm}$, though this similarity may partially be attributed to instrument limitations, as the lowest supersaturation setting was 0.11%, and so only critical supersaturations above this value may be derived (see Fig. S2 in the Supplement).

### 3.4 Aerosol sub-saturated water uptake

Aerosol water uptake at 90% relative humidity, $RH$, was measured using an HTDMA. The instrument ran well for the majority of OP3-III, with little deviation from the target $RH$. The growth factor probability distribution, $p(GF)$, (Fig. 5) is highly variable, with the same trends being followed at all sizes. Compared to other projects using the same measurement (such as that shown by Irwin et al., 2010), the growth factor probability distribution for a single scan is typically quite broad; clearly indicating a range of compositions at any given size, exhibiting a broad continuum of growth factors rather than falling into multiple externally mixed classes. The extent of this external mixing becomes increasingly distinct when the less hygroscopic mode with a growth factor of $\sim$1.1 separates from the more hygroscopic mode particles with their higher growth factors typically increasing with increasing dry diameter (Fig. 5). The more hygroscopic mode shown at the larger diameters appears to be an internal mixture, with a narrow distribution of growth factor values. The external mixing shown for dry diameters below 100 $\mathrm{nm}$ (32 $\mathrm{nm}$ and 53 $\mathrm{nm}$) cannot be said to account for the departure from the typical monotonic fraction activated pattern shown by Fig. 3, as the variation in activation data is much greater than the difference between screened and unscreened data.

Aerosol humidograms were performed fortnightly for each dry diameter, increasing the $RH$ stepwise on a 60 minute cycle (10 minutes for each diameter growth factor measurement) in steps of 2%. Fig. 6a shows the aerosol water uptake for each size between 10% $RH$ and 88% $RH$, the inset Fig. shows the DMPS number-size distribution during the period of this humidogram; characterised by low number concentrations for the first 6 hours, followed by very high number concentrations between 20 $\mathrm{nm}$ and 100 $\mathrm{nm}$, with a

peak around 50 nm for the remainder. Whilst the size distribution is variable across the humidogram sampling period, the lack of difference between day and night-time activated fractions shown in Fig. 2 despite the differences in number size distribution shown in Fig. 1c indicates that the variability in number distribution does not influence the water uptake behaviour substantially. CCNc data are unavailable for this time period. Back trajectory analysis has shown the period 26 June to 27 June to contain air originating from the Marine sector. The lack of a well-defined deliquescence point is consistent with aerosol comprising multiple components able to attract liquid water to the particles below the deliquescence point of commonly expected inorganic salts (Marcolli et al., 2004). The two smallest sizes (32 nm and 53 nm) do not achieve the same high growth factor of $1.4 - 1.5$ seen by the larger particles; consistent with activation data (Figs. 2 and 3).

Fig. 6b shows the humidogram taken between 5 July and 6 July; a Terrestrial period with higher variability in the DMPS number-size distribution (Fig. 6 inset) for the duration of the humidogram. It should be noted that no measurements were possible below 45% $RH$. The majority of the data from the humidogram corresponds to the morning and early afternoon of 6 July, which is characterised by low particle concentrations above 60 nm, but high concentrations between 20 nm and 60 nm in the late morning. As expected, particle growth factor increases with increasing dry diameter.

### 3.5 Hygroscopicity

Fig. 7a shows the average of the $RH$-corrected mean growth factor at 90% $RH$ for the Terrestrial sector plotted against that of the Marine sector, coloured as a function of particle dry diameter. The Marine sector shows an overall higher growth factor at each size than for the Terrestrial sector, with particles of $D_0$ = 32 nm showing the closest overall agreement in growth factor between the two sectors.

Consistent with these data, Fig. 7b shows that the Terrestrial sector requires a consistently higher supersaturation to activate the particles compared to that of the Marine sector, which more readily activates at each dry diameter. The largest variability in critical supersaturation is shown to be at the smallest dry diameters, which may be attributed to the influences of an externally mixed aerosol. Fig. 7b shows the same information as Fig. 3, as $S_{c,D_0}$ is derived from $F_A(S, D_0)$. The larger sizes show overall agreement for both sectors, which was previously shown in Table 1.

### 3.6 Reconciling sub- and supersaturated hygroscopicity

An aerosol particle's ability to behave as a CCN is dependent on both particle size and composition. The composition of a solution determines its water activity ($a_w$) and surface tension ($\sigma$) for a given water content. The relationship between a droplets size and saturation ratio ($S$) can be described using these parameters in the Köhler equation (Eq. 1) (Köhler, 1936; McFiggans et al., 2006),

$$S = a_w \exp K_e \tag{1}$$

where $K_e$ is the Kelvin or surface tension term.

The $\kappa$-Köhler model of Petters and Kreidenweis (2007), defines a single hygroscopicity parameter $\kappa$ to describe the particle activation behaviour, which can be derived from HTDMA and CCNc measurements:

$$S = \frac{GF_{D0,RH}^3 - 1}{GF_{D0,RH}^3 - (1-\kappa)} \exp\left(\frac{4\sigma_w M_w}{RT\rho_w D_0 GF_{D0,RH}}\right) \tag{2}$$

where $GF_{D_0,RH}$ is the growth factor at a given dry diameter, $D_0$, and relative humidity, $RH$. Equation 2 was used to calculate $\kappa$ for both HTDMA and CCNc measurements in the same manner as shown by Irwin et al. (2010), with instrumental uncertainties arithmetically propagated through to the final data products of critical supersaturation, threshold dry diameter for activation and number of CCN.

Fig. 8 directly compares HTDMA and CCNc derived critical supersaturations. Critical supersaturation retrieved from the S-step interpretated CCNc data (i.e. derived $S_{c,D0}$) has been plotted against dry diameter as has the critical supersaturation calculated from Equation 2 using HTDMA corrected mean growth factor derived $\kappa_{GF}$. Finally, using D-step CCNc data analysis, $D_{50,S}$ has been plotted against the corresponding corrected CCNc setpoint supersaturation. The predicted critical supersaturation from the HTDMA measurements (shown in red) clearly shows a consistently more hygroscopic aerosol than that derived from either CCNc technique. The D-step analysis (the dry diameter for activation at each supersaturation setting; of which there are 5) shows a typically less hygroscopic aerosol than measured and derived by the HTDMA analysis. The CCNc S-step analysis shows a larger variation in critical supersaturation as a function of particle dry diameter than for either of the other two derivations, though there is good overlap between CCNc derivation techniques in the 70 nm-100 nm size range. The disagreement between $D_{50,S}$ and $S_{c,D0}$ is most prominent at the edges of the dry diameter and/or supersaturation ranges. This may be attributed to the limitations, and thus increased uncertainty, of deriving these products in such close proximity to the edges of the instrument range (see Figures S2 and S3 in Supplement). It should be noted that the overall standard error in $D_{50,S}$ is smaller over the CCNc measurement range than for $S_{c,D0}$.

The hygroscopicity parameter $\kappa$ has been calculated for both HTDMA and CCNc data using Eq. 2. As the SMPS supplying the CCN did not measure at the same dry diameters as the HTDMA, the CCNc dry diameters have been binned around each HTDMA dry diameter, using $\sqrt{D_0 * D_1}$ for the lower bin edge and $\sqrt{D_1 * D_2}$ for the upper bin edge. The mean and standard deviation of $\kappa_{Sc}$ was calculated for each size bin, and plotted against mean $\kappa_{GF}$, shown in Fig. 9.

Values of $\kappa_{GF}$ tend to increase with particle size, whereas conversely, values of $\kappa_{Sc}$ tend to decrease with particle size. Though there is a large standard deviation for the smallest dry diameter bin ($41\ \mathrm{nm} < D_0 < 74\ \mathrm{nm}$), there is reasonable agreement seen between the instruments.

$\kappa_{GF}$ (circles) and $\kappa_{Sc}$ (triangles) were plotted for both Marine (blue) and Terrestrial (green) sectors against particle dry diameter (Fig. 10). The aerosol water uptake is typically evaluated to be lower when calculated from CCNc data than from HTDMA measurements and the derived $\kappa_{Sc}$ values are much smaller than those of $\kappa_{GF}$. The latter values are frequently in the 0.2-0.3 range, and the majority of data are within the range observed in previous studies of rainforest CCN (Gunthe et al., 2009; range $0.05 - 0.45$ using CCNc derived hygroscopicity).

A possible cause of the discrepancies between the values of $\kappa_{Sc}$ and $\kappa_{GF}$ could be due to instrumental differences rather than a fault with the model. The size-selection process involves drying the aerosol prior to entry into a DMA; any differences in the initial drying of the aerosol prior to size-selection will determine the water content in the particle and gaseous phase (air surrounding the particle) as the particle airflow strives to reach equilibrium. As neither drying system will dry to 0% $RH$, the resultant particle dry diameter will be larger than the completely dry particle diameter and, for example, in terms of HTDMA measurements, would result in a lower measured growth factor even if equilibrium is reached in the humidification section (due to the small overestimation of $D_0$). This behaviour has been shown previously by the multi-site study of Aklilu et al. (2006), where data from one HTDMA was successfully reconciled with the AMS (using the Zdanovskii, Stokes and Robinson mixing rule; Stokes and Robinson, 1966), with all components accounted for, whereas for the other HTDMA, it was necessary to excluded nitrate in order to achieve reconciliation. Furthermore, Gysel et al. (2007) reconciled HTDMA and AMS data using ZSR within uncertainty except for times of elevated nitrate concentrations, and Prenni et al. (2001) have shown similar behaviour for semi-volatile compounds. Mikhailov et al. (2004) have also shown this evaporative loss to occur as a function of $RH$ giving rise to errors in dry particle size on the order of several nanometers, and so the potential differences in initial sizing between instruments, though speculative, cannot be overlooked.

Further to size-selection, the relative amounts of gaseous and aqueous compounds in the aerosol sample flow stream will likely differ between different instrument sections, due to changes in the kinetics and the resultant departure from equilibrium. The CCNc has a scrubber which will remove volatile and semi-volatile compounds from the sheath flow, which is absent from the HTDMA's recirculating sheath. Therefore the relative amounts of liquid water and water vapour, in addition to SVOC in both aqueous and gaseous phases, will be different in the humidification sections of both instruments.

### 3.7 Calculation of the Number of Cloud Condensation Nuclei

Using values of $\kappa$, Eq. 2 can be used to calculate the threshold dry diameter for activation ($D_{thres}$) for HTDMA mean corrected growth factor data. Furthermore, the physical threshold dry diameter for activation can be directly derived from the CCNc data via two additional pathways (bypassing the need for $\kappa$); directly from D-step interpreted data, $D_{50,S}$, or by plotting $S_c - S_{set}$ vs $D_0$ where the intercept is interpreted as the physical threshold dry diameter (as shown by Fig. S4 in the Supplement). In order to calculate $N_{CCN}$, the DMPS number-size distribution is integrated using the trapezium rule between the largest dry diameter ($\sim$700 $\mathrm{nm}$) and the threshold dry diameter for activation from each method. Fig. 11 shows the results of this analysis from a variety of different methods. Fig. 11a shows $N_{CCN}$ calculated from the threshold dry diameter as derived by the $\kappa_{GF}$ vs the threshold dry diameter for activation derived from the critical supersaturation (bypassing kappa). Best agreement is at 0.48%, the errors in the $S_{c,D0}$ derived $N_{CCN}$ are larger than that for the HTDMA, with noticeable disagreement in the low $S$, low $N$ regime.

Fig. 11b shows $N_{CCN}$ calculated from S-step analysis (without $\kappa$) vs $N_{CCN}$ calculated from D-step analysis (again, without $\kappa$). As expected, theres a smaller error associated with $N_{CCN}$ derived using D-step interpreted data, compared to that of S-step interpreted data; as fewer analysis steps have been taken, and D-step analysis fits a sigmoidal function to more x-axis data points (see the uncertainty associated with each method in Figures S2 and S3 in the Supplement). Again, best agreement is observed at a supersaturation of 0.48%, but there is relatively good agreement throughout the $S$ range. The reason that the lower and upper supersaturations, $S_{set0}$ and $S_{set4}$ respectively, are not included is that this method of calculating $N_{CCN}$ ($S_{c,D0}$) uses the physical threshold dry diameter of the aerosol as described by plotting $S_c - S$ vs $D_0$ where the intercept for a given $S$ is the threshold dry diameter, and it is not possible to derive $S_{c,D0}$ outside of the $S$ range.

Figures 11 and 12 (and Fig. S5 in Supplement) show the comparison between $N_{CCN}$ derived from the HTDMA ($D_{thres,\kappa,GF}$) and D-step analysis CCNc analysis ($D_{thres,D50}$). The HTDMA data predicts higher numbers of CCN than data from the CCNc would suggest. Previous studies using these instruments (e.g. Irwin et al., 2010), have shown the converse to be true (i.e. that $N_{CCN}$ is underpredicted from HTDMA measurements). The largest difference between the two results however, is in the low $N$, low $S$ regime. The HTDMA does consistently over predict $N_{CCN}$ when compared to $N_{CCN}$ derived from D-step analysis, as a result of the HTDMA apparently measuring an aerosol with a higher water affinity than as reported from the CCNc.

In contrast, Amazonian measurements described by Roberts et al. (2001) report $N_{CCN}$ concentrations between

33 - 320 $\mathrm{cm}^{-3}$ for the range 0.15% - 1% supersaturation, which is lower than any of the $N_{CCN}$ predictions made with size-resolved aerosol water uptake measurements in this study. Size-resolved water uptake measurements from Amazonia as reported by Gunthe et al. (2009) predict $N_{CCN}$ to be between 10 and 500 $\mathrm{cm}^{-3}$ for the supersaturation range 0.10% to 0.82%, indicating differences in the aerosol over Bornean and the Amazonian rainforests.

## 4 Discussion

In this paper we present the first hygroscopicity study in an Asian rainforest and attempt to reconcile the HTDMA/CCNc data with the use of the popular $\kappa$-Köhler model. This paper also marks the first size-resolved particle water uptake measurements made in this region, with interpretation of the data aided through the use of a back trajectory cluster analysis. The $\kappa_{Sc}$ range was typically $0.05 - 0.37$ for the measured dry diameter and supersaturation ranges of $50 - 210$ nm and $0.11 - 0.73\%$ respectively. In comparison, the $\kappa_{GF}$ range was typically $0.17 - 0.37$ for the dry diameter range $32 - 258$ nm measured at 90% RH. This compares with the $\kappa$ range of $0.05 - 0.45$ for the dry diameter range 40-240 nm and supersaturation range $0.10 - 0.82\%$ found in the Amazon (Gunthe et al., 2009).

The aerosol number-size distributions are significantly different during the Terrestrial periods than the Marine, indicating multimodal behaviour and hence also possible external mixing. Sub-saturated water uptake measurements from the HTDMA at 90% showed the aerosol to comprise a variety of growth factors at each size, with a less hygroscopic mode around 1.1 in $p(GF)$, becoming more prominent with increasing aerosol size. Though the size-resolved aerosol composition data as measured by the AMS could not provide adequate information regarding the composition of particles for a given dry diameter, periods of high organic content (attributed to be that of Terrestrial origin by the back trajectory analysis) are characterised by a lower overall hygroscopicity at all sizes, with the Marine sector accounting for the more hygroscopic time periods.

Supersaturated measurements show a departure from the typical monotonic trend typically shown by the fraction of aerosol activated, $F_A(S, D_0)$, most notably at the higher supersaturations ($S_{set} > 0.37\%$ S) and smaller dry diameters ($D_0 < 120$ nm). The apparent complexity of the mixing state as illustrated by HTDMA measurements, is likely to manifest itself in the CCNc measurements as a source of uncertainty, though screening the data for periods of external mixing couldn't explain the discrepancies as the variation in activation data is much greater than the differences between screened and unscreened data. The greatest level of uncertainty from the CCNc measurements was attributed to the S-step analysis, and as such the D-step analysis is the recommended analysis pathway for this particular dataset.

The results can be compared to similar measurements made during the Convective and Orographically-induced Precipitation Study (COPS; Irwin et al., 2010) in Germany's Blackforest, during the summer of 2007. Values of $\kappa_{Sc}$ from moderately-polluted COPS were between 0.4 and 0.1 and values of $\kappa_{GF}$ were between 0.2 and 0.08, the reverse of the results from this project, where values for the HTDMA-derived hygroscopicity parameter were larger than when derived from CCNc measurements. Furthermore, typical values of $N_{CCN}$ during COPS were $3-4$ times those calculated during OP3, leading to the conclusion that aerosol in the tropical region of Borneo can be considered to be a synthesis of marine and continental aerosol traits, in a biogenically diverse setting. Due to the climatic importance of the tropical regions, and the apparent variability of various derived data products, such as $\kappa$, between regions, any anthropogenic perturbations to aerosol number and composition due to changes in land use in the tropics highlight the importance of studies of this type.

## 5 Conclusions

Size-resolved HTDMA and CCNc measurement of atmospheric aerosol in Borneo identified the aerosol to comprise a range of compositions over the measured size range ($D_0 = 32 - 258$ nm), and for the aerosol hygroscopicity to vary with changing air mass back trajectories, largely outside of uncertainty.

Reconciliations of the results from both instruments was performed through to predictions of $N_{CCN}$, where good agreement is seen between the HTDMA and CCN derived products. The HTDMA typically sees a more hygroscopic aerosol throughout the campaign than the CCNc ($\kappa_{GF} = 0.17 - 0.37$ compared to $\kappa_{S_c} = 0.05 - 0.37$), resulting in a higher predicted number of CCN. However, both methods predict the overall CCN concentration to be modest, which reinforces results from previous studies that suggest that rainforest aerosol may behave in a "marine" fashion (Roberts et al., 2001; Gunthe et al., 2009), though the predicted $N_{CCN}$ results from the Amazon are typically lower, with values of $N_{CCN}$ at $S = 0.73\%$ between 482 and 701 $\mathrm{cm}^{-3}$ for sub- and supersaturated measurement predictions respectively, in contrast to the much lower figures reported by Gunthe et al. (2009) ($\sim$163 $\mathrm{cm}^{-3}$ at $S = 0.82\%$).

In order to combat the issues of mixing state in future measurements of this type, the authors recommend a higher resolution set of CCNc measurements, at a higher number of supersaturation setpoints. The increased number of diameter measurements with allow for a better analysis of the aerosol behaviour at each diameter, and a higher number of supersaturations will reduce the uncertainty involved in fitting the data for $S_{c,D0}$ and $D_{50,S}$. In addition, any improvements in the measurement of aerosol size-resolved composition would be welcomed greatly, as it would enable an in depth analysis

of aerosol composition and its influence on hygroscopicity as a function of particle dry diameter (the AMS was not suitable on this occasion due to insufficient particle mass).

Acknowledgements: The Oxidant and Photochemical Particle Processes above a Southeast Asian tropical rainforest project (OP3) was funded by the National Environmental Research Council (NERC; NE/0021171/1). The authors wish to thank the Malaysian and Sabah Governments for their permission to conduct research in Malaysia; the Malaysian Meteorological Department for access to the Bukit Atur Global Atmosphere Watch station; Waidi Sinun of Yayasan Sabah and Glen Reynolds of the Royal Societys South East Asian Rain Forest Research Programme for logistical support at the Danum Valley Research Station and the all Royal Society research assistants. Special thanks to J Dorsey, K. Bower, M. Flynn, P. Williams for their help in the field. This work was also made possible with the Ph.D studentship of Martin Irwin (NER/S/A/2006/14036). This is paper 526 of the Royal Societys South-East Asian Rainforest Research Programme.

## References

Aklilu, Y., Mozurkewich, M., and Prenni, A.: Hygroscopicity of particles at two rural, urban influenced sites during Pacific 2001: Comparison with estimates of water uptake from particle composition, Atmospheric Environment, 40, 2650–2661, 2006.

Albrecht, B.: Aerosols, cloud microphysics, and fractional cloudiness, Science, 245, 1227–1230, 1989.

Allan, J., Jimenez, J., Williams, P., and Alfarra, M.: Quantitative sampling using an Aerodyne aerosol mass spectrometer: 1. Techniques of data interpretation and error analysis, J. Geophys. Res., 2003.

Allan, J. D., Alfarra, M. R., Bower, K. N., Coe, H., Jayne, J. T., Worsnop, D. R., Aalto, P. P., Kulmala, M., Hyötyläinen, T., Cavalli, F., and Laaksonen, A.: Size and composition measurements of background aerosol and new particle growth in a Finnish forest during QUEST 2 using an Aerodyne Aerosol Mass Spectrometer, Atmospheric Chemistry and Physics, 6, 315–327, doi: 10.5194/acp-6-315-2006, 2006.

Andreae, M. and Rosenfeld, D.: Aerosol–cloud–precipitation interactions. Part 1. The nature and sources of cloud-active aerosols, Earth Science Reviews, 89, 13–41, 2008.

Andreae, M., Rosenfeld, D., Artaxo, P., and Costa, A.: Smoking rain clouds over the Amazon, Science, 303, 1337–1342, 2004.

BADC: European Centre for Medium-Range Weather Forecasts. ECMWF Trajectories, Internet, Available from http://badc.nerc.ac.uk/data/ecmwf-trj/, 2009.

Broekhuizen, K., Chang, R., Leaitch, W., and Li, S.: Closure between measured and modeled cloud condensation nuclei (CCN) using size-resolved aerosol compositions in downtown Toronto, Atmospheric Chemistry and Physics Discussions, 6, 2006.

Canagaratna, M. R., Jayne, J. T., Jimenez, J. L., Allan, J. D., Alfarra, M. R., Zhang, Q., Onasch, T. B., Drewnick, F., Coe, H., Middlebrook, A., Delia, A., Williams, L. R., Trimborn, A. M., Northway, M. J., Decarlo, P. F., Kolb, C. E., Davidovits, P., and Worsnop, D. R.: Chemical and microphysical characterization of ambient aerosols with the aerodyne aerosol mass spectrometer, doi:10.1002/mas.20115, 2007.

Chen, Q., Farmer, D., Schneider, J., and . . . , S. Z.: Mass spectral characterization of submicron biogenic organic particles in the Amazon Basin, Geophys. Res. Lett., 36, 2009.

Chuang, P., Collins, D., and Pawlowska, H.: CCN measurements during ACE-2 and their relationship to cloud microphysical properties, Tellus, 2000.

Claeys, M., Graham, B., Gyorgy, V., Wang, W., Vermeylen, R., Pashynska, V., Cafmeyer, J., Guyon, P., Meinrat, O., Artaxo, P., and Maenhaut, W.: Formation of Secondary Organic Aerosols Through Photooxidation of Isoprene, Science, 303, 1173–1176, 2004.

Cross, E. S., Slowik, J. G., Davidovits, P., Allan, J. D., Worsnop, D. R., Jayne, J. T., Lewis, D. K., Canagaratna, M., and Onasch, T. B.: Laboratory and ambient particle density determinations using light scattering in conjunction with aerosol mass spectrometry, Aerosol Science and Technology, 41, 343–359, doi: 10.1080/02786820701199736, 2007.

Cubison, M. J., Coe, H., and Gysel, M.: A modified hygroscopic tandem DMA and a data retrieval method based on optimal estimation, Journal of Aerosol Science, 36, 846–865, 2005.

DeCarlo, P., Kimmel, J., Trimborn, A., Northway, M., Jayne, J., Aiken, A., Gonin, M., Fuhrer, K., Horvath, T., Docherty, K., Worsnop, D., and Jimenez, J. L.: Field-Deployable, High-Resolution, Time-of-Flight Aerosol Mass Spectrometer, Analytical Chemistry, 78, 8281–8289, 2006.

Duplissy, J., Gysel, M., Alfarra, M., Dommen, J., Metzger, A., Prevot, A., Weingartner, E., Laaksonen, A., Raatikainen, T., and Good, N.: Cloud forming potential of secondary organic aerosol under near atmospheric conditions, Geophys. Res. Lett, 35, 2008.

Dusek, U., Frank, G., Curtius, J., Drewnick, F., Schneider, J., Kürten, A., Rose, D., Andreae, M. O., Borrmann, S., and Pöschl, U.: Enhanced organic mass fraction and decreased hygroscopicity of cloud condensation nuclei (CCN) during new particle formation events, Geophysical Research Letters, 37, 2010.

Facchini, M. C., Decesari, S., Mircea, M., Fuzzi, S., and Loglio, G.: Surface tension of atmospheric wet aerosol and cloud/fog droplets in relation to their organic carbon econtent and chemical composition, Atmospheric Environment, 33, 4853–4857, 2000.

Feichter, J., Roeckner, E., and Lohmann, U.: Nonlinear aspects of the climate response to greenhouse gas and aerosol forcing, Journal of Climate, 17, 2384–2398, 2004.

Forster, P., Ramaswamy, V., Artaxo, P., Berntsen, T., Betts, R., Fahey, D., Haywood, J., Lean, J., Lowe, D., Myhre, G., Nganga, J., Prinn, R., Raga, G., Schulz, M., and Dorland, R. V.: Changes in Atmospheric Constituents and in Radiative Forcing. In: Climate Change 2007: The Physical Science Basis. Contribution of Working Group I to the Fourth Assessment Report of the Intergovernmental Panel on Climate Change, 2007.

Freud, E., Ström, J., Rosenfeld, D., and Tunved, P.: Anthropogenic aerosol effects on convective cloud microphysical properties in southern Sweden, Tellus B, 60, 286–297, 2008.

Goldstein, A. and Galbally, I.: Known and unexplored organic constituents in the earth's atmosphere, Environmental Science & Technology, 2007.

Good, N., Coe, H., and McFiggans, G.: Instrumentational operation and analytical methodology for the reconciliation of aerosol wa-

ter uptake under sub-and supersaturated conditions, Atmospheric Measurement Techniques Discussions, 3, 359–403, 2010a.

Good, N., Topping, D., Allan, J., Flynn, M., Fuentes, E., Irwin, M., Williams, P., Coe, H., and McFiggans, G.: Consistency between parameterisations of aerosol hygroscopicity and CCN activity during the RHaMBLe Discovery cruise, Atmos. Chem. Phys., 10, 3189–3203, 2010b.

Good, N., Topping, D. O., Duplissy, J., Gysel, M., Meyer, N. K., Metzger, A., Turner, S. F., Baltensperger, U., Ristovski, Z., Weingartner, E., Coe, H., and McFiggans, G.: Widening the gap between measurement and modelling of secondary organic aerosol properties?, Atmospheric Chemistry and Physics, 10, 2577–2593, 2010c.

Gunthe, S., King, S., Rose, D., Chen, Q., Roldin, P., Farmer, D., Jimenez, J., Artaxo, P., and Aneae, M.: Cloud condensation nuclei in pristine tropical rainforest air of Amazonia: size-resolved measurements and modeling of atmospheric aerosol composition and CCN activity, Atmospheric Chemistry and Physics, 9, 7551–7575, 2009.

Gysel, M., Crosier, J., Topping, D. O., Whitehead, J., Bower, K. N., Cubison, M. J., Williams, P. I., Flynn, M. J., McFiggans, G. B., and Coe, H.: Closure study between chemical composition and hygroscopic growth of aerosol particles during TORCH2, Atmospheric Chemistry and Physics, 7, 6131–6144, 2007.

Gysel, M., McFiggans, G., and Coe, H.: Inversion of tandem differential mobility analyser (TDMA) measurements, Journal of aerosol science, 40, 134–151, 2009.

Hallquist, M., Wenger, J. C., Baltensperger, U., Rudich, Y., Simpson, D., Claeys, M., Dommen, J., Donahue, N. M., George, C., Goldstein, A. H., Hamilton, J. F., Herrmann, H., Hoffmann, T., Iinuma, Y., Jang, M., Jenkin, M., Jimenez, J. L., Kiendler-Scharr, A., Maenhaut, W., McFiggans, G., Mentel, T. F., Monod, A., Prévôt, A. S. H., Seinfeld, J. H., Surratt, J. D., Szmigielski, R., and Wildt, J.: The formation, properties and impact of secondary organic aerosol: current and emerging issues, Atmospheric Chemistry and Physics, 9, 5155–5236, doi: 10.5194/acpd-9-3555-2009, 2009.

Henze, D. K. and Seinfeld, J. H.: Global secondary organic aerosol from isoprene oxidation, Geophysical Research Letters, 33, L09 812, doi:10.1029/2006GL025976, 2006.

Hewitt, C. N., Lee, J. D., Mackenzie, A. R., Barkley, M. P., Carslaw, N., Carver, G. D., Chappell, N. A., Coe, H., Collier, C., Commane, R., Davies, F., Davison, B., Dicarlo, P., Marco, C. F. D., Dorsey, J. R., Edwards, P. M., Evans, M. J., Fowler, D., Furneaux, K. L., Gallagher, M., Guenther, A., Heard, D. E., Helfter, C., Hopkins, J., Ingham, T., Irwin, M., Jones, C., Karunaharan, A., Langford, B., Lewis, A. C., Lim, S. F., Macdonald, S. M., Mahajan, A. S., Malpass, S., McFiggans, G., Mills, G., Misztal, P., Moller, S., Monks, P. S., Nemitz, E., Nicolas-Perea, V., Oetjen, H., Oram, D. E., Palmer, P. I., Phillips, G. J., Pike, R., Plane, J. M. C., Pugh, T., Pyle, J. A., Reeves, C. E., Robinson, N. H., Stewart, D., Stone, D., Whalley, L. K., and Yin, X.: Overview: oxidant and particle photochemical processes above a south-east Asian tropical rainforest (the OP3 project): introduction, rationale, location characteristics and tools, Atmospheric Chemistry and Physics, 10, 169–199, doi:10.5194/acp-10-169-2010, 2010.

Irwin, M., Good, N., Crosier, J., Choularton, T. W., and McFiggans, G.: Reconciliation of measurements of hygroscopic growth and critical supersaturation of aerosol particles in Southwest Germany, Atmos. Chem. Phys., 10, 11 737–11 752, doi: 10.5194/acp-10-11737-2010, 2010.

Jayne, J., Leard, D., and Zhang, X.: Development of an aerosol mass spectrometer for size and composition analysis of submicron particles, Aerosol Science and Technology, 33, 49–70, 2000.

Kanakidou, M., Seinfeld, J., Pandis, S., Barnes, I., Dentener, F., Facchini, M., Dingenen, R. V., Ervens, B., Nenes, A., and Nielsen, C.: Organic aerosol and global climate modelling: a review, Atmospheric Chemistry and Physics Discussions, 4, 5855–6024, 2004.

Köhler, H.: The nucleus in and the growth of hygroscopic droplets, Transactions of the Faraday Society, 32, 1152–1161, doi:DOI:10.1039/TF9363201152, 1936.

Laaksonen, A., Kulmala, M., O'dowd, C. D., Joutsensaari, J., Vaattovaara, P., Mikkonen, S., Lehtinen, K. E. J., Sogacheva, L., Maso, M. D., Aalto, P., Petäjä, T., Sogachev, A., Yoon, Y. J., Lihavainen, H., Nilsson, D., Facchini, M. C., Cavalli, F., Fuzzi, S., Hoffmann, T., Arnold, F., Hanke, M., Sellegri, K., Umann, B., Junkermann, W., Coe, H., Allan, J. D., Alfarra, M. R., Worsnop, D. R., Riekkola, M. L., Hyötyläinen, T., and Viisanen, Y.: The role of VOC oxidation products in continental new particle formation, Atmospheric Chemistry and Physics, 8, 2657–2665, doi: 10.5194/acp-8-2657-2008, 2008.

Liu, P., Ziemann, P., and Kittelson, D.: Generating particle beams of controlled dimensions and divergence: I. Theory of particle motion in aerodynamic lenses and nozzle expansions, Aerosol Science and Technology, 22, 293–313, 1995a.

Liu, P., Ziemann, P., and Kittelson, D.: Generating particle beams of controlled dimensions and divergence: II. Experimental evaluation of particle motion in aerodynamic lenses and nozzle expansions, Aerosol Science and Technology, 22, 314–324, 1995b.

Liu, P. S. K., Leaitch, W. R., Banic, C. M., Li, S. M., Ngo, D., and Megaw, W. J.: Aerosol observations at Chebogue Point during the 1993 North Atlantic Regional Experiment: Relationships among cloud condensation nuclei, size distribution, and chemistry, Journal of Geophysical Research, 101, 28 971–28,990, 1996.

Lohmann, U. and Feichter, J.: Global indirect aerosol effects: a review, Atmos. Chem. Phys, 5, 715–737, 2005.

Marcolli, C., , Luo, B., and Peter, T.: Mixing of the Organic Aerosol Fractions: Liquids as the Thermodynamically Stable Phases, J. Phys. Chem. A,, 108, 2216–2224, 2004.

Matthew, B. M., Middlebrook, A., and Onasch, T.: Collection Efficiencies in an Aerodyne Aerosol Mass Spectrometer as a Function of Particle Phase for Laboratory Generated Aerosols, Aerosol Science and Technology, 42, 884–898, doi:10.1080/02786820802356797, 2008.

McFiggans, G., Alfarra, M., Allan, J., Bower, K., and Coe, H.: Simplification of the representation of the organic component of atmospheric particulates, Faraday Discussions, 130, 341–362, doi: 10.1039/b419435g, 2005.

McFiggans, G., Artaxo, P., Baltensperger, U., Coe, H., Facchini, M. C., Feingold, G., Fuzzi, S., Gysel, M., Laaksonen, A., Lohmann, U., Mentel, T. F., Murphy, D. M., O'Dowd, C. D., Snider, J. R., and Weingartner, E.: The effect of physical and chemical aerosol properties on warm cloud droplet activation, Atmospheric Chemistry and Physics, 6, 2593–2649, 2006.

Medina, J., Nenes, A., Sotiropoulou, R., and Cottrell, L.: Cloud condensation nuclei closure during the International Consortium for Atmospheric Research on Transport and Transformation 2004 campaign: Effects of size-resolved composition, J. Geophys. Res, 112, D10S31, doi:10.1029/2006JD007588, 2007.

Mikhailov, E., Vlasenko, S., Niessner, R., and Pöschl, U.: Interaction of aerosol particles composed of protein and salts with water vapor: hygroscopic growth and microstructural rearrangement, Atmospheric Chemistry and Physics, 4, 323–350, doi:10.5194/acp-4-323-2004, 2004.

Petters, M. and Kreidenweis, S.: A single parameter representation of hygroscopic growth and cloud condensation nucleus activity, Atmospheric Chemistry and Physics, 7, 1961–1971, 2007.

Prenni, A. J., DeMott, P. J., Kreidenweis, S. M., Sherman, D. E., Russell, L. M., and Ming, Y.: The effects of low molecular weight dicarboxylic acids on cloud formation, Journal of Physical Chemistry A, 105, 11 240–11 248, 2001.

Pringle, K., Tost, H., and Pozzer, A.: Global distribution of the effective aerosol hygroscopicity parameter for CCN activation, Atmospheric Chemistry and Physics, 10, 5241 –5255, 2010.

Reutter, P., Su, H., Trentmann, J., Simmel, M., Rose, D., Gunthe, S. S., Wernli, H., Andreae, M. O., and Pöschl, U.: Aerosol- and updraft-limited regimes of cloud droplet formation: influence of particle number, size and hygroscopicity on the activation of cloud condensation nuclei (CCN), Atmospheric Chemistry and Physics, 9, 7067–7080, doi:10.5194/acp-9-7067-2009, 2009.

Rissler, J., Swietlicki, E., Zhou, J., Roberts, G., Andreae, M. O., Gatti, L. V., and Artaxo, P.: Physical properties of the submicrometer aerosol over the Amazon rain forest during the wet-to-dry season transition - comparison of modeled and measured CCN concentrations, Atmospheric Chemistry and Physics, 4, 2119–2143, doi:10.5194/acp-4-2119-2004, 2004.

Rissler, J., Vestin, A., Swietlicki, E., Fisch, G., Zhou, J., Artaxo, P., and Andreae, M.: Size distribution and hygroscopic properties of aerosol particles from dry-season biomass burning in Amazonia, Atmospheric Chemistry and Physics, 6, 471–491, 2006.

Roberts, G., Andreae, M., Zhou, J., and Artaxo, P.: Cloud condensation nuclei in the Amazon Basin:"Marine" conditions over a continent, Geophys. Res. Lett, 28, 2807–2810, 2001.

Roberts, G., Artaxo, P., Zhou, J., Swietlicki, E., and Andreae, M.: Sensitivity of CCN spectra on chemical and physical properties of aerosol: A case study from the Amazon Basin, Journal of Geophysical Research-Atmospheres, 107, 8070, doi:10.1029/2001JD000583, 2002.

Roberts, G., Nenes, A., and Seinfeld, J.: Impact of biomass burning on cloud properties in the Amazon Basin, J. Geophys. Res., 2003.

Roberts, G. C. and Nenes, A.: A continuous-flow streamwise thermal-gradient CCN chamber for atmospheric measurements, Aerosol Science and Technology, 39, 206–221, 2005.

Robinson, N. H., Hamilton, J. F., Allan, J. D., Langford, B., Oram, D. E., Chen, Q., Docherty, K., Farmer, D. K., Jimenez, J. L., Ward, M. W., Hewitt, C. N., Barley, M. H., Jenkin, M. E., Rickard, A. R., Martin, S. T., McFiggans, G., and Coe, H.: Evidence for a significant proportion of Secondary Organic Aerosol from isoprene above a maritime tropical forest, Atmospheric Chemistry and Physics Discussions, 10, 25 545–25 576, doi:10.5194/acpd-10-25545-2010, 2010a.

Robinson, N. H., Newton, H., Allan, J., Mills, G., Irwin, M., Lee, J., Chen, Q., Martin, S., McFiggans, G., and Coe, H.: Source attribution during the OP3 project using backwards air mass trajectories, Atmos. Chem. Phys (Preparation), 2010b.

Shinozuka, Y., Clarke, A. D., Decarlo, P. F., Jimenez, J. L., Dunlea, E. J., Roberts, G. C., Tomlinson, J. M., Collins, D. R., Howell, S. G., Kapustin, V. N., Mcnaughton, C. S., and Zhou, J.: Aerosol optical properties relevant to regional remote sensing of CCN activity and links to their organic mass fraction: airborne observations over Central Mexico and the US West Coast during MILAGRO/INTEX-B, Atmospheric Chemistry and Physics Discussions, 9, 12 519–12 558, doi:10.5194/acpd-9-12519-2009, 2009.

Snider, J., Guibert, S., Brenguier, J., and Putaud, J.: Aerosol activation in marine stratocumulus clouds: 2. Köhler and parcel theory closure studies, J. Geophys. Res, 108, 8629, 2003.

Stokes, R. and Robinson, R.: Interactions in aqueous nonelectrolyte solutions. I. Solute-solvent equilibria, The Journal of Physical Chemistry, 70, 2126–2130, 1966.

Topping, D. O., McFiggans, G. B., and Coe, H.: A curved multi-component aerosol hygroscopicity model framework: Part 1 - Inorganic compounds, Atmospheric Chemistry and Physics, 5, 1205–1222, 2005.

Tunved, P., Korhonen, H., Ström, J., and Hansson, H.: Is nucleation capable of explaining observed aerosol integral number increase during southerly transport over Scandinavia?, Tellus B, 59, 129–140, 2006.

Twomey, S.: Influence of Pollution on Shortwave Albedo of Clouds, Journal of the Atmospheric Sciences, 34, 1149–1152, 1977.

VanReken, T., Ng, N., and Flagan, R.: Cloud condensation nucleus activation properties of biogenic secondary organic aerosol, Journal of Geophysical Research, 110, 2005.

Vestin, A., Rissler, J., Swietlicki, E., and Frank, G.: Cloud-nucleating properties of the Amazonian biomass burning aerosol: Cloud condensation nuclei measurements and modeling, Journal of Geophysical Research, 112, D14 201, 2007.

Wang, J., Lee, Y., Daum, P., Jayne, J., and Alexander, M.: Effects of aerosol organics on cloud condensation nucleus (CCN) concentration and first indirect aerosol effect, Atmos. Chem. Phys, 8, 6325–6339, 2008.

Whitehead, J. D., Gallagher, M. W., Dorsey, J. R., Robinson, N., Gabey, A. M., Coe, H., McFiggans, G., Flynn, M. J., Ryder, J., Nemitz, E., and Davies, F.: Aerosol fluxes and dynamics within and above a tropical rainforest in South-East Asia, Atmospheric Chemistry and Physics, 10, 9369–9382, doi:doi:10.5194/acp-10-9369-2010, 2010.

Wiedensohler, A.: An approximation of the bipolar charge distribution for particles in the submicron size range, Journal of Aerosol Science, 19, 387–389, 1987.

Williams, P., McFiggans, G., and Gallagher, M.: Latitudinal aerosol size distribution variation in the Eastern Atlantic Ocean measured aboard the FS-Polarstern, Atmospheric Chemistry and Physics, 7, 2563–2573, 2007.

Zhou, J., Swietlicki, E., Hansson, H., and Artaxo, P.: Submicrometer aerosol particle size distribution and hygroscopic growth measured in the Amazon rain forest during the wet season, J. Geophys. Res, 107, 8055, 2002.

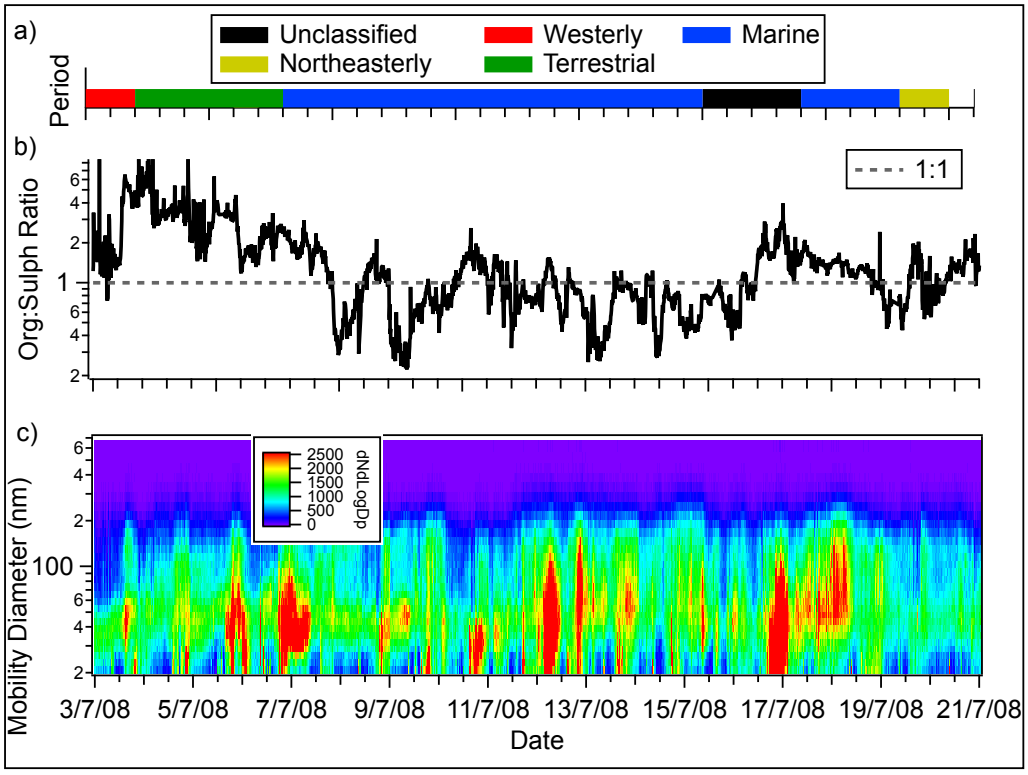


**Fig. 1.** a) the sectorisation of the OP3-III campaign, for the time series of the aerosol instrumentation used in this paper. b) the total organic:sulphate ratio as measured by the HR-AMS. c) the DMPS number-size distribution for the measurement period. The periods are defined as 0 Unclassified, 1 Westerly, 2 Coastal, 3 Marine, 4 Northeasterly and 5 Terrestrial.

**Table 1.** A table of mean critical supersaturation, $S_{c,D0}$, for each measured dry diameter, $D_0$, for the Marine and Terrestrial periods of OP3-III, with standard deviation, $\sigma$

| | Marine | | Terrestrial | |
|---|---|---|---|---|
| $D_0$ | $S_{c,D0}(\%)$ | $\sigma$ | $S_{c,D0}(\%)$ | $\sigma$ |
| 65 nm | 0.482 | 0.085 | 0.630 | 0.036 |
| 74 nm | 0.428 | 0.078 | 0.560 | 0.043 |
| 84 nm | 0.391 | 0.071 | 0.512 | 0.043 |
| 96 nm | 0.388 | 0.061 | 0.477 | 0.032 |
| 110 nm | 0.394 | 0.057 | 0.465 | 0.043 |
| 129 nm | 0.361 | 0.052 | 0.431 | 0.060 |
| 148 nm | 0.209 | 0.058 | 0.257 | 0.054 |
| 171 nm | 0.202 | 0.047 | 0.246 | 0.054 |
| 199 nm | 0.182 | 0.051 | 0.184 | 0.052 |
| 224 nm | 0.183 | 0.074 | 0.182 | 0.053 |

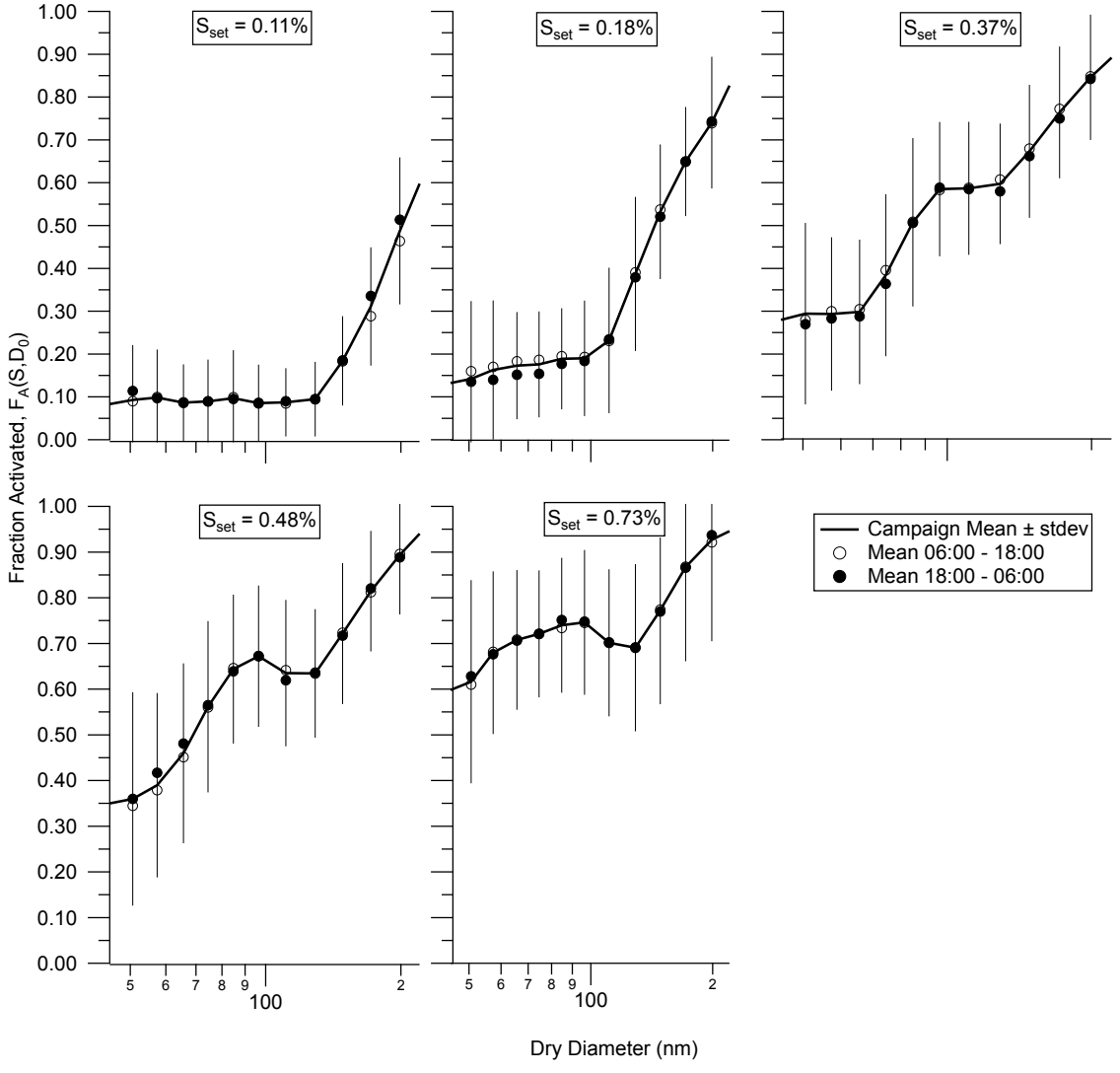


**Fig. 2.** The aerosol fraction activated $F_A(S, D_0)$ against dry diameter, for each $S_{set}$ used in OP3-III. The campaign mean is shown as a solid black line, with error bars illustrating the standard deviation. The data was segregated into day and night, denoted by hollow and solid circles respectively.

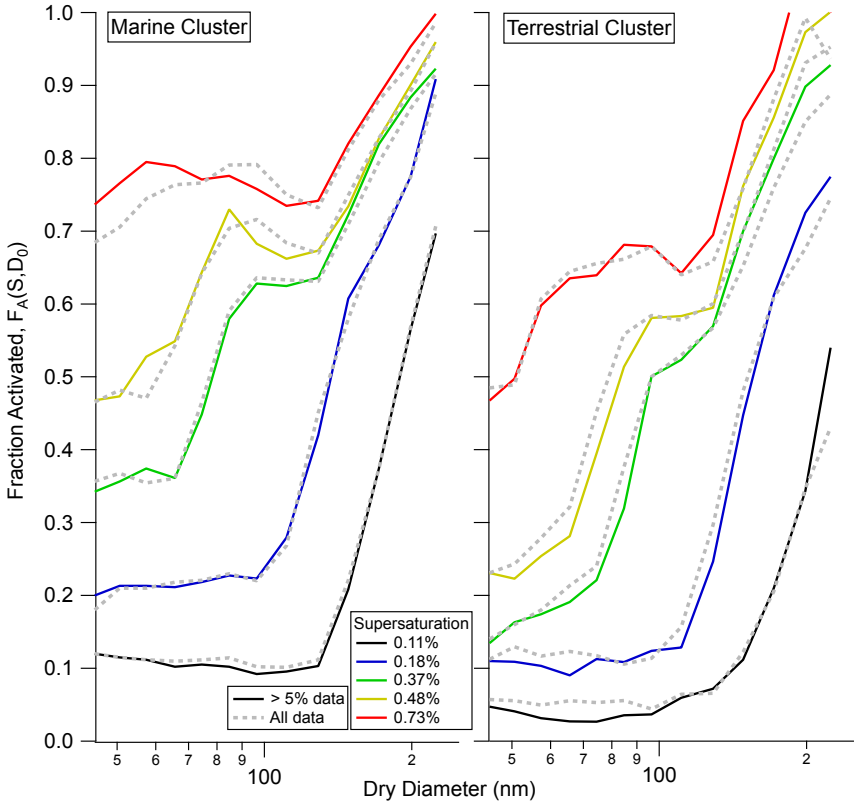


**Fig. 3.** The fraction activated at each supersaturation as a function of dry diameter, split for the sectorisations Marine and Terrestrial. The grey lines indicate the campaign mean data, and the coloured lines show data from when the HTDMA mean corrected growth factor had smaller than 5% deviation from the peak growth factor bin.

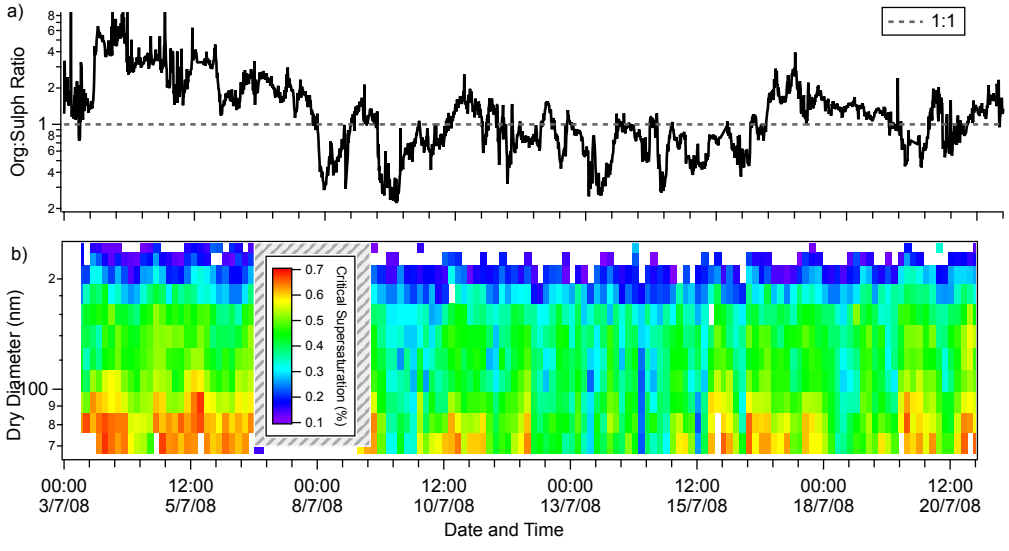


**Fig. 4.** a) the organic:sulphate ratio (solid) and 1:1 line (dashed) for OP3-III and b) the derived critical supersaturation as a function of dry diameter.

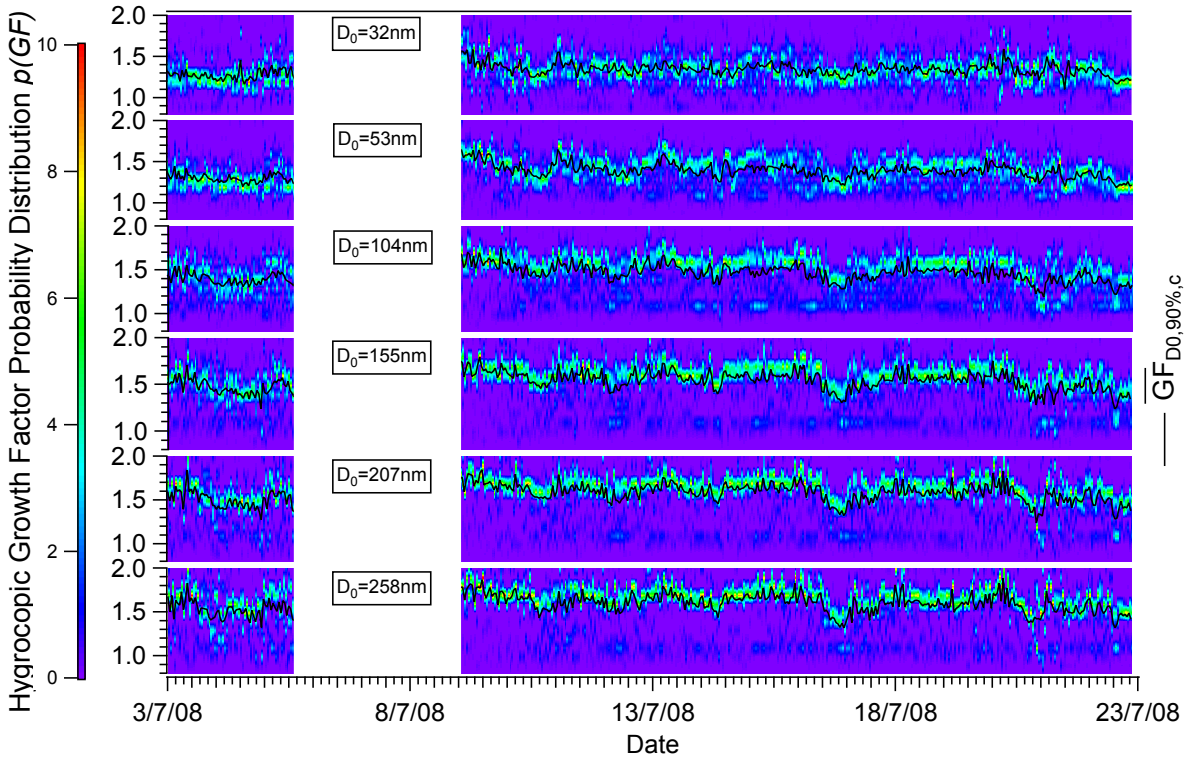


**Fig. 5.** The HTDMA growth factor probability distribution, $p(GF)$, and RH-corrected mean growth factor, $\overline{GF}_{D0,90\%,c}$ at 90%, for 6 dry diameters as measured by the HTDMA

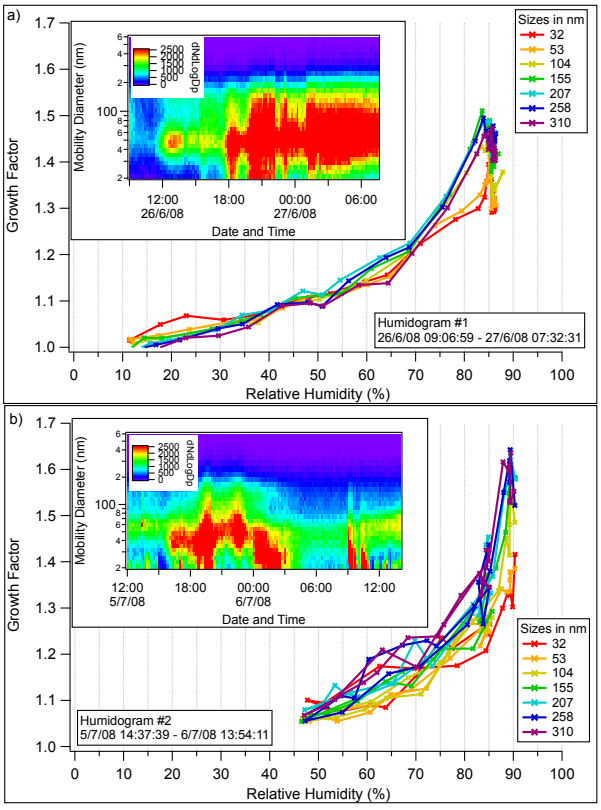


**Fig. 6.** a) A Humidogram taken before the CCNc calibrations were completed, during a Marine sector in OP3=III. b) A humidogram taking during a Terrestrial sector during OP3-III, data where $RH < 45\%$ were unavailable.

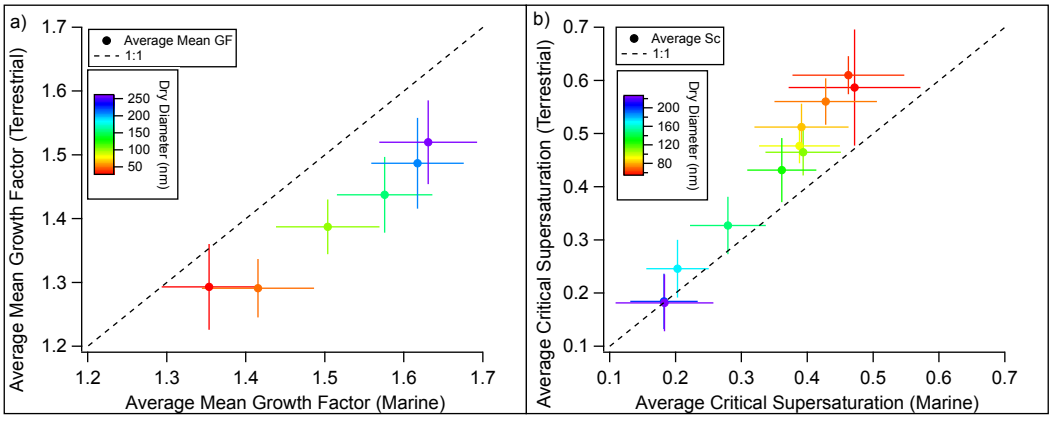


**Fig. 7.** a) The $RH$ corrected mean growth factor and b) critical supersaturation for terrestrial sectors plotted against marine sectors, as a function of dry particle diameter - indicated by the colourscale. The error bars denote the standard deviation.

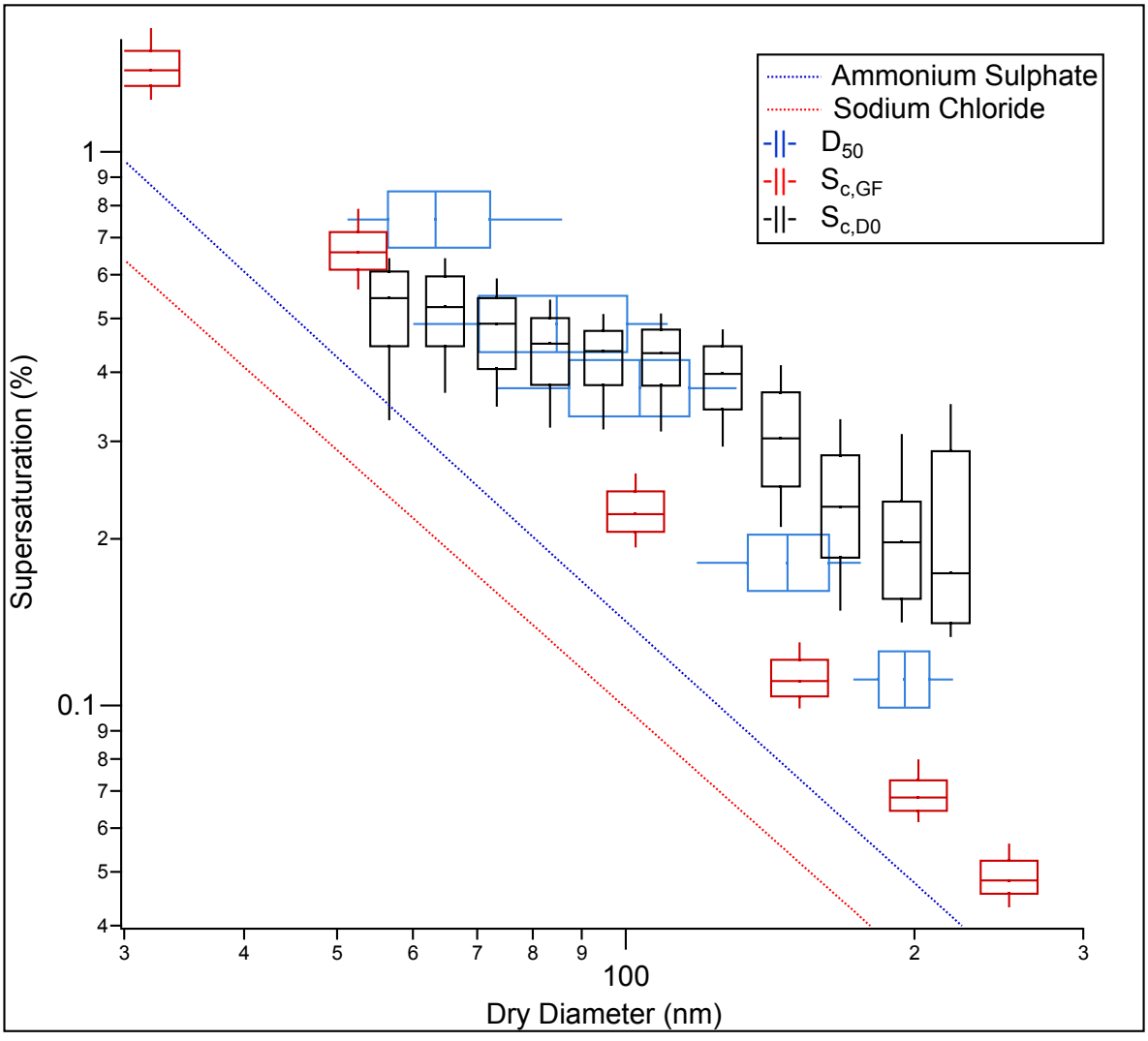


**Fig. 8.** Critical supersaturation vs dry diameter for the HTDMA results predicted using the $\kappa$ model, CCNc results using both derived $S_{c,D0}$ and derived $D_{50,S}$. The centreline of the box represents the median of the data, with the box edges representing the 25% and 75% quartiles and the whiskers the 10% and 90% quartiles. The dashed lines show the results of the ADDEM model (Topping et al., 2005) for inorganic salt particles.

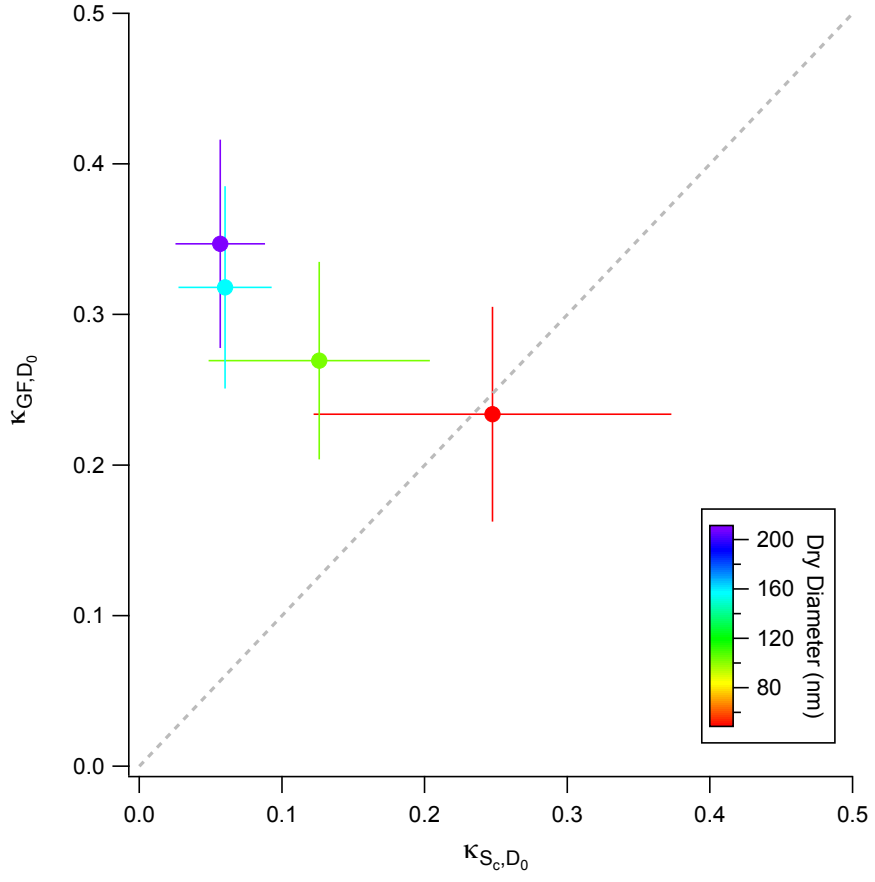


**Fig. 9.** $\kappa_{GF,D0}$ as measured from the HTDMA vs $\kappa_{Sc,D0}$ as measured by the CCNc, as a function of dry diameter. Note, the CCNc diameters are not on the same diameter base and have been binned as described in the main text.

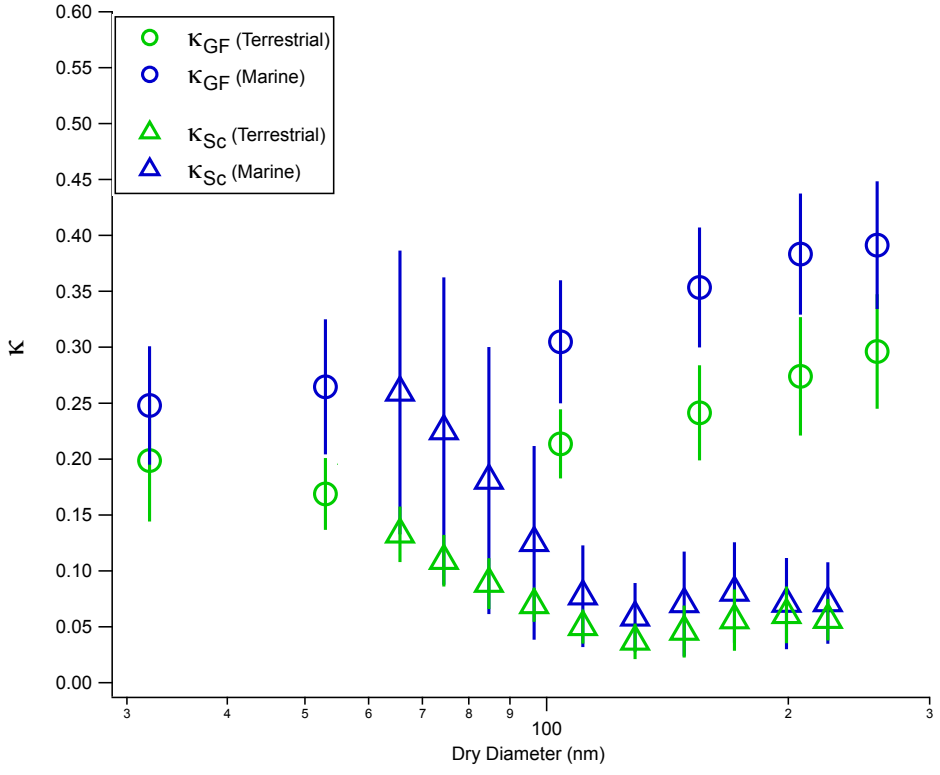


**Fig. 10.** $\kappa$ vs dry diameter, for the CCNc (triangles) and HTDMA (circles) measurements, both for *Terrestrial* (green) and *Marine* (blue) sectors.

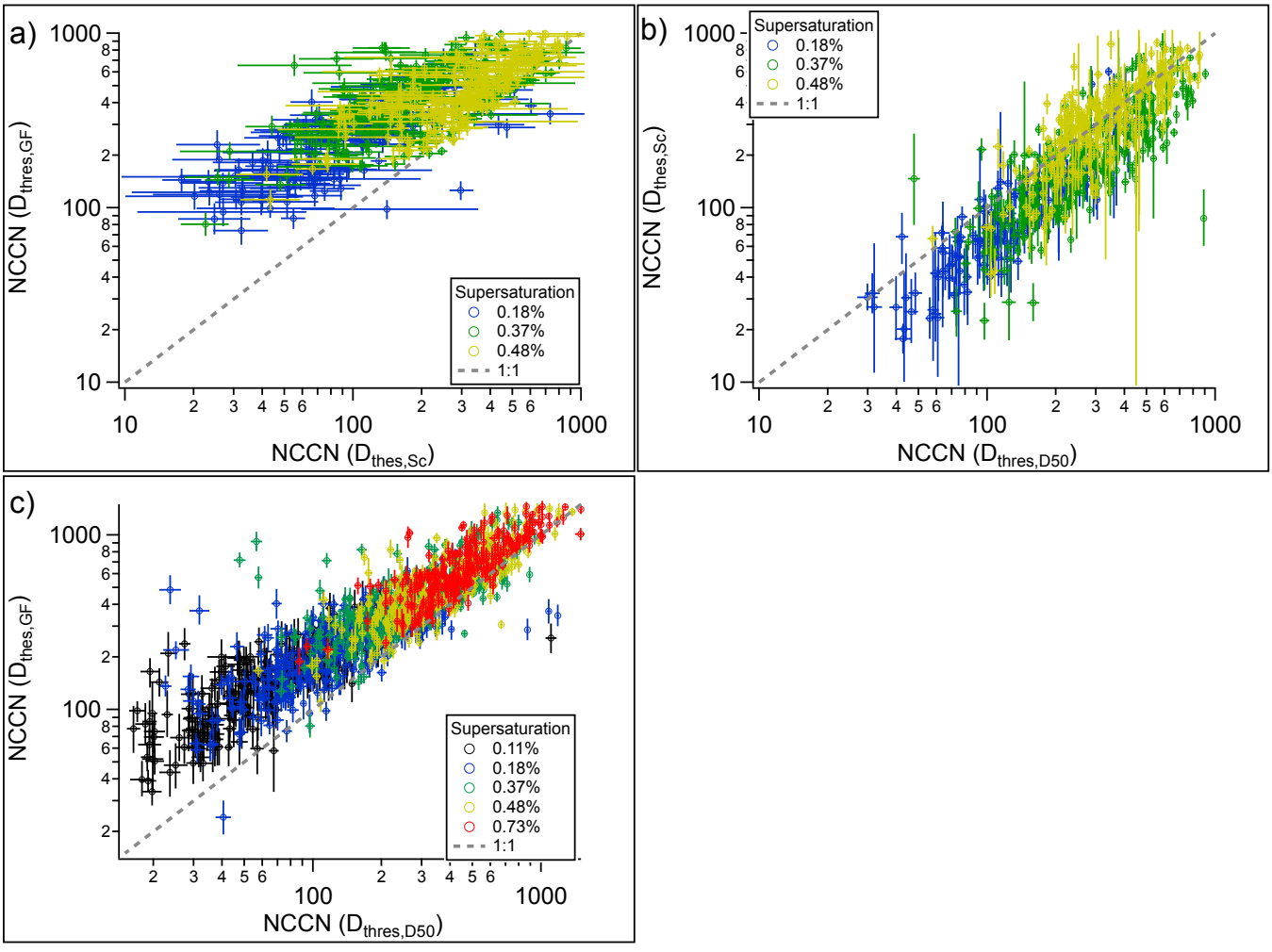


**Fig. 11.** $N_{CCN}$ vs $N_{CCN}$ for: a) HTDMA vs CCNc S-step analysis; b) CCNc S-step analysis vs CCNc D-step analysis; c) HTDMA vs CCNc D-step analysis

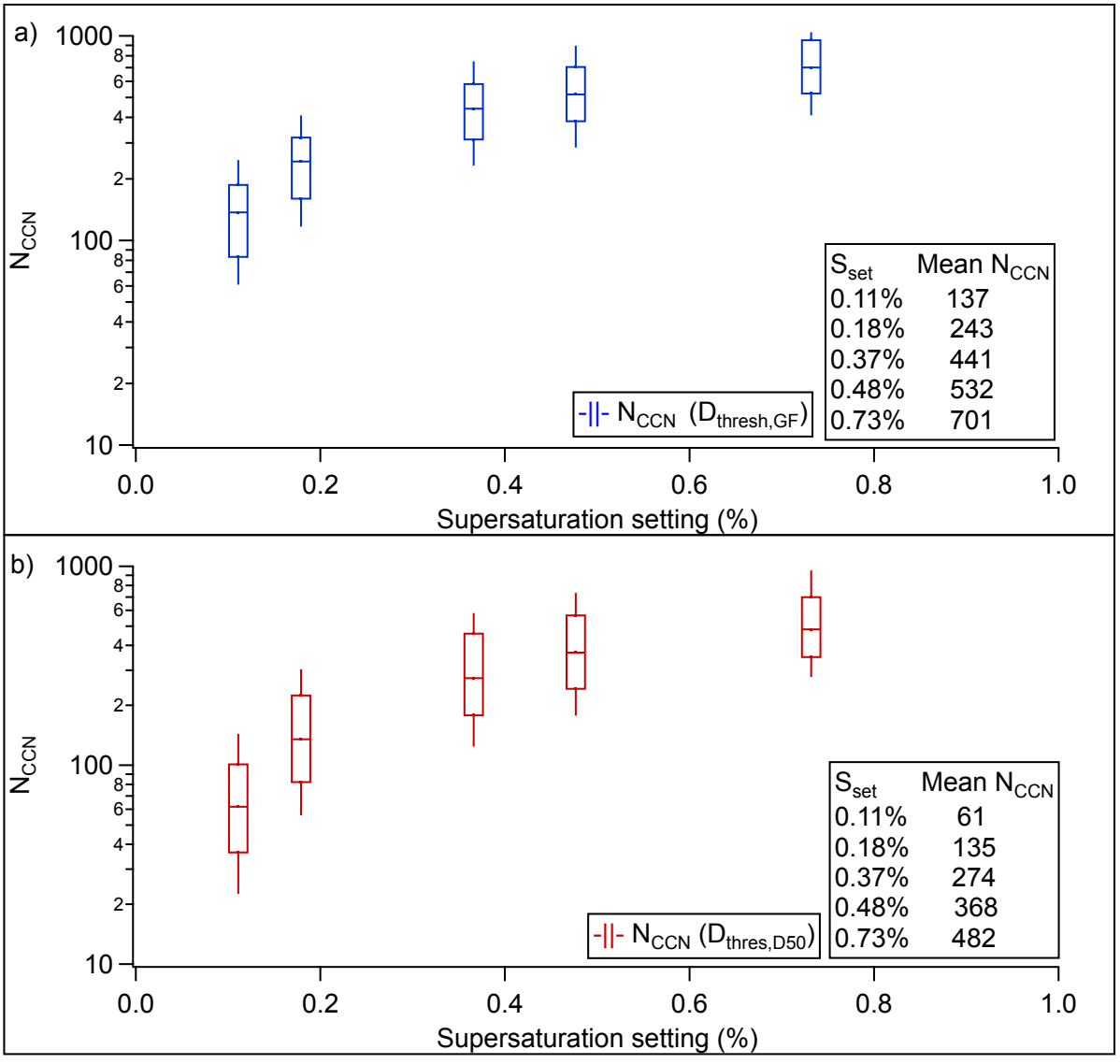


**Fig. 12.** $N_{CCN}$ vs $S_{set}$ for a) as derived from HTDMA data and b) derived from CCNc D-step analysis. The tables show the mean $N_{CCN}$ concentrations at each supersaturation.

## 5.4 Paper IV

Draft Title: **A multi-site study of the influences of number, size and composition in reconciling CCN concentrations**

In preparation for submission to Geophysical Research Letters.

# A multi-site study of the influences of number, size and composition in reconciling CCN concentrations

M. Irwin,[1] J. D. Allan,[1,2] N. Good,[1,3] M. Flynn,[1] N. Robinson,[1] G. McFiggans[1]

Identifying the relative importance of aerosol properties such as size and composition in determining cloud condensation nuclei (CCN) activity is fundamental to improving regional and global scale model CCN predictions. Here we present a multi-site CCN reconciliation study, comparing field measurements of the number of CCN ($N_{CCN}$) in three different environments to $N_{CCN}$ calculated under a number of scenarios, in order to test the sensitivity of the $N_{CCN}$ to the aerosol number-size distribution and composition. We find, in agreement with previous studies, that predictions based upon number-size distribution alone are capable of producing reasonable $N_{CCN}$ estimates, however the novel multi-site nature of this study demonstrates that deviations between predicted and measured $N_{CCN}$ were not consistent between different locations, and that the most successful reconciliations incorporated high temporal resolution, size-resolved hygroscopic growth factor measurements, CCN activity and the full aerosol number-size distribution. It is therefore necessary to fully characterise aerosol properties with size-resolved measurements in order to best represent regional differences in $N_{CCN}$.

## 1. Introduction

Significant uncertainties are associated with predicting the magnitude of the aerosol indirect effects on climate forcing. Changes to the number of cloud condensation nuclei ($N_{CCN}$) impact on various cloud properties, and several studies are currently focused upon developing the capability of regional and global models in predicting $N_{CCN}$ based on compositional information [e.g. WRF-Chem; Grell et al., 2005, GLOMAP; Spracklen et al., 2008]. An essential part of improving such models is understanding exactly how CCN activity, and thus $N_{CCN}$, relate to aerosol size and composition.

Anthropogenic perturbations to the number of CCN ($N_{CCN}$) can alter the cloud droplet number concentration (CDNC) [McFiggans et al., 2006], impacting on the aerosol indirect effects on climate [Twomey, 1977; Albrecht, 1989]. Increasing the CDNC results in more reflective clouds, though it has been shown that increasing $N_{CCN}$ does not necessarily lead to more cloud droplets, primarily due to the competition of water vapour experienced within a cloud [e.g. O'Dowd et al., 1999].

[1]School of Earth, Atmospheric and Environmental Sciences, The University of Manchester, Manchester, UK.

[2]National Centre for Atmospheric Science, The University of Manchester, Manchester, UK.

[3]now at: Laboratoire de Meteorologie Physique, Blaise Pascal Univ., 63000, Clermont Ferrand, France


0094-8276/10/$5.00

Numerous reconciliation studies have attempted to theoretically reproduce observed CCN concentrations with varying degrees of success [e.g. Roberts et al., 2002; Snider et al., 2003; Broekhuizen et al., 2006; Rissler et al., 2006; Medina et al., 2007; Gunthe et al., 2009]. It has been shown that the typical $20-50\%$ error in ambient CCN reconciliation studies results in a correspondingly lower, $10-25\%$, error in CDNC [Sotiropoulou et al., 2006].

Recent developments in measurement techniques have provided scope for a more in-depth examination of aerosol particle water uptake. In addition, single parameter approaches to describe particle hygroscopic behaviour, such as the $\kappa$-Köhler model, have recently become widely used [Petters and Kreidenweis, 2007]. This model has been shown to be sensitive to RH [Kreidenweis et al., 2008] and the aerosol mixing state [Wex et al., 2010], impacting on the predicted $N_{CCN}$ [e.g. Cubison et al., 2008].

In this work, measurements from three distinct field sites (continental, tropical and marine) are utilised in order to identify and rank the quantities that must be accurately reflected in order to predict $N_{CCN}$ correctly, with the ultimate long-term aim of improving the predictive capability of $N_{CCN}$ models. The Convective and Orographically-induced Precipitation Study [Wulfmeyer et al., 2008; Irwin et al., 2010b] measurements took place in continental Europe during July and August 2007 at a remote field site in the Black Forest, Southwest Germany. The Oxidant and Particle Photochemical Processes above a Southeast Asian tropical rainforest (Hewitt et al., 2010, Irwin et al., 2010c) measurements took place between March and July 2008 on the island of Borneo, Malaysia. The Reactive Halogens in the Marine Boundary Layer experiment (RHaMBLe), part of the part of the Aerosol Characterisation and Modelling in the Marine Environment (ACMME) study [Allan et al., 2009; Good et al., 2010], took place in May 2007 aboard the Discovery cruise D319 between England and the Cape Verde Islands.

We report here an analysis of hygroscopic reconciliation studies from these three projects using the $\kappa$-Köhler model, where the effects of assuming homogeneous aerosol composition and size distributions were explored through different averaging methods to evaluate their influence on $N_{CCN}$.

## 2. Measurements and Methods

For each project, size-resolved measurements of aerosol hygroscopic growth factor were made as a function of relative humidity using a Hygroscopic Tandem Differential Mobility Analyser (HTDMA), whilst CCN activity was measured as a function of supersaturations using a Cloud Condensation Nuclei counter (CCNc). Values of hygroscopic growth factor ($GF_{RH,D0}$) were defined as the ratio of the wet to dry particle diameter as measured sequentially by two differential mobility analysers at low and high RH (nominally $< 20\%$ and $\sim 90\%$). Values of the fraction of particles activated, $F_A$ was defined as the number of CCN divided by the number of condensation nuclei (CN) for a given size and supersaturation setting ($S_{set}$) range nominally $0.08-1\%$.

All measurements were performed for particles in the size range $20 - 350$nm dry ($< 20\%$RH) diameter.

Values of the hygroscopicity parameter $\kappa$ were calculated for corrected mean growth factor measurements as described by Equation 1:

$$S = \frac{\overline{GF}_c^3 - 1}{\overline{GF}_c^3 - (1-\kappa)} \exp\left(\frac{4\sigma_w M_w}{RT\rho_w D_0 \overline{GF}_c}\right) \quad (1)$$

where $S$ is the supersaturation (RH/100%), $\overline{GF}_c$ is the corrected mean growth factor, $\kappa$ is the hygroscopicity parameter, $\sigma$ is the surface tension of water, $M_w$ is the molecular weight of water, $R$ is the universal gas constant, $T$ is the temperature, $\rho_w$ is the density of water and $D_0$ is the dry diameter (from Irwin et al., 2010a).

To calculate $N_{CCN}$, the aerosol number-size distribution is integrated from the largest size to a threshold diameter for particle activation. The values of $\kappa$ were used to derive threshold diameters for activation for each $S_{set}$. Additionally, the threshold diameter was inferred from CCNc measurements as $D_{50,S}$, the diameter at which 50% of the particles activate for a given supersaturation, $S$. As this method gives high temporal resolution and captures changes in the threshold diameter due to particle composition changes without invoking the $\kappa$-model, it serves as a base measurement from which to compare other predictions of $N_{CCN}$.

Different approaches were used to investigate the relative importance of the aerosol number-size distribution and composition in the calculation of the NCCN for a given supersaturation. Five different methodologies were applied to each data set, averaging composition and number alternately for HTDMA and CCNc data, summarised in Table 1.

The effects of averaging the compositional influences on the calculated $N_{CCN}$ were investigated for CCNc and HTDMA data with methodologies M1 and M5 respectively, whereby the $D_{50,S}$ and $\kappa$ (i.e. the threshold activation diameters) were averaged for each $S_{set}$. Should such an approach adequately and systematically reconcile prediction and measurement, values of $\kappa$ could be approximated for different environments. However, it should be noted that these methods are ultimately sensitive to changes in the number size distribution throughout each measurement period, the sensitivities to which have been explored.

To investigate the impacts of assuming a 'typical' size distribution for a region, the aerosol number-size distribution was averaged for each study. $N_{CCN}$ was calculated for each derived threshold diameter from CCNc and HTDMA measurements respectively, describing methodologies M2 and M4 respectively. Finally, fully size-resolved reconciliation studies utilising both time resolved, derived threshold activation diameters and number-size distributions were performed for each of the experiments, denoted by M3 (described individually for COPS and OP3 by Irwin et al. [2010b] and Irwin et al., 2010c). The methodologies are summarised in Table 1.

## 3. Results

The predicted $N_{CCN}$ from each methodology were plotted against $N_{CCN}(D_{50,S})$, i.e. fully size and temporally resolved predicted $N_{CCN}$ from CCNc data. The slope has been calculated by fitting the data using orthogonal distance regression (ODR) constrained through the origin, in addition to the $r^2$ correlation fitted without constraint.

Though the absolute values of the slopes vary significantly between projects, similar trends, characteristic for each different methodology, were observed (see supplementary material for individual analysis figures). Each reconciliation method for RHaMBLe is shown as an example in Figure 1, and clearly demonstrates the trends characteristic of the different methodologies. The results of the slopes and $r^2$ correlation for the RHaMBLe reconciliation are summarised in Table 2. The results from COPS and OP3 are presented in the supplementary material, Figures S1 and S2 respectively. The results from each environment vary greatly in both terms of the slope and scatter of the data. Figure 2 shows the slope and correlation for M1 to M5 against supersaturation for each project. The size of the circle denotes the strength of the correlation, with the largest circles representing the best agreement.

The slope and correlation of M1 and M2 differ greatly, highlighting the sensitivity of $N_{CCN}$ to the shape of the aerosol number-size distribution. This difference is less pronounced for OP3 (Fig. S2), where there little difference in terms of slope, but a much weaker correlation. This is due to the high scatter of data from M1 and also indicates that the averaging the aerosol size distribution from OP3 has the least impact when compared to other environments. If the threshold diameter for activation is held constant (equivalent to assuming a single compositional component), then the slope and correlation are better than if the number-size distribution was assumed invariant for a region. This is because it is ultimately the total aerosol number size distribution that determines the upper limit for $N_{CCN}$ from any threshold diameter, invariant or otherwise.

In terms of HTDMA-CCNc hygroscopic reconciliation (i.e. M3 to M5), M3 consistently produced the best slope and correlation for all projects, through the use of individual $\kappa$ for each measurement to derive threshold diameters for activation from which $N_{CCN}$ is calculated for each measured size distribution. M4 suffers from the 'banding' artefact, such that a constant $N_{CCN}$ is calculated using the average size distributions for a wide range of $N_{CCN}$ derived from the unaveraged measurements, shown by M2, whereby the averaged aerosol number size distribution does not capture the variability in $N_{CCN}$ throughout a project. This is less sensitive at lower supersaturations for all environments, as there is typically a smaller fraction of activable particles as supersaturation decreases. Averaging the derived $\kappa$ values from the HTDMA measurements to predict $N_{CCN}$, as in M5, results in very similar behaviour to M3 (no averaging of data), though there is a reduction in correlation, most notably for COPS and OP3 (see supplementary material) and less so for the marine study, RHaMBLe. This reduced sensitivity could be attributed to the inorganic hygroscopic constituents dominating aerosol during the marine study, as aerosol with high inorganic content vary less in activation behaviour than for regimes dominated by organic components (COPS, OP3).

## 4. Discussion and Conclusions

The first two methods, M1 and M2 examine the relative importance of each individual $D_{50}$ measurement and each number-size distribution, respectively. M3-M5 investigate how the treatment of HTDMA data can influence reconciliation ability.

Attempts to reproduce the marine $N_{CCN}$ measured during the RHaMBLe project showed the most sensitivity to the aerosol number-size distribution, though for each project the correlation between measured and predicted values was always reduced when predictions were based on the averaged aerosol number-size distribution. Furthermore, this reduction leads to weaker reconciliation than if the threshold diameter for activation is averaged from each instrument

and $N_{CCN}$ calculated using individual number-size distributions. For COPS, $N_{CCN}$ was generally under-predicted, whereas for OP3, using HTDMA data typically led to an over-prediction whilst using CCNc data resulted in under-predictions (or is well correlated). The RHaMBLe measured and predicted $N_{CCN}$ correlate well at lower supersaturations whilst there tends to be an over-prediction at higher supersaturations. For each project, the variability in threshold diameter for activation at each supersaturation is significantly less than the variability in $N_{CCN}$ due to the aerosol number-size distribution.

The variable aerosol number-size distributions of M1, M3 and M5 give rise to a high amount of scatter with respect to each axis. Even if the threshold diameters for activation, *viz.* $D_{50,S}$ and $\kappa$, are kept constant, the variability in the aerosol number-size distribution results in a high amount of variability in calculated $N_{CCN}$. When the size distribution is a constant, i.e. campaign average, there is a ceiling $N_{CCN}$ that cannot be exceeded no matter what the derived threshold diameter. This results in the 'banding' shown by M2 and M4 for each campaign.

The results of these analyses are in agreement with the findings of Ervens et al. [2005], and confirm that is is necessary to capture the features of the aerosol size distribution in order to realistically describe cloud activation behaviour. Indeed, as highlighted by McFiggans et al. [2006], and in the continental study of Dusek et al. [2006], the greater influence of size compared to composition in determining the cloud droplet number illustrates that the aerosol size must be captured as a primary pre-requisite.

Our analysis reinforces the importance of measuring the aerosol number-size distribution at a high temporal resolution. However, corrections applied to HTDMA data to enable reconciliation with CCNc data for one experiment cannot be a priori applied in other experiments, as the deviation between the two measurements can be in either direction and is likely to differ in magnitude, depending on supersaturation. It must be stressed that although averaging composition (i.e. $D_{50}$ or $\kappa$) impacts less on $N_{CCN}$ compared to averaging the aerosol number-size distribution, high temporal resolution size-resolved measurements are still necessary to provide important information on the effects of composition on particle water uptake at a physical process level and should be included in order to achieve a full hygroscopic reconciliation. This approach provides constraints on the skill with which models that track composition and size-resolved distributions in either modal or sectional representations are able to replicate variations in $N_{CCN}$ on local and regional scales.

This study highlights the key constraints required to allow models to track composition and size resolved distributions in order to best replicate regional scale variability in $N_{CCN}$. Diagnostic testing of model predicted $N_{CCN}$ sensitivity to parameters such as size distribution must be used to determine whether a model predicts the right answer for the right reasons, or whether an apparent agreement between predicted and measured $N_{CCN}$ is simply fortuitous. Ultimately, these constraints may be incorporated into the larger scale models to address targeted questions regarding spatial and temporal CCN distributions.

**Acknowledgments.** The following projects were funded by the National Environmental Research Council (NERC): The Reactive Halogens in the Marine Boundary Layer experiment (RHaMBLe; NE/D006570/1), The UK Convective and Orographically-induced Precipitation Study (UK-COPS; NE/E016200/1) and the Oxidant and Photochemical Particle Processes above a Southeast Asian tropical rainforest project (OP3; NE/0021171/1). The Ph.D studentship of Martin Irwin was funded by NERC grant NER/S/A/2006/14036.

## References

Albrecht, B.: Aerosols, cloud microphysics, and fractional cloudiness, Science, 245, 1227–1230, 1989.

Allan, J. D., Topping, D. O., Good, N., Irwin, M., Flynn, M., Williams, P. I., Coe, H., Baker, A. R., Martino, M., Niedermeier, N., Wiedensohler, A., Lehmann, S., Müller, K., Herrmann, H., and McFiggans, G.: Composition and properties of atmospheric particles in the eastern Atlantic and impacts on gas phase uptake rates, Atmospheric Chemistry and Physics, 9, 9299–9314, doi:10.5194/acp-9-9299-2009, 2009.

Broekhuizen, K., Chang, R., Leaitch, W., and Li, S.: Closure between measured and modeled cloud condensation nuclei (CCN) using size-resolved aerosol compositions in downtown Toronto, Atmospheric Chemistry and Physics Discussions, 6, 2006.

Cubison, M. J., Ervens, B., Feingold, G., Docherty, K. S., Ulbrich, I. M., Shields, L., Prather, K., Hering, S., and Jimenez, J. L.: The influence of chemical composition and mixing state of Los Angeles urban aerosol on CCN number and cloud properties, Atmospheric Chemistry and Physics Discussions, 8, 5629–5681, doi:10.5194/acpd-8-5629-2008, 2008.

Dusek, U., Frank, G., Hildebrandt, L., Curtius, J., Schneider, J., Walter, S., Chand, D., Drewnick, F., Jung, D., Borrmann, S., and Andreae, M. O.: Size Matters More Than Chemistry for Cloud-Nucleating Ability of Aerosol Particles, Science, 312, 1375–1378, 2006.

Ervens, B., Feingold, G., and Kreidenweis, S.: Influence of water-soluble organic carbon on cloud drop number concentration, Journal of Geophysical Research-Atmospheres, 110, D18 211, doi:10.1029/2004JD005634, 2005.

Good, N., Topping, D., Allan, J., Flynn, M., Fuentes, E., Irwin, M., Williams, P., Coe, H., and McFiggans, G.: Consistency between parameterisations of aerosol hygroscopicity and CCN activity during the RHaMBLe Discovery cruise, Atmos. Chem. Phys., 10, 3189–3203, 2010.

Grell, G., Peckham, S., Schmitz, R., and McKeen, S.: Fully coupled "online" chemistry within the WRF model, Atmospheric Environment, 39, 6957–6975, 2005.

Gunthe, S., King, S., Rose, D., Chen, Q., Roldin, P., Farmer, D., Jimenez, J., Artaxo, P., and Aneae, M.: Cloud condensation nuclei in pristine tropical rainforest air of Amazonia: size-resolved measurements and modeling of atmospheric aerosol composition and CCN activity, Atmospheric Chemistry and Physics, 9, 7551–7575, 2009.

Hewitt, C. N., Lee, J. D., Mackenzie, A. R., Barkley, M. P., Carslaw, N., Carver, G. D., Chappell, N. A., Coe, H., Collier, C., Commane, R., Davies, F., Davison, B., Dicarlo, P., Marco, C. F. D., Dorsey, J. R., Edwards, P. M., Evans, M. J., Fowler, D., Furneaux, K. L., Gallagher, M., Guenther, A., Heard, D. E., Helfter, C., Hopkins, J., Ingham, T., Irwin, M., Jones, C., Karunaharan, A., Langford, B., Lewis, A. C., Lim, S. F., Macdonald, S. M., Mahajan, A. S., Malpass, S., McFiggans, G., Mills, G., Misztal, P., Moller, S., Monks, P. S., Nemitz, E., Nicolas-Perea, V., Oetjen, H., Oram, D. E., Palmer, P. I., Phillips, G. J., Pike, R., Plane, J. M. C., Pugh, T., Pyle, J. A., Reeves, C. E., Robinson, N. H., Stewart, D., Stone, D., Whalley, L. K., and Yin, X.: Overview: oxidant and particle photochemical processes above a south-east Asian tropical rainforest (the OP3 project): introduction, rationale, location characteristics and tools, Atmospheric Chemistry and Physics, 10, 169–199, doi:10.5194/acp-10-169-2010, 2010.

Irwin, M., Allan, J. D., and McFiggans, G.: Evaluation of errors in derived data products from water uptake measurements of atmospheric particulates, Atmos. Meas. Tech. Discuss., Submitted, 2010a.

Irwin, M., Good, N., and Crosier, J.: Reconciliation of measurements of hygroscopic growth and critical supersaturation of aerosol particles in Southwest Germany, Atmos. Chem. Phys. Discuss, 10, 17 073–17 111, 2010b.

Irwin, M., Robinson, N., Allan, J. D., Coe, H., and McFiggans, G.: Size-resolved aerosol water uptake and cloud condensation nuclei measurements as measured above a Southeast Asian rainforest during OP3, Atmospheric Chemistry and Physics Discussions, 2010c.

Kreidenweis, S., Petters, M., and DeMott, P.: Single-parameter estimates of aerosol water content, Environmental Research Letters, 3, 035 002, 2008.

McFiggans, G., Artaxo, P., Baltensperger, U., Coe, H., Facchini, M. C., Feingold, G., Fuzzi, S., Gysel, M., Laaksonen, A., Lohmann, U., Mentel, T. F., Murphy, D. M., O'Dowd, C. D., Snider, J. R., and Weingartner, E.: The effect of physical and chemical aerosol properties on warm cloud droplet activation, Atmospheric Chemistry and Physics, 6, 2593–2649, 2006.

Medina, J., Nenes, A., Sotiropoulou, R., and Cottrell, L.: Cloud condensation nuclei closure during the International Consortium for Atmospheric Research on Transport and Transformation 2004 campaign: Effects of size-resolved composition, J. Geophys. Res, 112, D10S31, 2007.

O'Dowd, C., Lowe, J., Smith, M., and Kaye, A.: The relative importance of non-sea-salt sulphate and sea-salt aerosol to the marine cloud condensation nuclei population: An improved multi-component aerosol-cloud droplet parametrization, Quarterly Journal of the Royal Meteorological Society, 125, 1295–1313, 1999.

Petters, M. and Kreidenweis, S.: A single parameter representation of hygroscopic growth and cloud condensation nucleus activity, Atmospheric Chemistry and Physics, 7, 1961–1971, 2007.

Rissler, J., Vestin, A., Swietlicki, E., Fisch, G., Zhou, J., Artaxo, P., and Andreae, M.: Size distribution and hygroscopic properties of aerosol particles from dry-season biomass burning in Amazonia, Atmospheric Chemistry and Physics, 6, 471–491, 2006.

Roberts, G., Artaxo, P., Zhou, J., Swietlicki, E., and Andreae, M.: Sensitivity of CCN spectra on chemical and physical properties of aerosol: A case study from the Amazon Basin, Journal of Geophysical Research-Atmospheres, 107, 8070, doi: 10.1029/2001JD000583, 2002.

Snider, J., Guibert, S., Brenguier, J., and Putaud, J.: Aerosol activation in marine stratocumulus clouds: 2. Köhler and parcel theory closure studies, J. Geophys. Res, 108, 8629, 2003.

Sotiropoulou, R., Medina, J., and Nenes, A.: CCN Predictions: Is theory sufficient for assessments of the indirect effect?, Geophysical Research Letters, 33, L05 816, 2006.

Spracklen, D. V., Carslaw, K. S., Kulmala, M., Kerminen, V.-M., Sihto, S.-L., Riipinen, I., Merikanto, J., Mann, G. W., Chipperfield, M. P., Wiedensohler, A., Birmili, W., and Lihavainen, H.: Contribution of particle formation to global cloud condensation nuclei concentrations, Geophysical Research Letters, 35, L06 808, doi:10.1029/2007GL033038, 2008.

Twomey, S.: Influence of Pollution on Shortwave Albedo of Clouds, Journal of the Atmospheric Sciences, 34, 1149–1152, 1977.

Wex, H., McFiggans, G., and Henning, S.: Influence of the external mixing state of atmospheric aerosol on derived CCN number concentrations, Geophysical Research Letters, 37, 2010.

Wulfmeyer, V, Behrendt, A., Bauer, H., Kottmeier, C., Corsmeier, U., Blyth, A., Craig, G., Schumann, U., Hagen, M., Crewell, S., Girolamo, P. D., Flamant, C., Miller, M., Montani, A., Mobbs, S., Richard, E., Rotach, M., Arpagaus, M., Russchenberg, H., Schlüssel, P., König, M., Gärtner, V., Steinacker, R., Dorninger, M., Turner, D., Weckwerth, T., Hense, A., and Simmer, C.: A research and Development Project of the World Weather research Program for Improving Quantitative Precipitation Forecasting in Low-Mountain regions, American Meteorological Society, 89, 1477–1486, 2008.

M. Irwin School of Earth, Atmospheric and Environmental Sciences, The University of Manchester, Manchester, UK, M139PL. (m.irwin@manchester.ac.uk)

G. McFiggans School of Earth, Atmospheric and Environmental Sciences, The University of Manchester, Manchester, M139PL, UK. (g.mcfiggans@manchester.ac.uk)

**Table 1.** Summary of the methodology of analyses

| Method | $\kappa_{GF}$ | $D_{50,S}$ | dNdLogDp |
|---|---|---|---|
| M1 | N/A | Averaged | Individual |
| M2 | N/A | Individual | Averaged |
| M3 | Individual | N/A | Individual |
| M4 | Individual | N/A | Averaged |
| M5 | Averaged | N/A | Individual |

**Table 2.** Methodology results for RHaMBLe

| S (%) | M1 Slope | M1 $R^2$ | M2 Slope | M2 $R^2$ | M3 Slope | M3 $R^2$ | M4 Slope | M4 $R^2$ | M5 Slope | M5 $R^2$ |
|---|---|---|---|---|---|---|---|---|---|---|
| 0.09 | 0.814 | 0.901 | 1.359 | 0.029 | 0.604 | 0.868 | 0.631 | 0.000 | 0.594 | 0.901 |
| 0.16 | 1.024 | 0.876 | 1.639 | 0.010 | 0.612 | 0.612 | 0.765 | 0.013 | 0.620 | 0.652 |
| 0.29 | 0.954 | 0.907 | 1.364 | 0.003 | 0.565 | 0.759 | 0.740 | 0.004 | 0.571 | 0.745 |
| 0.47 | 1.261 | 0.964 | 1.358 | 0.041 | 0.898 | 0.959 | 1.197 | 0.019 | 0.916 | 0.990 |
| 0.74 | 1.633 | 0.892 | 1.361 | 0.072 | 1.409 | 0.904 | 1.725 | 0.033 | 1.378 | 0.929 |

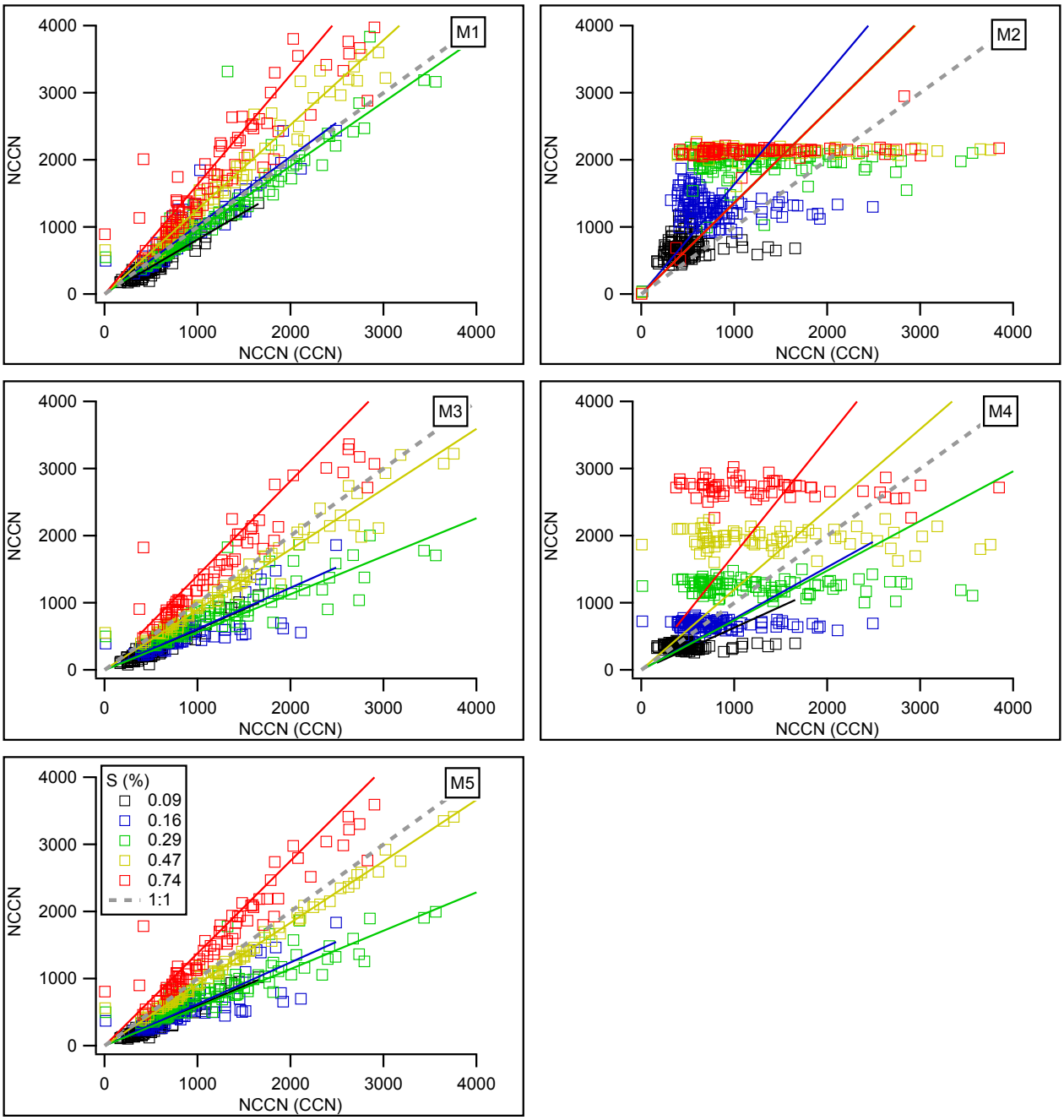


**Figure 1.** $N_{CCN}$ for each method M1-M5 plotted against $N_{CCN}$ from the CCN counter, for each $D_{50,S}$ during RHaMBLe

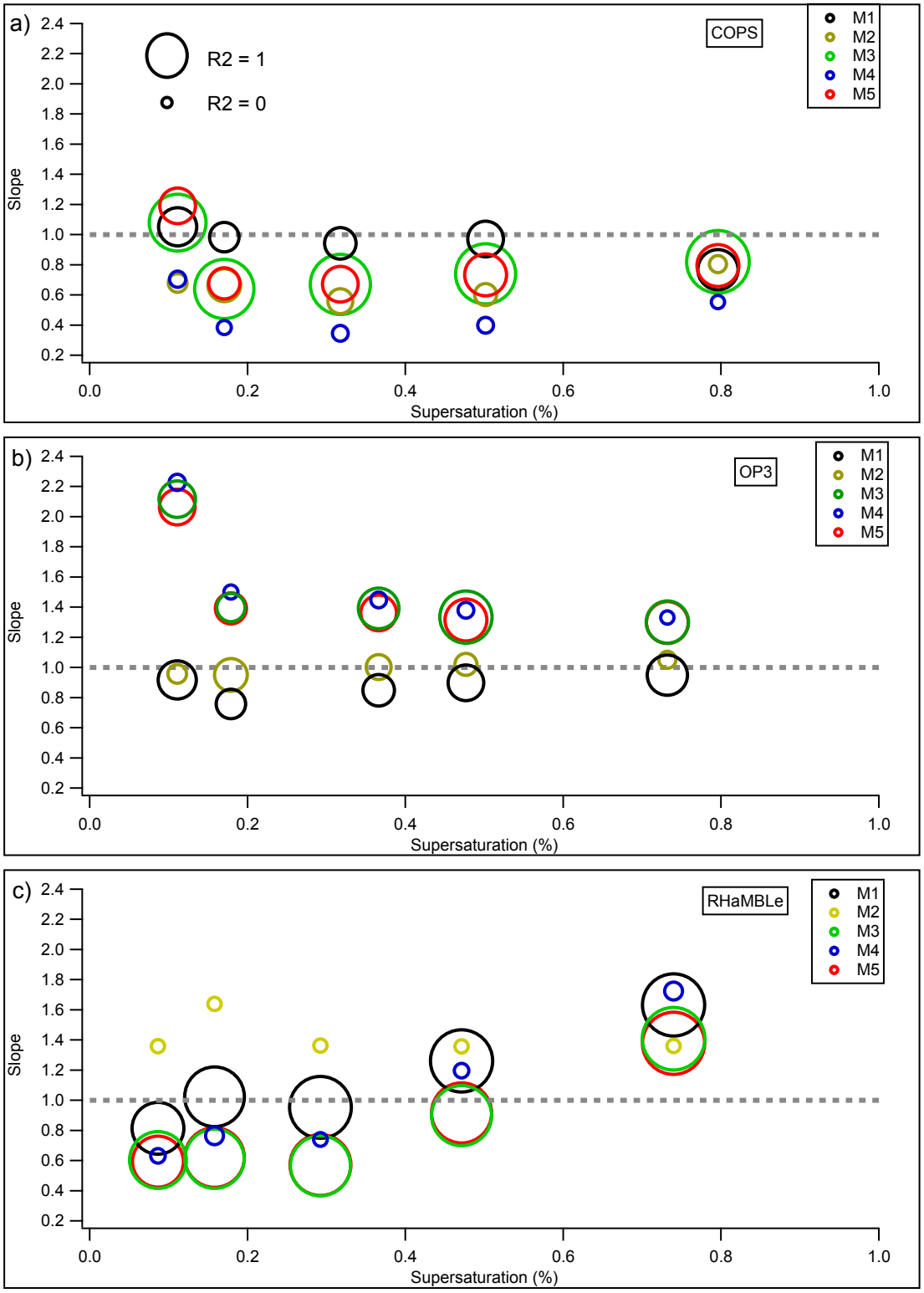


**Figure 2.** The slope of each methodology M1-M5 is plotted against supersaturation, with circles scaled to the $r^2$ of the fit (largest circle would be $R^2 = 1$ ) for each project; a) COPS, b) OP3 and c) RHaMBLe.

# 6 Appendix

## 6.1 CCNc Analysis Toolkit

At present, no standard for CCNc data analysis exists. Unlike bespoke HTDMA systems, the commercial success of the DMT-CCNc means that similar data-types are becoming increasingly ubiquitous in the field. Further to this, the analysis toolkit associated with TDMAinv from Gysel et al. (2009) allows for a consistent and reproducible set of analysis procedures. In order to successfully analyse CCNc data to a similarly high standard for multiple field projects in a timely fashion, it was necessary to develop a CCNc toolkit as part of this Thesis.

This appendix aims to highlight key features of the CCNc toolkit, hereafter referred to as *CIVET* (**C**CN **I**n**ve**stigational **T**oolkit). This toolkit is a work in progress, and any potential or current users should contact me regarding any updates to the software, or general usage queries.

### 6.1.1 Interface

CIVET runs using Igor Pro from Wavemetrics (www.wavemetrics.com). Igor Pro version 5 through to 6.1 have been verified to work consistently with CIVET. The CIVET package comprises multiple 'procedure' files, within which various analytical routines reside.

The majority of operations are conducted from the main panel. Version 1.00 of the main panel is shown in Figure A1. The panel is split into six main sections, each with a dedicated set of buttons and functions. The procedures can be worked through in steps, from 1 to 10, as labelled within the panel. In the following subsections, the purposes and functions behind each panel will be discussed.

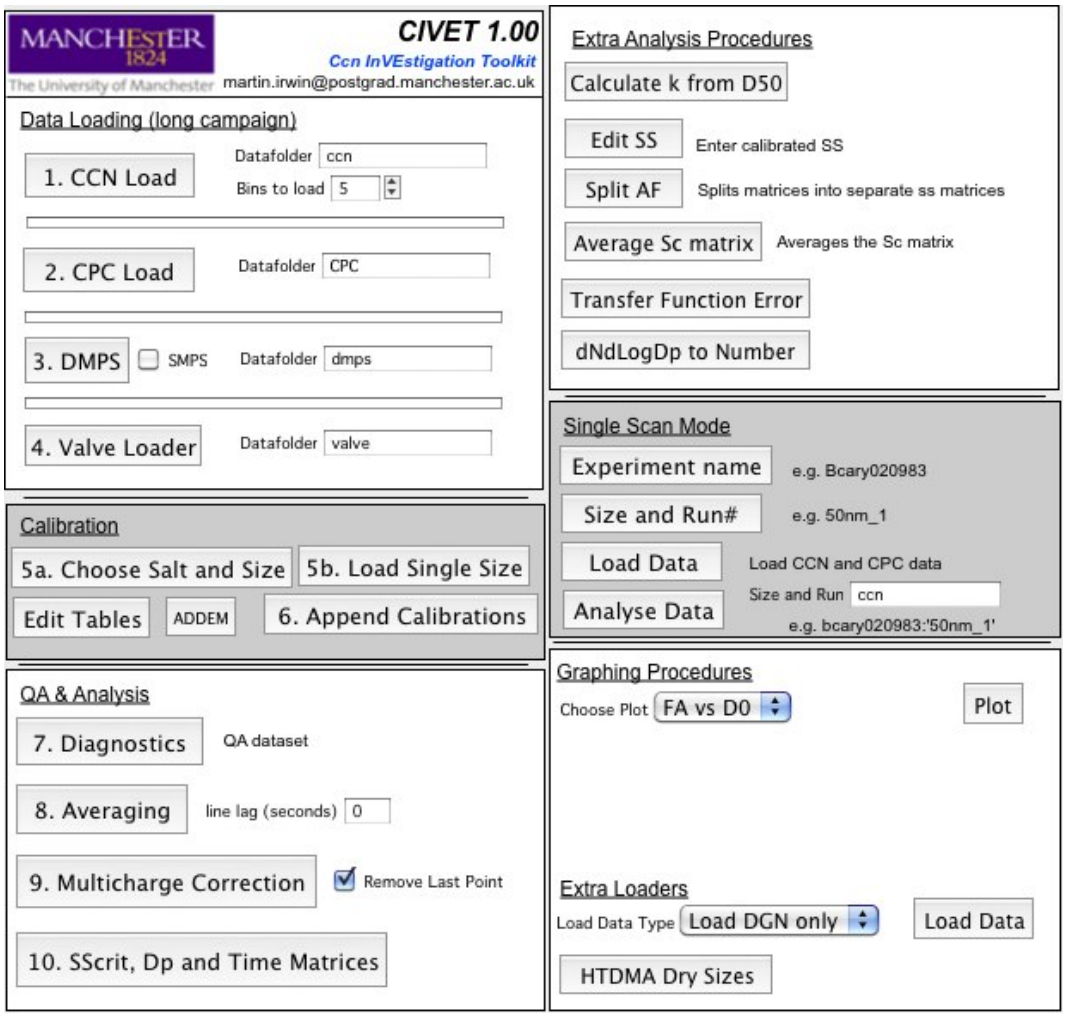


Figure A1: The CIVET main panel

### 6.1.2 Data Loading

Buttons 1–4 deal with the loading of various types of data and are self-explanatory. Upon clicking each button, the user must direct the software to a folder containing the data to be loaded.

**1. CCN Load**: This button specifically loads CCN data in the format output by DMT's 3.0–4.0 software packages. The number of bins to be loaded from the CCN histogram can be chosen, in addition to the repository folder within Igor (default is root:ccn).

**2. CPC Load**: This button loads time, date and number concentration data from a CPC file in the style of those from Holme Moss 2006, RHaMBLe and

COPS campaigns (due to being written during those campaigns). Should data not be in this format, it must be changed into this format prior to loading into the CCN toolkit. The CPC flow rate, in $\mathrm{Lmin}^{-1}$ must also be entered at the appropriate dialogue box.

**3. DMPS Load**: This button loads DMPS *.CCN* files only. A button can be checked if the data is the same as that collected during the OP3 campaign, where an SMPS with customised software was used to record the different aerosol dry diameter and voltage settings.

**3. Valve Load**: This button was designed for the loading of valve data from the RHaMBLE and COPS campaigns. If no data exists, "No Valve Data" can be chosen and a mask wave will be created.

### 6.1.3 Calibration

As described in detail in the papers, CCNc calibration is performed with both sodium chloride and ammonium sulphate, though the ammonium sulphate measurements are used to verify the calibration against the ADDEM data, as sodium chloride has an associated shape factor, and the high hygroscopicity of NaCl makes it harder to probe the $S_c$ of diameters larger than 100nm.

**5a. Choose Salt and Size**: This button creates a set of folders within the root: directory, based on which salt is chosen via a drop-down menu, and which dry diameter is entered into the dialogue box.

**5b. Load Single Size**: As the calibrations are performed manually, rather than as part of an automated system, each cycle of S-steps from the CCNc and CPC data must be loaded individually, for each size. Once the data is loaded, the user is greeted with Figure A2.

Figure A2 shows an example of the Fraction of Activated aerosol plotted against time for a calibration of the CCNc. Supersaturation setting is shown on the right axis. This graph illustrates the settling time at each supersaturation well. As the supersaturation setting (literally the temperature difference down the colulmn at this point, as outlined in Paper I) is increased from 0.11% to 0.12%, the activated fraction of aerosol jumps to over 0.5, indicating that the critical supersaturation is below this value.

In order to evaluate the critical supersaturation, multiple stepping cycles are performed for each dry diameter (there must be at least three dry diameter measurements). A graph marquee is drawn by hand around data which is deemed

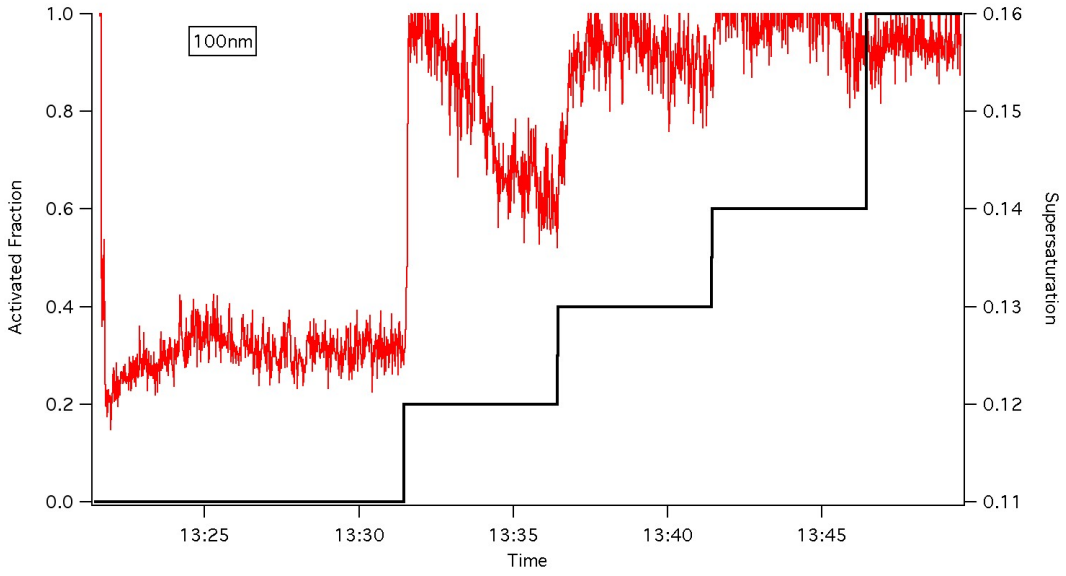


Figure A2: The fraction of aerosol activated is plotted against time and supersaturation.

to have settled at each supersaturation, and the contextual menu 'CCN Stats' is then clicked, which brings up another graph, showing the activated fraction against supersaturation, an example of which is shown in Figure A3.

Once the critical supersaturation for at least three dry diameters is derived and entered into the tables, which can be accessed at any time by clicking the **Edit Tables** button within the main panel. Once all sizes have associated sigmoid fits and critical supersaturations, clicking the **ADDEM** button plots these values against the ADDEM model for each respective dry diameter (shown by Fig. A4), and also displays the raw calibration with the ADDEM model on a $S_c$ vs $D_0$ plot (Fig. A5).

The code below takes the supersaturation setting data for the entire experiment and adjusts the values to bring them in line with the calibrations:

```
ss_setting[i]=(ss_setting_raw[i]-w_coef[0])/w_coef[1]
```

where $i$ is the number of points within the supersaturation wave (i.e. number of seconds of measurement), and w-coef[0] and w-coeff[1] are the output coefficients of the striaght line plotted in Fig. A4.

Once the supersaturation has been calibrated, the data is ready for quality assurance.

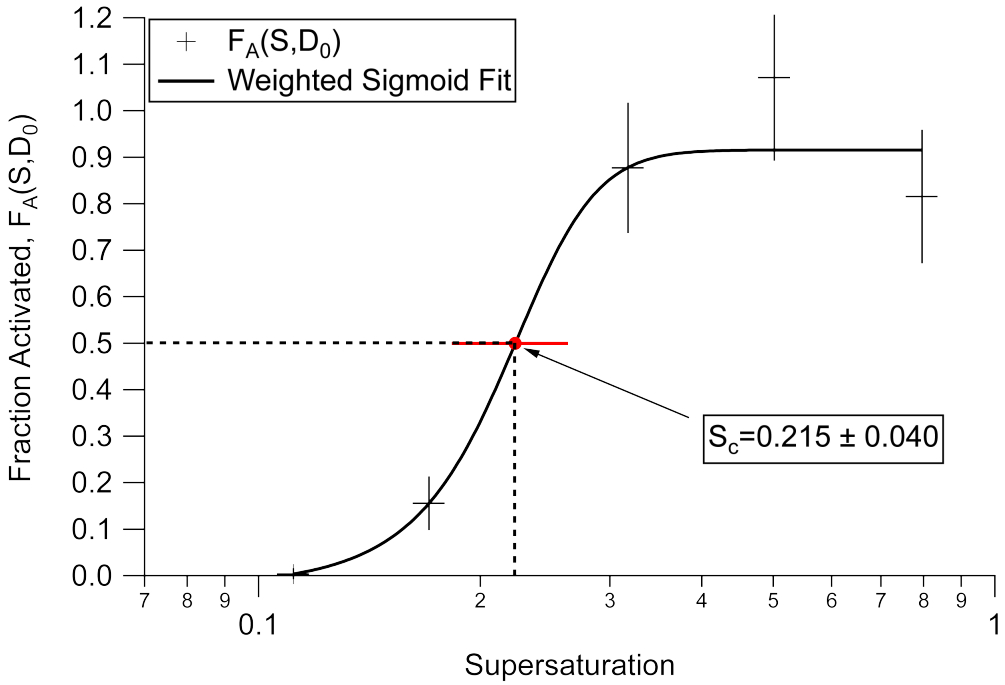


Figure A3: The fraction of aerosol activated is plotted against supersaturation, to derive the critical supersaturation (using the sigmoid function discussed in Papers I, II and III)

### 6.1.4 QA & Analysis

**7. Diagnostics**: This button performs a procedure to 'binarysearch' all of the different instrument data onto the same timebase; that of the CCNc. The net result is data waves of equal length, which allow for simple and quick graphical comparisons and the pruning of erroneous data.

**8. Averaging**: The data is then averaged such that each dry diameter measurement corresponds to one data point, and has associated CCNc and CPC number waves. The *line lag* parameter is used to account for any delay between the particles leaving the DMA and entering the CCNc column. This must estimated prior to measurement, with the use of a CPC counter. It is simple to spot this line lag if the dry diameter of a calibration aerosol is changed dramatically, as it will take a few seconds for the new aerosol population to reach the CPC counter.

**9. Multicharge Correction**: The CCNc and CPC data are corrected for multiple charges (up to three in the current toolkit) as outlined in Sect. 2.1.2 and Paper I. The 'Remove Last Point' checkbox will remove the last data point from

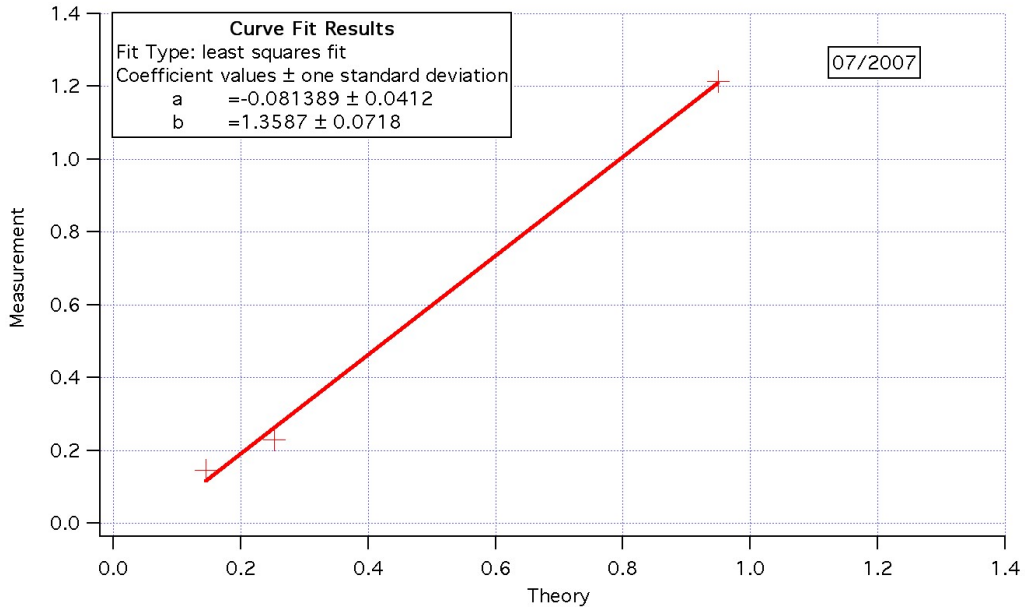


Figure A4: Derived critical supersaturation is plotted against ADDEM predicted critical supersaturation, resulting in the calibration coefficients shown in the textbox.

the analysis (i.e. largest measured diameter) if it is deemed to carry more than a single charge, after DMPS analysis.

**10. SScrit, Dp and Time Matrices**: The data is then placed into the 'root:multicharged' directory, whereby $S_{c,D_0}$ is derived for the data set, through the fitting of error-weighted sigmoidal functions to the activated fraction data array. The errors are have been derived from measurements such as flow, number concentration and temperature, as outlined in detail in Paper I.

### 6.1.5 Extra Analysis Procedures

This part of the toolkit is reserved for procedures that supplement the main core of the analysis toolkit, such as the calculation of $\kappa$ values from $D_{50,S}$ data as described in Paper I. **Edit SS** brings up a table into which the calibrated supersaturations should be entered. Then, clicking **Split AF** will 'split' the Activated Fraction, CCN, CPC, Diameter and Time matrices, according to their supersaturation. This procedure is useful if the wanting to either plot graphs or average data with respect to supersaturation. **Average Sc Matrix** will bring up a dialogue box, into which the number of hours of desired averaging is entered.

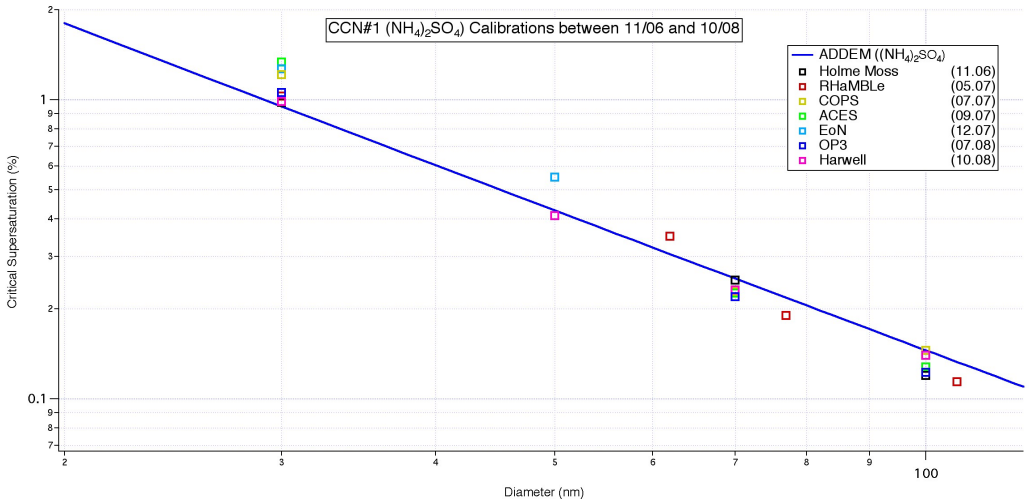


Figure A5: A plot of $S_c$ vs $D_0$ for Ammonium Sulphate calibrations of the DMT-CCNc between 11/06 and 10/08.

The $S_c$ measurements are typically performed on an hourly timebase, so values lower than 1 hour cannot be used. **Transfer Function Error** will output to the command line, one standard deviation of the diameter width associated with an ideal transfer function for a selected dry diameter. **dNdLogDp to Number** converts a dNdLogDp matrix to one containing counts, or vice versa depending on user requirements.

### 6.1.6 Single Scan Mode

The buttons here use almost identical procedures to those previous discussed in the calibration section. This panel was developed for a novel type of measurement associated with the aerosol chamber, whereby it was not possible to have a toolkit process entire experiments' worth of data, due to the ad-hoc nature of data collection.

### 6.1.7 Graphing Procedures

This drop-down menu enables the plotting of various graphs, such as fraction activated vs dry diameter, which is used to calculate $D_{50,S}$. Figure A6 shows an example scan, the panel of which has a slider along the top, to quickly navigate through the data set. Should data appear erroneous, a 'bad run' checkbox can

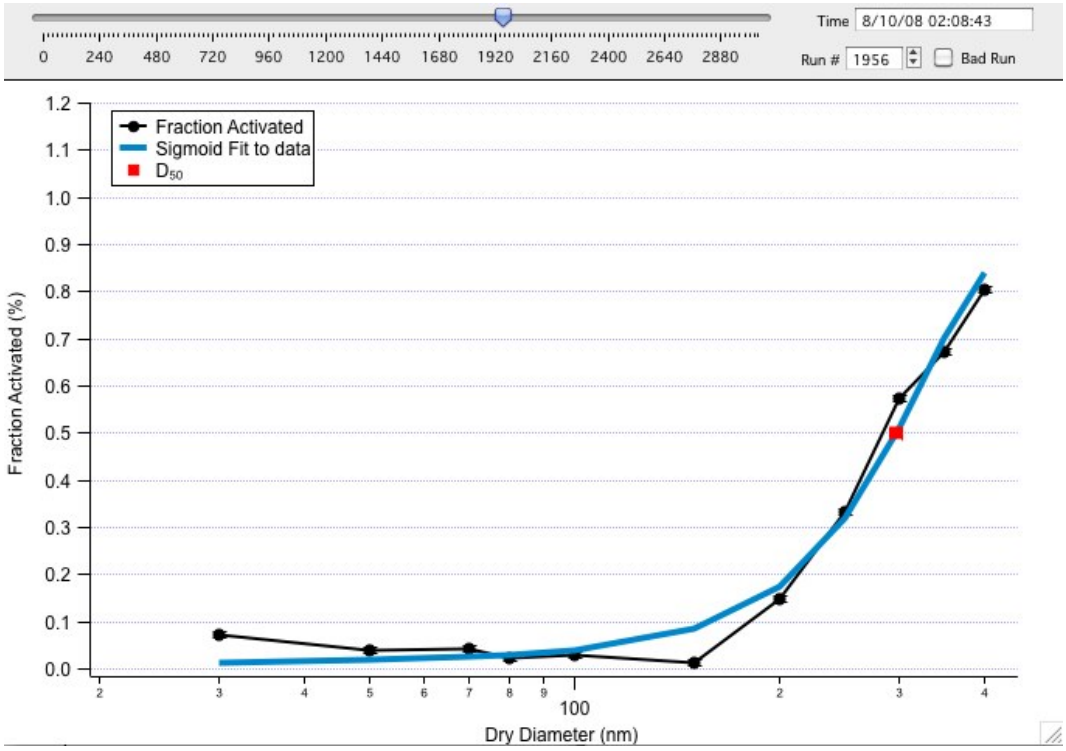


Figure A6: A example plot of $F_A(S, D_0)$ vs $D_0$ for ambient CCNc measurements.

be ticked, which then changes a mask wave, which is used by other functions (such as $\kappa$ derivations and $N_{CCN}$ calculations). This procedures was written with large-scale batch processing in mind, as the findings of Paper I and subsequent papers illustrate that $D_{50,S}$ results in the best quality CCNc data.

### 6.1.8 Extra Loaders

Further loading procedures have also been written for DMPS data, chamber data and HTDMA data. There are many other numerous pieces of code and procedures that come as part of the CCNc toolkit and will be expanded or explained in a CCNc users manual in the near future.

CIVET will undergo significant improvements over the coming months, and any user feedback is always appreciated.

## 6.2 Supplementary material for Paper II

# 1 Definition of terms and calculation procedures

## 1.1 HTDMA errors

The hygroscopic growth factor probability distribution $p(GF)$ was corrected for small deviations (typically ±2%RH) from the setpoint RH, as outlined by Gysel et al. (2009) and calculated as follows:

$$\overline{GF}_{D_0,RH,c} = \left(1 + (\overline{GF}^3_{D_0,RH_m} - 1)\frac{(1-RH_m)RH_t}{(1-RH_t)RH_m}\right)^{\frac{1}{3}} \quad \text{(S1)}$$

where $\overline{GF}_{D_0,RH,c}$ is the RH-corrected, mean, hyrgoscopic growth factor for a particle of dry diameter $D_0$, $\overline{GF}_{D_0,RH_m}$ is the uncorrected mean growth factor, $RH_m$ is the measured $RH$ and $RH_t$ is the target $RH$. A full explanation of the correction applied is described by Gysel et al. (2009).

In order to propagate the error associated with the change in growth factor from this correction, Eq. S1 is differentiated with respect to $RH_m$ to give:

$$\frac{\partial(\overline{GF}_{D_0,RH,c})}{\partial(RH_m)} = -\left((\overline{GF}_{D_0,RH_m} - 1)\frac{RH_t}{(1-RH_t)}\frac{1}{(RH_m)^2}\right)^{-\frac{1}{3}} \quad \text{(S2)}$$

An error simulation which forms part of the TDMAinv analysis was used on the data, with the results from the error simulation showing the sensitivity of the inversion result to small changes in the measurement due to added noise (incorporating counting statistics). This helps in, for example, judging whether two peaks in the growth factor probability distribution function, $p(GF)$, can be attributed to distinct modes or whether the structure of the $p(GF)$ can be reliably attributed to distinct modes or whether they are indistinguishable from instrument noise. This is outlined in detail by Gysel et al. (2009) and is shown in Figs. 4B and C therein. 100 error simulations are performed on $p(GF)$ for each growth factor bin, and the statistical mean of these taken. The standard deviation of the mean 100 simulations was then calculated, representing the effects of counting statistics and variability in size measurement, denoted by $\sigma_{p(GF)}$. These two errors are summed in quadrature, representing the HTDMA error, $GF_{error}$:

$$GF_{error} = \sqrt{\left(\frac{\partial(\overline{GF}_{D_0,RH,c})}{\partial(RH_m)}0.015\right)^2 + {\sigma_{p(GF)}}^2} \quad \text{(S3)}$$

where 0.015 relates to the precision of the measurement of $RH$ (1.5%) within the HTDMA used for the COPS experiment.

## 1.2 Fitting S-step and D-step CCNc data

Defined in the main text, the fitting function used for deriving the point at which $F_A(S, D_0) = 0.5$ is a sigmoidal function using orthogonal distance regression

(ODR), weighted according to the associated errors in each axis, using the Igor Pro software package and associated libraries (*ODRPACK95*, Boggs et al. 1989).

$$y = K_0 + \frac{K_1}{1 + \exp\left((x - K_2)/K_3\right)} \tag{S4}$$

Where $K_0$ is the base of the sigmoid (held to zero), $K_1$ is the maximum on the sigmoid (unconstrained to to minimise effects caused by systematic inaccuracies of either instrument), $K_2$ is the $x$ value at which $y = 0.5$ (either, $D_{50,S}$ or $S_{c,D0}$, depending on the x-axis used) and $K_3$ is the rate.

This function is used to derive both $D_{50,S}$ and $S_{c,D0}$ for CCNc data. An example of the sigmoidal fitting to D-step and S-step interpreted data is presented in Figure S1. The fitting algorithm outputs a standard error of the x-axis value at $y = 0.5$. This is the error propagated through further calculations of quantities such as $D_{thres}$ and $N_{CCN}$. S-step analysis is more sensitive to the relative positions of the data as there are only 5 data points (Fig S1a). Fitting D-step interpreted data with the sigmoidal function results in fit approaching a step function (Fig S1b).

## 1.3 CCNc Measurement Uncertainty

### 1.3.1 Uncertainty in $S_{set}$

In order to estimate the uncertainty in $S$ from the standard deviation of these quantities, the standard deviation ($\sigma$) of each measurement of temperature, flow and pressure ($T, Q$ and $P$ respectively, which are taken to vary independently) is multiplied by its differential value, summed in quadrature and divided by the square root of the number of observations ($N$; number of particles measured during an averaging period) to give the standard error in $S$:

$$\Delta S = \frac{\sqrt{\left(\frac{\partial S}{\partial T}\sigma T\right)^2 + \left(\frac{\partial S}{\partial Q}\sigma Q\right)^2 + \left(\frac{\partial S}{\partial P}\sigma P\right)^2}}{\sqrt{N}} \tag{S5}$$

The dependence of $\Delta S$ on $\sqrt{N}$ arises because the instrument detector (the OPC) only samples the conditions when a particle is detected. As $T$, $Q$ and $P$ have been assumed to vary randomly throughout the measurement period, the more particles detected, the more precise the average supersaturation will be.

### 1.3.2 Uncertainty in $D_0$

The range of diameters introduced into the CCNc for a given target diameter is described by the DMA transfer function. For this analysis, we have assumed an ideal, triangular transfer function (Knutson and Whitby, 1975), with symmetrical bounds 5% either side of the target dry diameter, $D_T$. One standard deviation of this transfer function is described by $\sigma = c\sqrt{1/6}$, where $c = 0.1D_T$ i.e. the width of the base of the transfer function. When propagating the error

associated with the diameter measurement of $D_T$, the standard error of $D_T$ has been used:

$$\Delta D_T = \frac{c\sqrt{(1/6)}}{\sqrt{N}} \tag{S6}$$

where $N$ is the number of particles counted.

### 1.3.3 Uncertainty in number concentration

The CCNc and CPC number concentration standard errors have been calculated by invoking Poisson statistics:

$$\Delta(\sum N) = \sqrt{\frac{\sum N}{Q \sum T}} \tag{S7}$$

where $N$ is the number of particles counted, substituted by either CCNc ($N(S, D_0)$) or CPC ($N(D_0)$), $Q$ is the flow rate and $T$ is the sampling time. The uncertainty in $N$ is calculated and then propagated through the multiple charging correction procedure.

The error associated with the activated fraction, $F_A(S, D_0)$ can then be calculated:

$$\Delta(\sum F_A(S, D_0)) = \frac{N(S, D_0)}{N(D_0)} \sqrt{\left(\frac{\Delta(\sum N(S, D_0))}{N(S, D_0)}\right)^2 + \left(\frac{\Delta(\sum N(D_0))}{N(D_0)}\right)^2} \tag{S8}$$

# References


[Boggs et al. (1989)] Boggs, P., Donaldson, J., Byrd, R., and Schnabel, R.: Algorithm 676: ODRPACK: software for weighted orthogonal distance regression, ACM Transactions on Mathematical Software (TOMS), 15, 364, 1989.

[Gysel et al. (2009)] Gysel, M., McFiggans, G., and Coe, H.: Inversion of tandem differential mobility analyser (TDMA) measurements, Journal of aerosol science, 40, 134–151, 2009.

[Knutson and Whitby (1975)] Knutson, E. and Whitby, K.: Aerosol classification by electric mobility: apparatus, theory, and applications, Journal of Aerosol Science, 6, 443–451, 1975.

[Rose et al. (2008)] Rose, D., Gunthe, S., Mikhailov, E., Frank, G., and Dusek, U.: Calibration and measurement uncertainties of a continuous-flow cloud condensation nuclei counter (DMT-CCNC): CCN activation of ammonium sulphate and sodium chloride particles in theory and experiment, Atmos. Chem. Phys, 8, 1153–1179, 2008.

## 2 Supplementary Figures

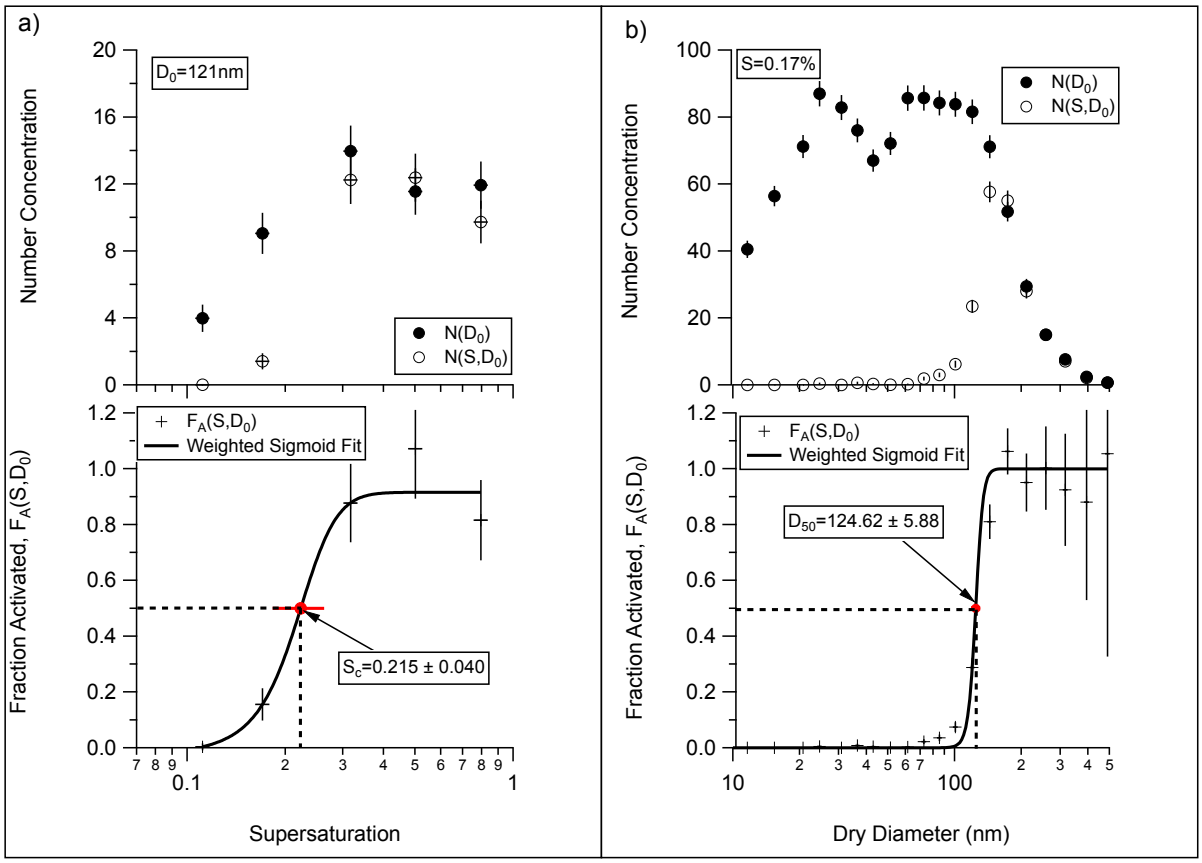


Figure S1: a) S-step interpreted data for $D_0 = 121$ nm, showing the relative number concentrations from CCNc and CPC, with their respective uncertainties in the top panel, and the bottom panel showing the sigmoid fit to $F_A(S, D_0)$ vs $S_{set}$. b) D-step interpreted data for the supersaturation setting 0.17%, illustrating the almost step-function sigmoidal fit to the D-step analysis, and subsequently reduced uncertainty.

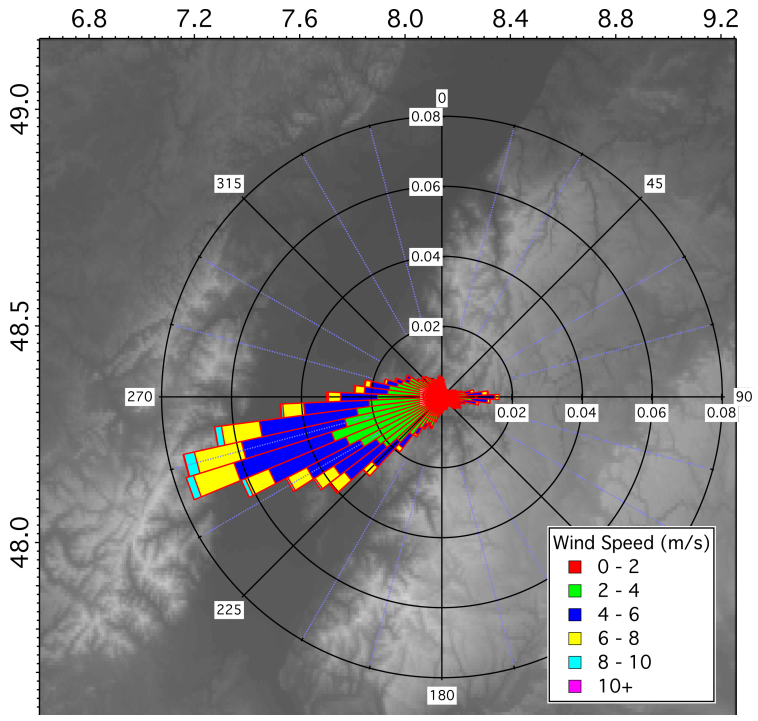


Figure S2: Wind rose centred on measurement location. The prevailing wind passing up the Rhine valley into the COPS region at around 5m/s average wind speed (measured at 1166m ABSL, 2m AGL).

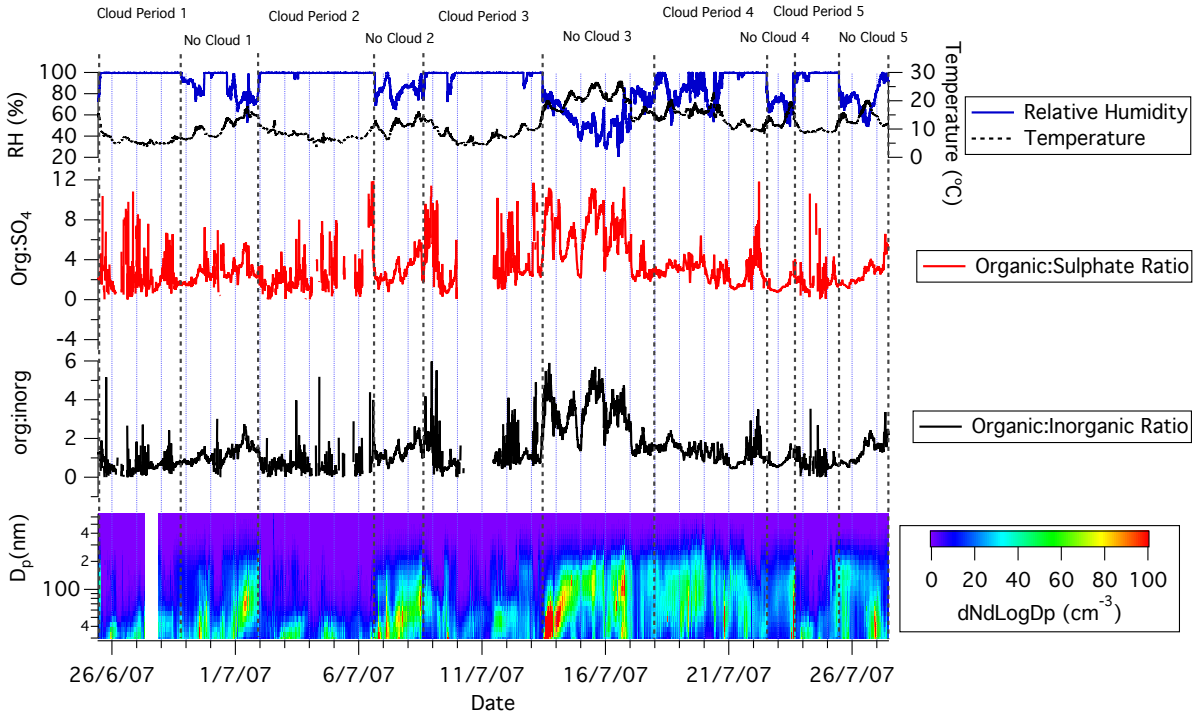


Figure S3: Relative Humidity ($RH$), organic:sulphate ratio, organic:inorganic ratio and $dNdlogDp$ for the measurement period, segregated into "cloud periods" and "no cloud" periods. Cloud periods are defined by $RH \geq 85\%$ and are characterised by a low organic:inorganic ratio and typically relatively low number concentrations ($D_0 < 600$ nm). 'No cloud' periods are characterised by higher a organic:sulphate ratio and tend to start with high concentrations of small ($\leq$ 40nm particles, which grows into a large ($\approx$150nm), strongly monomodal size distribution.

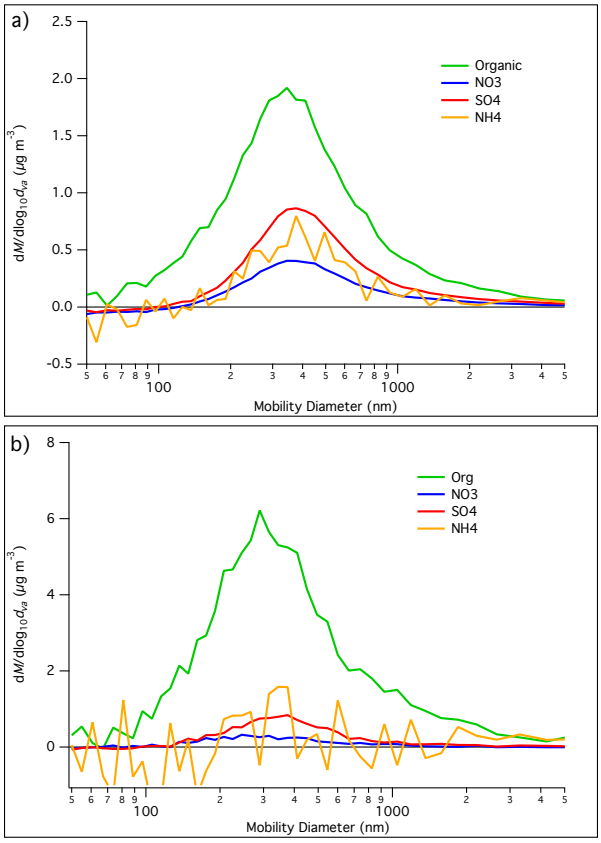


Figure S4: Size resolved AMS data for both a) $\leq$ 4:1 and b) $\geq$ 4:1 organic:sulphate ratio periods. The high organic to sulphate ratio periods (b) show a dramatic relative increase in organics above 100nm, with the majority of the organic fraction around 300nm.

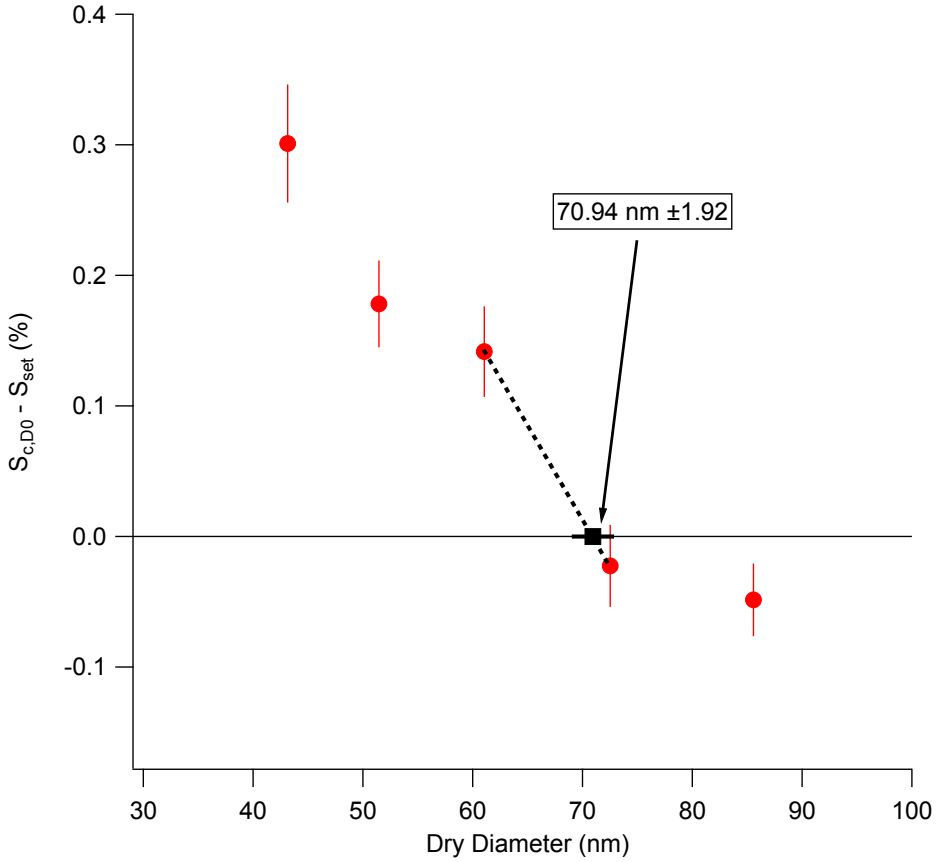


Figure S5: A graph showing $S_{c,D_0} - S_{set}$ vs $D_0$. The two data points straddling the zero line are linearly interpolated between, with the intercept defining the physical threshold diameter of the aerosol, $D_{thres,Sc}$. The errors on $D_{thres,Sc}$ are propagated using standard procedure.

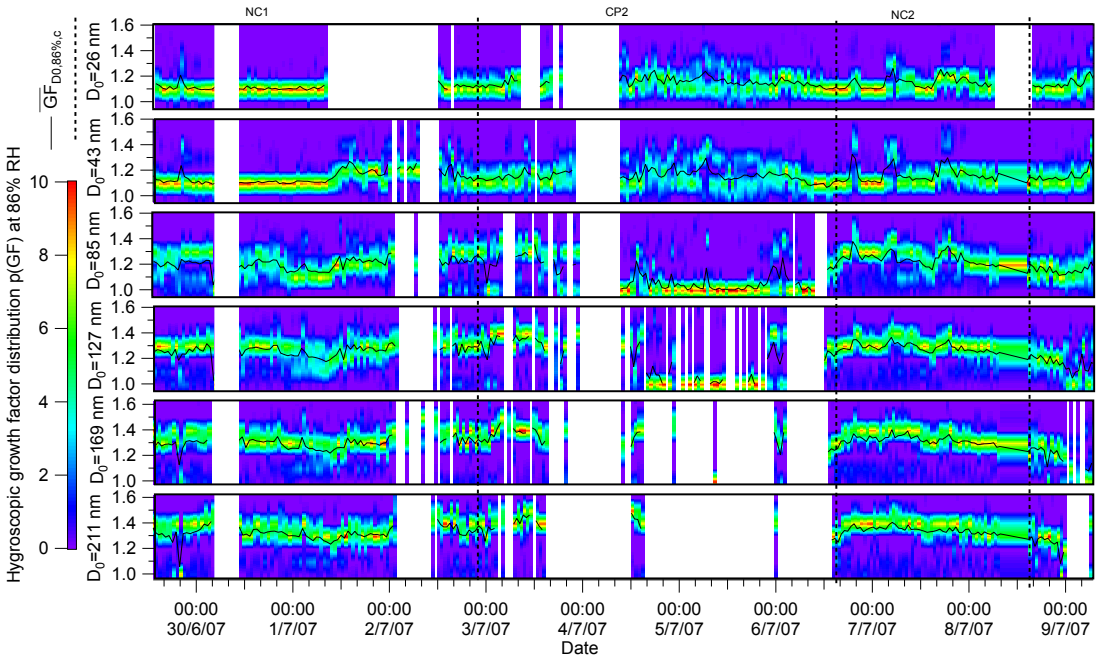


Figure S6: A reproduction of Figure 1, focussed on NC1 through NC2, showing measured HTDMA hygroscopic growth factor probability distribution, $p(GF)$, as a function of time. It can be seen that the HTDMA growth factor distribution is typically well represented by the mean growth factor, $GF_{D0,86\%,c}$, though there is an increasing prominence of bimodality seen with an increase of size.

## 6.3 Supplementary material for Paper III

**Supplementary Material to OP3 CCN-HTDMA Reconciliation Study**

**Section 1.1** shows the sigmoid function used to derive both critical supersaturation ($S_{c,D0}$) and the dry diameter at which 50% of the particles have activated ($D_{50,S}$) are calculated from CCNc and CPC data, as described in the main text.
**Section 1.2** highlights the specific CCNc measurement uncertainties and their calculation and Section 1.3 shows how the standard errors associated with the HTDMA measurements were calculated.

# 1 Definition of terms and calculation procedures

## 1.1 Fitting S-step and D-step CCNc data

Defined in the main text, the fitting function used for deriving the point at which $F_A(S, D_0) = 0.5$ is a sigmoidal function using orthogonal distance regression (ODR), weighted according to the associated errors in each axis, using the Igor Pro software package and associated libraries (*ODRPACK95*, Boggs et al. 1989).

$$y = K_0 + \frac{K_1}{1 + \exp\left((x - K_2)/K_3\right)} \tag{S1}$$

Where $K_0$ is the base of the sigmoid (held to zero), $K_1$ is the maximum on the sigmoid (unconstrained to to minimise effects caused by systematic inaccuracies of either instrument), $K_2$ is the $x$ value at which $y = 0.5$ (either, $D_{50,S}$ or $S_{c,D0}$, depending on the x-axis used) and $K_3$ is the rate.

This function is used to derive both $D_{50,S}$ and $S_{c,D0}$ for CCNc data. The fitting algorithm outputs a standard error of the x-axis value at $y = 0.5$, shown in Figures S2 and S3. These errors are propagated through to further calculations of quantities such as $D_{thres}$ and $N_{CCN}$. The standard error from S-step analysis is larger as the data consists of only 5 data points (each $S_{set}$) and hence is more sensitive to the relative positions of these data. Fitting D-step interpreted data results in a smaller standard error, Figures S2 and S3, as there are many more data points and thus higher resolution around each $D_{50,S}$.

## 1.2 CCNc Measurement Uncertainty

### 1.2.1 Uncertainty in $S_{set}$

In order to estimate the uncertainty in $S$ from the standard deviation of these quantities, the standard deviation ($\sigma$) of each measurement of temperature, flow and pressure ($T, Q$ and $P$ respectively, which are taken to vary independently) is multiplied by its differential value, summed in quadrature and divided by the square root of the number of observations ($N$; number of particles measured during an averaging period) to give the standard error in $S$:

$$\Delta S = \frac{\sqrt{\left(\frac{\partial S}{\partial T}\sigma T\right)^2 + \left(\frac{\partial S}{\partial Q}\sigma Q\right)^2 + \left(\frac{\partial S}{\partial P}\sigma P\right)^2}}{\sqrt{N}} \tag{S2}$$

The dependence of $\Delta S$ on $\sqrt{N}$ arises because the instrument detector (the OPC) only samples the conditions when a particle is detected. As $T$, $Q$ and $P$ have been assumed to vary randomly throughout the measurement period, the more particles detected, the more precise the average supersaturation will be.

### 1.2.2 Uncertainty in $D_0$

The range of diameters introduced into the CCNc for a given target diameter is described by the DMA transfer function. For this analysis, we have assumed an ideal, triangular transfer function (Knutson and Whitby, 1975), with symmetrical bounds 5% either side of the target dry diameter, $D_T$. One standard deviation of this transfer function is described by $\sigma = c\sqrt{1/6}$, where $c = 0.1D_T$ i.e. the width of the base of the transfer function. When propagating the error associated with the diameter measurement of $D_T$, the standard error of $D_T$ has been used:

$$\Delta D_T = \frac{c\sqrt{(1/6)}}{\sqrt{N}} \tag{S3}$$

where $N$ is the number of particles counted.

### 1.2.3 Uncertainty in number concentration

The CCNc and CPC number concentration standard errors have been calculated by invoking Poisson statistics:

$$\Delta(\sum N) = \sqrt{\frac{\sum N}{Q \sum T}} \tag{S4}$$

where $N$ is the number of particles counted, substituted by either CCNc ($N(S, D_0)$) or CPC ($N(D_0)$), $Q$ is the flow rate and $T$ is the sampling time. The uncertainty in $N$ is calculated and then propagated through the multiple charging correction procedure.

The error associated with the activated fraction, $F_A(S, D_0)$ can then be calculated:

$$\Delta(\sum F_A(S, D_0)) = \frac{N(S, D_0)}{N(D_0)} \sqrt{\left(\frac{\Delta(\sum N(S, D_0))}{N(S, D_0)}\right)^2 + \left(\frac{\Delta(\sum N(D_0))}{N(D_0)}\right)^2} \tag{S5}$$

### 1.3 HTDMA errors

The hygroscopic growth factor probability distribution $p(GF)$ was corrected for small deviations (typically ±2%RH) from the setpoint RH, as outlined by Gysel et al. (2009) and calculated as follows:

$$\overline{GF}_{D_0,RH,c} = \left(1 + (\overline{GF}^3_{D_0,RH_m} - 1)\frac{(1-RH_m)RH_t}{(1-RH_t)RH_m}\right)^{\frac{1}{3}} \quad \text{(S6)}$$

where $\overline{GF}_{D_0,RH,c}$ is the RH-corrected, mean, hyrgoscopic growth factor for a particle of dry diameter $D_0$, $\overline{GF}_{D_0,RH_m}$ is the uncorrected mean growth factor, $RH_m$ is the measured $RH$ and $RH_t$ is the target $RH$. A full explanation of the correction applied is described by Gysel et al. (2009).

In order to propagate the error associated with the change in growth factor from this correction, Eq. S6 is differentiated with respect to $RH_m$ to give:

$$\frac{\partial(\overline{GF}_{D_0,RH,c})}{\partial(RH_m)} = -\left((\overline{GF}_{D_0,RH_m} - 1)\frac{RH_t}{(1-RH_t)}\frac{1}{(RH_m)^2}\right)^{-\frac{1}{3}} \quad \text{(S7)}$$

An error simulation which forms part of the TDMAinv analysis was used on the data, with the results from the error simulation showing the sensitivity of the inversion result to small changes in the measurement due to added noise (incorporating counting statistics). This helps in, for example, judging whether two peaks in the growth factor probability distribution function, $p(GF)$, can be attributed to distinct modes or whether the structure of the $p(GF)$ can be reliably attributed to distinct modes or whether they are indistinguishable from instrument noise. This is outlined in detail by Gysel et al. (2009) and is shown in Figs. 4B and C therein. 100 error simulations are performed on $p(GF)$ for each growth factor bin, and the statistical mean of these taken. The standard deviation of the mean 100 simulations was then calculated, representing the effects of counting statistics and variability in size measurement, denoted by $\sigma_{p(GF)}$. These two errors are summed in quadrature, representing the HTDMA error, $GF_{error}$:

$$GF_{error} = \sqrt{\left(\frac{\partial(\overline{GF}_{D_0,RH,c})}{\partial(RH_m)}0.015\right)^2 + {\sigma_{p(GF)}}^2} \quad \text{(S8)}$$

where 0.015 relates to the precision of the measurement of $RH$ (1.5%) within the HTDMA used for the COPS experiment.

# References

[Boggs et al. (1989)] Boggs, P., Donaldson, J., Byrd, R., and Schnabel, R.: Algorithm 676: ODRPACK: software for weighted orthogonal distance regression, ACM Transactions on Mathematical Software (TOMS), 15, 364, 1989.

[Gysel et al. (2009)] Gysel, M., McFiggans, G., and Coe, H.: Inversion of tandem differential mobility analyser (TDMA) measurements, Journal of aerosol science, 40, 134–151, 2009.

[Knutson and Whitby (1975)] Knutson, E. and Whitby, K.: Aerosol classification by electric mobility: apparatus, theory, and applications, Journal of Aerosol Science, 6, 443–451, 1975.

[Rose et al. (2008)] Rose, D., Gunthe, S., Mikhailov, E., Frank, G., and Dusek, U.: Calibration and measurement uncertainties of a continuous-flow cloud condensation nuclei counter (DMT-CCNC): CCN activation of ammonium sulphate and sodium chloride particles in theory and experiment, Atmos. Chem. Phys, 8, 1153–1179, 2008.

## 2 Supplementary figures

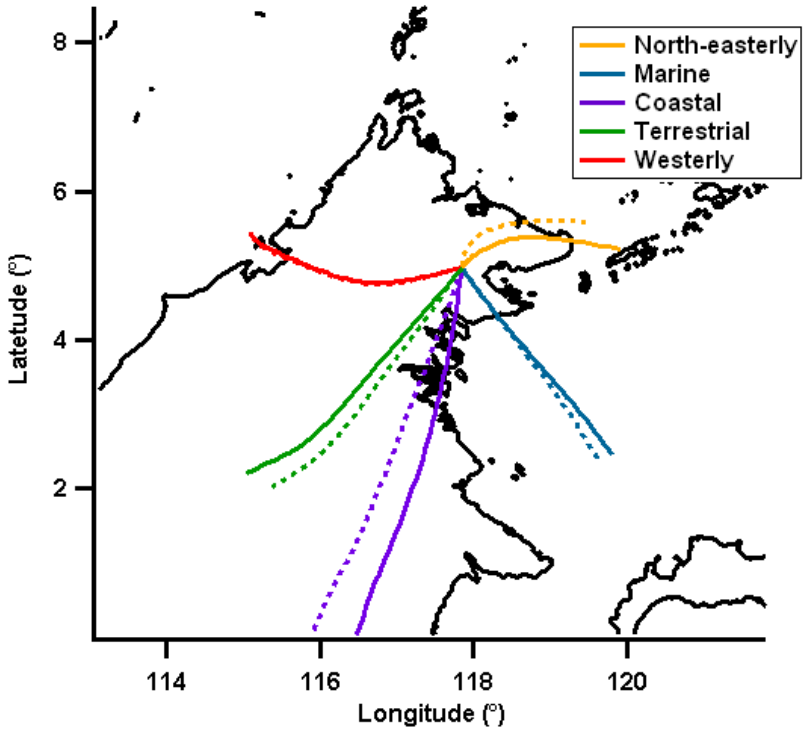


Figure S1: This plot shows the period classification mean latitude and longitude. The solid and dashed lines represent alternate back trajectory calculations. The majority of the data presented from OP3-III was attributed to Marine and Terrestrial clusters.

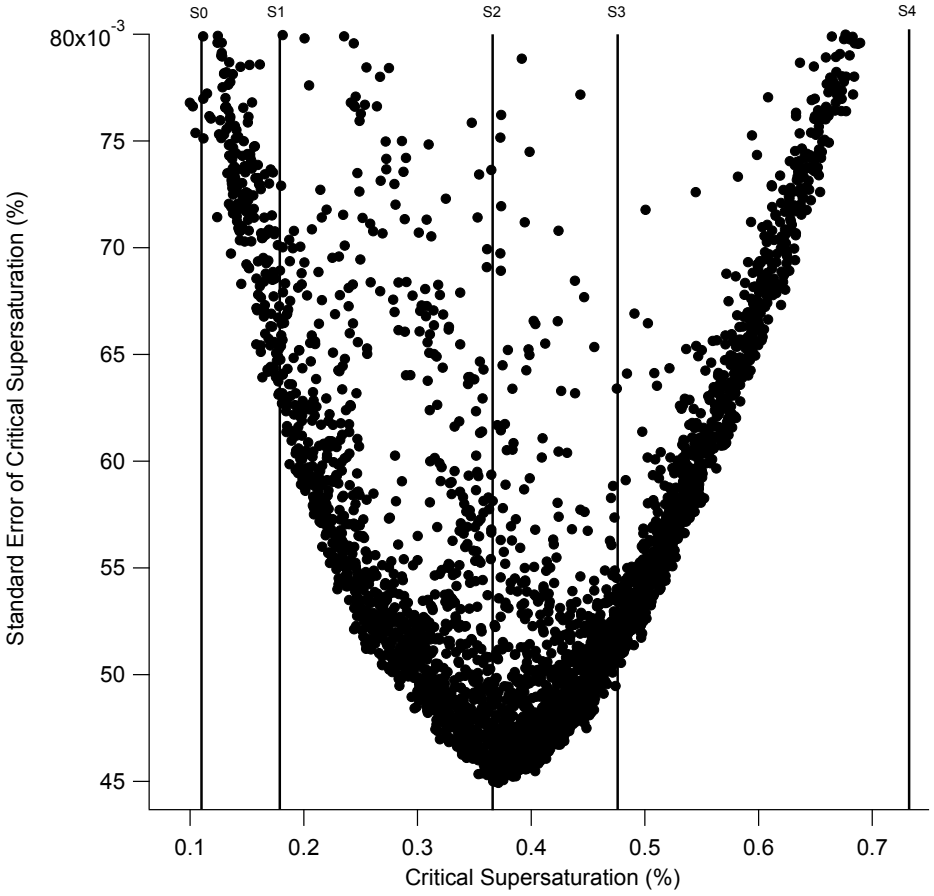


Figure S2: This plot shows the standard error of $S_{c,D0}$ plotted against the derivation of $S_{c,D0}$ from S-step analysis. The derivation of $S_{c,D0}$ has the smallest error at the central $S_{set}$ (S2). The closer the derived $S_{c,D0}$ of the particle to that of the bounds of the measurement (S0; S4), the larger the error from the fitting of the sigmoid. Data with large (relative) errors but a $S_{c,D0}$ between S1 and S3 may be influenced by mixing state or other variables within the sigmoid fitting function.

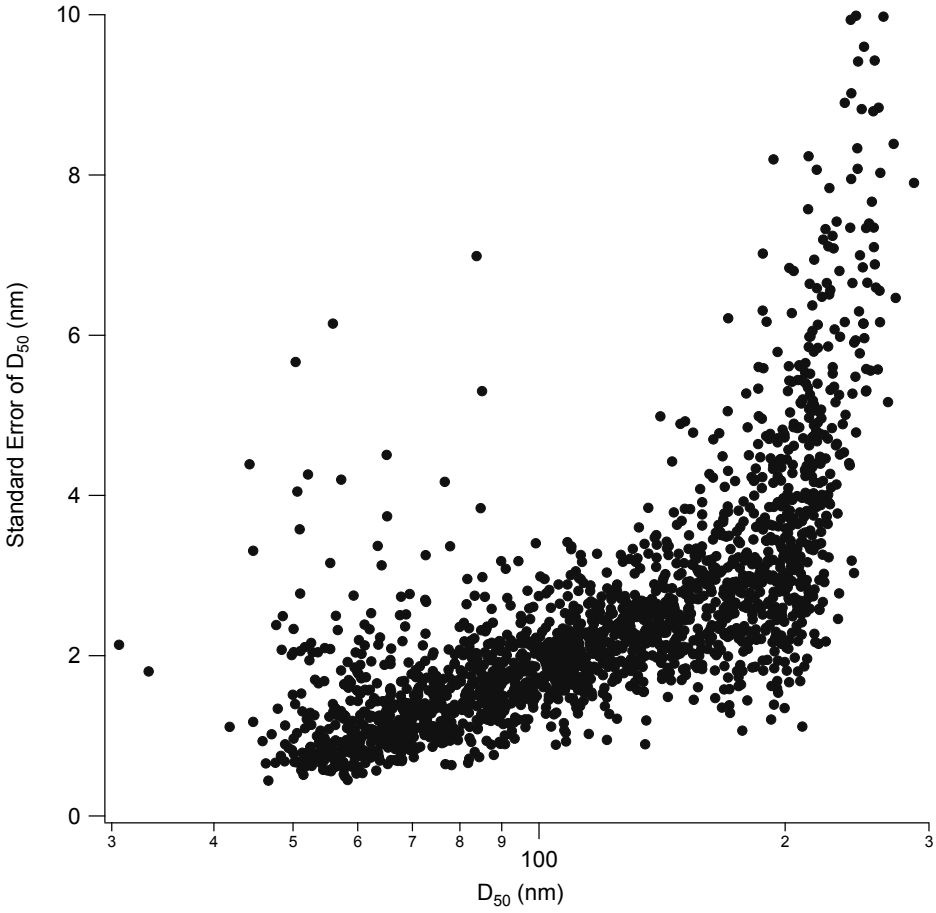


Figure S3: The error associated with fitting data using D-step analysis is, as expected, different to that associated with S-step analysed data. Only at over 200 nm does the error increase significantly. This is because, as shown in Figure 2, the fraction of aerosol activated (on average) is over 50% at the lowest supersaturation. When $F_A$ is just under 50% then the error will be large, but if over 50% then no sigmoid can be plotted.

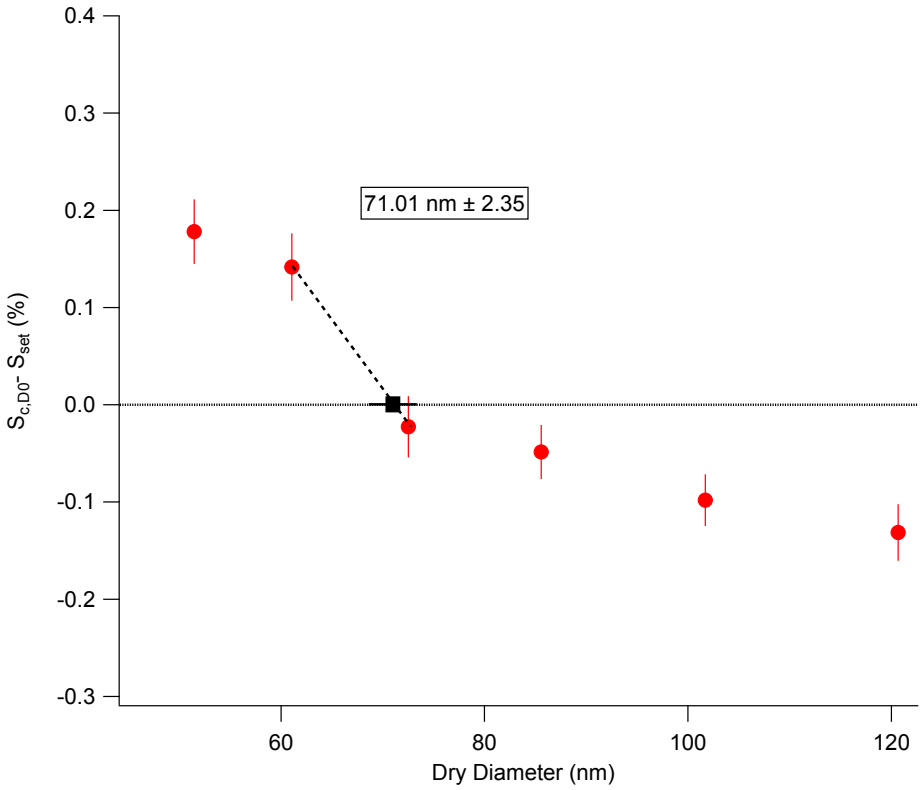


Figure S4: A graph showing $S_{c,D_0} - S_{set}$ vs $D_0$. The two data points straddling the zero line are linearly interpolated between, with the intercept defining the physical threshold diameter of the aerosol, $D_{thres,Sc}$. The errors on $D_{thres,Sc}$ are propagated using standard procedure.

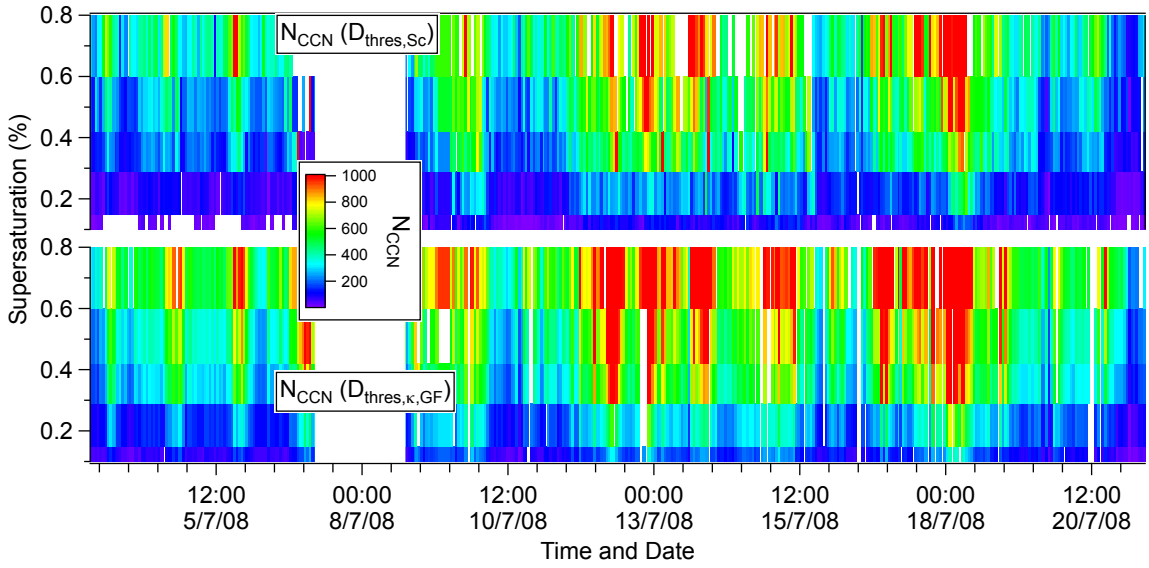


Figure S5: A time series for the OP3-III campaign showing a comparison of predicted $N_{CCN}$ from CCNc (top) S-step analysis and HTDMA measurements respectively, as a function of bin-edge supersaturation (left axis).

## 6.4 Supplementary material for Paper IV

# 1 Supplement to Figure 2

## 1.1 Continental Europe (COPS)

Figure 2a shows the slope and correlation for each of the $N_{CCN}$ calculation methods M1-M5 against supersaturation for COPS, with the strength of the correlation ($r^2$) represented by the size of the markers. The best agreement is attributed to method M1, in which the $D_{50,S}$ is averaged and $N_{CCN}$ derived for each aerosol number-size distribution. Both the agreement and overall correlation between points is higher for M1 than M2, which uses an averaged aerosol number-size distribution. The correlation is weaker and the slope further from 1:1 due to this averaging artefact. Method M3 has both the best agreement and strongest correlation out of the methods reconciling HTDMA to CCNc measurements. Averaging the aerosol number-size distribution, as done for M4, results in the worst correlation overall reconciliation of data, as the variability in the number-size distribution is not captured adequately through the process of averaging and bears little resemblance to the measurements from the CCNc. M5 improves on this greatly by averaging the hygroscopicity parameter $\kappa_{GF}$, and though the $R^2$ correlation is weaker than if individual $\kappa_{GF}$ measurements are used (M3), the overall agreement is much closer. The overall trend for COPS is to under predict $N_{CCN}$ using each of the methods, and is most sensitive to the averaging of the aerosol number-size distribution as shown by M2 and M4. Averaging $\kappa_{GF}$, M5, results in good agreement and a better correlation, with the best overall correlation given by M3, and the closest method to 1:1 given by M1, using averaged $D_{50,S}$ CCNc data.

## 1.2 Tropical Island (OP3)

Figure 2b shows the slope of the methods M1-M5 against supersaturation for the OP3. M1 is closest to 1:1 agreement with the $N_{CCN}$ calculated from individual $D_{50,S}$ and the individual size distribution, which shows the sensitivity of the CCNc measurements with respect to $D_{50,S}$. However, the high scatter of the data results in an overall low correlation than M2, where $N_{CCN}$ is calculated using the average aerosol number-size distribution. Though M2 has a better correlation, the value of the slopes show that averaging the aerosol number-size distribution for this project results in an under prediction of $N_{CCN}$ at each supersaturation. Representing the HTDMA and CCNc reconciliation are methods M3-M5, which illustrate the systematic bias between the instruments. The reconciliation with least scatter is attributed to M3, which uses each derived $D_{thres(\kappa,GF)}$ measurement to calculate $N_{CCN}$ by integrating each number-size distribution. Of almost identical correlation and slope to M3 is M5; where $D_{thres(\kappa,GF)}$ has been derived for a constant $\kappa$ from the HTDMA, in order to calculate $N_{CCN}$ for each individual number-size distribution. M4 shows the weakest correlation, with each $\kappa$ derived from the HTDMA used to calculate $D_{thres(\kappa,GF)}$, to calculate $N_{CCN}$ for an averaged number-size distribution.

### 1.3 Marine environment (RHaMBLe)

Figure 2c shows the slope of the methods M1-M5 against supersaturation for RHaMBLe. Methods M1, M3 and M5 have the best overall correlation, though exhibit the same trend of underprediction of $N_{CCN}$ at low $S$ and overpredicting $N_{CCN}$ with at higher $S$. Method M2 is the least correlated out of all measurements, illustrating the importance of the aerosol number-size distribution for these marine measurements, resulting in an almost constant overprediction of $N_{CCN}$ at each supersaturation. M4 also shows poor correlation, further enforcing this interpretation. Correlation is strong for the project regardless of whether the threshold diameter for activation is averaged or not. The trends between CCNc and HTDMA data are similar, shown by the slopes of M1 and M3/5.

## 2 Slopes and correlations for COPS and OP3

Table 1: Methodology results for COPS

| S (%) | M1 Slope | M1 R2 | M2 Slope | M2 R2 | M3 Slope | M3 R2 | M4 Slope | M4 R2 | M5 Slope | M5 R2 |
|---|---|---|---|---|---|---|---|---|---|---|
| 0.11 | 1.052 | 0.775 | 0.679 | 0.005 | 1.080 | 0.873 | 0.704 | 0.024 | 1.191 | 0.759 |
| 0.17 | 0.984 | 0.931 | 0.665 | 0.055 | 0.640 | 0.923 | 0.385 | 0.090 | 0.677 | 0.929 |
| 0.32 | 0.943 | 0.978 | 0.559 | 0.203 | 0.670 | 0.946 | 0.346 | 0.004 | 0.671 | 0.955 |
| 0.50 | 0.971 | 0.980 | 0.604 | 0.110 | 0.740 | 0.945 | 0.400 | 0.022 | 0.734 | 0.939 |
| 0.80 | 0.768 | 0.983 | 0.805 | 0.007 | 0.820 | 0.988 | 0.553 | 0.095 | 0.795 | 0.986 |

Table 2: Methodology results for OP3

| S (%) | M1 Slope | M1 R2 | M2 Slope | M2 R2 | M3 Slope | M3 R2 | M4 Slope | M4 R2 | M5 Slope | M5 R2 |
|---|---|---|---|---|---|---|---|---|---|---|
| 0.11 | 0.917 | 0.502 | 0.958 | 0.105 | 2.117 | 0.467 | 2.228 | 0.055 | 2.065 | 0.453 |
| 0.18 | 0.758 | 0.324 | 0.950 | 0.395 | 1.397 | 0.303 | 1.501 | 0.019 | 1.392 | 0.362 |
| 0.37 | 0.848 | 0.370 | 1.003 | 0.229 | 1.393 | 0.547 | 1.449 | 0.046 | 1.362 | 0.449 |
| 0.48 | 0.898 | 0.450 | 1.021 | 0.174 | 1.335 | 0.781 | 1.380 | 0.051 | 1.316 | 0.579 |
| 0.73 | 0.949 | 0.538 | 1.051 | 0.071 | 1.302 | 0.584 | 1.332 | 0.001 | 1.299 | 0.574 |

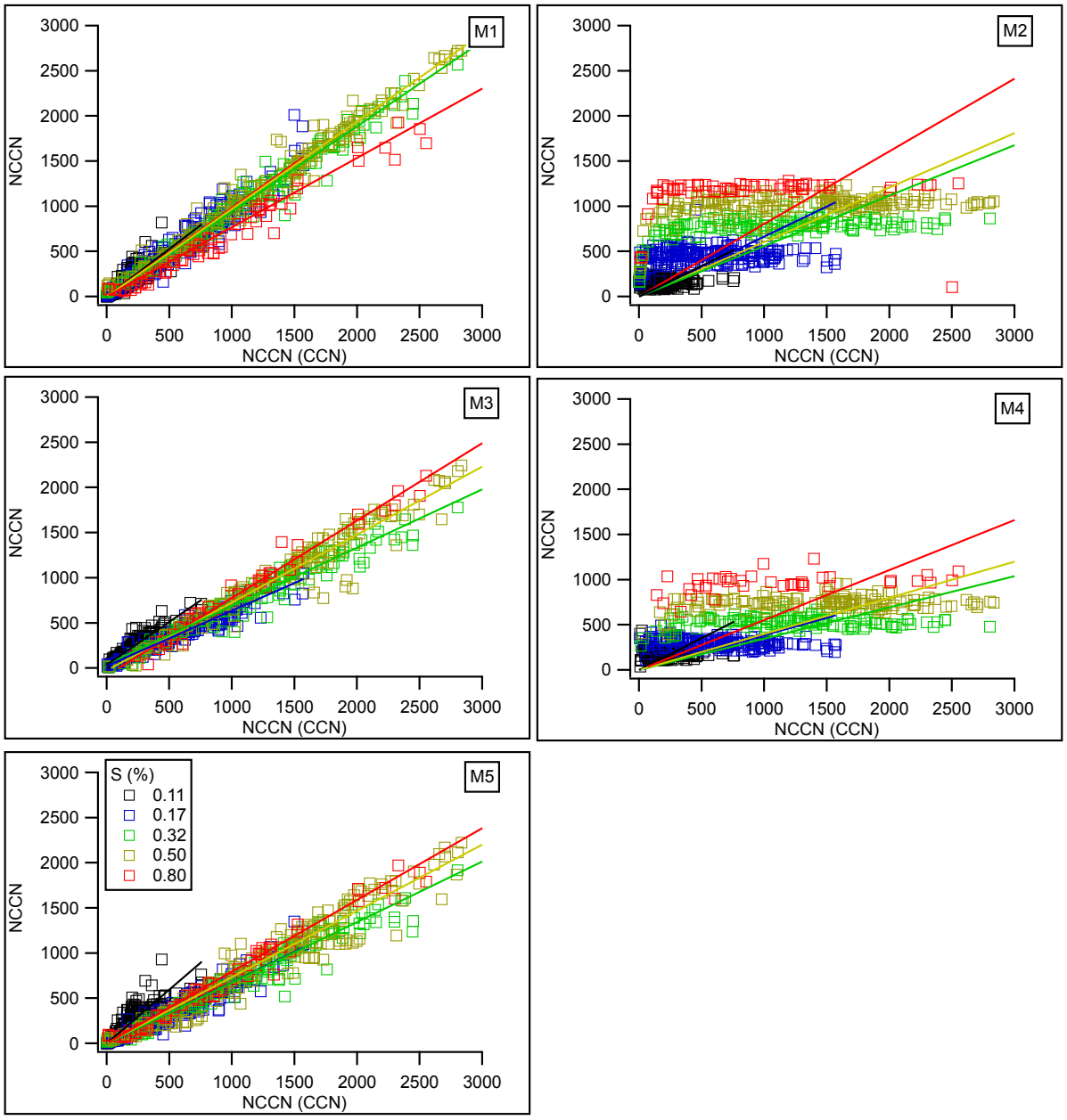


Figure 1: $N_{CCN}$ for each method M1-M5 plotted against $N_{CCN}$ from the CCN counter, for each $D_{50,S}$ during COPS

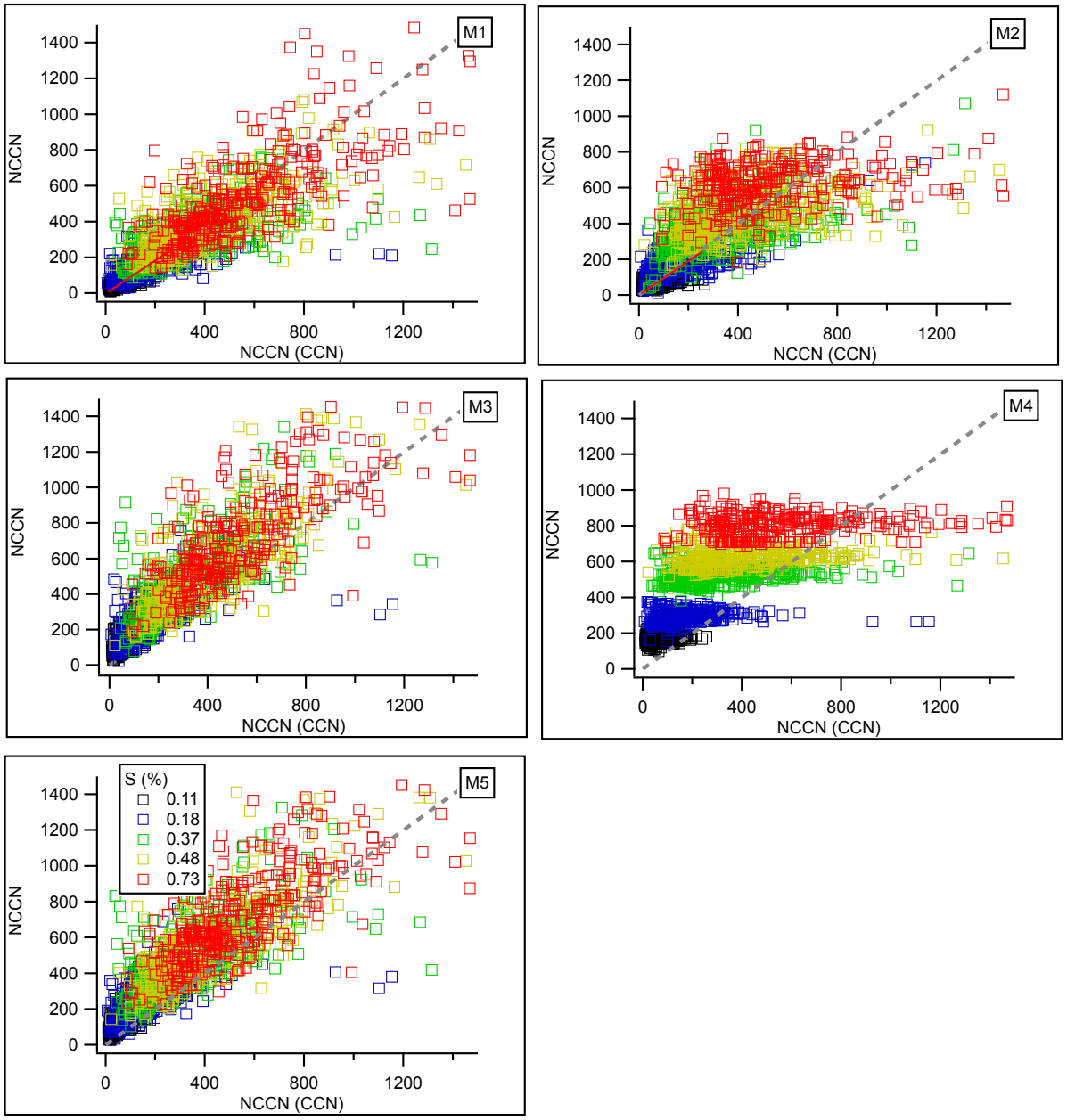


Figure 2: $N_{CCN}$ for each method M1-M5 plotted against $N_{CCN}$ from the CCN counter, for each $D_{50,S}$ during OP3